

Simulation Study for Geodetic Parameter Recovery at Europa and Callisto

Inaugural dissertation
of the Faculty of Science,
University of Bern

presented by

William Desprats

from France

Supervisor of the doctoral thesis:

Dr. Daniel Arnold

Astronomical Institute, University of Bern

Co-supervisors of the doctoral thesis:

Dr. Stefano Bertone

INAF, Astrophysical Observatory of Torino, Italy

University of Maryland, College Park, USA

Prof. Dr. Michel Blanc

IRAP, CNRS-Université Paul Sabatier, Toulouse, France

Prof. Dr. Adrian Jäggi

Astronomical Institute, University of Bern

Simulation Study for Geodetic Parameter Recovery at Europa and Callisto

Inaugural dissertation
of the Faculty of Science,
University of Bern

presented by

William Desprats

from France

Supervisor of the doctoral thesis:

Dr. Daniel Arnold

Astronomical Institute, University of Bern

Co-supervisors of the doctoral thesis:

Dr. Stefano Bertone

INAF, Astrophysical Observatory of Torino, Italy

University of Maryland, College Park, USA

Prof. Dr. Michel Blanc

IRAP, CNRS-Université Paul Sabatier, Toulouse, France

Prof. Dr. Adrian Jäggi

Astronomical Institute, University of Bern

Accepted by the Faculty of Science.

Bern, 13th February 2024

The Dean

Prof. Dr. Marco Herwegh

©Copyright William Desprats

The material in this publication is protected by copyright law.
This work is licensed under a Creative Commons Attribution
4.0 International License

<https://creativecommons.org/licenses/by/4.0/>



Year: 2024

Title: Simulation Study for Geodetic Parameter Recovery at Europa and Callisto

Author: William Desprats

Acknowledgements

First and foremost, I would like to thank Dr. Daniel Arnold for his full commitment as guide during these four years. He was thorough and always had interesting ideas to test, which I enjoyed discussing. I don't think I could have had a better supervisor for my PhD. I am grateful to have met Dr. Stefano Bertone, who took me under his wing during my first time in Bern. Our collaborations have always been very motivating and efficient. I want to thank Prof. Dr. Adrian Jäggi for hosting me at the Astronomical Institute of the University of Bern and for offering me the opportunity to conduct this research. And also Prof. Dr. Michel Blanc, who had been one of the first to introduce me to the world of research and for the enabled valuable international collaborations.

I also want to thank the colleagues from Astronomical Institute for their help and support, especially Cyril, Emilio, Julian, Linda and Martin, for the good moments we shared during our PhD time. A special mention to Martin for the helpful exchanges regarding implementations within the Bernese GNSS Software.

Thanks to all who contributed to the success of this work, but more particularly to my mother, my two sisters Aurélie and Josiane and my partner Céline for their love and comprehension. I am also truly grateful to have had my father, who couldn't see the end of this journey. He was the first to reassure me on the path to choose.

Contents

| | | |
|----------|--|----------|
| 1 | Introduction | 1 |
| 1.1 | The Jupiter System | 1 |
| 1.1.1 | The Jovian environment | 1 |
| 1.1.2 | The Galilean moons | 2 |
| 1.2 | Exploration of Europa and Callisto | 4 |
| 1.2.1 | Next decade’s planned missions | 4 |
| 1.2.2 | Recent mission proposals | 5 |
| 1.3 | Scope of this work | 7 |
| 2 | Models and observables | 9 |
| 2.1 | Orbit modelling | 9 |
| 2.2 | Force model of an orbiter at the Galilean moons | 12 |
| 2.2.1 | Synthetic gravity field | 12 |
| 2.2.2 | Solid tides | 15 |
| 2.2.3 | Third-body perturbations | 16 |
| 2.2.4 | Non-gravitational accelerations | 16 |
| 2.2.5 | Empirical accelerations and pseudo-stochastic parameters | 17 |
| 2.3 | Generalized orbit determination | 18 |
| 2.3.1 | Non-linear least-squares adjustment | 18 |
| 2.3.2 | Variational equations | 19 |
| 2.3.3 | Stacking Normal Equation Systems | 21 |
| 2.3.4 | General processing scheme | 21 |
| 2.4 | Rotation model | 24 |
| 2.4.1 | IAU Conventions | 24 |
| 2.4.2 | Updated models and librations | 26 |
| 2.4.3 | Partial derivatives of rotation model | 27 |
| 2.5 | Accelerometer model | 28 |
| 2.6 | Doppler observables | 29 |
| 2.6.1 | Formulation of the two-way Doppler observables | 29 |
| 2.6.2 | Assessment of numerical errors in Doppler observables | 31 |
| 2.6.3 | Noise model | 34 |
| 2.7 | Laser altimetry data | 35 |
| 2.7.1 | Altimetric range simulation | 36 |
| 2.7.2 | Crossover discrepancy | 38 |
| 2.7.3 | Crossover partial derivatives | 39 |
| 2.8 | Internal structure modelling | 40 |

| | | |
|----------|--|------------|
| 2.8.1 | Moment of Inertia | 41 |
| 2.8.2 | Putative subsurface ocean and ice-shell | 44 |
| 2.8.3 | Summary | 46 |
| 3 | Low altitude orbit design around Jovian moons | 49 |
| 3.1 | Repetitive Ground Track Orbits | 49 |
| 3.2 | Orbit refinement | 52 |
| 3.2.1 | The Hill model | 52 |
| 3.2.2 | Differential correction | 53 |
| 3.3 | Evolution of the orbital elements | 56 |
| 3.3.1 | Perturbing equations in the local orbital frame | 56 |
| 3.3.2 | Choice of inclination | 59 |
| 3.4 | Orbit propagation in an extended force model | 60 |
| 3.4.1 | Reference plane of the Hill model | 61 |
| 3.4.2 | Definition of an orbit scenario | 62 |
| 3.4.3 | Reducing the orbit discontinuities | 64 |
| 4 | Orbit determination and geodetic parameter recovery using Doppler observations only | 69 |
| 4.1 | Orbit determination quality | 70 |
| 4.1.1 | Orbit deficiencies | 71 |
| 4.1.2 | Length of the estimation arc | 74 |
| 4.1.3 | Importance of the ground station tracking | 76 |
| 4.1.4 | Orbit and global parameters | 78 |
| 4.2 | Gravity field recovery strategies | 79 |
| 4.2.1 | Using pseudo-stochastic pulses | 81 |
| 4.2.2 | Co-estimation of the low-degree gravity field coefficients | 82 |
| 4.2.3 | Comparison | 83 |
| 4.3 | Low orbit design for gravity field recovery: case of Europa | 84 |
| 4.3.1 | Ground tracks repetition | 85 |
| 4.3.2 | Earth beta-angle | 87 |
| 4.3.3 | Altitude | 90 |
| 4.3.4 | Inclination | 91 |
| 4.3.5 | Eclipses by Jupiter | 92 |
| 4.4 | Estimation of rotation parameters | 96 |
| 4.5 | Mitigation strategies for non-gravitational accelerations: case of Callisto | 99 |
| 4.5.1 | Pseudo-stochastic pulses | 100 |
| 4.5.2 | On-board accelerometer | 102 |
| 4.5.3 | Empirical accelerations | 104 |
| 4.5.4 | Comparison and impact on gravity field recovery | 107 |
| 5 | Combination of altimetry crossover and Doppler observables | 111 |
| 5.1 | Combination procedure and search for crossover discrepancies | 112 |
| 5.1.1 | Description of the combination | 112 |
| 5.1.2 | Distribution of the crossover discrepancies | 114 |
| 5.2 | Improvement of the estimated orbital elements | 117 |

| | | |
|----------|---|------------|
| 5.2.1 | Impact of topography roughness on orbit parameters | 117 |
| 5.2.2 | Orbit improvement and orbit geometries | 119 |
| 5.3 | Impact on the estimation of accelerometer biases | 123 |
| 5.4 | Estimation of the complete set of geodetic parameters | 125 |
| 5.4.1 | Impact of topography roughness on rotation parameters only | 125 |
| 5.4.2 | Inclusion of the gravity field coefficients with different topographies . | 127 |
| 5.4.3 | Contribution of altimetry for different orbit configurations | 130 |
| 6 | Summary and conclusions | 135 |
| | Bibliography | 139 |
| | Scientific environment and publications | 153 |

List of Figures

| | | |
|------|--|----|
| 1.1 | Europa, Ganymede and Callisto surfaces from Galileo Orbiter | 2 |
| 2.1 | Osculating orbital elements $(a, e, i, \Omega, \omega, u)$ | 10 |
| 2.2 | Magnitude of accelerations on a Europa orbiter. | 12 |
| 2.3 | Magnitude of accelerations on a Callisto orbiter. | 13 |
| 2.4 | Geoid heights of the Callisto and Europa synthetic gravity fields. | 14 |
| 2.5 | GRAVDET2 flowchart | 22 |
| 2.6 | Generalized orbit determination flowchart. | 23 |
| 2.7 | Orientation of the planets and their satellites from the IAU Reports | 25 |
| 2.8 | Geometry of Europa's libration. | 27 |
| 2.9 | Computation of the geometric distance. | 32 |
| 2.10 | Numerical error model on Doppler observables computation($\tau = 60$ s). | 33 |
| 2.11 | Noise model for two-way Ka-band Doppler at $\tau = 60$ s. | 35 |
| 2.12 | Small-scale topography. | 37 |
| 2.13 | Schematic illustration of altimeter crossover approach. | 38 |
| 2.14 | Workflow of the pyXover code | 39 |
| 2.15 | Precession of the poles in a Cassini state. | 43 |
| 2.16 | Overlapping measurements constraining the ice shell and ocean thickness. | 44 |
| 2.17 | Admittances for different ice shell characteristics. | 46 |
| 2.18 | From the estimation of geodetic and geophysical parameters to the characterisation of the interior of the icy moons. | 46 |
| 3.1 | 3:118 RGTO ($i = 89^\circ$, $h = 135$ km) in Europa-fixed frame. | 50 |
| 3.2 | Orbital plane of the probe at t_0 and t_s with respect to Jupiter and Earth. | 53 |
| 3.3 | Orbital plane of the probe with respect to the Earth characterised by β_{Earth} | 57 |
| 3.4 | Comparison of 5:197 Europa RGTO starting on equatorial or orbital plane. | 61 |
| 3.5 | Crossing points w.r.t. the equatorial plane for 1:40 and 3:118 RGTOs. | 63 |
| 3.6 | β_{Earth} function of the initial location number c_0 for a 1:40 RGTO | 63 |
| 3.7 | Amplitude of the orbit discontinuities for improved force-models. | 67 |
| 4.1 | Orbit differences for each arc in the $(\mathbf{e}_1, \mathbf{e}_2, \mathbf{e}_3)$ frame for a 5:197 RGTO | 72 |
| 4.2 | Velocity differences for each arc in the $(\mathbf{e}_1, \mathbf{e}'_2, \mathbf{e}'_3)$ frame for a 5:197 RGTO | 72 |
| 4.3 | Orbital elements correlations w.r.t. β_{Earth} for ~ 28 h arcs | 73 |
| 4.4 | Orbital elements correlations w.r.t. β_{Earth} for ~ 86 h arcs | 75 |
| 4.5 | Orbit differences for different β_{Earth} and arc lengths. | 75 |
| 4.6 | Tracking from the Chinese DSN. | 76 |
| 4.7 | Orbit differences for every arc in for an RGTO around Europa. | 79 |

| | | |
|------|--|-----|
| 4.8 | Correlations between osculating orbital elements for a 26:1023 Europa RGTO. | 80 |
| 4.9 | Difference degree amplitudes of reference solution EURSOL01. | 80 |
| 4.10 | Difference degree amplitude estimating up to d/o 90 using pulses. | 82 |
| 4.11 | Degree amplitudes for solutions with increasing number of coefficients. . . . | 83 |
| 4.12 | Doppler residuals and orbit differences for each iteration and each methods. | 84 |
| 4.13 | Difference degree amplitudes for different RGTO parameters. | 86 |
| 4.14 | Degree amplitudes for $m:R$ RGTOs showing the benefit of a Kaula constraint for $m \geq 3$ | 87 |
| 4.15 | Ground tracks from a 26:1023 RGTO visible from Earth with $\beta_{Earth} = 58^\circ$ | 88 |
| 4.16 | Critical latitude ϕ_c with respect to Earth as a function of β_{Earth} | 88 |
| 4.17 | Differences of gravity field coefficients recovered for several β_{Earth} values. . . | 89 |
| 4.18 | Degree amplitude of solutions for different β_{Earth} w/ or w/o Kaula constraint. | 89 |
| 4.19 | RMS of geoid height differences and critical latitude as a function of β_{Earth} . | 90 |
| 4.20 | Degree amplitudes and geoid height differences for solutions with different altitudes. | 91 |
| 4.21 | β_{Earth} variation over 3 months for a polar orbit and an 80° -inclined orbit. . | 92 |
| 4.22 | Differences of gravity field coefficients recovered from polar and non polar orbits. | 93 |
| 4.23 | Ground coverage with occultation from Jupiter for different β_{Earth} | 94 |
| 4.24 | Degree and order amplitude for different β_{Earth} w/ Jupiter occultations. . . | 95 |
| 4.25 | Degree amplitude of solutions for different β_{Earth} w/ or w/o Kaula constraint. | 95 |
| 4.26 | Difference degree amplitude considering different constraints on rotation parameters. | 97 |
| 4.27 | Correlations between gravity field and unconstrained rotation parameters. . . | 97 |
| 4.28 | Correlations between gravity field and constrained rotation parameters. . . . | 98 |
| 4.29 | Non-gravitational accelerations for $\beta_{Sun} \approx -72^\circ$ and $\beta_{Sun} \approx -1^\circ$ | 100 |
| 4.30 | Orbit determination flowchart for NGA mitigation | 100 |
| 4.31 | Pulse constraints estimated using VCE. | 101 |
| 4.32 | Orbit differences using pulses to mitigate NGA. | 102 |
| 4.33 | RMS error of estimated accelerometer biases for $\beta_{Earth} = 72^\circ$ and $\beta_{Earth} = 1^\circ$. | 103 |
| 4.34 | RMS error of estimated accelerometer biases for $\beta_{Earth} = 72^\circ$ and $\beta_{Earth} = 1^\circ$. | 104 |
| 4.35 | RMS error of estimated empirical parameters for $\beta_{Earth} = 72^\circ$ | 105 |
| 4.36 | RMS error of estimated empirical parameters for $\beta_{Earth} = 1^\circ$ | 106 |
| 4.37 | RMS error of orbit differences using empirical modelling. | 107 |
| 4.38 | RMS of orbit differences for several mitigation strategies for $\beta_{Earth} = 1^\circ$ and $\beta_{Earth} = 72^\circ$ | 108 |
| 4.39 | Difference degree amplitude for several mitigation strategies for $\beta_{Earth} = 1^\circ$ and $\beta_{Earth} = 72^\circ$ | 109 |
| 5.1 | Flowchart for Doppler and altimetry crossovers combination. | 113 |
| 5.2 | Distribution of the crossovers along latitudes ϕ for different β_{Earth} | 115 |
| 5.3 | Distribution of the crossover discrepancies with different topography model. | 116 |
| 5.4 | Crossover discrepancies at 10 Hz and 30 Hz. | 117 |
| 5.5 | RMS of orbit differences with/without crossover combination for $\beta_{Earth} = 1^\circ$. | 119 |
| 5.6 | Correlation map between orbital elements for a Doppler only orbit. | 120 |
| 5.7 | Correlation map between orbital elements for a Doppler and crossover orbit. | 120 |

| | | |
|------|---|-----|
| 5.8 | RMS of orbit differences with/without crossover combination for $\beta_{Earth} = 72^\circ$. | 121 |
| 5.9 | Average absolute correlations between orbital elements for a Doppler orbit. | 121 |
| 5.10 | Average absolute correlations between orbital elements for a Doppler and crossover orbit. | 122 |
| 5.11 | Estimated accelerometer biases with/without altimetry crossover combination. | 123 |
| 5.12 | RMS of orbit differences with/without altimetry crossover combination. | 124 |
| 5.13 | Ground coverage of Callisto from a polar orbiter for $\beta_{Earth} = 1^\circ$. | 125 |
| 5.14 | Errors of rotation parameters and Love number h_2 , for Doppler-only solution or combining Doppler and crossovers. | 127 |
| 5.15 | Errors of rotation parameters and Love number h_2 estimating gravity field parameters, for Doppler-only solution or combining Doppler and crossovers. | 129 |
| 5.16 | Correlations between gravity field and rotation parameters with/without crossover combination. | 129 |
| 5.17 | Correlations between gravity field and rotation parameters with/without small-scale topography. | 130 |
| 5.18 | Difference degree amplitude of gravity field solutions using only Doppler or combining with crossovers observations with different topography models. | 131 |
| 5.19 | Difference degree amplitude of gravity field solutions using only Doppler or combining with crossovers observations for different β_{Earth} . | 132 |
| 5.20 | Correlations between gravity field and rotation parameters with/without crossover combination for $\beta_{Earth} = 1^\circ$. | 133 |
| 5.21 | Correlations between gravity field and rotation parameters with/without crossover combination for $\beta_{Earth} = 72^\circ$. | 134 |

List of Tables

| | | |
|-----|---|-----|
| 2.1 | List of estimated parameters. | 23 |
| 2.2 | Polynomial coefficients for Europa and Callisto orientation. | 24 |
| 2.3 | Coefficients of the trigonometric part for Europa and Callisto orientation. | 25 |
| 2.4 | NASA Deep Space Network | 29 |
| 2.5 | Chinese Deep Space Network | 30 |
| 2.6 | Spacecraft turnaround ratio M_2 | 30 |
| 3.1 | $m:R$ RGTO with their altitude and cycle intertrack for Europa and Callisto. | 51 |
| 3.2 | Orbit discontinuities for 5:197 Europa RGTOs with improved force models. | 66 |
| 3.3 | Orbit discontinuities for 1:142 Callisto RGTOs with improved force models. | 68 |
| 4.1 | Tracking time and orbit differences after an orbit-only fit, for different station schedules. | 77 |
| 4.2 | Number of observations, $(\Delta g)_{\text{WRMS}}$ and max. degree recovered, after solving for all parameters, for different station schedules. | 78 |
| 4.3 | Number of iterations and computation time for each method to recover a 90-degree gravity field. | 83 |
| 4.4 | Constraints and formal errors of rotation parameters estimated freely or using VCE. | 96 |
| 4.5 | Formal uncertainties of the geophysical parameters from JUICE and MAGIC simulations, completed with our results | 99 |
| 4.6 | Empirical parameters fitting the true non-gravitational accelerations. | 105 |
| 5.1 | Observation residuals and orbit differences for $\beta_{\text{Earth}} = 1^\circ$ and for different topography models. | 118 |
| 5.2 | Crossover discrepancy residuals and orbit differences for different orbits. | 122 |
| 5.3 | Formal errors of rotation parameters and Love number h_2 , considering different observation types and topography models for $\beta_{\text{Earth}} = 1^\circ$ | 126 |
| 5.4 | True errors of rotation parameters and Love number h_2 , considering different observation types and topography models for $\beta_{\text{Earth}} = 1^\circ$ | 127 |
| 5.5 | Formal errors of rotation parameters and Love numbers, considering different observation types and topography models, and gravity field parameters. | 128 |
| 5.6 | True errors of rotation parameters and Love numbers, considering different observation types and topography models, and gravity field parameters. | 128 |
| 5.7 | True and formal errors of rotation parameters and Love numbers h_2 and k_2 , estimated with gravity field parameters. | 133 |

Acronyms

3GM Gravity and Geophysics of Jupiter and the Galilean Moons. 4

AIUB Astronomical Institute of the University of Bern. 7, 153

BELA BepiColombo Laser Altimeter. 36, 37, 116

BSW Bernese GNSS Software. 7, 8, 10, 11, 20, 22, 23, 29, 31, 34, 36, 37, 39, 40, 49, 60–64, 66, 69, 112, 113, 116, 135–137

CMA Celestial Mechanics Approach. 18, 69, 70, 78

CNSA Chinese National Science Administration. 7

DEM Digital Elevation Model. 37, 115–118, 129, 130

DSN Deep Space Network. 29, 69, 76–78, 84, 98, 99, 112, 135

DST Deep Space Transponder. 35

ESA European Space Agency. 4, 6

GALA GAnymede Laser Altimeter. 4, 36, 38, 116

GINs Géodésie par Intégrations Numériques Simultanées. 7

GNSS Global Navigation Satellite System. 7

IAU International Astronomical Union. 24–27, 96

ICRF International Celestial Reference Frame, *Glossary*: ICRF. 24

IPT Io Plasma Torus. 1, 30, 34

JEM Joint Europa Mission. 6

JPL Jet Propulsion Laboratory. 12

JUICE Jupiter Icy Moons Explorer. 4–6, 28, 38, 49, 50, 98, 99, 112, 135, 137

LRO Lunar Reconnaissance Orbiter. 111

MAGIC Magnetism, Altimetry, Gravity, and Imaging of Callisto. 6, 91, 98, 99

MGS Mars Global Surveyor. 111

MoI Moment of Inertia. 3, 41–43, 46, 98

NAIF Navigation and Ancillary Information Facility. 11

NASA National Aeronautics and Space Administration. 4–6, 29, 76, 84, 135

NEQ Normal Equation. 21, 23, 40, 78, 81, 82, 100, 113, 116–118, 123, 132

ODE Ordinary Differential Equations. 49

PRP Planetary Radiation Pressure. 17, 28, 104

RDA Radau-Darwin Approximation. 3, 41, 42

RGTO Repetitive Ground Track Orbit. 49–51, 54, 59, 61–68, 72, 73, 75, 77–80, 85, 87–90, 92–96, 99–101, 103–107, 112, 135

RMS Root Mean Square, *Glossary: RMS*. 23, 33, 34, 70–72, 74, 77–79, 81, 83, 84, 90, 91, 102–108, 118, 119, 121, 122, 124

RSW Local Orbital Frame, *Glossary: RSW*. 17, 39, 57, 107

SPK Spacecraft Kernel. 11, 12, 37, 113, 114

SRP Solar Radiation Pressure. 17, 28, 104

STD Standard Orbit. 11, 37, 40, 113, 116

STM State Transition Matrix. 54, 55, 65

TVN Local Orbital Frame, *Glossary: TVN*. 39, 40

VCE Variance Component Estimation. 21, 94, 96–98, 100–102, 105, 107, 108, 117, 118, 122–125, 131, 132, 136, 137

Glossary

ICRF The International Celestial Reference Frame (ICRF) realizes an ideal reference system, the International Celestial Reference System (ICRS), by precise equatorial coordinates of extragalactic radio sources observed in Very Long Baseline Interferometry (VLBI) programmes. The ICRS equator is close to the mean equator of the Earth at J2000.0 (2000-01-01, 12:00 TT) and the origin of right ascension of the ICRS is close to the dynamical equinox at J2000.0.

RMS The Root Mean Square (RMS) denotes the quadratic mean formed as the square root of the mean square for a set of $\{x_1, \dots, x_N\}$ by $m_{\text{RMS}} = \sqrt{\frac{1}{N} \sum_{n=1}^N x_n^2}$.

RSW R, S and W are defining the axes of a right-handed Cartesian coordinate system called local orbit frame, where the axes are pointing in radial (R), along-track (S) and cross-track (W) direction with its origin in the satellite's centre of mass.

TVN T, V and N are defining the axes of a right-handed Cartesian coordinate system called local orbit frame, where the axes are pointing in the transverse direction (T), along the velocity vector (V) and normal to the orbital plane (N) with its origin in the satellite's centre of mass.

Chapter 1

Introduction

1.1 The Jupiter System

1.1.1 The Jovian environment

Jupiter, by far the largest planet of the Solar System, formed around 4.5 billion years ago out of the proto-nebula. This gas giant has been confirmed to be orbited by more than 95 moons [Sheppard et al., 2023]. These moons are classified in three groups: the inner moons, the Galilean moons, and the multitude of irregular moons (which are divided into prograde and retrograde satellites). The four Galilean moons (Io, Europa, Ganymede and Callisto) were discovered in 1610 by Galileo Galilei. They formed from the Jovian circumplanetary disk [e.g., Sasaki et al., 2010], and are located within the magnetosphere of Jupiter, which is the largest structure within the Solar System, starting at 75 Jupiter radii ($R_J = 71\,492$ km) in the direction of the Sun, and stretching beyond the orbit of Saturn.

Jupiter's magnetic field, about 20 times stronger than the Earth's magnetic field, is generated from the rapid rotation of Jupiter, with a period of 9 h 55 min, and its conductive metallic hydrogen outer mantle acting as a massive dynamo. The harshest region of Jupiter's strong radiation belts extends slightly beyond Europa's orbit ($< 10R_J$), thus including also the orbit of Io. Because of the large difference between the rotation rate of Jupiter's magnetosphere, and the much slower revolution period of Io (40 h 28 min), approximately one ton per second of ions is swept from the atmosphere of Io and is accelerated because of the magnetosphere. This creates a large plasma torus (IPT), the diameter of which is equivalent to Jupiter's diameter. A less important process also affects Europa, creating a cold gas torus along Europa's orbit. On the other hand, Ganymede and Callisto are located in the middle of the magnetosphere ($10R_J - 40R_J$), and are subjected to a less radiative environment, but still protected from the solar winds.

The first probe exploring the Jupiter system was Pioneer 10 in 1973, followed by Pioneer 11 in 1974 [Fimmel et al., 1977], witnessing for the first time the unexpected intensity of the radiation environment. The analysis of the flyby of each probe allowed for a first refinement of the mass of the Jovian system. A few years later, the Voyager program allowed for Voyager 1 and 2 [Morrison and Samz, 1980] flybys Jupiter once each in 1979, discovering Jupiter's rings [Smith et al., 1979] and the volcanic activity on Io. Ulysses [Bame

et al., 1992] followed several years later and performed two flybys of Jupiter in 1992 and 2004, leading to a better characterisation of the magnetosphere of Jupiter. The Sun was, however, the main focus of this mission, and Jupiter allowed the probe to go into a polar orbit around its much larger target.

The Galileo mission [Russell, 2012] was the first mission to insert a probe into orbit around Jupiter in 1995. It enabled ground breaking discoveries despite its limitations (only the S-band antenna was operative), including the first strong evidence of subsurface oceans below the icy surfaces of the outer Galilean moons. In the meantime, in its course toward Saturn, the Cassini-Huygens [Russell, 2005] probe flew by Jupiter in 2000, and several years later, in 2007, the New Horizons mission [Stern, 2009] passed by the Jovian system. More recently, the Juno mission [Bolton et al., 2010] was inserted into orbit around Jupiter in 2016 and dedicated most of its investigation to Jupiter. However, after a mission extension, Juno had the opportunity to fly by the three inner Galilean moons [Hansen et al., 2022].

1.1.2 The Galilean moons

Surface features, geological activity and subsurface ocean

The Voyager and Galileo missions revealed a young, bright and deformed surface at Europa. High-resolution images from the Galileo’s imager (see Fig. 1.1, left) showed that the surface is criss-crossed by *lineae*, dark cracks and ridges, separated by smooth bands, with only a few large craters [Greeley et al., 2004]. This surface appears to be renewed through recent or geologic activity [Howell and Pappalardo, 2020]. On the contrary, Callisto has an ancient surface covered with craters (see Fig. 1.1, right), it does not appear to have been modified by internal processes [Greeley et al., 2000], and is thus considered as a record keeper of the formation and evolution of the Jovian satellites.

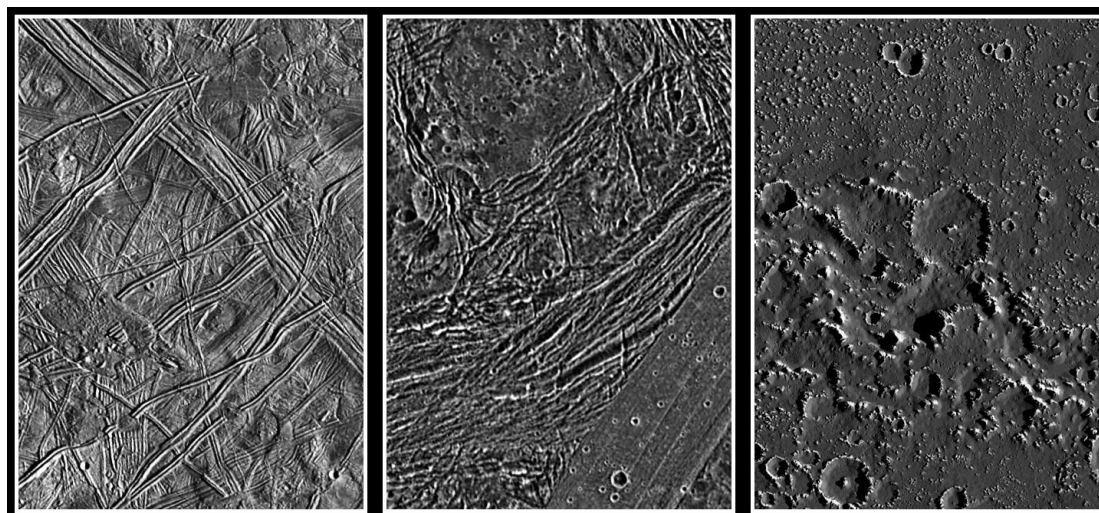


Figure 1.1: Europa (left), Ganymede (center) and Callisto (right) surfaces from the Solid-State Imaging of Galileo orbiter (Credit: NASA/JPL/DLR).

Io, Europa and Ganymede are trapped in a 4:2:1 mean motion resonance, called “Laplace

resonance”, leading to a continuous dissipation of tidal energy, resulting in a source of internal heating [e.g., Peale and Lee, 2002]. Water plumes emerging from the surface of Europa have been identified using images from the Hubble Space Telescope [Roth et al., 2014, Sparks et al., 2017] and in Galileo magnetometer and plasma wave data [Jia et al., 2018]. Although the origin of these plumes is unclear [Roberts et al., 2023], they suggest that Europa is geologically active, and they indicate the potential for additional shallow liquid water reservoirs beneath Europa’s icy surface [Howell and Pappalardo, 2020]. On the other hand, tidal heating contributes insignificant heat to Callisto.

The detection of induced magnetic fields within the icy Galilean moons from Galileo magnetometer data remains the strongest observational evidence of subsurface oceans as they can be explained by the presence of an electrically conducting fluid layer (i.e., a salty ocean) beneath the surface [Khurana et al., 1998, Kivelson et al., 2000]. The evidence for an ocean beneath the surface of Callisto is not as strong as the evidence for oceans in Ganymede and Europa. Indeed, the observed magnetic field signal may also be explained by induction within a highly conductive Callisto ionosphere [Hartkorn and Saur, 2017].

Internal structure

The data from Galileo’s flybys of Europa and Callisto allowed the determination of the degree-2 gravity field coefficients of the Galilean moons. Europa flybys were unfortunately relatively close to the equator, and the four flybys considered in Anderson [1998] did not allow for an independent estimation of J_2 and C_{22} . Europa’s interior was thus assumed to be in hydrostatic equilibrium (see Sect. 2.8.1), which allowed to introduce a constraint of $J_2/C_{22} = 10/3$. The dimensionless Moment of Inertia factor (MoI) was inferred using the Radau-Darwin Approximation (RDA, see Sect. 2.8.1), and its value of 0.346 ± 0.005 suggests that Europa’s internal structure is differentiated [Anderson, 1998] into a metallic core, a silicate mantle and a water ice-liquid outer shell. More recently, a reanalysis of Galileo data was performed using six Europa flybys with more modern orbit determination techniques [Casajus et al., 2022]. The degree-2 coefficients were estimated without assuming a hydrostatic constraint, and the MoI was found to be larger (0.3547 ± 0.0024), suggesting a thinner ice-water shell and a less dense interior. Europa was found statistically in hydrostatic equilibrium, but because of the coverage of the flybys, the errors are still large, e.g., regarding the estimation of J_2 .

Similarly, the inclinations of the five Callisto flybys considered in Anderson [2001] were rather low. Assuming hydrostatic equilibrium, the degree-2 gravity coefficients were computed, and the RDA allowed for an estimation of the MoI 0.3549 ± 0.0042 [Anderson, 2001], which is too large to comply with a full separation of rock and ice [Anderson et al., 1998, Anderson, 2001]. Additionally, the lack of an intrinsic magnetic field of Callisto [Khurana et al., 1997] is consistent with its partial differentiation (no iron core). However, non-hydrostatic effects could be significant at Callisto [Smith et al., 2020], and because Callisto is a slowly rotating body, even modest internal mass variations will significantly influence its MoI [McKinnon, 1997], and would even allow for a fully differentiated interior [Gao and Stevenson, 2013].

1.2 Exploration of Europa and Callisto

As suggested in Sect. 1.1.1, Europa and Callisto are privileged destinations for the upcoming phase of Solar System exploration. Indeed, the characterisation of these two moons will address two of the key science themes of ESA’s Cosmic Vision (2015-2025) [Bignami et al., 2005]: “What are the conditions for planet formation and the emergence of life?” and “How does the Solar System work?”.

On the one hand, the accumulated clues for Europa’s habitability make this moon one of the best candidate to search for life. Dedicated missions to Europa would help to acquire a better understanding of this complex system, and of various interactions of Europa within the Jovian system. On the other hand, Callisto is a celestial record keeper. Its ancient surface is particularly suited to learn about the formation and evolution of the Jovian satellites.

1.2.1 Next decade’s planned missions

Two probes are expected to visit the Jovian system in the 2030 decade: ESA’s mission Jupiter Icy Moons Explorer [JUICE; Grasset et al., 2013] and NASA’s Europa Clipper [Phillips and Pappalardo, 2014].

JUICE

ESA’s JUICE is the first large mission within ESA’s Cosmic Vision program [Bignami et al., 2005] and was launch on 14-04-2023. Its main focus is to study Ganymede as a planetary object and a possible habitat [Grasset et al., 2013]. JUICE will insert in orbit around Ganymede at the end of an extensive tour through the Jupiter system. After two transitive elliptical phases separated by a 5000 km-altitude circular orbit, the probe will reach a 500 km-altitude circular orbit around Ganymede.

Among the various instruments on board of JUICE, the GAnymede Laser Altimeter [GALA; Hussmann et al., 2019] and the Gravity and Geophysics of Jupiter and the Galilean Moons [3GM; Shapira et al., 2016] radio science experiment are of particular interest for this work. 3GM will contribute to the characterisation of the interior state of Ganymede, inform on the presence of a deep ocean and other gravity anomalies, study Ganymede and Callisto surface properties, and perform atmospheric science at Jupiter, Ganymede, Europa, Callisto, and of the Jupiter rings. GALA will characterise the topography and tidal deformations of Ganymede. Synergies between these two instruments are expected. For instance, the ice crust thickness will be constrained by determining the tidal response using altimetry [GALA, see Steinbrügge et al., 2015] and gravity potential measurements [3GM, see Cappuccio et al., 2020], as well as the estimation of the amplitudes of the physical librations [GALA, see Steinbrügge et al., 2019].

Nevertheless, the study of Callisto and Europa will also be enabled by the Jovian tour. Indeed, besides reducing the velocity of the probe before Ganymede orbit insertion, the Jovian tour is the opportunity to fly by other moons to characterise them and their interactions. The objectives of the 2 flybys of Europa, with closest approaches of 400 km, are

to

- determine the composition of the non-ice material, especially as related to habitability,
- search for liquid water under the most active sites,
- study the recently active sites.

During the 21 flybys of Callisto, with closest approaches between 200 km and 400 km, JUICE will

- characterise the outer shells of Callisto, including the ocean,
- determine the composition of the non-ice material,
- study the past activity via Callisto.

Several studies were performed to evaluate the expected gravity field which can be recovered from Europa [Cappuccio et al., 2022] and from Callisto [Di Benedetto et al., 2021, Cappuccio et al., 2022, Genova et al., 2022].

Europa Clipper

NASA’s Europa Clipper is expected to be launched in Oct. 2024. Unlike JUICE in the case of Ganymede, Clipper will not directly orbit Europa, but will stay in orbit around Jupiter and perform a series of 49 flybys of Europa starting in 2030, with closest approaches between 25 km and 100 km. The probe will thus spend most of its time outside of the high-radiation environment of Jupiter’s inner magnetosphere that can be damaging to electronics [Phillips and Pappalardo, 2014].

The Europa Clipper mission will characterize Europa’s potential habitability by [Howell and Pappalardo, 2020]:

- characterizing the ice shell and any subsurface water, including their heterogeneity, ocean properties, and the nature of surface–ice–ocean exchange,
- understanding the habitability of Europa’s ocean through composition and chemistry,
- understanding the formation of surface features, including sites of recent or current activity, and characterizing high science-interest localities.

One important component of this mission is the Gravity and Radio Science (G/RS) investigation [Mazarico et al., 2023] whose primary objective is to measure the tidal Love number k_2 , as its precise determination would provide independent evidence for a global subsurface ocean. Additionally, an improved estimation of Europa’s static gravity field and of its orientation parameters from G/RS investigations would provide additional constraints on the internal structure, together with complementary measurements from the onboard radar REASON [Steinbrügge et al., 2018a] and the wide angle camera EIS [Park et al., 2015], allowing for the estimation of tidal deformations.

1.2.2 Recent mission proposals

As it will be done for JUICE in the case of Ganymede, a mission including an orbiter around Europa or Callisto would enable global and uniform mapping of these two Galilean

moons, as well as recovering their gravity fields and other geodetic parameters to much higher resolution (see, e.g., Wu et al. [2001], Wahr et al. [2006] for Europa, and Smith et al. [2020] for Callisto), and complement the investigation initiated by Europa Clipper and JUICE, respectively. An orbiter would thus achieve a more detailed characterisation of the presence and the extent of the ocean and its relation to the deeper interior. There have been several proposed missions to send an orbiter around Europa, e.g., the Jupiter Europa Orbiter [Clark et al., 2009], HADES [Böttcher et al., 2009], and the Joint Europa Mission [Blanc et al., 2020a], and to send an orbiter around Callisto, e.g., MAGIC [Smith et al., 2019] and Gan De [Blanc et al., 2020b], which would then allow for a more direct comparison with Europa and Ganymede.

Joint Europa Mission

The Joint Europa Mission (JEM) is an ambitious collaborative proposal between ESA and NASA with the objectives of fully characterising Europa’s habitability from an orbiter, searching for bio-signatures in the environment of Europa (surface, subsurface and exosphere) by the combination of an orbiter and a lander [Blanc et al., 2020a].

The orbiter’s platform, which represented ESA’s contribution, was foreseen to insert into a low orbit around Europa after the separation of the lander. Because of the highly radiative environment and of its effect on the electronics, the mission’s lifetime was foreseen to last only 3 months after reaching the final science orbit, despite assumptions about reduced radiation doses. Indeed, complex trajectories traced by charged particles in the combined Jovian and European magnetic fields may offer radiation shielding at low altitude around Europa [Truscott et al., 2011]. Nevertheless, such an orbiter would be able to study a broader frequency range of magnetic fluctuations than what Clipper would sense during its flybys, to increase the accuracy of Europa’s gravity field and tidal Love number recovery as suggested by simulation analyses performed in the framework of JEM [Blanc et al., 2020a], and overall to complement the investigations of Europa Clipper.

MAGIC

The Magnetism, Altimetry, Gravity, and Imaging of Callisto (MAGIC) mission is a concept dedicated to a full geophysical investigation of Callisto. The three main objectives of MAGIC are according to [Smith et al., 2019] to

- determine the internal structure of Callisto,
- definitively test for the properties of Callisto’s ocean,
- determine the age and state of Callisto’s ice shell.

To this end, a 50 km-altitude polar orbiter has been proposed, for a nominal duration of 1 year, to characterise Callisto’s induced magnetic field, its topography and gravity, and to image its surface at unprecedented resolution for an icy moon [Smith et al., 2019].

As it is usual for planetary missions, the telecommunication system could also be used for gravity and radio science investigations. In this sense, comprehensive numerical simulations and covariance analyses have been performed for MAGIC mission scenarios by Genova et al. [2022], showing the expected estimates of Callisto’s gravity field, orientation

and geophysical parameters, and how they would contribute to the determination of Callisto’s internal structure. An altimeter was also considered to measure tidal deformations, which, combined to a measurement of the tidal gravitational response, would help inferring the thickness of the ice-shell (see Sect. 2.8.2). Moreover, the combination of altimetry and gravity measurements would assess current hypotheses of non-hydrostatic components in the gravity field [Smith et al., 2020].

Gan De

The Chinese National Science Administration (CNSA) announced that the Tianwen-4 mission will target both the Jupiter system [Wei et al., 2018] and Uranus. The main probe will be captured by Jupiter, and after separation, a secondary probe will continue towards Uranus. The end target of the main probe is Callisto [Wang, 2022]. However, the mission scenario is not yet fixed. In this sense, the Gan De initiative [Blanc et al., 2020b], named after the first astronomer to have claimed an observation of a moon of Jupiter four centuries BC, proposed scientific objectives and a mission scenario for the Jupiter component of Tianwen-4 [Wei et al., 2018], as one of the science inputs feeding the design of that mission by the CNSA.

Gan De addresses one key scientific question: “How did the Jupiter System form?”. This question be answered by an extensive characterisation of Callisto as its bulk composition, interior and surface terrains keep records of its early eons. The ~ 77 or so irregular satellites, orbiting far out beyond the region occupied by the Galilean satellites also contribute to the answer, and are unique and precious remnants of the populations of planetesimals which orbited the outer Solar System at the time of Jupiter’s formation.

The mission scenario proposed is a first Jovian orbital tour to fly by and characterize several irregular satellites [Jing and Li, 2023], followed by an injection into a Callisto orbit to characterize its surface and interior, investigate its degree of differentiation, and search for the possible existence of an internal ocean.

1.3 Scope of this work

The measurement of geodetic and geophysical parameters of a celestial body is a key element for its global characterisation, as they constitute important constraints on the internal structure of the body, together with its interactions within its environment. In the case of planetary bodies, this is commonly done by using radio tracking data from the analyses of spacecrafts orbiting or passing by the celestial body. Several reference software packages within the international community (GEODYN, MONTE, GINS ...) have the capability to process these data and to estimate such global parameters.

We use a development version of the Bernese GNSS Software [BSW; Dach et al., 2015], a scientific, high precision, multi-GNSS (Global Navigation Satellite System) data processing software developed at the Astronomical Institute of the University of Bern (AIUB). This development version was adapted to estimate planetary gravity fields, first in the case of Earth’s moon [Jäggi et al., 2015, Arnold et al., 2015], using Doppler observables [Bertone

et al., 2021a], and was later extended for satellite systems [*e.g.*, Desprats et al., 2023, and this work, for the Jovian system]. In order to process altimetry data, we additionally combine the BSW with pyXover, a Python suite of altimetry analysis tools for planetary geodesy [Bertone et al., 2020]. Chapter 2 describes the force models, the observables, and the estimation process that we use and developed for this work.

As discussed in Sect. 1.2, a low altitude, near polar and quasi circular orbit around one of the Galilean moons, *e.g.*, Europa or Callisto, would be particularly well suited to drastically improve our knowledge of these moons, and to answer key scientific questions. However, as detailed in Sect. 1.2.2, the mission profile can be quite different from one mission proposal to another, and may also change after the mission selection. The choice of the science orbits remains thus flexible, despite being one of the key elements of mission design. Moreover, candidate orbits have to fit all mission science requirements and to satisfy multiple mission and instrument constraints. An orbit meeting all these additional requirements might be, *e.g.*, less suited for gravity field recovery. Quantifying the accuracy to which geodetic parameters can be recovered based on different orbits is thus of great importance for a proper orbit selection.

In this regard, Chapter 3 describes the implementation of an orbit design tool, which we use to generate extensive sets of orbits suitable for global characterisation purposes in Jupiter’s complex environment, and the strategy we followed to systematically assess their sensitivity to the estimation of geodetic and geophysical parameters. While the performance of different mission scenarios is usually assessed by covariance analyses, in this work we perform extensive full closed-loop simulations, in order to precisely assess how well the orbit and the geodetic parameters can be recovered. We study low-altitude orbiters around Europa and Callisto for a typical mission duration of three months duration. However many results of this work can also be applied to other planetary bodies.

In Chapter 4, we discuss the orbit determination and the estimation of geodetic parameters such as the gravity field, the Love number k_2 and the rotation parameters when using only Doppler observables. We also explore strategies to recover gravity field parameters with a very limited a priori knowledge of the gravity field (as it is currently the case for the Galilean moons), and explore mitigation strategies for poorly modelled non-gravitational accelerations. Finally, in Chapter 5, we study the benefit of combining altimetry crossovers with Doppler data, including potential improvements in terms of orbit and geodetic parameter estimations, but also for the estimation of the the Love number h_2 and inferred internal properties.

Chapter 2

Models and observables

The modelling of the spacecraft trajectory is central to a mission aiming at characterizing the celestial body around which it orbits. It is needed to provide a precise knowledge of the position of the spacecraft (Sect. 2.1), which is also of interest for the other components of the mission, e.g., for the geolocation of images or other measurements. However, the determination of the orbit (Sect. 2.3) can also indirectly improve the considered models, such as the background force model (Sect. 2.2) and rotation model (Sect. 2.4) which describe the environment of the spacecraft. Indeed, the generalized orbit determination consists of adjusting model parameters based on a given set of observations (described in Sects. 2.5, 2.6 and 2.7). Moreover, the improvement of the knowledge of geodetic parameters leads to better constraints on the internal structure of the celestial body (Sect. 2.8), providing answers to the scientific questions described in Chapter 1.

2.1 Orbit modelling

In the framework of the two-body problem, where the spacecraft is only subject to the gravitational pull of the central body modelled as a point mass, the trajectory of a spacecraft in orbit around a celestial body is entirely described in terms of its initial conditions, or, equivalently, in terms of six Keplerian orbital elements. The motion of the spacecraft is restricted to a fixed plane, called the orbital plane. The conic section within this plane, i.e., the shape of the orbit, is characterized by the semi-major axis a and the eccentricity e . The orientation of the orbital plane with respect to a reference frame is given by the inclination i and the longitude of the ascending node Ω . The angle between the ascending node line and the periapsis of the orbit is called the argument of pericenter ω . We characterize the position of the spacecraft along its orbit at any epoch by its angle with respect to the ascending node, called the argument of latitude u . There is a mathematical equivalence between the position vector \mathbf{r} and the velocity vector $\dot{\mathbf{r}}$ at every epoch and the 6 Keplerian elements [Beutler, 2005].

In the two-body problem, all orbital elements are constant in time, except for the argument of latitude u . However, in the case of additional external forces acting on the spacecraft (as described in Sect. 2.2), the orbit is “perturbed”, and the previously defined constant orbital elements vary with time. An example of the variation of the inclination i and longitude of the ascending node Ω due to perturbing forces is given in Sect. 3.3. The

six previously mentioned orbital elements are then called “osculating” orbital elements and refer to an osculating epoch (Fig. 2.1).

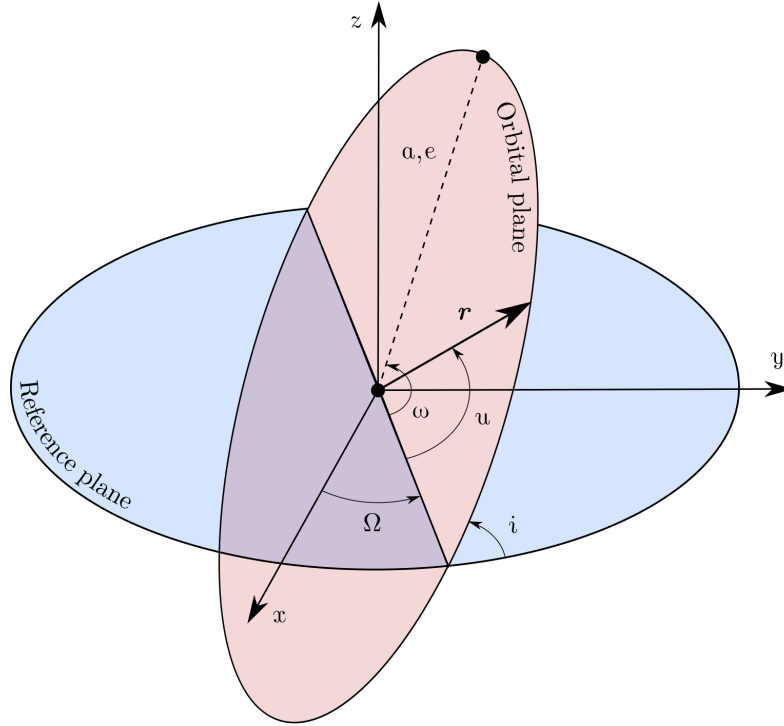


Figure 2.1: Osculating orbital elements (a , e , i , Ω , ω , u).

In general, the orbit of the spacecraft is governed by the equations of motion, which can be written, in a quasi inertial frame, as

$$\ddot{\mathbf{r}} = -\mu_G \frac{\mathbf{r}}{r^3} + \mathbf{f}_p(t, \mathbf{r}, \dot{\mathbf{r}}, q_1, \dots, q_d) = \mathbf{f}, \quad (2.1)$$

where \mathbf{r} is the position vector of the spacecraft center of mass with respect to the center of mass of the central celestial body, r its absolute value, a dot denotes time derivative, μ_G is the standard gravitational parameter of the celestial body and \mathbf{f}_p collects all perturbation accelerations beyond the central term (acceleration due to central point mass only). The q_i , $i = 1, \dots, d$, denote the parameters used to represent different kinds of orbit perturbations (e.g., empirical orbit parameters or gravity field parameters described in Sect. 2.2).

The orbit of the spacecraft is the result of the integration of the equations of motion (2.1), which we performed using two different software packages. A relatively simple force model was used for the orbit design (see Chapter 3), which was entirely performed in MATLAB. For the rest of the simulation study, we used the Bernese GNSS Software [BSW; Dach et al., 2015] to integrate the equations of motion, by using the collocation method described in Beutler [2005]. The orbits are stored in terms of a polynomial representation. Within each integration interval, the orbit position can be evaluated as

$$\mathbf{r}(t) = \sum_{k=0}^q \mathbf{a}_k \left(\frac{t - t_0}{h} \right)^k, \quad (2.2)$$

with q the degree of the polynomial, \mathbf{a}_k the 3 dimensional vector containing the coefficients of degree k , h the interval size on which the polynomial is defined and t_0 the midpoint of the interval. The size of each interval h is constant, as well as the degree q of the different polynomials. However, t_0 is different for each interval. In order to access the orbit in terms of position $\mathbf{r}(t)$ and velocity $\dot{\mathbf{r}}(t)$ at different steps of our simulation, the integration coefficients are stored using the BSW internal standard binary format STD.

Nevertheless, we also considered other file formats to read the propagated trajectory in different software packages. We chose the SPK format (type 2) [see SPK required reading; Semenov, 2021] from NAIF (Navigation and Ancillary Information Facility), which can be easily read using the SPICE toolkit [Acton Jr, 1996]. We implemented a direct conversion from the STD format to the SPK format by changing the orbit representation. The orbit from an SPK file is described using Chebyshev polynomials of the first kind $(T_k)_{k \in \mathbb{N}}$ which fulfil

$$T_k(\cos \theta) = \cos k\theta, \quad \forall k \in \mathbb{N}, \quad \forall \theta \in \mathbb{R}. \quad (2.3)$$

Using these polynomials, the orbit is written similarly to Eq. (2.2) as

$$\mathbf{r}(t) = \sum_{k=0}^q \mathbf{c}_k T_k(s(t)), \quad (2.4)$$

assuming the same order q as in Eq. (2.2) and with the associated sets of 3 dimensional coefficients \mathbf{c}_k , and with

$$s(t) = 2 \frac{t - t_0}{h} - 1 \in [-1; 1]. \quad (2.5)$$

The conversion from the BSW polynomial representation to Chebyshev polynomial representation, i.e., the relation between the two sets of coefficients \mathbf{a}_k and \mathbf{c}_k , relies on the discrete orthogonality of the Chebyshev polynomials, which can be derived as follows. The nodes of a Chebyshev polynomial of degree N , i.e., the values s_k for which $T_N(s_k) = 0$, are deduced from the definition (2.3) so that

$$s_k = \cos \left(\frac{2k - 1}{2N} \pi \right), \quad k = 1 \dots N. \quad (2.6)$$

It can be easily shown that for all $i = 1 \dots N$ and $j = 1 \dots N$,

$$\sum_{k=1}^N T_i(s_k) T_j(s_k) = \begin{cases} 0 & \text{if } i \neq j \\ N/2 & \text{if } i = j \neq 0 \\ N & \text{if } i = j = 0 \end{cases}. \quad (2.7)$$

In particular, for $N = q + 1$, we can derive a relation between the Chebyshev coefficients and the trajectory evaluated at times t_k , corresponding to the nodes s_k

$$\mathbf{c}_l = \begin{cases} \frac{1}{q+1} \sum_{k=1}^{q+1} \mathbf{r}(t_k) & \text{if } l = 0 \\ \frac{2}{q+1} \sum_{k=1} \mathbf{r}(t_k) T_k(s_k) & \text{if } l \neq 0 \end{cases}, \quad (2.8)$$

with

$$s_k = \cos\left(\frac{2k-1}{2(q+1)}\pi\right), \quad t_k = t_0 + (1+s_k)\frac{h}{2}, \quad k = 1 \dots q+1. \quad (2.9)$$

Once the Chebyshev coefficients are computed, the orbit can be written to a binary SPK file using dedicated SPICE routines. This newly implemented conversion tool facilitates the interface between the different software packages used in this work, which can thus make use of SPICE routines to access stored orbits.

2.2 Force model of an orbiter at the Galilean moons

In this section, we describe the different forces acting on the spacecraft in our integration of the equations of motion (2.1). They are summarized in Fig. 2.2 for a Europa orbiter, and in Fig. 2.3 for a Callisto orbiter.

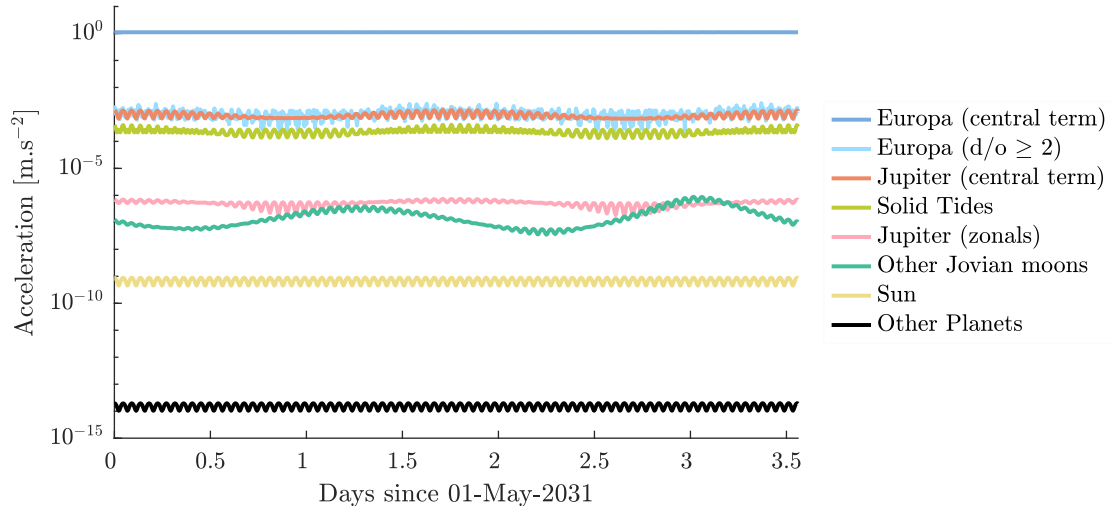


Figure 2.2: Magnitude of accelerations considered in this study for a 134 km orbiter around Europa during one Europa day (≈ 3.55 Earth days)

The positions of Solar System planets were retrieved from the DE430 JPL ephemerides [Folkner et al., 2014], and the position of the bodies within the Jovian system from the ephemerides JUP310 [Jacobson, 2013].

2.2.1 Synthetic gravity field

The gravity field of a celestial body is determined by its internal mass distribution. In the case of a spherical homogeneous body, it can be reduced to the central term (see Eq. 2.1). Otherwise the acceleration \mathbf{a}_g acting on a spacecraft, resulting from non-homogeneities, can be computed from the gradient of the gravitational potential V as

$$\mathbf{a}_g = \nabla V, \quad (2.10)$$

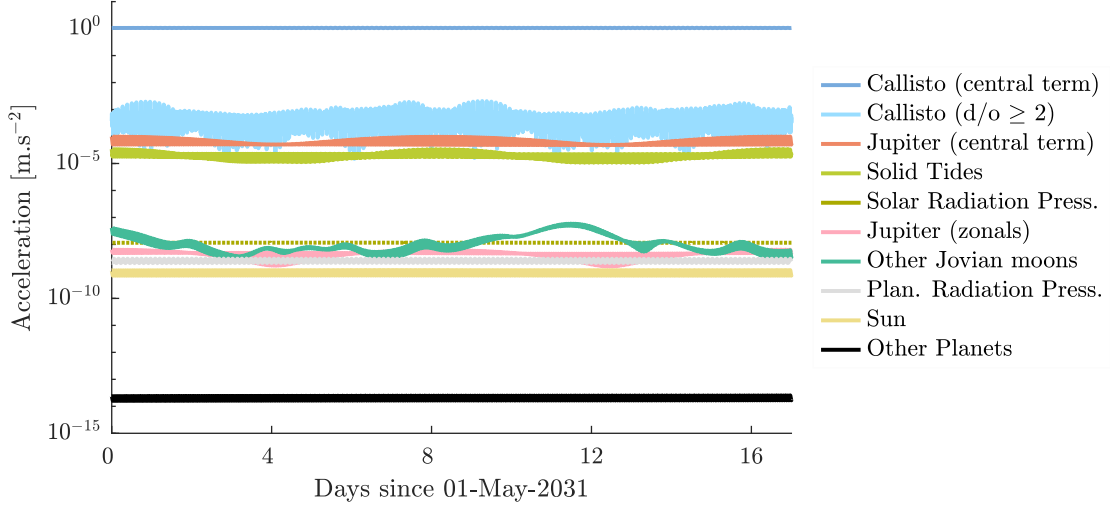


Figure 2.3: Magnitude of accelerations considered in this study for a 197 km orbiter around Callisto during one Callisto day (≈ 16.67 Earth days).

where V can be decomposed in spherical harmonics such that [Kaula, 1966]

$$V(r, \lambda, \phi) = \frac{\mu_G}{r} \cdot \sum_{n=2}^{n_{max}} \sum_{m=0}^n \left(\frac{R_G}{r} \right)^n \bar{P}_{nm}(\sin \phi) (\bar{C}_{nm} \cos m\lambda + \bar{S}_{nm} \sin m\lambda), \quad (2.11)$$

where λ and ϕ are longitude and latitude in a central body-fixed reference frame, R_G is the equatorial radius of the celestial body [$R_E = 1562.6$ km for Europa and $R_C = 2410.3$ km for Callisto; Archinal et al., 2018]. \bar{P}_{nm} are the fully normalized Legendre functions of degree n and order m , and \bar{C}_{nm} and \bar{S}_{nm} are the fully normalized spherical harmonic coefficients, which are derived from the unnormalised Legendre functions and spherical harmonic coefficients as

$$\bar{P}_{nm} = N_{nm} P_{nm} \quad \text{and} \quad (\bar{C}_{nm}, \bar{S}_{nm}) = (C_{nm}, S_{nm}) / N_{nm}, \quad (2.12)$$

with

$$N_{nm} = \sqrt{\frac{(n-m)!(2n+1)(2-\delta_{0m})}{(n+m)!}}, \quad \text{and} \quad \delta_{0m} = \begin{cases} 1 & \text{if } m = 0 \\ 0 & \text{if } m \neq 0 \end{cases}. \quad (2.13)$$

The degree-0 coefficient \bar{C}_{00} corresponds to the central term and is already included in Eq. (2.1). The degree-1 coefficients relate to the coordinates of the center of mass. They are zero when considering a coordinate system with the origin at the center of mass. The coefficients \bar{C}_{21} and \bar{S}_{21} are connected to the mean spin pole, and are zero if the coordinate axes of the body-fixed frame we consider (see Sect. 2.4) coincide with the principal axes of inertia. An ellipsoidal potential of a synchronous rotating moon can then be defined from \bar{C}_{20} and \bar{C}_{22} [Van Hoolst et al., 2008], which relate to a reference triaxial ellipsoid approximating the equilibrium figure of the moon, as detailed in Sect. 2.8.1. The geoid height above the reference ellipsoid can be computed from the spherical harmonic coefficients (Eq. 2.11) so that [Ilk et al., 2005]

$$g_{\lambda, \phi} = R_G \cdot \sum_{n=2}^{n_{max}} \sum_{m=0}^n \bar{P}_{nm}(\sin \phi) (\bar{C}'_{nm} \cos m\lambda + \bar{S}_{nm} \sin m\lambda), \quad (2.14)$$

with $\bar{C}_{nm}^{\prime} = \bar{C}_{nm} - \bar{C}_{nm}^{ell}$, and where \bar{C}_{nm}^{ell} are the coefficients of the ellipsoid normal potential. Because we define the reference ellipsoid from the degree-2 coefficients of the reference gravity field (see Sect. 2.8.1), we have $\bar{C}_{2m}^{ell} = \bar{C}_{2m}$, and $\bar{C}_{nm}^{ell} = 0$ for $n > 2$.

The most recent field estimates of Callisto rely on the data analysis of the Galileo probe, which only performed a limited number of flybys. Consequently, only the degree-2 gravity field coefficients have been estimated for Callisto under hydrostatic assumption [Anderson, 2001]. More recently, Juno flew by Europa, providing more data to possibly improve the knowledge of Europa’s gravity field, as it was done for Ganymede by Casajus et al. [2022]. To our knowledge, Europa’s gravity field has not been improved using Juno’s recent flyby [29 Sept. 2022, see, e.g. Hansen et al., 2022]. Galileo data were recently reprocessed by Casajus et al. [2021] to update Europa’s gravity field model. However, these new estimates would not change the scope of this work. We thus based our analysis on estimates by Anderson [1998].

In any case, since the higher degree gravity field coefficients of the Galilean moons are not yet known, we generated a synthetic gravity field from degree 3 to $n_{max} = 100$ for each of the considered moons. The gravity field coefficients were thereby derived from the Earth Moon’s gravity field model GRGM900C [Lemoine et al., 2014], appropriately scaled by the squared ratio of the surface gravity of Callisto or Europa and of the Moon, so that

$$(\bar{C}_{nm}, \bar{S}_{nm})_G = \left(\frac{\mu_M}{\mu_G}\right)^2 \left(\frac{R_G}{R_M}\right)^4 \cdot (\bar{C}_{nm}, \bar{S}_{nm})_M, \quad \text{with } n > 2, m \geq 0, \quad (2.15)$$

where M stands for the Moon. It is important to note that the Moon’s gravity field has a rather large dynamic range, much more, e.g., than Venus, and also has mass concentrations (mascons). The strong power resulting from Moon-derived gravity fields may rise the signal to noise in comparison to a weaker field, which may affect some conclusions discussed in Chapter 4, such as the maximum gravity field degree which can be recovered in a given scenario. In the following, we label these two synthetic reference gravity field models as CALGLMo (Fig. 2.4, left) and EURGLMo (Fig. 2.4, right), for Callisto and Europa, respectively. It is important to note that the mass distribution is not unique to a single gravity field model. The characterization of the internal structure relies on additional constraints, which are discussed in Sect. 2.8.

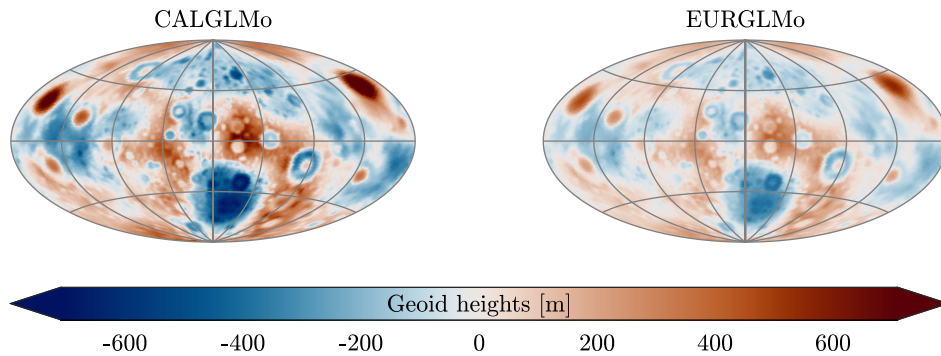


Figure 2.4: Geoid height (Aitoff projection) of Callisto (left) and Europa (right) above their reference ellipsoid, derived from the synthetic gravity fields CALGLMo and EURGLMo.

2.2.2 Solid tides

Jupiter’s gravitational force produces a deformation of the Galilean moons. The amplitude of the radial deformation induced by tides is parametrised by the Love number h_2 (see Sect. 2.7.1). The tidal secondary potential induced by the mass redistribution, is instead modelled via a change of the degree-2 gravity field coefficients [Petit and Luzum, 2010], as

$$\Delta\bar{C}_{2m} - i\Delta\bar{S}_{2m} = \frac{k_{2m}}{5} \frac{\mu_J}{\mu_G} \left(\frac{R_G}{r_J} \right)^3 \bar{P}_{2m}(\sin \phi_J) e^{-im\lambda_J}, \quad (2.16)$$

where k_{2m} is the Love number for degree 2 and order m , r_J , λ_J and ϕ_J denote the spherical coordinates of Jupiter in a Callisto or Europa-fixed reference system, and μ_J denotes the gravity constant of Jupiter.

The mean corrections on the \bar{C}_{20} , \bar{C}_{22} and \bar{S}_{22} coefficients are not zero. Indeed, for degree 2 and orders 0 and 2, Eq. 2.16 can be written as

$$\begin{aligned} \Delta\bar{C}_{20} &= \frac{k_{20}}{2\sqrt{5}} \frac{\mu_J}{\mu_G} \left(\frac{R_G}{r_J} \right)^3 (3\sin^2 \phi_J - 1), \\ \Delta\bar{C}_{22} &= \frac{k_{22}}{2} \sqrt{\frac{3}{5}} \frac{\mu_J}{\mu_G} \left(\frac{R_G}{r_J} \right)^3 (1 - \sin^2 \phi_J) \cos 2\lambda_J, \\ \Delta\bar{S}_{22} &= \frac{k_{22}}{2} \sqrt{\frac{3}{5}} \frac{\mu_J}{\mu_G} \left(\frac{R_G}{r_J} \right)^3 (1 - \sin^2 \phi_J) \sin 2\lambda_J. \end{aligned} \quad (2.17)$$

The time independent part of these corrections produces a permanent deformation, smaller in the case of \bar{S}_{22} . We chose to separate the permanent tidal corrections on \bar{C}_{20} and \bar{C}_{22} so that

$$\begin{aligned} \Delta\bar{C}_{20}^{perm} &= -\frac{k_{20}}{2\sqrt{5}} \frac{\mu_J}{\mu_G} \left(\frac{R_G}{a_G} \right)^3, \\ \Delta\bar{C}_{22}^{perm} &= \frac{k_{22}}{2} \sqrt{\frac{3}{5}} \frac{\mu_J}{\mu_G} \left(\frac{R_G}{a_G} \right)^3, \end{aligned} \quad (2.18)$$

with a_G the mean semi-major axis of the orbit of the Galilean moon around Jupiter [$a_E = 671\,261$ km for Europa and $a_C = 1\,883\,134$ km for Callisto; Lainey et al., 2006]. Permanent tides can be included in the \bar{C}_{20} and \bar{C}_{22} coefficient of gravity field model of the Galilean moons. In this case, the gravity field is labelled “zero tide”, similarly to the Earth’s geopotential conventions (see Petit and Luzum [2010]). If the permanent deformation is not included, the gravity field model is then “conventional tide free”. The gravity field models considered in this work are *zero tide*. Thus, before applying the corrections from Eq. (2.16), the $\Delta\bar{C}_{2m}^{perm}$ must be removed from \bar{C}_{2m} , with $m = 0, 2$, so that the permanent tide is counted only once.

In this study, we assumed $k_{2m} = k_2$ for $m = 0, 1, 2$, and chose $k_2 = 0.257$ for Europa [Wahr et al., 2006, Mazarico et al., 2015] and $k_2 = 0.3$ for Callisto. The position of Jupiter with respect to the Galilean moons is given by the ephemerides JUP310 [Jacobson, 2013] and can be obtained using SPICE routines. We neglected the tides induced by the other Galilean

satellites. Indeed, if we assume similar values for the Love numbers of the different tidal contributions between the Galilean moons, the largest contribution to the correction on the degree-2 gravity field coefficients of Callisto and Europa would come from Ganymede and it would be $< 1.5 \times 10^{-3}$ times the correction due to Jupiter-induced tides.

2.2.3 Third-body perturbations

The gravitational pull of other planetary bodies also perturbs the spacecraft. We considered the perturbation of all Solar System planets as point masses, in addition to the other Galilean moons. The acceleration of the spacecraft caused by a 3^{rd} body b is then given by

$$\mathbf{a}_{3,b} = -\mu_b \left(\frac{\mathbf{r} - \mathbf{r}_b}{|\mathbf{r} - \mathbf{r}_b|^3} + \frac{\mathbf{r}_b}{|\mathbf{r}_b|^3} \right), \quad (2.19)$$

where μ_b is the gravity constant of the body b , and \mathbf{r}_b is the position vector of the body b with respect to the central body.

Being the largest planet in the Solar System, Jupiter's perturbation is undoubtedly the most important in the Jovian system. Its influence is even more important in the case of Europa, being closer to Jupiter than Callisto. We thus decided to take into account the mass distribution of Jupiter by also considering its zonal gravity field coefficients up to degree 6 [Jacobson, 2013]. Similar to Eq. (2.11), the gravity potential of Jupiter can be written as

$$V_J(\mathbf{r}) = V_J(r, \lambda, \phi) = -\frac{\mu_J}{r} \cdot \sum_{n=2}^6 \left(\frac{R_J}{r} \right)^n \bar{J}_n \bar{P}_{n0}(\sin \phi), \quad (2.20)$$

where $\bar{J}_n = -\bar{C}_{n0}$ is Jupiter's normalised zonal gravity field coefficient of degree n and R_J the equatorial radius of Jupiter [$R_J = 71\,492$ km; Archinal et al., 2018]. The full third-body perturbation of Jupiter can then be expanded so that

$$\mathbf{a}_{3,J} = -\mu_J \left(\frac{\mathbf{r} - \mathbf{r}_J}{|\mathbf{r} - \mathbf{r}_J|^3} + \frac{\mathbf{r}_J}{|\mathbf{r}_J|^3} \right) + \nabla V_J(\mathbf{r} - \mathbf{r}_J) - \nabla V_J(-\mathbf{r}_J). \quad (2.21)$$

We did not consider the latest gravity field model obtained from Juno [Durante et al., 2022], but the change of the induced accelerations of probes orbiting around Europa and Callisto is negligible with acceleration differences below 1×10^{-14} m/s².

The next most important third-body perturbations come from the other Galilean moons, which show distinctive important time variations (see Fig. 2.3), due to their different orbital periods. Despite being at 5 AU from Jupiter, the Sun still has a considerable influence in the Jovian system, exceeding the influence of the other planets.

2.2.4 Non-gravitational accelerations

The interaction of emitted photons from the Sun on a given surface results in an exchange of momentum, which is characterized by the flux density of solar radiation. For our purpose,

we considered a constant value $S_0 = 1362 \text{ W/m}^2$ at 1 AU. The flux density Φ at a distance r from the Sun, expressed in AU, is then given by scaling the solar constant as

$$\Phi(r) = S_0 \left(\frac{1 \text{ AU}}{r} \right)^2. \quad (2.22)$$

Radiation pressure generates a force on the surface of the spacecraft. In this work, the spacecraft is modelled as a cannonball, with a cross-section $A_c = 85 \text{ m}^2$, a mass $m = 1800 \text{ kg}$, and a diffusion coefficient $\delta = 0.12$, corresponding to the fraction of diffusely reflected photons. The force due to the direct Solar Radiation Pressure (SRP) can then be expressed as an acceleration as [Milani et al., 1987]

$$\mathbf{a}_{SRP}(r) = -f_s \frac{\Phi(r)}{c} \frac{A_c}{m} \left(1 + \frac{4}{9} \delta \right) \mathbf{e}_{Sun}, \quad (2.23)$$

with c being the speed of light in vacuum, \mathbf{e}_{Sun} the unit vector pointing from the center of the cannonball to the Sun, and f_s a geometric shadow function computed according to Doornbos [2012], considering only eclipses from the central body.

We additionally considered indirect radiation pressure such as Planetary Radiation Pressure (PRP) due to reflected and emitted radiation from a planetary body. The reflected radiation pressure is produced by reflection and scattering of incident solar radiation from the moon's surface on the daylight side which is described by the albedo factor. The emitted radiation pressure is produced by thermal IR re-emission of the direct solar radiation absorbed by the moon from its entire surface. Because there are currently no maps for the moons' albedo and thermal emission, we use a uniform albedo coefficient $\alpha = 0.68$ for Europa and $\alpha = 0.2$ for Callisto [Morrison and Morrison, 1977]. For a cannonball, PRP can be expressed as [Rodriguez-Solano, 2009]

$$\mathbf{a}_{PRP} = \frac{\Phi(r_s)}{c} \left(\frac{R_G}{r} \right)^2 \frac{A_c}{m} \left(\frac{2\alpha}{3\pi} ((\pi - \Psi) \cos \Psi + \sin \Psi) + \frac{1 - \alpha}{4} \right) \left(1 + \frac{4}{9} \delta \right) \mathbf{e}_r, \quad (2.24)$$

with r_s the distance between the Sun and the moon, α the albedo of the moon, Ψ the angle between the Sun, the moon and the satellite, and \mathbf{e}_R the unit vector pointing from the center of mass of the moon to the center of the cannonball.

2.2.5 Empirical accelerations and pseudo-stochastic parameters

Under certain circumstances, considering empirical accelerations helps improving orbits and reducing observation residuals. These are accelerations with parameters that can be arbitrarily chosen. Usually, these parameters are then estimated to compensate unmodelled or mismodelled forces in the generalized orbit determination process (Sect. 2.3). However, using such parameters is tricky and risks over-parametrising the problem. In this work, we made use of constant and once-per-revolution accelerations, which can be expressed as

$$\mathbf{a}_{emp} = \mathbf{b}_0 + \mathbf{c}_1 \cos u + \mathbf{s}_1 \sin u, \quad (2.25)$$

where u is the argument of latitude of the spacecraft. \mathbf{b}_0 , \mathbf{c}_1 and \mathbf{s}_1 are 3-dimensional vectors for a total of 9 parameters that we express in the Local Orbital Frame (RSW), i.e.,

in the radial (R), along-track (S) and cross-track (W) direction, defined as

$$\mathbf{e}_r = \frac{\mathbf{r}}{\|\mathbf{r}\|}, \quad \mathbf{e}_w = \frac{\mathbf{r} \times \dot{\mathbf{r}}}{\|\mathbf{r} \times \dot{\mathbf{r}}\|}, \quad \text{and} \quad \mathbf{e}_s = \mathbf{e}_w \times \mathbf{e}_r. \quad (2.26)$$

Another means to absorb modelling deficiencies are pseudo-stochastic orbit parameters, e.g., pseudo-stochastic pulses (instantaneous velocity changes), as additional empirical parameters (see Beutler [2005] and Jäggi [2007] for more details). However, these parameters must be carefully constrained. We set them evenly (e.g., every 60 minutes) in all 3 directions (radial, along-track and cross-track) and estimate their amplitudes.

2.3 Generalized orbit determination

In order to estimate orbit and geodetic parameters, we considered the CMA [Beutler et al., 2010], which has been successfully applied to planetary probes in Arnold et al. [2015], Bertone et al. [2021a] and Desprats et al. [2023]. This approach is recapitulated in the following section.

2.3.1 Non-linear least-squares adjustment

Let us assume that a set of model parameters \mathbf{x} can be mapped to the observations \mathbf{l} by using an functional model \mathbf{g} . We can write

$$\mathbf{l} + \mathbf{e} = \mathbf{g}(\mathbf{x}), \quad (2.27)$$

with \mathbf{e} being the residuals. If our functional model \mathbf{g} is linear, we can directly use a least-squares adjustment to estimate the model parameters \mathbf{x} by minimizing $\mathbf{e}^T \mathbf{e}$. However, because our observation model \mathbf{g} is generally not linear, we linearise \mathbf{g} around a priori model parameters \mathbf{x}_0 , so that

$$\mathbf{g}(\mathbf{x}) \approx \mathbf{g}(\mathbf{x}_0) + \frac{\partial \mathbf{g}}{\partial \mathbf{x}}(\mathbf{x}_0)(\mathbf{x} - \mathbf{x}_0), \quad (2.28)$$

where $\frac{\partial \mathbf{g}}{\partial \mathbf{x}}(\mathbf{x}_0)$ is the Jacobian of \mathbf{g} evaluated at \mathbf{x}_0 . We note this set of derivatives as the first design matrix \mathbf{A} , so that

$$\mathbf{A} = \frac{\partial \mathbf{g}}{\partial \mathbf{x}}(\mathbf{x}_0). \quad (2.29)$$

The observation equations (2.27) can then be rewritten in their linearised form as

$$\begin{aligned} \mathbf{e} &= \mathbf{A}(\mathbf{x} - \mathbf{x}_0) - (\mathbf{l} - \mathbf{g}(\mathbf{x}_0)) \\ &= \mathbf{A} \quad \delta \mathbf{x} \quad - \quad \delta \mathbf{l}, \end{aligned} \quad (2.30)$$

where $\delta \mathbf{l}$ is often referred to as O-C (observed - computed) term, $\delta \mathbf{x}$ is the solved for correction of the parameters with respect to their a priori values. To represent the observation error, we introduce the weight matrix as

$$\mathbf{P} = \mathbf{Q}_{11}^{-1} = \sigma_0^2 \mathbf{C}_{11}^{-1}, \quad (2.31)$$

with \mathbf{Q}_{ll} the a priori cofactor matrix of observations, σ_0 the a priori standard deviation of unit weight and \mathbf{C}_{ll} the a priori covariance matrix of observations. In case of uncorrelated observations, the weight matrix \mathbf{P} is diagonal with $P_{ll} = \sigma_0^2/\sigma_l^2$, with σ_l^2 the a priori variance of the observation l .

The solution of Eq. (2.30) is obtained by minimizing $\mathbf{e}^T \mathbf{P} \mathbf{e}$, which gives

$$(\mathbf{A}^T \mathbf{P} \mathbf{A}) \delta \mathbf{x} - \mathbf{A}^T \mathbf{P} \delta \mathbf{l} = \mathbf{N} \delta \mathbf{x} - \mathbf{b} = 0, \quad (2.32)$$

where $\mathbf{N} = \mathbf{A}^T \mathbf{P} \mathbf{A}$ is usually called “normal equation” matrix and $\mathbf{b} = \mathbf{A}^T \mathbf{P} \delta \mathbf{l}$ is the right-hand side of the normal equation system.

In case \mathbf{N} is regular, the solution vector is obtained via the inverse of \mathbf{N} :

$$\mathbf{x} = \mathbf{x}_0 + \mathbf{N}^{-1} \mathbf{b}. \quad (2.33)$$

The estimated a posteriori sigma of unit weight is computed as

$$m_0 = \sqrt{\frac{\mathbf{e}^T \mathbf{P} \mathbf{e}}{n - u}}, \quad (2.34)$$

with n being the number of observations, and u the number of adjusted parameters. The covariance matrix of the adjusted model parameters is given by

$$\mathbf{C}_{xx} = m_0^2 \mathbf{Q}_{xx} = m_0^2 \mathbf{N}^{-1}, \quad (2.35)$$

where \mathbf{Q}_{xx} is the cofactor matrix of the adjusted model parameters. The a posteriori standard deviation of the adjusted model parameters is then given by

$$m_x = \sqrt{C_{xx}} = m_0 \sqrt{Q_{xx}}. \quad (2.36)$$

In some cases, it is useful to confine parameters to a restricted range, i.e., to constrain them to a given reference value. This is particularly helpful to prevent singularities of the matrix \mathbf{N} . Constraints are realized by adding artificial observations such as $p_i = 0$, with the weight σ_0^2/σ_i^2 , where σ_i is the standard deviation of the estimated parameter p_i . This translates into the addition of these weights to the diagonal elements of the normal equation matrix \mathbf{N} corresponding to the parameters to constrain.

Because we approximated the functional model \mathbf{g} by truncating the Taylor series to the first order, the process has to be iterated until convergence to minimise the error of the full non-linear observation equation (Eq. 2.27).

2.3.2 Variational equations

In this section, we describe how the Jacobian of our functional model \mathbf{g} , needed in the linearisation of \mathbf{g} (Eq. 2.28), is computed. The observations considered in this work depend on the model parameters \mathbf{x} , and on the spacecraft position at two different epochs, i.e., the position \mathbf{r}_1 at epoch t_1 and the position \mathbf{r}_2 at epoch t_2 (see Sects. 2.6 and 2.7). However,

the spacecraft position also depends on the model parameters. The functional model \mathbf{g} is thus a composite function, which we explicitly denote \mathbf{g}^* :

$$\mathbf{g}(\mathbf{x}) = \mathbf{g}^*(\mathbf{r}_1(\mathbf{x}), \mathbf{r}_2(\mathbf{x}), \mathbf{x}). \quad (2.37)$$

The partial derivatives of the functional model \mathbf{g} with respect to a model parameter $p_i \in \mathbf{x}$ are obtained using the chain rule, so that

$$\frac{\partial \mathbf{g}}{\partial p_i} = \frac{\partial \mathbf{g}^*}{\partial \mathbf{r}_1} \frac{\partial \mathbf{r}_1}{\partial p_i} + \frac{\partial \mathbf{g}^*}{\partial \mathbf{r}_2} \frac{\partial \mathbf{r}_2}{\partial p_i} + \frac{\partial \mathbf{g}^*}{\partial \mathbf{x}}. \quad (2.38)$$

The composition is usually only implicit in the literature, and \mathbf{g}^* is assimilated to \mathbf{g} . \mathbf{g} is then a mixed function, i.e., a function for which at least one variable appears both implicitly and explicitly (\mathbf{x} in Eq. (2.37)). In this case, the derivatives of such a mixed function are referred to as total derivatives, and noted $\frac{d\mathbf{g}}{dp_i}$, in contrast to the partial derivatives noted $\frac{\partial \mathbf{g}}{\partial p_i}$ which refers to the explicit variable only. For more concision, we adopted this convention in the following. Equation (2.38) can thus be rewritten as

$$\frac{d\mathbf{g}}{dp_i} = \frac{\partial \mathbf{g}}{\partial \mathbf{r}_1} \frac{\partial \mathbf{r}_1}{\partial p_i} + \frac{\partial \mathbf{g}}{\partial \mathbf{r}_2} \frac{\partial \mathbf{r}_2}{\partial p_i} + \frac{\partial \mathbf{g}}{\partial p_i}, \quad (2.39)$$

which is another expression for the chain rule with direct and indirect dependencies. Note that if p_i is not explicitly in the formulation of the observable, the partial derivative $\frac{\partial \mathbf{g}}{\partial p_i}$ is zero. The expression of the partial derivatives of the observation model with respect to the position $\frac{\partial \mathbf{g}}{\partial \mathbf{r}}$ depends on the considered observable type, and will be detailed in Sect. 2.6.1 and in Sect. 2.7.3.

The partial derivatives of the position vector \mathbf{r} with respect to any parameter p_i are the result of the integration of the variational equations. By differentiating the equations of motion (2.1) with respect to a parameter p_i and by using the chain rule, we get

$$\frac{\partial \ddot{\mathbf{r}}}{\partial p_i} = \frac{\partial \mathbf{f}}{\partial \mathbf{r}} \frac{\partial \mathbf{r}}{\partial p_i} + \frac{\partial \mathbf{f}}{\partial \dot{\mathbf{r}}} \frac{\partial \dot{\mathbf{r}}}{\partial p_i} + \frac{\partial \mathbf{f}}{\partial p_i}, \quad (2.40)$$

which can be rewritten as

$$\ddot{\mathbf{z}}_{p_i} = \frac{\partial \mathbf{f}}{\partial \mathbf{r}} \mathbf{z}_{p_i} + \frac{\partial \mathbf{f}}{\partial \dot{\mathbf{r}}} \dot{\mathbf{z}}_{p_i} + \frac{\partial \mathbf{f}}{\partial p_i}, \quad \text{with} \quad \mathbf{z}_{p_i} := \frac{\partial \mathbf{r}}{\partial p_i}. \quad (2.41)$$

In the BSW, the variational equations related to the six initial orbital elements $o_i, i = 1 \dots 6$, are integrated together with the primary equations. The partial derivatives with respect to the other parameters $q_i, i = 1 \dots n_q$, are computed as a linear combination of \mathbf{z}_{o_i} , where the coefficients are computed using Gaussian quadrature [Beutler, 2005]. For more efficiency, \mathbf{z}_{q_i} are stored as degree-20 polynomial coefficients on 180s intervals, so that they can be later evaluated. However, when estimating a large number of parameters the number of polynomial coefficients can be quite large, and since we usually need the partials sequentially in time, we only store the coefficients related to one interval, and overwrite them for the next interval when needed.

Once the partials derivatives \mathbf{z}_{p_i} are computed for all parameters p_i , and once the derivatives of the observation model are computed for each observation, the design matrix \mathbf{A} can be assembled following Eq. (2.39).

2.3.3 Stacking Normal Equation Systems

In case of a large number of observations, it becomes interesting to consider separated observation blocks and to process them in parallel. Normal Equation Systems (NEQ, see Sect. 2.3.1) can then be worked on with an observation subset, and later assembled to form a global NEQ containing all the observations. For K independent observation blocks, the equation system (2.30) and (2.31) can be rewritten with

$$\delta \mathbf{l} = \begin{pmatrix} \delta \mathbf{l}_1 \\ \delta \mathbf{l}_2 \\ \vdots \\ \delta \mathbf{l}_K \end{pmatrix}, \quad \mathbf{A} = \begin{pmatrix} \mathbf{A}_1 \\ \mathbf{A}_2 \\ \vdots \\ \mathbf{A}_K \end{pmatrix}, \quad \mathbf{P} = \begin{pmatrix} \mathbf{P}_1 & 0 & \dots & 0 \\ 0 & \mathbf{P}_2 & \dots & 0 \\ 0 & 0 & \ddots & 0 \\ 0 & 0 & \dots & \mathbf{P}_K \end{pmatrix}. \quad (2.42)$$

Because the observation blocks are assumed to be independent, the weight matrix P is block diagonal. The contribution to the full NEQ can be consequently computed according to

$$\mathbf{N}_k = \mathbf{A}_k^T \mathbf{P}_k \mathbf{A}_k, \quad \mathbf{b}_k = \mathbf{A}_k^T \mathbf{P}_k \delta \mathbf{l}_k, \quad k = 1 \dots K. \quad (2.43)$$

As mentioned in Sect. 2.3.1, each observation can be weighted with respect to its a priori variance via the weight matrix \mathbf{P}_k . However, the weighting step can also be performed at the level of the NEQs. This is particularly useful, for instance, to weight a group of observations with respect to another. With σ_k the variance of unit weight of the observation block k , and σ_0^2 the a priori variance of unit weight, the full NEQ is assembled as

$$\mathbf{N} = \sum_{k=1}^K \frac{\sigma_0^2}{\sigma_k^2} \mathbf{N}_k, \quad \mathbf{b} = \sum_{k=1}^K \frac{\sigma_0^2}{\sigma_k^2} \mathbf{b}_k. \quad (2.44)$$

Observations can be grouped by observation type or by time span (e.g., daily NEQs or monthly NEQs). This is particularly useful to process batches of observations in parallel. Moreover, parameters can be constrained after the individual NEQs related to the true observations have been computed. Indeed, since constraints can be seen as artificial observations (see Sect. 2.3.1), ‘‘constraining’’ NEQs can be defined and combined to the true observations as Eq. (2.44) [see also Lasser, 2023].

Weights can be set manually or determined by more advanced techniques such as Variance Component Estimation [VCE; see e.g., Kusche, 2003]. We used VCE to determine the relative weight between observation types, and to obtain reliable constraints for some parameters. In both cases, VCE provides optimal weights between sets of NEQs. This iterative process computes the variance of unit weight of block k as

$$\sigma_k^2 = \frac{\mathbf{e}_k^T \mathbf{P}_k \mathbf{e}_k}{n_k - \text{tr}(\mathbf{N}_k \mathbf{N}^{-1})}, \quad (2.45)$$

where n_k is the number of observations of block k and tr is the trace operator. Notice that the full normal equation matrix \mathbf{N} has to be inverted at each iteration.

2.3.4 General processing scheme

In this work, we followed different procedures to estimate orbit and geodetic parameters, depending on the type of the parameter estimated, and the type of observations included.

In this section, we describe the primary processing scheme, adopted in Desprats et al. [2023], which is divided into an initial arc-wise orbit determination, followed by a generalized orbit improvement.

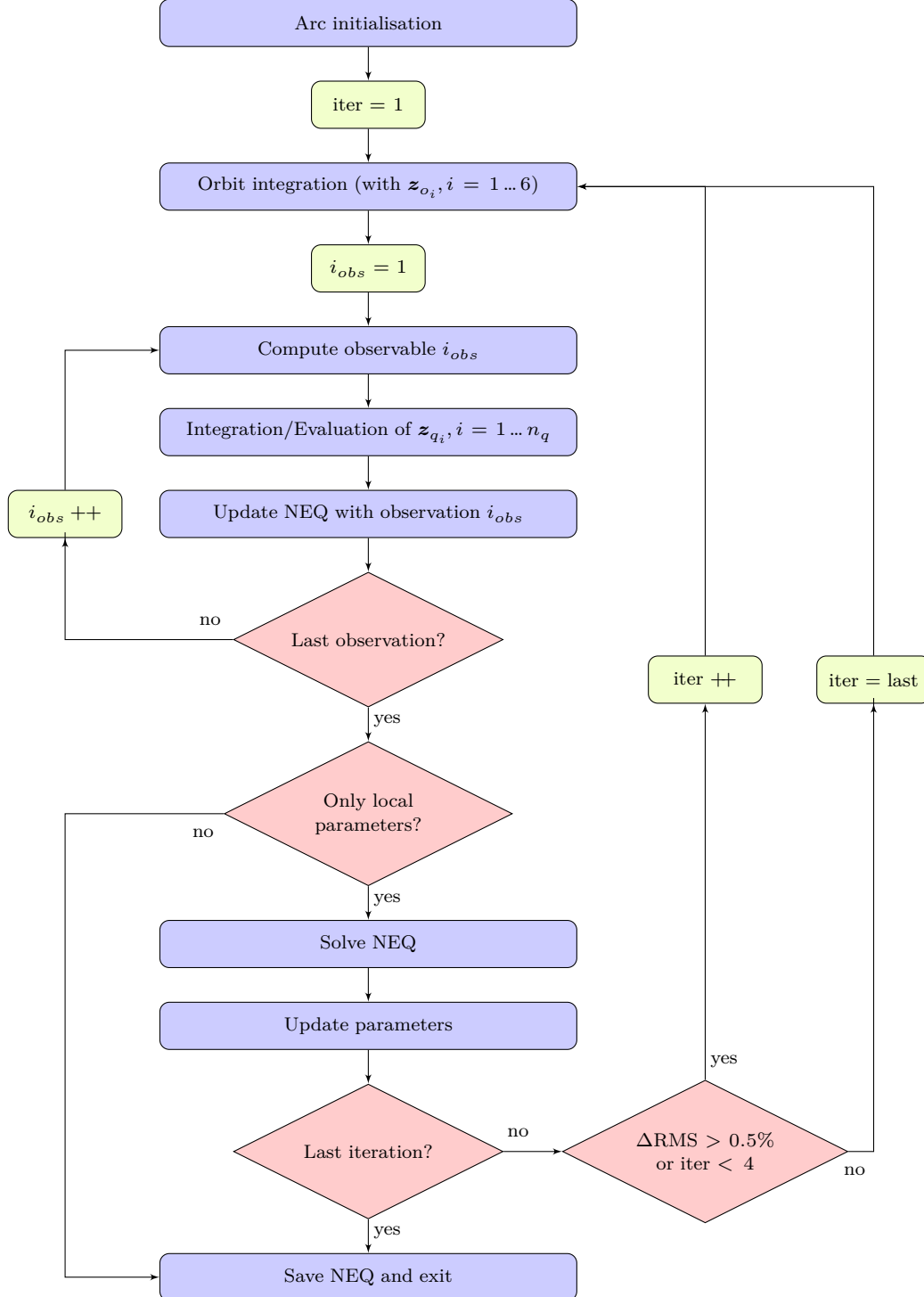


Figure 2.5: GRAVDET2 flowchart for one arc.

The initial arc-wise orbit determination is performed in GRAVDET2, a program from a development branch of the BSW (see Fig. 2.5). As discussed in Sect. 4.1, the length of an arc is not fixed, and is between 24 h and 30 h. The equations of motion (2.1) are numeri-

cally integrated as described in Sect. 2.1 with the variational equations (2.41) for the six initial Keplerian osculating elements, based on the fixed background force models detailed in Sect. 2.2. Each observable is computed according to our model (see Sect. 2.6.1). Then the partial derivatives of the orbit with respect to each local (or arc-specific) parameter are obtained following Sect. 2.3.2. This allows for a first least squares adjustment of arc-specific parameters (e.g., the six initial Keplerian osculating elements, see Tab. 2.1) to minimize the observation residuals (see Sect. 2.3.1). This process is repeated for at least 4 iterations, and until the relative Root Mean Square (RMS) change of residuals between one iteration and the previous one is below 0.5%.

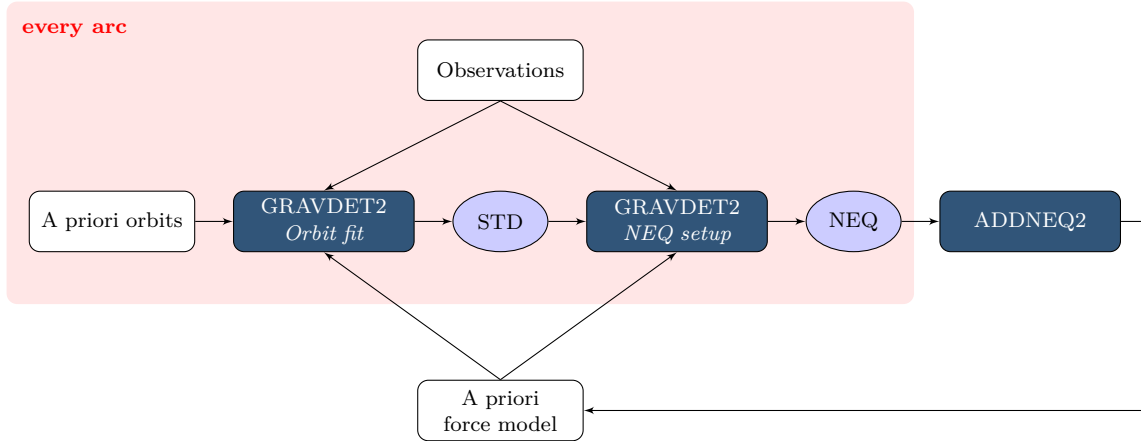


Figure 2.6: Generalized orbit determination flowchart.

Table 2.1: List of estimated parameters.

| Parameter | Number | Type |
|---------------------------------------|--|--------------|
| Osculating orbital elements | 6 (at the start of each arc) | local |
| Pseudo-stochastic pulses | 3 (\approx twice per orbit rev.) | local |
| Constant acceleration | 3 (stacked on n arcs) | local/global |
| Once-per-revolution acc. coefficients | 6 (stacked on n arcs) | local/global |
| k_2 Love number | 1 ($k_2 = k_{20} = k_{21} = k_{22}$) | global |
| h_2 Love number | 1 | global |
| Gravity field coefficients | 8278 (up to d/o 100) | global |
| Rotation parameters | 4 | global |

Based on the updated orbits, the equations of motion and the variational equations are once more integrated in GRAVDET2 to compute the partial derivatives with respect to both arc-specific and global parameters (Tab. 2.1), thus allowing us to set up the NEQs for all parameters and for all arcs separately. However, the arc-wise NEQs are not solved separately. They are stacked for the whole mission span (e.g., 26 Europa days), as described in Sect. 2.3.3 using the BSW program ADDNEQ2 (Fig. 2.6). Arc-specific parameters may be pre-eliminated [see, e.g., Dach et al., 2015] prior to NEQ stacking and the accumulated NEQ is inverted to retrieve corrections to the global parameters as well as to the local parameters which have not been pre-eliminated. The complete procedure is iterated until convergence is observed.

The different parameters considered in this work are summarized in Tab. 2.1. Empirical parameters are treated either as local parameters, i.e., constant during one arc, or semi-global, i.e., constant during n arcs. In the latter case, the procedure depicted in Fig. 2.6 is slightly modified (e.g., Fig. 4.30), to first improve the orbit with stacked empirical parameters, before solving for global parameters (see Sect. 4.5).

2.4 Rotation model

2.4.1 IAU Conventions

We followed the recommendations of the International Astronomical Union (IAU) to model the rotation of Jupiter, Callisto and Europa. The position of the north pole is defined by its right ascension α^n , and declination δ^n , and the position of the prime meridian is defined by its longitude W in the International Celestial Reference Frame (ICRF) (see Fig. 2.7). Based on the latest report of the IAU working group on cartographic coordinates and rotation elements [Archinal et al., 2018] in the case of Europa and Callisto, these rotation parameters take the following form

$$\begin{aligned}\alpha^n &= \alpha_0 + \alpha_1 T + \sum_{i=4}^8 A_i \sin J^i, \\ \delta^n &= \delta_0 + \delta_1 T + \sum_{i=4}^8 D_i \cos J^i, \\ W &= w_0 + w_1 d + \sum_{i=4}^8 W_i \sin J^i,\end{aligned}\tag{2.46}$$

with $J^i = J_0^i + J_1^i T$, T the interval in Julian centuries from the standard epoch J2000 (2000-01-01, 12:00 TT) and d the interval in days from the standard epoch (J2000). The polynomial coefficients of the rotation model (offsets and rates) of Callisto and Europa are given in Tab. 2.2. The arguments of the trigonometric functions J^i (for $4 \leq i \leq 8$) are related to the proper modes in longitudes of the pericenters of the Galilean moons [Lieske, 1979], and are given in Tab. 2.3, with the associated amplitudes for Callisto and Europa.

Table 2.2: Polynomial coefficients (offsets and rates) of the right ascension and declination of the north pole, and of the location of the prime meridian of Europa and Callisto [Archinal et al., 2018].

| | $\alpha_0(^{\circ})$ | $\alpha_1(^{\circ}/\text{cent.})$ | $\delta_0(^{\circ})$ | $\delta_1(^{\circ}/\text{cent.})$ | $w_0(^{\circ})$ | $w_1(^{\circ}/\text{day})$ |
|----------|----------------------|-----------------------------------|----------------------|-----------------------------------|-----------------|----------------------------|
| Europa | 268.08 | -0.009 | 64.51 | 0.003 | 36.022 | 101.3747235 |
| Callisto | 268.72 | -0.009 | 64.83 | 0.003 | 259.51 | 21.5710715 |

The transformation from the ICRF to the body-fixed frame (BF) is performed via the rotation matrix \mathbf{R}_{IN}^{BF} , which can be decomposed into elementary rotation matrices for each of the Euler angles as

$$\mathbf{R}_{IN}^{BF} = \mathbf{R}_3(W) \mathbf{R}_1\left(\frac{\pi}{2} - \delta^n\right) \mathbf{R}_3\left(\frac{\pi}{2} + \alpha^n\right),\tag{2.47}$$

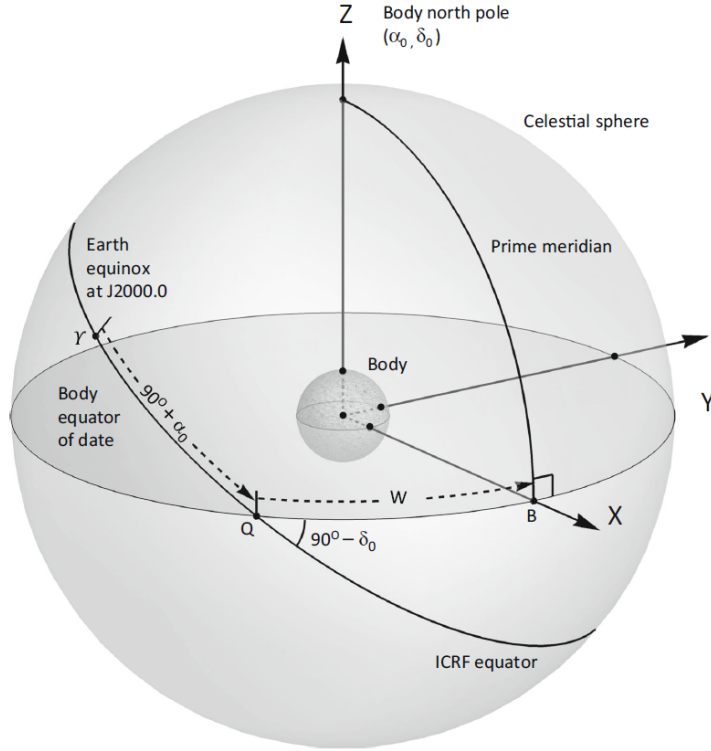


Figure 2.7: Orientation of the planets and their satellites from the IAU Reports [Archinal et al., 2018].

Table 2.3: Arguments of the trigonometric functions for the orientation of the Galilean moons in the Jovian system and their amplitude for the right ascension and declination of the north pole, and for the location of the prime meridian of Europa and Callisto [Archinal et al., 2018].

| | i | 4 | 5 | 6 | 7 | 8 |
|----------|--------------------------------|--------|--------|--------|--------|--------|
| | $J_0^i(^{\circ})$ | 355.80 | 119.90 | 229.80 | 352.25 | 113.35 |
| | $J_1^i(^{\circ}/\text{cent.})$ | 1191.3 | 262.1 | 64.3 | 2382.6 | 6070.0 |
| Europa | $A_i(^{\circ})$ | 1.086 | 0.060 | 0.015 | 0.009 | |
| | $D_i(^{\circ})$ | 0.468 | 0.026 | 0.007 | 0.002 | |
| | $W_i(^{\circ})$ | -0.980 | -0.054 | -0.014 | -0.008 | |
| Callisto | $A_i(^{\circ})$ | | -0.068 | 0.590 | | 0.010 |
| | $D_i(^{\circ})$ | | -0.029 | 0.254 | | -0.004 |
| | $W_i(^{\circ})$ | | 0.061 | -0.533 | | -0.009 |

with $\mathbf{R}_i(\theta)$ the 3×3 elemental rotation matrices about the i^{th} coordinate axis, defined for any angle θ as

$$\mathbf{R}_1(\theta) = \begin{pmatrix} 1 & 0 & 0 \\ 0 & \cos \theta & \sin \theta \\ 0 & -\sin \theta & \cos \theta \end{pmatrix}, \quad \mathbf{R}_3(\theta) = \begin{pmatrix} \cos \theta & \sin \theta & 0 \\ -\sin \theta & \cos \theta & 0 \\ 0 & 0 & 1 \end{pmatrix}. \quad (2.48)$$

2.4.2 Updated models and librations

Discussion on updated models

The IAU models for the rotation of the satellites of Jupiter rely on a few key assumptions. First, the angle between the orbit pole (i.e., the normal to the satellite orbital plane in motion around Jupiter) and the spin pole, or the obliquity, is expected to be very small for these bodies. Because the orbit pole orientations are much more constrained by observations than the spin poles, the IAU models explicitly assume zero obliquity, i.e., that the spin poles and the orbit poles are aligned. Moreover, the forced librations are ignored, and finally the orientation of the prime meridians of the satellites of Jupiter is fixed, and oriented toward Jupiter at periapse. In other words, because of current observational limits, the IAU rotation models of Jupiter’s satellites stem from the study of the orbital motion of the satellites around Jupiter.

There have been several improvements over the recent decades on the modelling of the orbital motion of the Galilean moons [see, e.g., Lainey et al., 2006]. However, none of the subsequent updates to the rotation models of Jupiter’s satellites was adopted by the IAU conventions, which haven’t changed since IAU 1994 [Davies et al., 1995]. Thus, the rotation model that we use is inconsistent with the orbital model that we consider [Jacobson, 2013], as for instance the orbit pole has changed, and is not aligned with the spin pole any more. In other words, the obliquity computed from the estimated spin pole coefficients is expected to be non-zero.

Because the current rotation models that we use do not reflect the improved knowledge of the orbital motion in the Jupiter system, Steinbrügge et al. [2019] decided to use more recent ephemerides to update the values from the IAU models, but following the same assumptions. In doing so, the rotation and orbit models would be more consistent, but the obliquity would be zero. Bills and Scott [2022] also updated the orbit pole model according to the latest ephemerides. However, instead of assuming zero obliquity, they computed fully damped spin pole trajectories, and estimated forced librations.

Nevertheless, we decided to remain consistent with the IAU convention in this simulation study, but with a minor modification to add forced librations as discussed below.

Forced librations

The gravitational attraction of Jupiter creates an equatorial bulge on its moons (see Sect. 2.2.2). Moreover, since the orbit of the moons are eccentric, the orbital speed is variable and the static equatorial bulges are not oriented toward Jupiter (see Fig. 2.8 in case of Europa, assuming zero obliquity). Therefore, Jupiter exerts a time-variable gravitational torque on the satellites, modifying their rotation angle (not represented in Fig. 2.8).

These periodic variations of the rotation angle are called forced longitudinal librations and have not been detected so far for Jupiter’s icy satellites, and thus are not given by the current IAU rotation model. In order to investigate how well the forced librations could be detected, we extended the IAU convention and added a forced libration at the

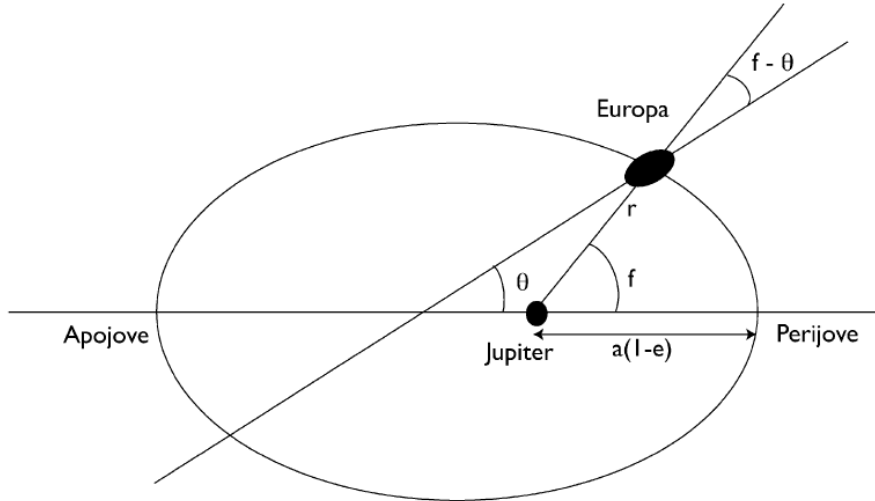


Figure 2.8: Geometry of Europa’s libration. The long axis of Europa makes an angle θ with the major axis of the orbit and f is the true anomaly [from Van Hoolst et al., 2008].

orbital period. We used an additional term for Europa’s and Callisto’s short term libration in longitude W_l , corresponding to the main libration from Rambaux et al. [2011], with $J_0^l = 222.825^\circ$ and $J_1^l = 102.1142^\circ/\text{day}$ for Europa and with $J_0^l = 311.189^\circ$ and $J_1^l = 21.5692^\circ/\text{day}$ for Callisto. The a priori amplitude of the main longitudinal libration W_l is set to 0° , so that the evaluation of the a priori rotation model remains consistent with IAU models. The amplitude W_l can therefore be estimated using our rotation model, together with other rotation parameters as described in the following section.

2.4.3 Partial derivatives of rotation model

In this work, we focus on the estimation of a subset of the rotation parameters, namely α_0, δ_0, w_1 and W_l . In order to estimate these rotation parameters, we have to solve the variational equations related to these parameters (see Sect. 2.3.2), which rely on the computation of the partial derivatives of the force model, with respect to the mentioned parameters (see Eq. (2.41)). Only the accelerations related to the gravitational potential of the central body (\mathbf{a}_g in Eq. (2.10)) depend on the rotation model, as they are first computed in the body-fixed frame, and then converted to the inertial frame. We then have

$$\frac{\partial \mathbf{f}_p}{\partial p_i} = \frac{\partial \mathbf{R}_{IN}^{BF}}{\partial p_i} \mathbf{a}_g. \quad (2.49)$$

The partial derivatives of the rotation matrix \mathbf{R}_{IN}^{BF} with respect to each rotation parameter can be derived from Eq. (2.46). In particular, for α_0, δ_0, w_1 and W_l , the partial derivatives are

$$\begin{aligned} \frac{\partial \mathbf{R}_{IN}^{BF}}{\partial \alpha_0} &= \frac{\partial \mathbf{R}_{IN}^{BF}}{\partial \alpha^n}, & \frac{\partial \mathbf{R}_{IN}^{BF}}{\partial \delta_0} &= \frac{\partial \mathbf{R}_{IN}^{BF}}{\partial \delta^n}, \\ \frac{\partial \mathbf{R}_{IN}^{BF}}{\partial w_1} &= d \frac{\partial \mathbf{R}_{IN}^{BF}}{\partial W}, & \frac{\partial \mathbf{R}_{IN}^{BF}}{\partial W_l} &= \sin(J_l) \frac{\partial \mathbf{R}_{IN}^{BF}}{\partial W}. \end{aligned} \quad (2.50)$$

The partial derivatives of the rotation matrix with respect to α^n , δ^n and W can be computed from Eq. (2.47) so that

$$\begin{aligned}\frac{\partial \mathbf{R}_{IN}^{BF}}{\partial \alpha^n} &= \mathbf{R}_3(W) \mathbf{R}_1\left(\frac{\pi}{2} - \delta^n\right) \frac{\partial \mathbf{R}_3}{\partial \alpha^n}\left(\frac{\pi}{2} + \alpha^n\right), \\ \frac{\partial \mathbf{R}_{IN}^{BF}}{\partial \delta^n} &= -\mathbf{R}_3(W) \frac{\partial \mathbf{R}_1}{\partial \delta^n}\left(\frac{\pi}{2} - \delta^n\right) \mathbf{R}_3\left(\frac{\pi}{2} + \alpha^n\right), \\ \frac{\partial \mathbf{R}_{IN}^{BF}}{\partial W} &= \frac{\partial \mathbf{R}_3}{\partial W}(W) \mathbf{R}_1\left(\frac{\pi}{2} - \delta^n\right) \mathbf{R}_3\left(\frac{\pi}{2} + \alpha^n\right),\end{aligned}\tag{2.51}$$

with the derivatives of the elementary rotation matrices, which are derived for any angle θ from Eqs. (2.48) as

$$\frac{\partial \mathbf{R}_1}{\partial \theta}(\theta) = \begin{pmatrix} 0 & 0 & 0 \\ 0 & -\sin \theta & \cos \theta \\ 0 & -\cos \theta & -\sin \theta \end{pmatrix}, \quad \frac{\partial \mathbf{R}_3}{\partial \theta}(\theta) = \begin{pmatrix} -\sin \theta & \cos \theta & 0 \\ -\cos \theta & -\sin \theta & 0 \\ 0 & 0 & 0 \end{pmatrix}.\tag{2.52}$$

2.5 Accelerometer model

A precise modelling of non-gravitational accelerations is a challenging task affected by multiple error sources. Radiation pressure accelerations depend on the mass and on the geometry of the spacecraft, but also on the properties of the materials composing it (see Eqs. 2.23 and 2.24). Even if these properties are well calibrated before flight, they can change during the mission time, e.g., because of material ageing. In addition, errors in the reconstruction of the spacecraft attitude also directly affect their modelling. Moreover, the movement of the fuel within the tank of the spacecraft during attitude manoeuvres generates non-gravitational acceleration which are difficult to model (fuel sloshing).

For all of these reasons, it can be interesting to have an accelerometer on board of the spacecraft. In this work, we studied the benefit of an on-board accelerometer to measure accelerations induced by direct SRP and PRP. Depending on the mass of the probe, and the amplitude of the attitude manoeuvres, the magnitude of fuel sloshing-induced accelerations can be significant. However, modelling sloshing to simulate the accelerations is beyond the scope of this work, but was done in other studies (see e.g., Cappuccio and Cascioli [2018], Cappuccio et al. [2020] in case of JUICE).

The accelerations \mathbf{a}_{acc} measured by the on-board accelerometer are affected by uncertainties which can be modelled as

$$\mathbf{a}_{acc} = \lambda(\mathbf{a}_{SRP} + \mathbf{a}_{PRP}) + \mathbf{b}_0 + \boldsymbol{\varepsilon}_{acc},\tag{2.53}$$

with λ a scale factor, \mathbf{b}_0 biases expressed in the accelerometer reference frame, and $\boldsymbol{\varepsilon}_{acc}$ the measurement noise. In our setup, we simulated accelerometer measurements by evaluating the SRP and PRP affecting the spacecraft, as described in Sect. 2.2.4. We thus set the scale factor $\lambda = 1$, and we considered the biases constant over the entire mission, with $\mathbf{b}_0 = 42 \text{ nm/s}^2$ in radial, along-track and cross-track directions [see, e.g., Cappuccio and Cascioli, 2018], together with a Gaussian white noise $\boldsymbol{\varepsilon}_{acc}$ of standard deviation

$\sigma_{acc} = 10 \text{ nm/s}^2$ in all three directions.

In reality, the biases of the accelerometer change during the mission duration, e.g., after desaturation manoeuvres. We thus do not consider them as global parameters, which are estimated over the entire mission, but we rather consider them constant on shorter time spans, typically several days. The biases are estimated as constant accelerations (see Sect. 2.2.5), and the length of the time span on which they are estimated has been investigated in Sect. 4.5.2. The estimation of the scale factor was discarded in this study.

2.6 Doppler observables

One of the most common tracking methods for deep space probes is radiometric tracking. In this work, we consider Doppler observables, which correspond to Doppler shifts of microwave signal exchanges between one or two ground antennas and the spacecraft, depending on the spacecraft transmitter mode. In one-way mode, the signal is emitted from the spacecraft and received by a ground station. In case of two-way tracking, an uplink signal is first sent from a ground station, received by the spacecraft and coherently sent back to the same ground station. If the downlink signal is sent to a different ground station, we talk about three-way Doppler observables. In this work, we only consider two-way Doppler observables.

2.6.1 Formulation of the two-way Doppler observables

The frequency of a radio signal exchanged between the spacecraft and ground stations on Earth changes between emission and reception of the signal. At first order, the change of frequency is proportional to the velocity of the spacecraft along the line of sight. Doppler observables, which are collected at the receiving station, are the average values of this Doppler shift over a period of time called count interval T_c or integration time. In this work, we considered two-way Doppler observables emitted and received from ground stations of either the NASA Deep Space Network [DSN, Asmar and Renzetti, 1993] or from the Chinese Deep Space Network [He et al., 2022]. The coordinates of the three ground stations from each network are given in Tabs. 2.4 and 2.5.

Table 2.4: NASA Deep Space Network

| Name | Coordinates | | Band |
|---------------------|-------------|-------------|------------------|
| Goldstone, USA | 35°25'36"N | 116°53'24"W | S and X band |
| Madrid, Spain | 40°25'53"N | 4°14'53"W | S, X and Ka-band |
| Canberra, Australia | 35°24'5"S | 148°58'54"E | S, X and Ka-band |

Radioscience observables are computed in the BSW following the formulation of Moyer [2003] for unramped two-way Doppler observables:

$$F = \frac{M_2 f_T(t_1)}{T_c} (\rho_e - \rho_s), \quad (2.54)$$

Table 2.5: Chinese Deep Space Network

| Name | Coordinates | | Band |
|--------------------|-------------|-------------|------------------|
| Jiamusi, China | 46°29′36″N | 130°46′13″E | S and X band |
| Kashgar, China | 38°25′24″N | 76°42′44″E | S, X and Ka-band |
| Neuquén, Argentina | 38°11′29″S | 70°8′59″W | S, X and Ka-band |

with M_2 the spacecraft transponder turnaround ratio (see Tab. 2.6), f_T the constant transmitter frequency at emission time t_1 , and ρ_s and ρ_e the precision round-trip light times between the ground station and the spacecraft antenna.

Table 2.6: Spacecraft turnaround ratio M_2 [Moyer, 2003].

| Uplink Band | Downlink Band | | |
|----------------|--------------------|--------------------|---------------------|
| | S | X | Ka |
| S | $\frac{240}{221}$ | $\frac{880}{221}$ | $\frac{3344}{221}$ |
| | $\frac{240}{749}$ | $\frac{880}{749}$ | $\frac{3344}{749}$ |
| X | $\frac{240}{3599}$ | $\frac{880}{3599}$ | $\frac{3344}{3599}$ |
| | $\frac{240}{3599}$ | $\frac{880}{3599}$ | $\frac{3344}{3599}$ |

The computation of the round-trip light times at the start (s) or at the end (e) of the Doppler count interval τ can be separated between the first leg $\rho_{12,s/e}$ from the transmitting station 1 to the spacecraft antenna 2, and the second leg $\rho_{23,s/e}$ from the spacecraft antenna 2 to the receiving station 3, such that

$$\begin{aligned} \rho_{s/e} &= \rho_{12,s/e} + \rho_{23,s/e} \\ &= \frac{r_{12,s/e}}{c} + \tau_{12,s/e} + \frac{r_{23,s/e}}{c} + \tau_{23,s/e}, \end{aligned} \quad (2.55)$$

with $r_{ij,s/e}$ the Euclidean distance between point i at time $t_{i,s/e}$ and point j at time $t_{j,s/e}$, and $\tau_{ij,s/e}$ the sum of the signal delays for each leg. We included the Shapiro gravitational delay [Shapiro, 1964] on light propagation due to the gravity fields of the Sun, Earth and Jupiter. The delays due to Earth’s troposphere and Earth’s ionosphere were not considered in our simulations. They are assumed to be fully calibrated, and the residual noise due to the media which the signal travels through will be discussed in Sect. 2.6.3. For similar reasons, we have not considered delays due to the Io Plasma Torus (IPT) and of Europa’s ionosphere [Kliore et al., 1997]. Current and future models of the IPT (see, e.g., Phipps [2019]) and of Europa’s ionosphere would help to at least partially calibrate the signal delay [Casajus et al., 2022, Mazarico et al., 2023].

Doppler observables are then simulated under the following conditions: minimum spacecraft elevation of 10° above the horizon and no occultations of the spacecraft line of sight by the Sun, Jupiter and the Galilean moon around which the spacecraft is orbiting.

The total derivatives of computed two-way Doppler observables with respect to the con-

sidered parameters p_i are

$$\begin{aligned} \frac{dF}{dp_i} &= \frac{\partial F}{\partial \mathbf{r}_s} \frac{\partial \mathbf{r}_s}{\partial p_i} + \frac{\partial F}{\partial \mathbf{r}_e} \frac{\partial \mathbf{r}_e}{\partial p_i} + \frac{\partial F}{\partial p_i} \\ &= \frac{M_2 f_T(t_1)}{\tau} \left(\frac{\partial \rho_e}{\partial \mathbf{r}_e} \frac{\partial \mathbf{r}_e}{\partial p_i} - \frac{\partial \rho_s}{\partial \mathbf{r}_s} \frac{\partial \mathbf{r}_s}{\partial p_i} \right) + \frac{\partial F}{\partial p_i}, \end{aligned} \quad (2.56)$$

where \mathbf{r}_s and \mathbf{r}_e are the position vectors of the spacecraft at the start and the end of the integration interval, respectively. The partial derivatives of the round-trip light-times with respect to the considered parameters are described in Moyer [2003], together with the observational partial derivatives $\frac{\partial F}{\partial p_i}$, e.g., for frequency or range biases (which we do not consider in this study).

2.6.2 Assessment of numerical errors in Doppler observables

The computation of Doppler observables is very sensitive to numerical noise, because of finite floating-point arithmetic in the representation of times and distances. Indeed, a floating-point number represented in double-precision (64-bits) has a maximum absolute value of the relative error, or machine epsilon, of 1.11×10^{-16} , corresponding to ≈ 0.08 mm range error at 5 AU. A floating-point number can also be represented in quadruple precision (128-bits), decreasing the machine epsilon to 9.63×10^{-35} . However, this precision improvement comes at the cost of increased computational load. Therefore, the computation has to be handled with care.

Already for the GRAIL data analysis in the BSW presented by Bertone et al. [2021a], the handling of observation epochs was treated by separating the fractional part of the day from its integer part to increase numerical precision with double precision floats. However, when dealing with the tracking of planetary probes in the outer Solar System, the light time between the probe and a ground antenna is increased from a few seconds at the Moon to 30 – 50 minutes in the case of the Jupiter system. This consequently increases the numerical error when computing the difference between the round-trip light times, which can be written as

$$\begin{aligned} \rho_e - \rho_s &= \rho_{12,e} + \rho_{23,e} - (\rho_{12,s} + \rho_{23,s}) \\ &= \rho_{12,e} - \rho_{12,s} + \rho_{23,e} - \rho_{23,s} \\ &= \frac{r_{12,e} - r_{12,s}}{c} + \frac{r_{23,e} - r_{23,s}}{c} + \tau_{12,e} - \tau_{12,s} + \tau_{23,e} - \tau_{23,s}. \end{aligned} \quad (2.57)$$

The different terms of Eq. (2.57) have similar values at the start and at the end of the integration interval. The precise computation of their differences can lead to round-off errors. Since the geometric distance between the ground station and the antenna spacecraft has the largest contribution to the light times, computing their difference between the end and the start of the integration interval causes the largest loss of numerical precision. In the following steps, we focus on $\rho_{12,s}$, but the same consideration can be done with $\rho_{12,e}$, $\rho_{23,s}$ and $\rho_{23,e}$. The geometric distance between the ground station at t_1 and the antenna

spacecraft at t_2 is decomposed as shown in Fig. 2.9 so that

$$\begin{aligned}
 r_{12,s} &= |\mathbf{r}_{B \rightarrow J}(t_2) + \mathbf{r}_{J \rightarrow G}(t_2) + \mathbf{r}(t_2) + \mathbf{r}_{ant}(t_2) - [\mathbf{r}_{B \rightarrow E}(t_1) + \mathbf{r}_{E \rightarrow sta}(t_1)]| \\
 &= |\mathbf{r}_{B \rightarrow J}(t_2) + \mathbf{r}_{J \rightarrow G}(t_2) - \mathbf{r}_{B \rightarrow E}(t_1) + [\mathbf{r}(t_2) + \mathbf{r}_{ant}(t_2) - \mathbf{r}_{E \rightarrow sta}(t_1)]| \\
 &= \sqrt{\sum_{k=1}^6 \sum_{l=1}^3 x_{12kl,s}^2},
 \end{aligned} \tag{2.58}$$

where

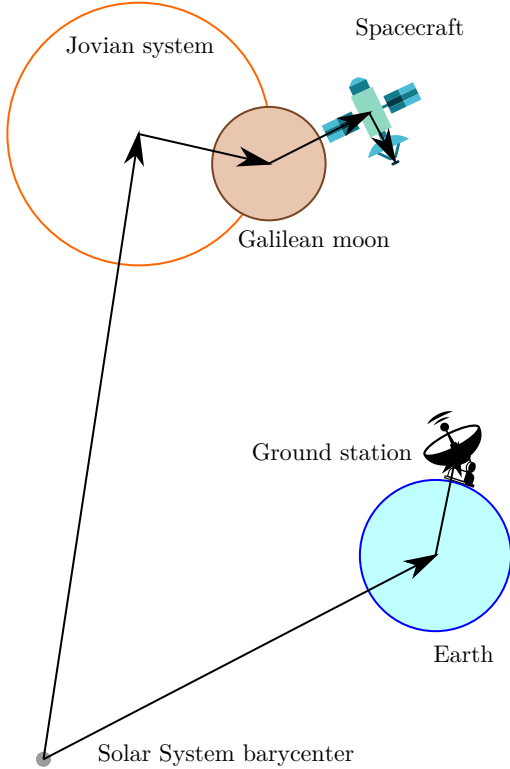


Figure 2.9: Computation of the geometric distance.

- $x_{12kl,s}$ is the l^{th} component of the position vector of the k^{th} term of the leg 12, at the start of the Doppler count interval τ ,
- $\mathbf{r}_{B \rightarrow E}$ is the position vector of the Earth with respect to the Solar System barycentre,
- $\mathbf{r}_{J \rightarrow G}$ is the position vector of the Galilean moon with respect to the barycentre of the Jovian system,
- $\mathbf{r}_{B \rightarrow J}$ is the position vector of the Jovian system's barycentre with respect to the solar system barycentre,
- $\mathbf{r}_{E \rightarrow sta}$ is the position vector of the emitting station with respect to the center of the Earth,
- \mathbf{r} is the position vector of the spacecraft center of mass with respect to the center of the Galilean moon,
- \mathbf{r}_{ant} is the position vector of the antenna with respect to the center of mass of the satellite.

We followed the approach from Zannoni and Tortora [2013] to formulate a numerical error model to assess the numerical noise introduced by our orbit determination software for the tracking of probes in the Jovian system. This model takes into consideration the maximum absolute value of the relative error, and the effect of the numerous operations introducing further errors, by assuming a statistical model to represent the numerical error. As shown in Fig. 2.10 when using only double precision (64-bit), there are significant variations of noise with time, related to the distance between Earth and Jupiter, which is the largest contributor to the geometric distance, and thus to the numerical noise when computing Doppler observations.

We investigated two solutions to minimize the occurrence of numerical errors. The first one is to use quadruple (128-bit) precision to compute and store the distances, and then compute the round-trip light times difference also in quadruple precision, before going back

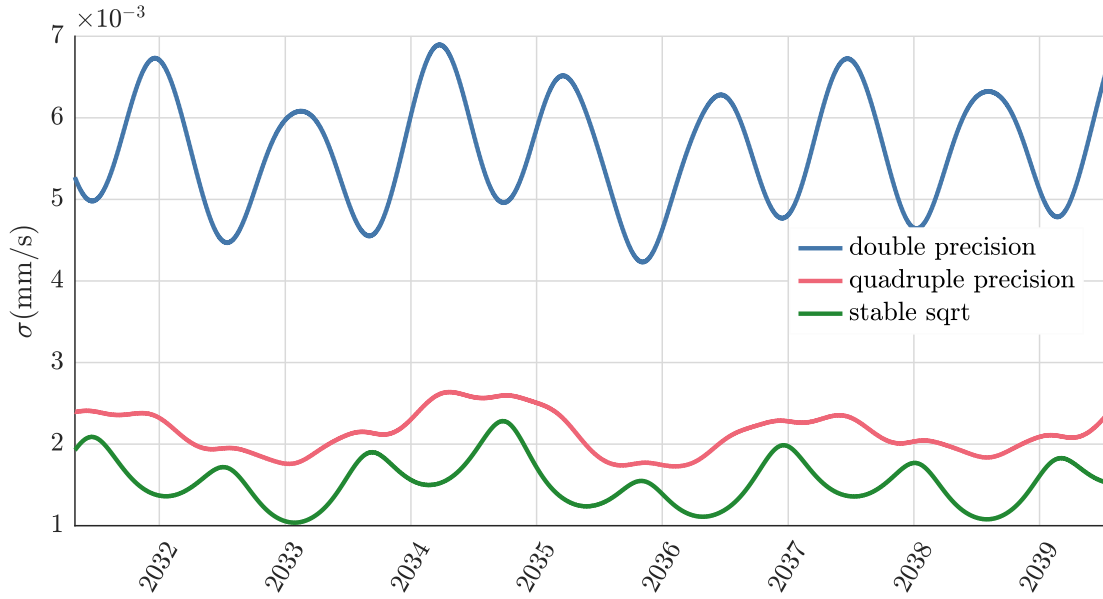


Figure 2.10: Numerical error model on Doppler observables computation ($\tau = 60$ s).

to double precision (64-bit). By only using quadruple precision at specific locations in the code, the performance was not heavily affected. The numerical noise was then reduced by a factor of 2.5, from an upper bound of $7.4 \times 10^{-3} \text{ mm s}^{-1}$ to $2.9 \times 10^{-3} \text{ mm s}^{-1}$, for two-way Doppler.

We also compared the RMS of the Doppler residuals for an orbit fitted around Europa by two-way Doppler observables with only double precision, and with localized quadruple precision, without any additional source of error (zero-tests). In our controlled simulation environment, the RMS of the Doppler residuals was reduced by several orders of magnitude (from $8.0 \times 10^{-4} \text{ mm s}^{-1}$ to below $4.0 \times 10^{-9} \text{ mm s}^{-1}$).

We additionally considered another solution, i.e., to rewrite the distance differences as

$$r_{ij,e} - r_{ij,s} = \frac{r_{ij,e}^2 - r_{ij,s}^2}{r_{ij,e} + r_{ij,s}}, \quad (2.59)$$

allowing us to circumvent the difference of square roots by working directly with the differences of each component and each term of Eq. (2.58). If $x_{ijkl,e}$ and $x_{ijkl,s}$ are the l^{th} component of the position vector of the k^{th} term of the leg ij , respectively at the end and the start of the Doppler count interval τ , we can then write

$$\begin{aligned} r_{ij,e} - r_{ij,s} &= \sum_{k=1}^6 \sum_{l=1}^3 \frac{x_{ijkl,e}^2 - x_{ijkl,s}^2}{r_{ij,e} + r_{ij,s}} \\ &= \sum_{k=1}^6 \sum_{l=1}^3 (x_{ijkl,e} - x_{ijkl,s}) \frac{(x_{ijkl,e} + x_{ijkl,s})}{r_{ij,e} + r_{ij,s}}, \end{aligned} \quad (2.60)$$

which is numerically more stable when $x_{ijkl,s} \approx x_{ijkl,e}$. By doing so, we could reduce the numerical noise slightly more in comparison to localized quadruple precision (below

$3.3 \times 10^{-9} \text{ mm s}^{-1}$). This is also visible when adapting the numerical error model of Zannoni and Tortora [2013] (see Fig. 2.10). Equation (2.60) can then be computed using double precision only, since quadruple precision does not visibly reduce the numerical error.

It should be noted that the RMS of the Doppler residuals given in this section do not represent the level of accuracy that can be reached using realistic data, which will be discussed in Chapter 4. However, they illustrate the improvement we introduced in treating numerical errors within the BSW. After adopting the presented solutions, the numerical error is negligible with respect to other important sources of physical noise, which are discussed in Sect. 2.6.3.

2.6.3 Noise model

The Doppler observations are affected by various sources of noise [Asmar et al., 2005, Iess et al., 2014a], which we discuss in this section. We describe a noise model in which each contribution is characterised by its Allan deviation $\sigma_y(\tau)$ [Barnes et al., 1971], where τ is the Doppler integration time (see Fig. 2.11). For a given τ the Allan deviation can be converted to an equivalent noise on the line-of-sight velocity σ_v , or a more practical equivalent noise which we directly add to the Doppler observable σ_f such as

$$\sigma_v = c \sigma_y(\tau), \quad \text{and} \quad \sigma_f = f_T \sigma_y(\tau). \quad (2.61)$$

The propagation of the signal through media with variable refractive index causes frequency fluctuations. Random refractive index fluctuations in interplanetary media, such as the solar plasma and the IPT, are proportional to f_T^{-2} [Asmar et al., 2005]. It means that K-band signals ($\approx 32 \text{ GHz}$) will be less affected by this dispersive noise than X-band ($\approx 8.4 \text{ GHz}$) or S-band ($\approx 2.3 \text{ GHz}$) signals. The noise due to solar plasma highly depends on the distance of the line of sight between the Earth and the probe with respect to the Sun, which is characterized by the solar elongation γ_{SEP} (angle between the Sun, the Earth and the spacecraft, also called Sun-Earth-Probe angle). We modelled the solar plasma noise for two-way X-band Doppler observations at $\tau = 60 \text{ s}$ as [Iess et al., 2012]

$$\sigma_y^{plasma} = 10^{-14} \times \begin{cases} 1.76 \sin(\gamma_{SEP})^{-1.98} + 6.25 \sin(\gamma_{SEP})^{0.06} & \text{if } \gamma_{SEP} \in [0^\circ, 90^\circ] \\ (1.76 + 6.25) \sin(\gamma_{SEP})^{1.05} & \text{if } \gamma_{SEP} \in]90^\circ, 170^\circ] \\ 1.27 & \text{if } \gamma_{SEP} \in]170^\circ, 180^\circ] \end{cases}. \quad (2.62)$$

Since plasma noise is proportional to f_T^{-2} [Asmar et al., 2005], the solar plasma noise model has to be scaled accordingly when using S-band or Ka-band signals.

The refractive index is also fluctuating in the troposphere, mainly due to water vapour fluctuations [Asmar et al., 2005]. The noise induced by the ‘‘wet component’’ of the troposphere is, however, not dispersive. We adopted a noise model with a seasonal variation, similar to Iess et al. [2012], which can be written as

$$\sigma_y^{tropo} = [6.5 - 3.5 \cos(2\pi(t - t_0))] \times 10^{-14}, \quad (2.63)$$

with t in years and $t_0 = 2010$ years for a station in the northern hemisphere, and $t_0 = 2010.5$ years for a station in the southern hemisphere, so that the noise coming from the

wet troposphere is maximum in summertime, and minimum in wintertime. Wet troposphere noise depends highly on the ground station location, but we decided that this model is a sufficient approximation for our simulation.

Because of wind, gravitational loading, and thermal deformation, the antennas of the ground stations are also a source of noise which can be evaluated as $\sigma_y^{GS} = 1.6 \times 10^{-14}$ at $\tau = 60$ s [Iess et al., 2014a]. We assumed $\sigma_y^{S/C} = 1.8 \times 10^{-14}$ for all the spacecraft electronics, which are generally dominated by noise from the Deep Space Transponder (DST) [Iess et al., 2014a].

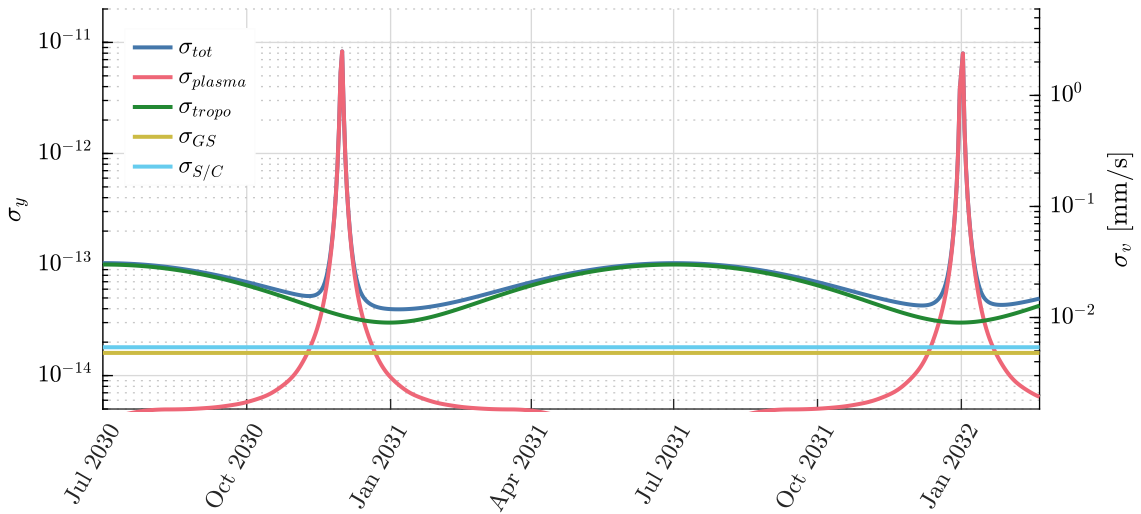


Figure 2.11: Noise model for two-way Ka-band Doppler received at a station in the northern hemisphere at $\tau = 60$ s.

It is important to note that the noise induced by the radio signal propagation in a dispersive medium (e.g., solar plasma) can be cancelled using multi-frequency radio systems [Bertotti et al., 1993]. Additionally, the use of water vapour radiometers at the ground stations would allow the calibration of the wet tropospheric noise. However, since these considerations depend on the mission architecture and on the ground station considered, we decided to follow a more conservative approach in this work. We simulated realistic Doppler observations by applying a Gaussian white noise of variance

$$(\sigma_y^{tot})^2 = (\sigma_y^{plasma})^2 + (\sigma_y^{tropo})^2 + (\sigma_y^{GS})^2 + (\sigma_y^{S/C})^2. \quad (2.64)$$

For some investigations in this work presented in Chapter 4, we also considered a fixed level of Gaussian white noise, $\sigma_v = 0.10 \text{ mm s}^{-1}$ (one-way) at $\tau = 60$ s integration time, to encompass the major relevant noise sources.

2.7 Laser altimetry data

Besides Doppler tracking data, laser altimetry data were simulated for a probe orbiting Callisto using pyXover, a Python suite of altimetry analysis tools for planetary geodesy [Bertone

et al., 2020]. Realistic laser altimeter measurements are simulated from the spacecraft to the surface of Callisto by considering a synthetic topography model (Sect. 2.7.1).

Although our formulation is valid regardless of the altimeter pointing, in this work we only assumed nadir pointing measurements to avoid the additional complexity of defining an attitude law for the spacecraft or the instrument. In Sect. 2.7.2, we follow the same formulation previously which has been used for crossover analyses of the MESSENGER probe at Mercury [Bertone et al., 2021b], to compute crossover discrepancies at Callisto. In order to combine the crossover analysis with our generalized Doppler orbit determination, we extract the crossover discrepancies and their partial derivatives from pyXover (Sect. 2.7.3) and set-up an interface to the BSW routines, as detailed in Chapter 5.

2.7.1 Altimetric range simulation

The laser altimeter range $LA(t)$ is modelled as the distance between the spacecraft and the topography $T(\phi, \lambda)$ of the moon at the sub-satellite point,

$$LA(t) = r(t) - T(\phi, \lambda) - u_r(\mathbf{r}, t) + \varepsilon_{range}, \quad (2.65)$$

where ϕ and λ are the latitude and longitude of the probe at t , respectively. u_r is the radial deformation due to Jupiter-induced tides, which can be expressed as [see, e.g., Van Hoolst and Jacobs, 2003]

$$u_r(\mathbf{r}, t) = \frac{h_2}{g} \frac{GM_J}{2} \frac{R_G^2}{d_J^3} (3 \cos^2 \psi - 1), \quad (2.66)$$

with ψ being the angle between \mathbf{r} and the direction from the center of the moon to Jupiter, g the gravitational acceleration at the surface, d_J the distance between the centres of mass of the Jupiter and Callisto, and h_2 the Love number of degree 2. ε_{range} represents the white noise contributions we add to simulate realistic altimetric ranges. The main sources of errors for an altimeter are: the instrument intrinsic errors $\varepsilon_{range}^{instr}$, which are below 0.2 m in the case of BELA [Steinbrügge et al., 2018b, HosseiniArani, 2020] and GALA [Hussmann et al., 2019], errors in pointing, and alignment which depend on the altitude h , spacecraft pointing uncertainties $\Delta\Phi$, and surface slope S , so that [see, e.g., Steinbrügge et al., 2015]

$$\varepsilon_{range}^{pointing} = h \tan S \tan \Delta\Phi. \quad (2.67)$$

We get $\varepsilon_{range}^{pointing} \sim 1$ m for a probe orbiting at $h = 200$ km by assuming in average $S = 6^\circ$ and $\Delta\Phi = 10''$ [see, e.g., Villamil et al., 2021].

The absence of highly accurate topographic models for the Galilean moons prevents using altimetric ranges as direct measurements [Mazarico et al., 2018, Goossens et al., 2020]. Nevertheless, the topography can be cancelled at crossover locations by defining differential measurements between ranges to the same surface location at different epochs (i.e., crossover discrepancies, see Sect. 2.7.2). However, an important source of uncertainty in the processing of altimetry crossover is related to interpolating between the bouncing points of the laser altimeter ranges and the crossover location on the surface. These uncertainties can be taken into account as part of the altimetric ranges noise budget (see, e.g., Villamil et al. [2021]) as they depend on topography, the velocity of the probe with respect to the

surface of Callisto, and on the sampling rate of the altimeter instrument. We compare this approach with the interpolation error we get by considering a detailed topography model (see Chapter 5).

Since no Digital Elevation Model (DEM) for the Galilean moons is currently available, we consider a global DEM of Mercury for the similar-sized Callisto [Becker et al., 2016]. However, the chosen global DEM presents only large scale features with an effective resolution down to several km/pixel. In order to also take into account smaller-scale features, we simulate a small-scale topography, based on a tile of $0.25^\circ \times 0.25^\circ$ (i.e., $10 \text{ km} \times 10 \text{ km}$), which periodically and continuously repeats on the surface of Callisto over the longitudes and latitudes. This texture is computed following Bertone et al. [2021b] by using a fractal noise map composed by five superposed levels (see Fig. 2.12): the main noise level has an amplitude of 30 m on a 600 m baseline, while for each of the following ones the amplitude is divided by $\sqrt{2}$ and the baseline is halved. The total topography T considered for the Galilean moon when simulating our altimetry dataset is then the sum of the large scale topography T_{DEM} and of the small-scale topography T_{local} , so that

$$T(\lambda, \phi) = T_{DEM}(\lambda, \phi) + T_{local}(\lambda, \phi). \quad (2.68)$$

It is important to note that we defined T_{local} based on past analyses at Mercury, which might not represent the actual (currently unknown) small-scale topography of Callisto. The magnitude of small-scale topography has a direct impact on the interpolation error for the crossover analysis. For instance, a smoother small-scale topography would yield a lower interpolation error.

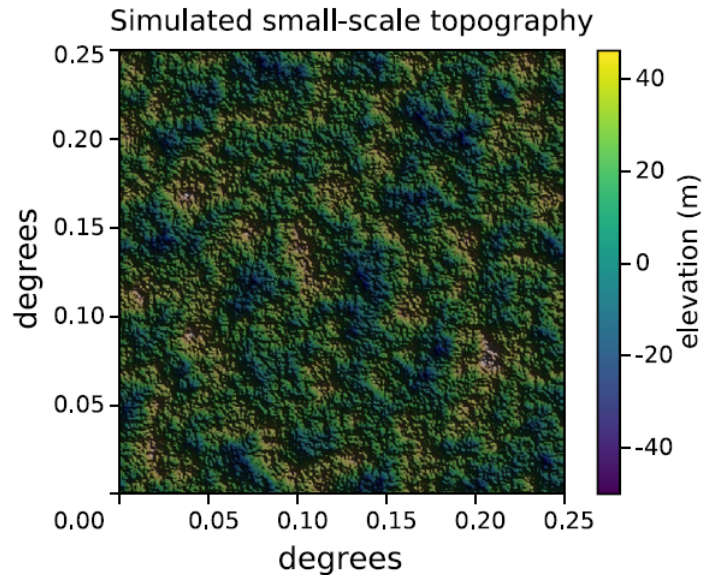


Figure 2.12: Small-scale topography [Bertone et al., 2021b].

We simulate altimetric ranges using pyAltsim, a program of the pyXover software library, based on spacecraft orbits integrated in the BSW (see Sect. 2.1), converted from STD to SPK format, and read in pyXover using SPICE routines [Acton Jr, 1996]. We mainly considered a 10 Hz sampling, consistent with BepiColombo Laser Altimeter [BELA; Thomas

et al., 2021], but we also performed a few tests at 30 Hz, the nominal sampling rate of the GAnymede Laser Altimeter [GALA; Hussmann et al., 2019] on board of JUICE. However, such a higher sampling increases the amount of data, and thus the computational load and related challenges.

2.7.2 Crossover discrepancy

A crossover point is a location at which two distinct ground-tracks, i.e., the projections of the orbit on the ground surface along the line-of-sight of the altimeter, intersect. The search for the location of all crossovers during the mission duration is central to this analysis, as all combinations between all ground-tracks have to be analysed. This is efficiently performed in pyXover, as detailed in Bertone et al. [2021b]. Differential measurements at crossover locations (Fig. 2.13) are particularly interesting [Shum et al., 1990, Rowlands et al., 1999], as they are due to a combination of errors in the spacecraft orbit and attitude, interpolation errors of the surface topography between the altimeter footprints, and geophysical signals (e.g., mismodellings in orientation or vertical tides model).

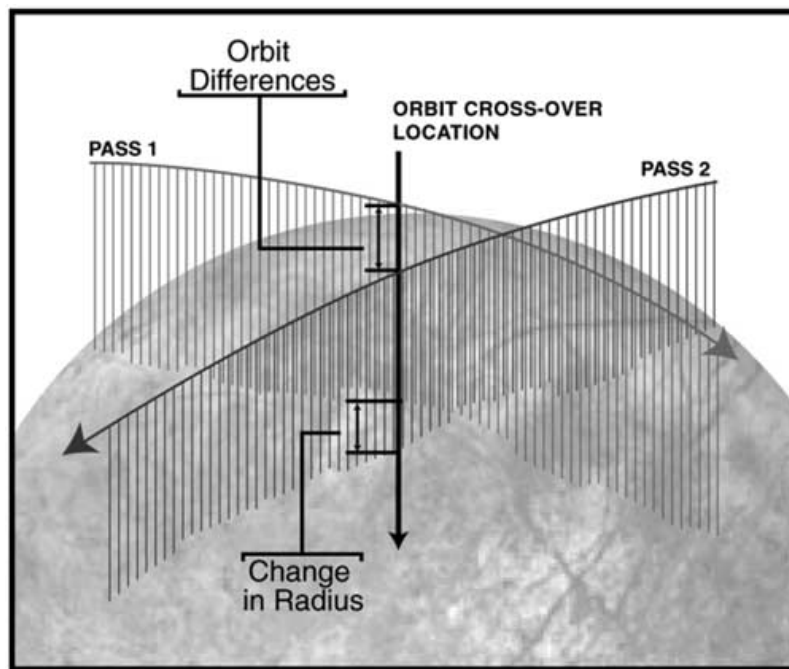


Figure 2.13: Schematic illustration of altimeter crossover approach [Neumann et al., 2001].

The search and the computation of the crossover observables starts with the geolocation of the laser altimetry bouncing points on the surface of the moon (see Fig. 2.14). Each altimetry measurement gets assigned a set of latitude ϕ , longitude λ and elevation η , corresponding to the radial component of the geolocalised range measurements. Then, the partial derivatives with respect to the orbit parameters, the rotation parameters α_0 , δ_0 , w_1 and W_l , and the tidal parameter h_2 are computed along each track by finite differencing (except for h_2 , whose derivatives are computed analytically, see Bertone et al. [2021b]). In pyXover, the orbit parameters are orbit corrections modelled as 3 constant offsets estimated

on each track in the Local Orbital Frame (TVN), defined as

$$\mathbf{e}_v = \frac{\dot{\mathbf{r}}}{\|\dot{\mathbf{r}}\|}, \quad \mathbf{e}_n = \frac{\mathbf{r} \times \dot{\mathbf{r}}}{\|\mathbf{r} \times \dot{\mathbf{r}}\|}, \quad \text{and} \quad \mathbf{e}_t = \mathbf{e}_v \times \mathbf{e}_n. \quad (2.69)$$

The Local Orbital Frame (TVN) considered in pyXover is different from the Local Orbital Frame (RSW) used in the BSW (see Sect. 2.2.5). \mathbf{e}_r and \mathbf{e}_s are close to \mathbf{e}_t and \mathbf{e}_v , respectively, but they are only equal when the probe is at one of the two apsides, or if the orbit is perfectly circular. However, \mathbf{e}_n and \mathbf{e}_w are both in the direction of the normal to the orbital plane.

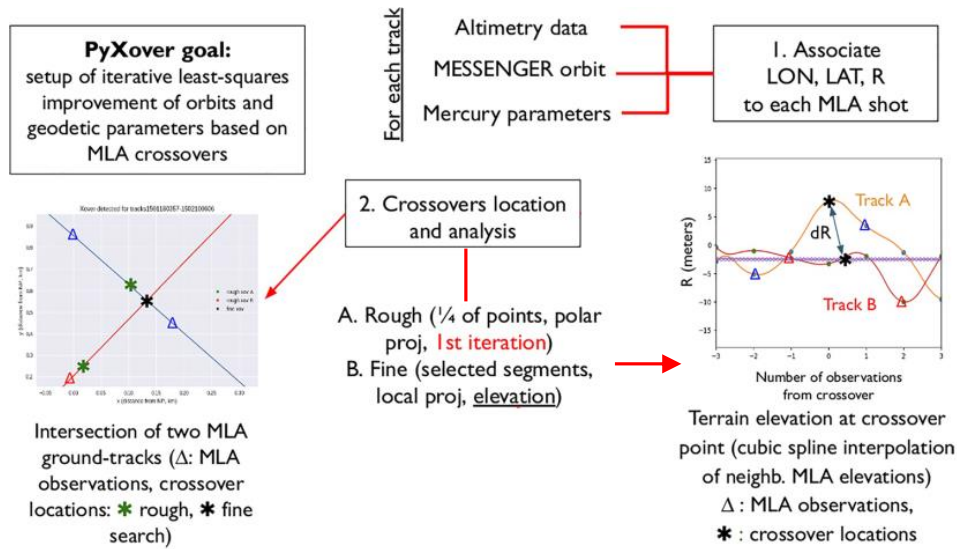


Figure 2.14: Workflow of the pyXover code: (1) geolocation of altimetry data and (2) crossovers location, adapted from Bertone et al. [2021b].

Finally, the intersections between the ground tracks are identified, and the crossover discrepancy ν between two tracks A and B is computed as the difference in elevation at the crossover point, such that

$$\nu = \eta_A - \eta_B. \quad (2.70)$$

The crossover observables and their partial derivatives computed in pyXover, can either be processed as in Bertone et al. [2021b] within pyXover to find corrections to the considered parameters, or they can be exported to the BSW for a joint analysis with Doppler observables (see Chapter 5).

2.7.3 Crossover partial derivatives

The crossover discrepancy is modelled as a function of errors in the a priori orbit, deviations from the rotation model, and mismodelling of tidal deformations. In an ideal case, we would expect $\nu = 0$. As mentioned in Sect. 2.7.2, the orbit parameters in pyXover are parametrised as offsets in the Local Orbital Frame (TVN). Since the BSW uses a different orbit parametrisation, i.e., initial osculating orbital elements for each arc, the partial

derivatives have to be adapted accordingly.

For each parameter p_j , the total derivative of the crossover discrepancy ν_i can be written as

$$\frac{d\nu_i}{dp_j} = \frac{\partial\nu_i}{\partial\Delta_{i,1}} \frac{\partial\Delta_{i,1}}{\partial p_j} + \frac{\partial\nu_i}{\partial\Delta_{i,2}} \frac{\partial\Delta_{i,2}}{\partial p_j} + \frac{\partial\nu_i}{\partial p_j}, \quad (2.71)$$

with $\Delta_{i,1}$ and $\Delta_{i,2}$ the orbit offsets of respectively the first and second track of the crossover i . Using chain rule, we can then derive

$$\frac{d\nu_i}{dp_j} = \frac{\partial\nu_i}{\partial\Delta_{i,1}} \frac{\partial\Delta_{i,1}}{\partial\mathbf{r}_1} \frac{\partial\mathbf{r}_1}{\partial p_j} + \frac{\partial\nu_i}{\partial\Delta_{i,2}} \frac{\partial\Delta_{i,2}}{\partial\mathbf{r}_2} \frac{\partial\mathbf{r}_2}{\partial p_j} + \frac{\partial\nu_i}{\partial p_j}, \quad (2.72)$$

with $\mathbf{r}_k = \mathbf{r}(t_k)$. The position of the spacecraft is reconstructed from the orbit offset according to $\mathbf{r}_k = \mathbf{r}_{0,k} + \mathbf{R}_k \Delta_{i,k}$, with \mathbf{R}_k denoting the rotation matrix from the Local Orbital Frame (TVN) to the inertial frame at t_k , and $\mathbf{r}_{0,k}$ being the a priori value of \mathbf{r}_k . We then have

$$\frac{\partial\Delta_{i,k}}{\partial\mathbf{r}_k} = \frac{\partial\mathbf{R}_k^T}{\partial\mathbf{r}_k} (\mathbf{r}_k - \mathbf{r}_{0,k}) + \mathbf{R}_k^T = \frac{\partial\mathbf{R}_k^T}{\partial\mathbf{r}_k} \mathbf{R}_k \Delta_{i,k} + \mathbf{R}_k^T. \quad (2.73)$$

We compute the total derivatives by evaluating Eq. (2.73) with all the parameters set to their a priori value, i.e., in particular by setting $\Delta_{i,k} = 0$, so that

$$\frac{d\nu_i}{dp_j} = \frac{\partial\nu_i}{\partial\Delta_{i,1}} \mathbf{R}_1^T \frac{\partial\mathbf{r}_1}{\partial p_j} + \frac{\partial\nu_i}{\partial\Delta_{i,2}} \mathbf{R}_2^T \frac{\partial\mathbf{r}_2}{\partial p_j} + \frac{\partial\nu_i}{\partial p_j}. \quad (2.74)$$

The partial derivatives $\frac{\partial\nu_i}{\partial\Delta_{i,k}}$ are computed in pyXover, as mentioned in Sect. 2.7.2, together with the partials $\frac{\partial\nu_i}{\partial p_j}$ for $p_j \in \{\alpha_0, \delta_0, w_1, h_2\}$ and $\frac{\partial\nu_i}{\partial p_j} = 0$ for other parameters. The epochs of the crossovers, the crossover discrepancies, and their partial derivatives are exported from pyXover to XOVNEQ, a program within the BSW developed in the frame of this work. XOVNEQ reads the observation files from pyXover, and then uses the previously integrated STD orbit to compute the total derivatives according to Eq. (2.74) to set up NEQs which can then be combined with other observables within the BSW (see Sect. 2.3.3). See Sect. 5.1.1 for a more detailed description of the combination.

2.8 Internal structure modelling

The gravity field of a celestial body can be computed directly from the internal mass distribution, but the gravity field alone is not enough to unambiguously determine the internal structure of a celestial body. This is even true if one assumes radial density profiles. One can nevertheless rely on a number of reasonable assumptions to help constraining possible internal structure models, such as fixing the number of layers, the chemical composition of the body or the equation of state. Other quantities, such as the rotational state, the moments of inertia, and the tidal deformations can further constrain the internal structure. In the following, we briefly describe some key constraints which can be derived from the geodetic parameters we estimate in this work.

2.8.1 Moment of Inertia

The Moment of Inertia (MoI) of a body b with respect to a given axis Δ is defined as the integral over the body so that

$$I_{\Delta} = \iiint_b \rho r_{\Delta}^2 dV, \quad (2.75)$$

where ρ is the density of the of the infinitesimal volume dV , and r_{Δ} its perpendicular distance to the axis Δ . It is an indicator of the internal mass distribution of the moon, as it gives information on the density profile of the body. For instance, a sphere of mass M and radius R , with a homogeneous density has a mean MoI I of $0.4MR^2$. However, in case of an ellipsoid of revolution, we distinguish the polar principal moment of inertia C with respect to the rotational axis, and the equatorial principal moments of inertia A and B . I and C can be determined from the degree-2 gravity field coefficient and with several assumptions, which we describe in the following.

Hydrostatic equilibrium

A body has reached hydrostatic equilibrium if the forces due to gravity and to pressure gradient cancel out. In addition, if there is no large density variation inside the body and if the perturbations arising from tides and from rotation are small [Gao and Stevenson, 2013], the normalized mean Moment of Inertia (MoI) of a synchronous rotating moon can be determined from the Radau-Darwin Approximation (RDA) [Radau, 1885, Hubbard and Anderson, 1978], so that

$$\bar{I} = \frac{I}{MR^2} = \frac{A + B + C}{3MR^2} = \frac{2}{3} \left(1 - \frac{2}{5} \sqrt{\frac{4 - k_f}{1 + k_f}} \right), \quad (2.76)$$

with k_f the fluid (or secular) Love number, which describes the reaction of the moon to a perturbing potential after all viscous stresses have relaxed [Munk et al., 1977]. The fluid Love number k_f should not be confused with the tidal Love number k_2 . Strictly speaking, k_2 is only related to the short-period tides, and k_f is related to the static tides [Van Hoolst et al., 2013].

For a synchronously rotating body (such as the Galilean moons) deformed by rotation and tides, the fluid Love number k_f can be inferred from the degree-2 gravity zonal (zero tide) coefficient by noting that [Rappaport et al., 1997]

$$J_2 = \frac{5}{6} k_f q_r, \quad \text{with} \quad q_r = \frac{\Omega^2 R_G^3}{GM_G}, \quad (2.77)$$

where the rotation parameter q_r is the ratio between the centrifugal and gravitational forces at the moon's equator. Note that in case of hydrostatic equilibrium, there is a relation between the degree-2 sectorial and zonal coefficients. This hydrostatic relation, which is a necessary but not sufficient condition for hydrostatic equilibrium of synchronous satellites, can be approximated by $J_2/C_{22} = 10/3$ for slow rotators. For Europa, a higher order approximation is instead necessary, so that $J_2/C_{22} = 3.324$ [Tricarico, 2014].

The hydrostatic relation $J_2/C_{22} = 10/3$ has been considered to estimate the degree-2 coefficients of Europa [Anderson, 1998] and Callisto [Anderson, 2001] from Galileo data. Indeed, J_2 and C_{22} could not be estimated independently because the flybys (four at Europa and five at Callisto) were located around the equator, and because equatorial flybys are not well suited to estimate zonal coefficients.

Hydrostatic equilibrium was also assumed by Anderson [2001], and the MoI of Callisto has been computed using the RDA ($\bar{I} = 0.3549 \pm 0.0042$). This tells us that Callisto is probably not fully differentiated. Indeed, if Callisto would be fully differentiated, the MoI would be 0.38 [McKinnon, 1997]. In the case of Europa, its measured MoI [Anderson, 1998, $\bar{I} = 0.346 \pm 0.005$], also assuming hydrostatic equilibrium, suggests that the moon is fully differentiated into a metallic core surrounded by a rock mantle and a water outer shell.

However, hydrostatic equilibrium is not guaranteed for Callisto or Europa. Deviation from hydrostatic equilibrium has been identified for several moons of the Solar System, e.g. Titan [Iess et al., 2010, Durante et al., 2019] and Ganymede [Casajus et al., 2022]. As Callisto is a slow rotator, even small internal mass variations would significantly influence its MoI [McKinnon, 1997]. The non hydrostatic effects would then be more critical than for Europa. Indeed, if Callisto is not in hydrostatic equilibrium, the MoI estimated by Anderson [2001] would be too large. The existence of non-hydrostatic effects could then disprove an incomplete differentiation of Callisto's internal structure [Gao and Stevenson, 2013]. However, additional topographic data could be used to infer the non-hydrostatic components [Iess et al., 2014b, Hemingway et al., 2018].

With a low altitude polar orbiter, the gravity field can be estimated without assuming hydrostatic equilibrium. In case this equilibrium is a posteriori valid, we can evaluate the mean Moment of Inertia of the moon.

Triaxial ellipsoid

As briefly mentioned in Sect. 2.2.1, the degree-2 gravity field coefficients can also be used to define a triaxial ellipsoid as a quadrupole equipotential surface in the frame of the hydrostatic equilibrium assumption [Van Hoolst et al., 2008]. The equation of the triaxial ellipsoid can be written as

$$r_{ell}(\lambda, \phi) = \frac{abc}{\sqrt{(bc \cos \phi \sin \lambda)^2 + (ca \sin \phi \sin \lambda)^2 + (ab \sin \phi)^2}}, \quad (2.78)$$

with $a > b > c$ the principal axes, ϕ the latitude and λ the longitude. The principal axes can be approximated by the degree-2 gravity field coefficients and the rotation parameter q_r . Indeed, r_{ell} can be expressed to first order with the flattening coefficients (see e.g., Van Hoolst and Dehant [2002]) and by using associated Legendre polynomials, as

$$r_{ell}(\lambda, \phi) = r_0 \left(1 - \frac{2}{3} \alpha P_{20}(\sin \phi) + \frac{1}{6} \beta P_{22}(\sin \phi) \cos 2\lambda \right), \quad (2.79)$$

with r_0 the mean radius of the ellipsoid surface and with the polar flattening and the equatorial flattening, respectively, defined as

$$\alpha = \frac{(a+b)/2 - c}{(a+b)/2}, \quad \text{and} \quad \beta = \frac{a-b}{a}. \quad (2.80)$$

Van Hoolst et al. [2008] expressed the flattening in terms of J_2 , C_{22} and q_r , so that

$$\alpha = \frac{3}{2}J_2 + \frac{5}{4}q_r, \quad \text{and} \quad \beta = 6C_{22} + \frac{3}{2}q_r. \quad (2.81)$$

If the reference frame coincides with the principal axes of inertia, we also have $S_{22} = C_{21} = S_{21} = 0$. The principle axes can be reconstructed from the flattening coefficients as

$$\begin{aligned} a &= r_0 \left(1 + \frac{1}{3}\alpha + \frac{1}{2}\beta \right), \\ b &= r_0 \left(1 + \frac{1}{3}\alpha - \frac{1}{2}\beta \right), \\ c &= r_0 \left(1 - \frac{2}{3}\alpha \right). \end{aligned} \quad (2.82)$$

From obliquity

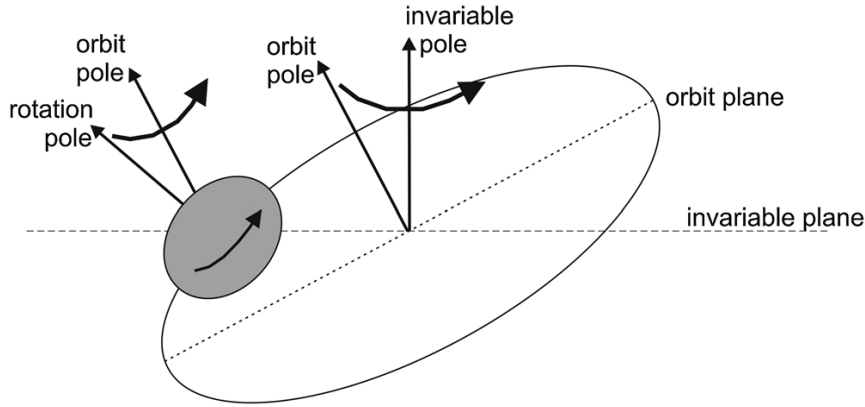


Figure 2.15: Precession of the instantaneous orbit pole \mathbf{n} around an invariable pole \mathbf{k} and of the rotation pole (or spin pole) \mathbf{s} of the moon around the orbit pole \mathbf{n} . In a Cassini state, \mathbf{n} , \mathbf{s} and \mathbf{k} remain coplanar [extracted from Nimmo and Pappalardo, 2016].

The polar MoI C of synchronous moons can be derived from the obliquity ϵ independently from the above-mentioned hydrostatic equilibrium hypothesis. The obliquity ϵ is the angle between the orbit pole \mathbf{n} and the spin pole \mathbf{s} , the latter computed from the estimates of its right ascension α^n , and its declination δ^n (see Sect. 2.4.1). If the obliquity is tidally damped, and if the moon occupies a classical Cassini state [Bills and Nimmo, 2008], then the orbit pole \mathbf{n} and the spin pole \mathbf{s} remain coplanar as they circle a third (invariable) pole \mathbf{k} (Fig. 2.15). The orbit pole precesses then at a uniform rate $\dot{\Omega}$ about the invariant pole. The normalised polar MoI can then be obtained as [Eq. 10 of Bills and Nimmo, 2011]

$$\frac{C}{MR^2} = \frac{2}{3} \frac{n}{\dot{\Omega}} \frac{(C_{22}/2 + (J_2 + C_{22}) \cos \epsilon) \sin \epsilon}{\sin(i - \epsilon)}, \quad (2.83)$$

with i the inclination of the orbit pole with respect to the invariant pole, with $\mathbf{s} \cdot \mathbf{k} = \cos(i - \epsilon)$, and n the mean motion of the moon around Jupiter. The obliquity of the Galilean moons is expected to be small, thus difficult to measure. Chen et al. [2014] predicted obliquities of 0.05° for Callisto and 0.00014° for Europa.

2.8.2 Putative subsurface ocean and ice-shell

The presence of a subsurface ocean on each of the icy moons of Jupiter can be confirmed through three main geophysical approaches [Nimmo and Pappalardo, 2016]: magnetic induction [Khurana et al., 2002], radar sounding [Blankenship et al., 2009], and geodetic approaches. Moreover, the ocean and the ice-shell thickness can be constrained from a combination of several measurement techniques (see Fig. 2.16). In this section we will briefly describe several geodetic measurements contributing to the characterisation of the ice-shell and of the putative ocean, which are of prime interest in this work.

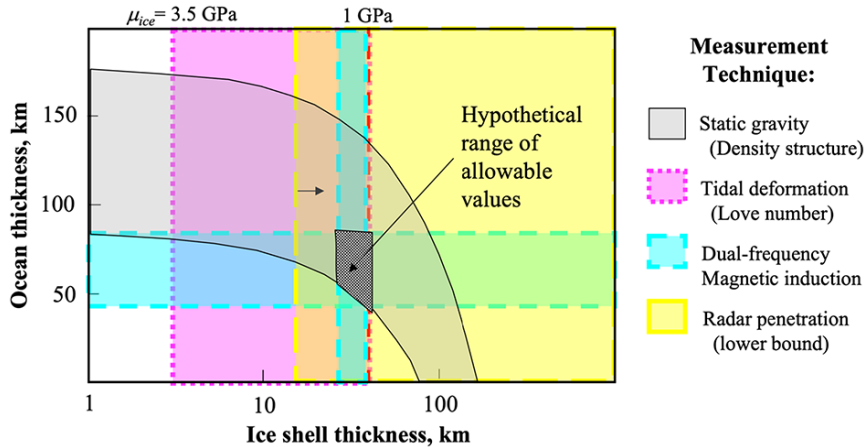


Figure 2.16: Overlapping measurements combination to constrain the ice shell and ocean thickness of Europa [extracted from Roberts et al., 2023].

Tidal response

A precise measurement of the body’s tidal response is the first element which can provide evidence of a subsurface ocean [Wu et al., 2001]. The tidal response of a celestial body is composed of vertical surface displacements (characterised by the h_2 Love number, see Sect. 2.7.1), and of time-variable gravity related to the tidal bulge (characterized by the k_2 Love number, see Sect. 2.2.2). The analysis of laser altimetry crossovers makes the estimation of h_2 possible, and k_2 is estimated together with the static gravity field, using radio tracking.

The precise estimation of either k_2 or h_2 would unambiguously confirm the presence of a subsurface ocean. Indeed, with an ocean that decouples the surface ice from the rocky interior, the amplitude of the semi-diurnal tide on Europa is roughly 30 m, while it is approximately 1 m in the absence of an ocean [Moore and Schubert, 2000]. Because of the larger distance to Jupiter, the amplitude of the tides on Callisto are expected to be smaller. They could nevertheless exceed 5 m in presence of a global ocean, but would be limited to maximum 0.3 m in absence of an ocean [Moore and Schubert, 2003].

The thickness of the ice is instead more difficult to infer from h_2 or k_2 alone. However, the quantity $1 + k_2 - h_2$ would provide a better estimate of the ice thickness, even though the

precise determination of the thickness is highly dependent on the rigidity of the shell [Wahr et al., 2006].

Librations

The determination of the amplitude of the longitudinal librations (see Sect. 2.7.1) can provide additional constraints on the putative ocean, even though it would not be sufficient by itself to assess its existence.

In this work, we did not distinguish the libration of the ice-shell from the libration of the interior. However, in the presence of a global ocean, the ice shell is decoupled from the interior and may librate separately [Wu et al., 2001]. In addition, if the shell is assumed to be rigid, accurate measurements of the amplitude of the ice-shell librations from the orbit could be used to constrain the thickness and density of the shell [Rambaux et al., 2011, Baland and Van Hoolst, 2010]. Both the presence of an elastic shell and the viscosity of the ice [Jara-Oru e and Vermeersen, 2014] reduce the sensitivity of the librations to the thickness of the icy shell. However, the librations amplitude can still constrain the density and the rigidity of the ice-shell [Van Hoolst et al., 2013].

The libration of the inner layers is expected to be at least one order of magnitude smaller than the libration of the outer-shell [Van Hoolst et al., 2013]. Therefore, even if the gravity field measurement is sensitive to its effect [Baland and Van Hoolst, 2010], the latter would be difficult to measure.

Obliquity

Measuring the obliquity ϵ can provide additional evidences on the existence of a putative ocean below the icy shell. An outer ice-shell decoupled from the interior would be a reasonable explanation for a measured obliquity different from the obliquity predicted for an entirely solid moon, thus suggesting a global subsurface ocean. In addition, a decoupled shell would induce different obliquity measurements at the surface and from gravity, because of differently oriented solid interior, as it is the case of Titan [Bills and Nimmo, 2011, Baland et al., 2011].

In the presence of a subsurface ocean, accurate obliquity measurements can improve constraints on the ice thickness and coupling processes in the interior of the Galilean moons [Baland et al., 2012].

Static gravity field

The knowledge of the static gravity field may be used to study the properties of the hydrosphere of the Galilean moons. For instance, as mentioned in Genova et al. [2022], the comparison of gravity and topography helps to characterise the ice shell. The gravity computed from the topographic relief (i.e., Bouguer correction) can be compared to the observed gravity field to determine the Bouguer anomalies, which can be used to provide constraints on the lateral variation of the ice-shell [Wieczorek, 2015]. Moreover, the gravity field is expected to correlate with topography at high degrees, whereas the signal from the

lithosphere and the mantle-ocean interface is attenuated [Genova et al., 2022]. In the case of Callisto, Genova et al. [2022] computed the gravity/topography admittance profiles with several internal structure models. At high degrees, the admittance become independent from the elastic thickness of the lithosphere (Fig. 2.17a). On the contrary, the admittance highly depends on the ice-shell density (Fig. 2.17b). This means that estimating the gravity field of Callisto up to d/o 80 allows for a full characterisation of the ice-shell.

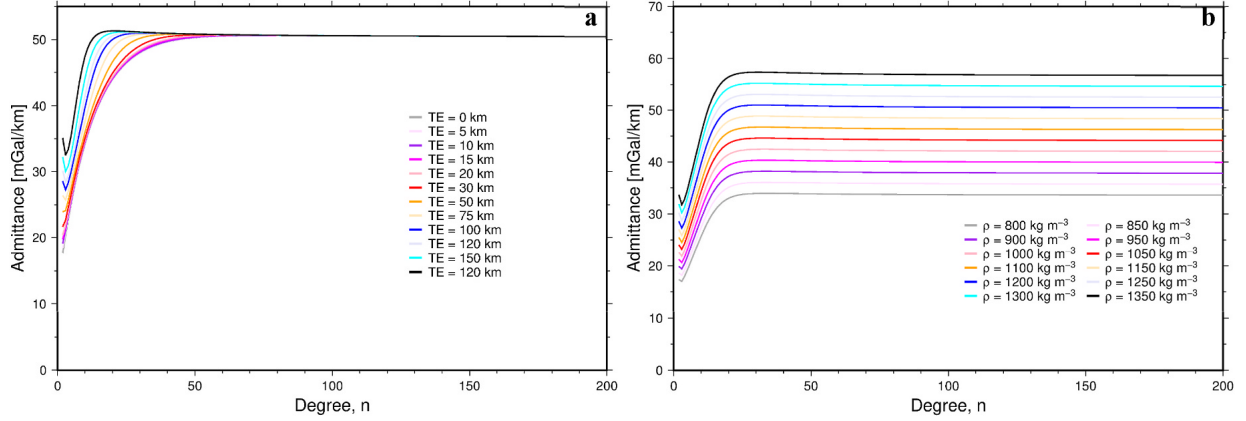


Figure 2.17: Admittances for ice shell thickness = 200 km, when fixing (a) the ice shell density $\rho = 1200 \text{ kg/m}^3$ or (b) the lithosphere elastic thickness of $TE=100 \text{ km}$ [extracted from Genova et al., 2022].

2.8.3 Summary

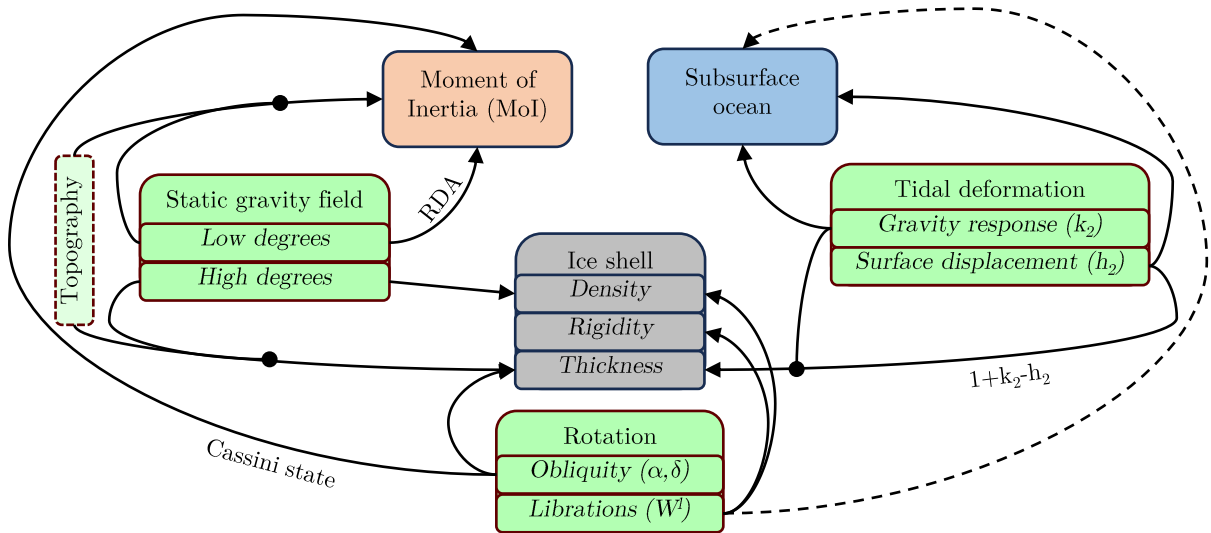


Figure 2.18: From the estimation of geodetic and geophysical parameters to the characterisation of the interior of the icy moons.

The determination of the internal mass distribution (via the MoI) and the characterisation of the putative subsurface ocean and the surrounding ice-shell of the icy moons of

Jupiter are key objectives for the future exploration of the Jovian system (see Sect. 1.2), and can be achieved by estimating geodetic and geophysical parameters, as discussed in the previous sections and summarised in Fig. 2.18. In this work, we focus on the estimation of the gravity field and rotational parameters, and of the tidal Love numbers k_2 and h_2 , but one may note that the combination of complementary techniques and measurements, such as radar sounding and topography would provide tighter constraints on the interior of the icy moons.

Chapter 3

Low altitude orbit design around Jovian moons

The design of orbits suitable for scientific investigations is the entry point of our study. In general, we consider low altitude, high inclination and near circular orbits to provide a global mapping of the moon to the extent possible, but this procedure can be applied also for other type of orbits, such as elliptic orbits. The spacecraft orbits we considered are designed in a restricted three-body system consisting of Jupiter, one of the Galilean moons (Europa or Callisto), and a spacecraft with negligible mass. We derive in this chapter a set of orbits for the massless spacecraft according to parameters of interest associated with different orientations of the orbital plane with respect to other celestial bodies of interest, e.g., the Earth or the Sun. The orbit design procedure was implemented during this work in MATLAB, using in particular *ode113* solver for the integration of Ordinary Differential Equations [ODE; Shampine and Reichelt, 1997], and the orbits generated have been afterwards introduced in the Bernese GNSS Software [BSW; Dach et al., 2015].

3.1 Repetitive Ground Track Orbits

Repetitive Ground Track Orbits (RGTO) are beneficial for the observation of time varying phenomena on the ground, as repeated observations of a given point of the surface of the celestial body are ensured. RGTO are commonly used for Earth observation missions [see, e.g., Colombo, 1984, Donlon et al., 2021] and are, e.g., also considered for the Jupiter Icy Moons Explorer mission (JUICE) around Ganymede [Ortore et al., 2015, Boutonnet and Varga, 2020]. It is important to note that we can still study non-repetitive orbits in the framework of RGTO if we set the repetition cycle duration to be larger or equal to the mission duration.

The ground tracks of an $m:R$ RGTO repeat after m revolutions of the moon around itself. In the case of Europa, $m = 1$ and $m = 26$ correspond to cycle duration of 3.55 and 92.33 Earth days, respectively. For Callisto, $m = 1$ and $m = 6$ corresponds to cycle duration of 16.67 and 100.02 Earth days, respectively. Within this period the probe completes R revolutions around the moon. This translates into

$$mD_n = RT_n , \tag{3.1}$$

where D_n is the nodal day of the moon, and T_n is the nodal period of the probe. m and R are two integers prime to each other, i.e., every m nodal days ground tracks return to the same position. In order to study non-repetitive orbits with RGTO, we have to set the repetition cycle duration to be larger or equal to the mission duration. For instance, if we consider such RGTO with $m = 26$ for Europa, and $m = 6$ for Callisto, the ground tracks would only repeat after 26 Europa days and 6 Callisto days, longer than a 3 months mission. The whole set of associated orbit tracks defines a grid in the moon-fixed reference frame (see Fig. 3.1). We limit the investigation to low altitude (100–200 km) and high inclination

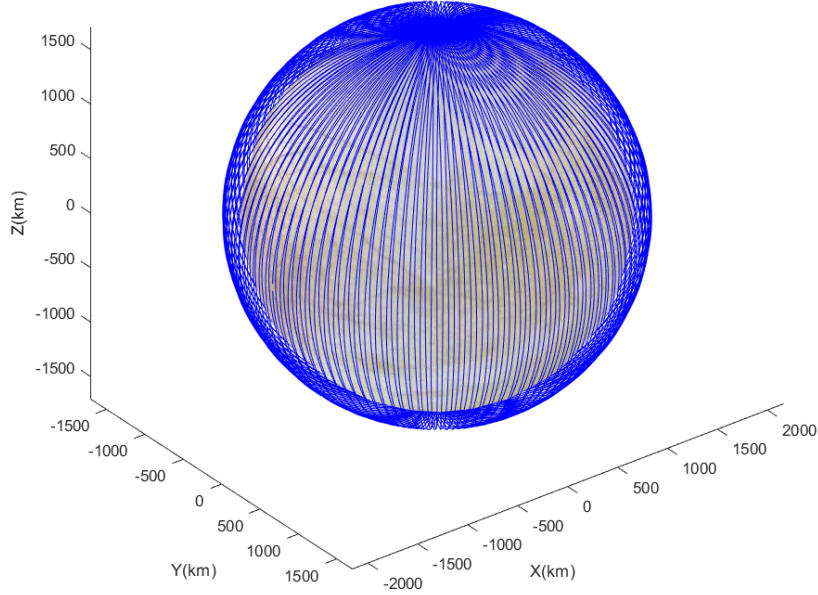


Figure 3.1: 3:118 RGTO ($i = 89^\circ$, $h = 135$ km) in Europa-fixed frame. After 118 revolutions around Europa and 3 Europa days (10.65 Earth days), the probe will follow the same ground track.

(80° – 100°) orbits, because they ensure a high global coverage and are thus relevant for forthcoming mission such as JUICE [Grasset et al., 2013] and for mission proposals such as Blanc et al. [2020a]. In the frame of the two body problem, the sidereal period T_n is given by

$$T_n = 2\pi\sqrt{a^3/\mu_G}, \quad (3.2)$$

with a being the semi-major axis of the probe’s orbit (see Fig. 2.1) and μ_G the standard gravitational parameter of the Galilean moon. Hence, if a is bounded, so is the nodal period T_n . For a considered revisit time m , there is then a finite number of integers R satisfying the ground track repetition condition given by Eq. (3.1) (see Tab. 3.1).

These orbits provide a homogeneous ground track coverage. We can define the spatial resolution by the equatorial distance between the ground tracks. We call this constant distance “cycle intertrack”, which is given by

$$\delta_{eq} = \frac{2\pi R_G}{R}, \quad (3.3)$$

Table 3.1: m : R RGTO with their altitude and cycle intertrack fulfilling the orbit requirements for Europa (left) and Callisto (right). The two numbers in the 2^{nd} column denote the minimum and maximum possible values of R for an altitude between 100 km and 200 km.

| m | R | Altitude | Cycle intertrack (at equator) | | m | R | Altitude | Cycle intertrack (at equator) | |
|-----|------|----------|----------------------------------|---------|-----|-----|----------|----------------------------------|---------|
| 1 | 38 | 181 km | 258 km | (9.47°) | 1 | 146 | 196 km | 104 km | (2.47°) |
| | 40 | 123 km | 245 km | (9.00°) | | 154 | 105 km | 98 km | (2.34°) |
| 2 | 75 | 197 km | 131 km | (4.80°) | 2 | 293 | 190 km | 52 km | (1.23°) |
| | 81 | 109 km | 121 km | (4.44°) | | 307 | 110 km | 49 km | (1.17°) |
| 3 | 113 | 192 km | 87 km | (3.19°) | 5 | 729 | 198 km | 21 km | (0.49°) |
| | 122 | 104 km | 80 km | (2.95°) | | 772 | 100 km | 20 km | (0.47°) |
| 26 | 973 | 199 km | 10 km | (0.37°) | 6 | 875 | 198 km | 17 km | (0.41°) |
| | 1061 | 101 km | 9 km | (0.34°) | | 925 | 103 km | 16 km | (0.39°) |

with R_G being the equatorial radius of the Galilean moon [$R_E = 1562.6$ km for Europa and $R_C = 2410.3$ km for Callisto; Archinal et al., 2018]. This gap depends only on the number of orbit revolutions between repetitions, noted as R . Large cycle intertracks, i.e., a lower spatial resolution of the ground tracks, can be detrimental to the recovery of global geodetic or geophysical parameters, like, e.g., parameters describing the gravity field (see Sect. 4.3.1). Table 3.1 shows the cycle intertrack for different RGTO. A lower R corresponds to a higher altitude, and to a larger cycle intertrack (see Eq. 3.3).

The design of an RGTO is initiated by the search for a first guess orbit which satisfies approximately Eq. (3.1), followed by the refinement of this orbit using a differential corrector (Sect. 3.2.2). Using the polynomial approach detailed in Cinelli et al. [2015], we compute a set of initial guess orbital elements (semi-major axis a , eccentricity e , inclination i and argument of periapsis ω), describing a given m : R RGTO. This approach is based on the ground track repetition condition given by Eq. (3.1). The semi-major axis a then satisfies Eq. (10) of Cinelli et al. [2015]

$$d_T a^7 + d_1 a^{5.5} + d_K a^4 + d_2 a^2 + d_4 = 0, \quad (3.4)$$

where d_T is related to third body perturbations, d_1 is related to characteristics of the moon's orbit, d_K is related to the Keplerian motion of the spacecraft around the moon, d_2 and d_4 are related to perturbations due to J_2 . Eq. (3.4) is obtained by fixing the other orbital elements (e , i , ω), and is a function of the ratio R/m , of the physical parameters of Europa or Callisto, and of the mean motion of Europa or Callisto around Jupiter.

For each pair (m , R), we solve the degree-14 polynomial equation obtained by squaring Eq. (3.4) for the semi-major axis a while fixing e , i and ω . In this study, we choose to focus on near-circular orbits. We thus fix e and ω to 0. From the multiple solutions obtained from the degree-14 polynomial equation, we verify that they satisfy Eq. (3.4), and select those falling within the range of studied altitudes. Usually, only the altitude of one of them is between 100 km and 200 km.

As Eq. (3.4) was derived by approximating third body perturbations, it only provides a first guess orbit. Such an orbit then needs to be refined according to a more realistic force model to ensure ground track repetition. In addition, the initial longitude of the ascending node, Ω , has yet to be defined at this stage, which completes the characterization of the geometry of the orbital plane with respect to the third body Jupiter and with respect to other perturbing bodies.

3.2 Orbit refinement

3.2.1 The Hill model

The first guess orbits described in the previous section do not meet precisely the condition for ground track repetition Eq. (3.1) because of approximations in the derivation of Eq. (3.4). We considered the Hill model [Lara and Russell, 2007] to refine these orbits. This model takes into account the influence of Europa or Callisto and Jupiter as point masses, plus the effect of the J_2 and C_{22} gravity field coefficients of the central Galilean moon.

We define the Jupiter-moon rotating frame with the x -axis pointing from Jupiter to the moon, the y -axis in direction of the velocity vector of the moon around Jupiter, and the z -axis perpendicular to the orbital plane of the moon around Jupiter (see Fig. 3.2). In this frame centered around the moon, the spacecraft equations of motion are

$$\dot{\mathbf{r}} + 2\mathbf{n}_J \times \dot{\mathbf{r}} = \nabla_{\mathbf{x}} U_{tot}, \quad (3.5)$$

with

$$U_{tot} = \frac{n_J^2}{2}(x^2 + y^2) + U_G + U_J, \quad (3.6)$$

and where $\mathbf{r} = (x, y, z)$ is the spacecraft position in the rotating frame, \mathbf{n}_J is the angular velocity vector of the moon around Jupiter, n_J its magnitude ($2.0483 \times 10^{-5} \text{ rad s}^{-1}$ for Europa, and $4.3575 \times 10^{-6} \text{ rad s}^{-1}$ for Callisto), and U_G and U_J are the gravitational potentials of the Galilean moon and Jupiter, respectively. For $r \ll r_J$, where $r = \|\mathbf{r}\|$ and r_J is the distance of the moon to Jupiter, the gravitational potential of Jupiter as a point mass can be approximated by

$$U_J = \frac{n_J^2}{2}(3x^2 - r^2). \quad (3.7)$$

Assuming hydrostatic equilibrium (Sect. 2.8.1) for Europa and Callisto ($J_2 = \frac{10}{3}C_{22}$), their gravitational potential U_G can be separated into two contributions: the potential due to the central point mass and the degree-2 gravity field coefficients potential U_p defined so that

$$U_G = \frac{\mu_G}{r} + U_p = \frac{\mu_G}{r} + \frac{\mu_G}{r} \frac{R_G^2}{r^2} \frac{J_2}{5} \frac{7x^2 - 2y^2 - 5z^2}{r^2}, \quad (3.8)$$

where μ_G is the standard gravitational parameter of the Galilean moon [$\mu_E = 3202.72 \text{ km}^3 \text{ s}^{-2}$, Anderson, 1998] and [$\mu_C = 7179.292 \text{ km}^3 \text{ s}^{-2}$, Anderson, 2001].

3.2.2 Differential correction

For convenience, we decided in the following steps to fix the longitude of the ascending node Ω at the initial epoch t_0 so that the initial position vector of the probe $\mathbf{r}(t_0)$ lies on the axis from Jupiter to the Galilean moon, opposite to Jupiter, and that the initial velocity in x -direction vanishes. In the rotating frame, the initial state vector can then be written as $\mathbf{X}(t_0) = (x_0, 0, 0, 0, \dot{y}_0, \dot{z}_0)$ (see Fig. 3.2). We subsequently performed a differential correction to refine the orbit to ensure its periodicity in a two-step iterative process adapted from Russell [2006] and Pavlak [2013].

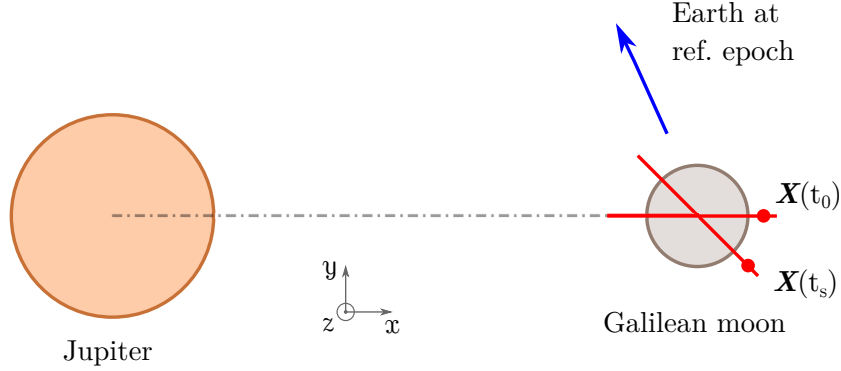


Figure 3.2: Orbital plane of the probe (in red) at t_0 and t_s with respect to Jupiter and Earth. The red dots represent crossing points with respect to the Galilean moon equatorial plane ($z_0 = z_s = 0$).

The equations of motion of the Hill model provided by Eq. (3.5) are invariant under the transformation $t \rightarrow -t, y \rightarrow -y, z \rightarrow -z$. Indeed when applying this transformation to $\mathbf{r} = (x, y, z)$ and to its time derivatives, we obtain

$$\begin{aligned} (x, y, z) &\rightarrow (x, -y, -z), \\ (\dot{x}, \dot{y}, \dot{z}) &\rightarrow (-\dot{x}, \dot{y}, \dot{z}), \\ (\ddot{x}, \ddot{y}, \ddot{z}) &\rightarrow (\ddot{x}, -\ddot{y}, -\ddot{z}). \end{aligned} \tag{3.9}$$

If \mathbf{r} and its time derivatives verify Eq. (3.5), we see that the right side of Eq. 3.9 also verifies Eq. (3.5), proving the invariance the Hill model under this transformation. It means that the trajectory of a probe starting at $\mathbf{r}(t_0) = (x_0, y_0, z_0)$ is a 180° rotation around the x -axis of a backward integrated trajectory of a probe starting at $(x_0, -y_0, -z_0)$. This property is called axi-symmetry (around the x -axis).

Because of this symmetry, if an orbit starts on the x -axis, and if there, the orbit is perpendicular to the x -axis, i.e.,

$$\mathbf{r}(t_0) = (x_0, 0, 0), \quad \text{and} \quad \dot{\mathbf{r}}(t_0) = (0, \dot{y}_0, \dot{z}_0), \tag{3.10}$$

the resulting propagated orbit and its image (180° rotation around the x -axis) will form one continuous trajectory. Enforcing the condition

$$y_{T_{1/2}} = z_{T_{1/2}} = \dot{x}_{T_{1/2}} = 0 \tag{3.11}$$

ensures that the trajectory crosses perpendicularly the x -axis at $t = t_0 + \frac{T}{2}$. Here, e.g., $y_{T_{1/2}}$ denotes the spacecraft y -coordinate after having it propagated from $t = t_0$ and during $T_{1/2} = \frac{T}{2}$. Then, the trajectory and its image will result in an orbit which closes after the period T .

We consequently decided to look for such axi-symmetric $m:R$ RGTOs, with the initial conditions (3.10). In order to find these orbits, we performed a differential correction, which we derived by means of the Newton-Raphson method. Let us define the free variable \mathbf{Y} as

$$\mathbf{Y} = \begin{pmatrix} x_0 \\ \dot{y}_0 \\ \dot{z}_0 \\ T_{1/2} \end{pmatrix}, \text{ and the function } \mathbf{F}(\mathbf{Y}) = \begin{pmatrix} y_{T_{1/2}} \\ z_{T_{1/2}} \\ \dot{x}_{T_{1/2}} \end{pmatrix}, \quad (3.12)$$

The constraint (3.11) can then be enforced by $\mathbf{F}(\mathbf{Y}) = 0$, which can be solved iteratively, so that for every iteration k and for $\mathbf{Y}^{k+1} = \mathbf{Y}^k + \delta\mathbf{Y}^k$ we get

$$\mathbf{F}(\mathbf{Y}^k) = -\mathbf{DF}(\mathbf{Y}^k) \cdot \delta\mathbf{Y}^k, \quad (3.13)$$

with,

$$\delta\mathbf{Y} = \begin{pmatrix} \delta x_0 \\ \delta \dot{y}_0 \\ \delta \dot{z}_0 \\ \delta T_{1/2} \end{pmatrix} \quad (3.14)$$

and

$$\begin{aligned} \mathbf{DF}(\mathbf{Y}) &= \frac{\partial \mathbf{F}}{\partial \mathbf{Y}} \\ &= \begin{pmatrix} \frac{\partial y}{\partial x_0} & \frac{\partial y}{\partial y_0} & \frac{\partial y}{\partial z_0} & \frac{\partial y}{\partial T_{1/2}} \\ \frac{\partial z}{\partial x_0} & \frac{\partial z}{\partial y_0} & \frac{\partial z}{\partial z_0} & \frac{\partial z}{\partial T_{1/2}} \\ \frac{\partial \dot{x}}{\partial x_0} & \frac{\partial \dot{x}}{\partial y_0} & \frac{\partial \dot{x}}{\partial z_0} & \frac{\partial \dot{x}}{\partial T_{1/2}} \end{pmatrix} \\ &= \begin{pmatrix} \Phi_{21} & \Phi_{25} & \Phi_{26} & \dot{y}_{T_{1/2}} \\ \Phi_{31} & \Phi_{35} & \Phi_{36} & \dot{z}_{T_{1/2}} \\ \Phi_{41} & \Phi_{45} & \Phi_{46} & \ddot{x}_{T_{1/2}} \end{pmatrix}, \end{aligned} \quad (3.15)$$

where we omitted the k indices, and with $\Phi(t, t_0)$ the State Transition Matrix (STM). The latter maps an initial perturbation of $(\mathbf{r}(t_0), \dot{\mathbf{r}}(t_0))$ at t_0 to the resulting perturbation at t , such that

$$\Phi(t, t_0) = \begin{pmatrix} \frac{\partial x}{\partial x_0} & \frac{\partial x}{\partial y_0} & \frac{\partial x}{\partial z_0} & \frac{\partial x}{\partial \dot{x}_0} & \frac{\partial x}{\partial \dot{y}_0} & \frac{\partial x}{\partial \dot{z}_0} \\ \frac{\partial y}{\partial x_0} & \frac{\partial y}{\partial y_0} & \frac{\partial y}{\partial z_0} & \frac{\partial y}{\partial \dot{x}_0} & \frac{\partial y}{\partial \dot{y}_0} & \frac{\partial y}{\partial \dot{z}_0} \\ \frac{\partial z}{\partial x_0} & \frac{\partial z}{\partial y_0} & \frac{\partial z}{\partial z_0} & \frac{\partial z}{\partial \dot{x}_0} & \frac{\partial z}{\partial \dot{y}_0} & \frac{\partial z}{\partial \dot{z}_0} \\ \frac{\partial \dot{x}}{\partial x_0} & \frac{\partial \dot{x}}{\partial y_0} & \frac{\partial \dot{x}}{\partial z_0} & \frac{\partial \dot{x}}{\partial \dot{x}_0} & \frac{\partial \dot{x}}{\partial \dot{y}_0} & \frac{\partial \dot{x}}{\partial \dot{z}_0} \\ \frac{\partial \dot{y}}{\partial x_0} & \frac{\partial \dot{y}}{\partial y_0} & \frac{\partial \dot{y}}{\partial z_0} & \frac{\partial \dot{y}}{\partial \dot{x}_0} & \frac{\partial \dot{y}}{\partial \dot{y}_0} & \frac{\partial \dot{y}}{\partial \dot{z}_0} \\ \frac{\partial \dot{z}}{\partial x_0} & \frac{\partial \dot{z}}{\partial y_0} & \frac{\partial \dot{z}}{\partial z_0} & \frac{\partial \dot{z}}{\partial \dot{x}_0} & \frac{\partial \dot{z}}{\partial \dot{y}_0} & \frac{\partial \dot{z}}{\partial \dot{z}_0} \end{pmatrix}. \quad (3.16)$$

The STM is integrated along the orbit with the initial condition $\Phi(t_0, t_0) = \mathbf{I}_6$.

Since Eq. (3.13) is under-determined, we decided to add a constraint by fixing the inclination i_0 at t_0 . Using Eq. (3.10) the inclination can be written as

$$\tan(i_0) = \frac{\dot{z}_0}{\dot{y}_0 + n_J x_0}. \quad (3.17)$$

We first reduced the problem by fixing the half-period $T_{1/2}$ by numerically integrating the trajectory until the orbit crosses R times the equatorial plane at $t = t_0 + T_{1/2}$, to then enforce the constraint $z_{T_{1/2}} = 0$. Introducing $z_{T_{1/2}} = 0$ into Eq. (3.13) and considering (3.14) and (3.15) then yields

$$z_{T_{1/2}} = \Phi_{31} \delta x_0 + \Phi_{35} \delta \dot{y}_0 + \Phi_{36} \delta \dot{z}_0 + \dot{z}_{T_{1/2}} \delta T_{1/2} \stackrel{!}{=} 0, \quad (3.18)$$

so that

$$\delta T_{1/2} = -\frac{1}{\dot{z}_{T_{1/2}}} (\Phi_{31} \delta x_0 + \Phi_{35} \delta \dot{y}_0 + \Phi_{36} \delta \dot{z}_0).$$

We can then rewrite Eq. (3.13), always omitting the k indices, with a reduced function

$$\begin{aligned} \tilde{\mathbf{F}}(\mathbf{Y}) &= \begin{pmatrix} y_{T_{1/2}} \\ \dot{x}_{T_{1/2}} \end{pmatrix} \\ &= - \left(\begin{pmatrix} \Phi_{21} & \Phi_{25} & \Phi_{26} \\ \Phi_{41} & \Phi_{45} & \Phi_{46} \end{pmatrix} - \frac{1}{\dot{z}_{T_{1/2}}} \begin{pmatrix} \dot{y}_{T_{1/2}} \\ \ddot{x}_{T_{1/2}} \end{pmatrix} (\Phi_{31} \quad \Phi_{35} \quad \Phi_{36}) \right) \begin{pmatrix} \delta x_0 \\ \delta \dot{y}_0 \\ \delta \dot{z}_0 \end{pmatrix}. \end{aligned} \quad (3.19)$$

We further reduce the number of free variables by using Eq. (3.17) to compute \dot{y}_0 , so that

$$\dot{y}_0 = \dot{z}_0 \cot(i_0) - n_J x_0. \quad (3.20)$$

By introducing Eq. (3.20) into Eq. (3.19), we finally get

$$\tilde{\mathbf{F}}(\mathbf{Y}) = -\mathbf{A} \cdot \delta \tilde{\mathbf{Y}} \quad (3.21)$$

with

$$\begin{aligned} \mathbf{A} &= \begin{pmatrix} \Phi_{21} & \Phi_{26} \\ \Phi_{41} & \Phi_{46} \end{pmatrix} + \begin{pmatrix} \Phi_{25} \\ \Phi_{45} \end{pmatrix} (-n_J \quad \cot(i_0)) \\ &\quad - \frac{1}{\dot{z}_{T_{1/2}}} \begin{pmatrix} \dot{y}_{T_{1/2}} \\ \ddot{x}_{T_{1/2}} \end{pmatrix} ((\Phi_{31} \quad \Phi_{36}) + \Phi_{35} (-n_J \quad \cot(i_0))), \end{aligned}$$

and the correction to the reduced free variable vector $\tilde{\mathbf{Y}}$ given by

$$\delta \tilde{\mathbf{Y}} = \begin{pmatrix} \delta x_0 \\ \delta \dot{z}_0 \end{pmatrix}.$$

To summarize, at every iteration the orbit and the STM are propagated until the orbit crosses the equatorial plane R times, defining the half-period $T_{1/2}$. The resulting

$\Phi(t_0 + T_{1/2}, t_0)$, $\dot{\mathbf{r}}(t_0 + T_{1/2})$ and $\ddot{\mathbf{r}}(t_0 + T_{1/2})$ are used to compute corrections on x_0 and \dot{z}_0 based on Eq. (3.21), while \dot{y}_0 is recomputed using Eq. (3.20). This procedure is repeated until convergence to the desired level.

During the differential correction, the semi-major axis a can move by a few meters from the solution of Eq. (3.4). The orbits are also not precisely circular anymore, but their eccentricity remains below 0.003. One can note that the differential correction can be adapted to refine the orbit in more complex force models, for example by taking into account higher degrees and orders of the moon gravity fields model.

Once the initial state vector $\mathbf{X}(t_0)$ is corrected, the resulting propagated orbit defines our *reference orbit*. It is important to note that these orbits do not have a reference epoch at this point: by fixing one, we get an orbital plane configuration with respect to the other bodies of interest in this study (e.g., Jupiter, Earth, Sun).

3.3 Evolution of the orbital elements

The inclination of the orbit plays a crucial role in the estimation of global geodetic or geophysical parameters, like the gravity field. First, a significant polar gap in the ground coverage of the central body, induced by an inclined orbit, would limit the recovery of zonal and near-zonal spherical harmonic coefficients (see Sect. 4.3.4). Additionally, the inclination influences the evolution of the probe's orbital plane geometry due to orbit perturbation and hence its visibility from Earth. This geometry is characterized by the angle between the orbital plane of the probe and the Earth direction (β_{Earth}).

When neglecting the obliquity of the Galilean moons ($< 0.1^\circ$) and the inclination of their orbital planes with respect to the ecliptic ($< 2^\circ$), β_{Earth} is related to the longitude of the Earth with respect to the relevant moon in the ecliptic plane (Ω_{Earth}), to the longitude of the ascending node of the probe around the moon Ω and to its inclination i (see Fig. 3.3) by

$$\sin(\beta_{Earth}) = \sin(\Omega - \Omega_{Earth}) \cdot \sin(i), \quad (3.22)$$

where Ω_{Earth} depends on the Solar System geometry at the mission date.

In this section, we investigate the evolution of the longitude of the ascending node of the designed orbits to quantify the variation of β_{Earth} and of the inclination to fix the mean inclination based on the inclination at t_0 .

3.3.1 Perturbing equations in the local orbital frame

We analyse the evolution over time of the inclination i and of the longitude of the ascending node Ω using the Gaussian perturbation equations [e.g., Beutler, 2005] to express their time derivatives as a function of the forces perturbing the Keplerian motion. In our case, the perturbing forces are the third-body attraction of Jupiter, and the force induced by the degree-2 gravity field of the central body. The time derivatives of both the inclination and

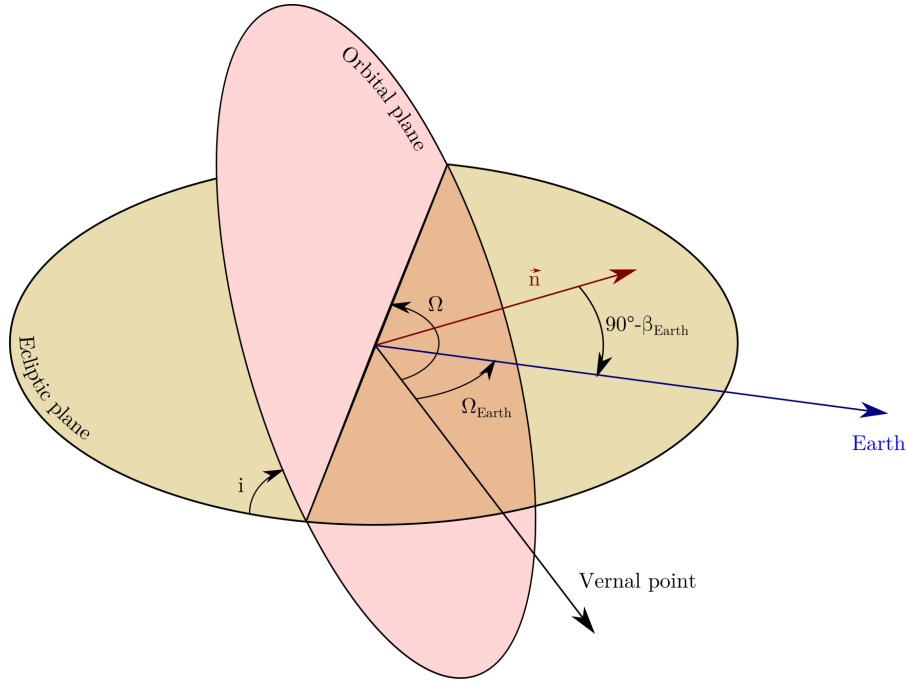


Figure 3.3: Geometry of the orbital plane of the probe with respect to the Earth characterised by the β_{Earth} angle.

the longitude of the ascending node only depend on the cross-track component of these perturbing forces, such that

$$\begin{aligned}\frac{di}{dt} &= \frac{r \cos(u)}{h} (N_J + N_P), \\ \frac{d\Omega}{dt} &= \frac{r \sin u}{h \sin i} (N_J + N_P),\end{aligned}\tag{3.23}$$

where r is the distance of the probe to the central body, u is the argument of latitude of the probe, $h = \|\mathbf{r} \times \dot{\mathbf{r}}\|$ is the norm of the angular momentum and

$$N_J = \nabla_{\mathbf{x}}(U_J)_{loc} \cdot \mathbf{e}_w, \quad \text{and} \quad N_P = \nabla_{\mathbf{x}}(U_P)_{loc} \cdot \mathbf{e}_w,$$

where loc indicates the RSW (i.e., in the radial (R), along-track (S) and cross-track (W), defined in Eq. 2.26) and U_J and U_P are potentials in the rotating frame rot , which are given by Eqs. (3.7) and (3.8) and can be rewritten as

$$\begin{aligned}U_J &= \frac{3x^2 - r^2}{2} n_J^2, \\ U_P &= \frac{\mu_G R_G^2 J_2}{r} \frac{g(\mathbf{r}_{rot})}{r^2},\end{aligned}\tag{3.24}$$

with $g(\mathbf{r}_{rot}) = 7x^2 - 2y^2 - 5z^2$ and $\mathbf{r}_{rot} = (x, y, z)$.

Relation between the rotating frame, the inertial frame and the local orbital frame

Let us neglect once again the obliquity of the moons ($< 0.1^\circ$) and the inclination of the moon's orbital plane with respect to the ecliptic ($< 2^\circ$). The rotating frame is then obtained

by a rotation around the z -axis from the inertial frame. Assuming that at epoch $t = 0$, Jupiter and its chosen moon lie on the x -axis of the inertial frame, we can write

$$\mathbf{r}_{\text{rot}} = \mathbf{R}_3(n_J t) \cdot \mathbf{r}_{\text{in}},$$

where \mathbf{r}_{rot} and \mathbf{r}_{in} are the components of the position vectors in the rotating frame and in the inertial frame, and $\mathbf{R}_i(\theta)$ is the 3×3 matrix representing a rotation about the i -th coordinate axis by an angle θ .

Additionally, the transformation between the inertial frame and the local orbital frame can be written as

$$\mathbf{r}_{\text{loc}} = \mathbf{R}_3(u) \cdot \mathbf{R}_1(i) \cdot \mathbf{R}_3(\Omega) \cdot \mathbf{r}_{\text{in}},$$

which yields

$$\mathbf{r}_{\text{loc}} = \mathbf{R}_{\text{tot}}(u, i, u_J) \cdot \mathbf{r}_{\text{rot}} \quad (3.25)$$

with $\mathbf{R}_{\text{tot}}(u, i, u_J) = \mathbf{R}_3(u) \cdot \mathbf{R}_1(i) \cdot \mathbf{R}_3(-u_J)$ and $u_J = n_J t - \Omega$ the argument of latitude of Jupiter around the moon.

Once the gradients of the potentials are computed in the rotating frame, they need to be converted to the local orbital frame, so that

$$\nabla_{\mathbf{x}}(U_J + U_P)_{\text{loc}} = \mathbf{R}_{\text{tot}}(u, i, u_J) \cdot \nabla_{\mathbf{x}}(U_J + U_P)_{\text{rot}}.$$

Additionally, it follows from Eq. (3.25) that \mathbf{r}_{rot} is

$$\begin{aligned} x &= r (\cos u \cos u_J + \sin u \cos i \sin u_J), \\ y &= r (-\cos u \sin u_J + \sin u \cos i \cos u_J), \\ z &= r (\sin u \sin i). \end{aligned} \quad (3.26)$$

The perturbing accelerations

In the rotating frame, the accelerations due to the third body and to the degree-2 gravity field are respectively

$$\begin{aligned} \nabla_{\mathbf{x}} U_J &= n_J^2 \begin{pmatrix} 2x \\ -y \\ -z \end{pmatrix}, \\ \nabla_{\mathbf{x}} U_P &= -\frac{\mu_G}{r^2} \frac{R_G^2}{r^2} \frac{J_2}{5} \begin{pmatrix} \frac{x}{r} \left(\frac{5g(x,y,z)}{r^2} - 14 \right) \\ \frac{y}{r} \left(\frac{5g(x,y,z)}{r^2} + 4 \right) \\ \frac{z}{r} \left(\frac{5g(x,y,z)}{r^2} + 10 \right) \end{pmatrix}. \end{aligned} \quad (3.27)$$

In the local orbital frame of the probe around the Galilean moon, the cross-track components of these accelerations are computed using Eqs. (3.25) and (3.26) in Eq. (3.27), so that

$$\begin{aligned} N_J &= -N_{J,0} \sin i \left(3 \cos u \sin 2u_J + 3 \sin u \cos i (1 - \cos 2u_J) \right), \\ N_P &= -N_{P,0} \sin i \left(3 \cos u \sin 2u_J + \sin u \cos i (5 - 3 \cos 2u_J) \right), \end{aligned} \quad (3.28)$$

with

$$N_{J,0} = \frac{1}{2}n_J^2 r, \quad N_{P,0} = \frac{3}{5} \frac{\mu_G}{r^2} \frac{R_G^2}{r^2} J_2.$$

In the case of near-circular orbits, $r \approx a$, which gives

$$N_{J,0} = \frac{1}{2}n_J^2 a, \quad N_{P,0} = \frac{3}{5}n^2 \frac{R_G^2}{a} J_2,$$

since $n^2 a^3 = \mu_G$, with n the mean motion of the probe around the moon, and a the semi-major axis of the probe's orbit.

The cross track component of all the perturbing forces considered in the Hill model is obtained by summing N_J and N_P from Eq. (3.28), so that

$$\begin{aligned} N_J + N_P = & -\sin i \left(3(N_{J,0} + N_{P,0}) \cos u \sin 2u_J \right. \\ & \left. + \sin u \cos i \left((3N_{J,0} + 5N_{P,0}) - 3(N_{J,0} + N_{P,0}) \cos 2u_J \right) \right), \end{aligned}$$

and which we can finally substitute into Eq. (3.23).

3.3.2 Choice of inclination

The β_{Earth} angle changes during a 3 months mission, but this change can be limited with a careful choice of the orbit inclination, in order to precisely study the impact of β_{Earth} on the parameter estimation (see, e.g., Sect. 4.3.2). For a mission mid-2031, the time variation $\dot{\Omega}_{Earth}$ is approximately $0.1^\circ/\text{day}$. $\dot{\Omega}$ is caused by the J_2 coefficient of the moon's gravity field and by the influence of Jupiter as a third body, and it depends on the orbital characteristics of the probe, mainly the inclination, see Cinelli et al. [2015]. Indeed, following Sect. 3.3.1 for near polar and quasi circular orbits, the time-derivative of the longitude of the ascending node can be written as

$$\begin{aligned} \frac{d\Omega}{dt} = & -\frac{r}{h} \left(3(N_{J,0} + N_{P,0}) \sin u \cos u \sin 2u_J \right. \\ & \left. + \sin^2 u \cos i \left((3N_{J,0} + 5N_{P,0}) - 3(N_{J,0} + N_{P,0}) \cos 2u_J \right) \right). \end{aligned}$$

The argument of latitude of the probe u and the argument of latitude of Jupiter around the Galilean moon u_J are respectively T_n -periodic and D_n -periodic. If we consider an $m:R$ RGTO, we can use the periodicity condition from Eq. (3.1), to isolate the secular term relevant for the long term evolution so that

$$\begin{aligned} \left(\frac{d\Omega}{dt} \right)_{\text{secular}} &= \frac{1}{RT_n} \int_0^{RT_n} \frac{d\Omega}{dt} dt \\ &= -\frac{a}{2h} (3N_{J,0} + 5N_{P,0}) \cos i \\ &= -\frac{3}{2n} \left(\frac{1}{2}n_J^2 + n^2 \left(\frac{R_G}{a} \right)^2 J_2 \right) \cos i. \end{aligned}$$

The orbits investigated in this work result in $\dot{\Omega} \in [-0.74^\circ, 0.74^\circ]/\text{day}$ in case of Europa and in $\dot{\Omega} \in [-0.045^\circ, 0.045^\circ]/\text{day}$ in case of Callisto. For instance, we obtain $\dot{\Omega} = -0.1^\circ/\text{day}$

$\approx -\dot{\Omega}_{Earth}$ for an 88.6° -inclined orbit around Europa. This implies $\dot{\beta}_{Earth} = 0^\circ/\text{day}$, i.e., a quasi-fixed geometry of the probe orbital plane with respect to Earth, which is particularly useful to study the impact of β_{Earth} on the parameter estimation (see Sects. 4.1 and 4.3.2).

The inclination of an orbit designed according to Sect. 3.2.2 can be chosen via the inclination i_0 at t_0 , which is different from the mean inclination i_m . The relation between i_0 and i_m can be derived from the Gaussian perturbation equation for the inclination i . Similarly to $\dot{\Omega}$, for near-polar orbits ($\cos i \approx 0$) and quasi circular orbits, the time-derivative of the inclination (3.23) can be expressed as

$$\frac{di}{dt} = -4K_i \cos^2 u \sin 2u_J, \quad (3.29)$$

with

$$K_i = \frac{3}{4} \frac{r \sin i}{h} (N_{J,0} + N_{P,0}) \quad (3.30)$$

$$= \frac{3}{4} \frac{\sin i}{h} \left(\frac{1}{2} n_J^2 a^2 + \frac{3}{5} n^2 R_G^2 J_2 \right). \quad (3.31)$$

Considering $\dot{u}_J = n_J - \dot{\Omega} \approx n_J \ll n$, Eq. (3.29) can be integrated via the first order perturbation calculation method (i.e., by setting $K_i = K_{i_m}$), which yields

$$i(t) = i_m + K_{i_m} \frac{\cos(2u_J)}{n_J}, \quad (3.32)$$

with i_m the mean inclination. Because the initial conditions of the probe's orbit are fixed at $(x_0, 0, 0, 0, \dot{y}_0, \dot{z}_0)$ in the rotating frame (see Fig. 3.2 with $x_0 > 0$), we also have $u_J(t_0) = 180^\circ$, providing a simple relation between the mean inclination i_m and the inclination i_0 at the initial time t_0 , such that

$$i_0 = i_m + \frac{K_{i_m}}{n_J}. \quad (3.33)$$

Equation (3.33) thus allows us to choose the mean inclination during the refinement of the orbit detailed in Sec. 3.2. For example, in order to get a 117 km altitude orbit around Europa with a mean inclination of 89° , the orbit design should target an orbit with an initial inclination of 89.9° .

3.4 Orbit propagation in an extended force model

The design of the orbits considered in this work assumes several simplifications. First, Callisto and Europa are in a circular orbit around Jupiter, and only the forces related to the two primary bodies (Jupiter and its relevant moon) are considered. All the other perturbing forces described in Sect. 2.2 are discarded. Moreover, the gravitational attraction of Jupiter is approximated in the Hill model, and only the low degree coefficients of the gravity field of Callisto or Europa are taken into account. Finally, the obliquity of the Galilean moons is assumed to be zero, as discussed in Sect. 2.4.2. In this section, we focus on the discrepancies between the designed orbit and the orbit propagated in a higher fidelity model in the BSW. We also define a procedure to use the designed orbit by accounting for these discrepancies.

3.4.1 Reference plane of the Hill model

In the Hill model, the orbital plane of the secondary body (Europa or Callisto) around the primary (Jupiter) coincides with the equatorial plane of the secondary (see Sect. 3.2.1). In other words, the orbit pole is identical to the spin pole. However the rotation model used in the BSW does not enforce that the angle between the two poles, or obliquity, is zero (see Sect. 2.4.2). As a result, when converting the orbit from the rotating frame to the inertial frame, we have to specify whether the “reference plane” of the Hill model refers to the equatorial plane of the secondary, or to the osculating orbital plane of the secondary around Jupiter at the starting epoch.

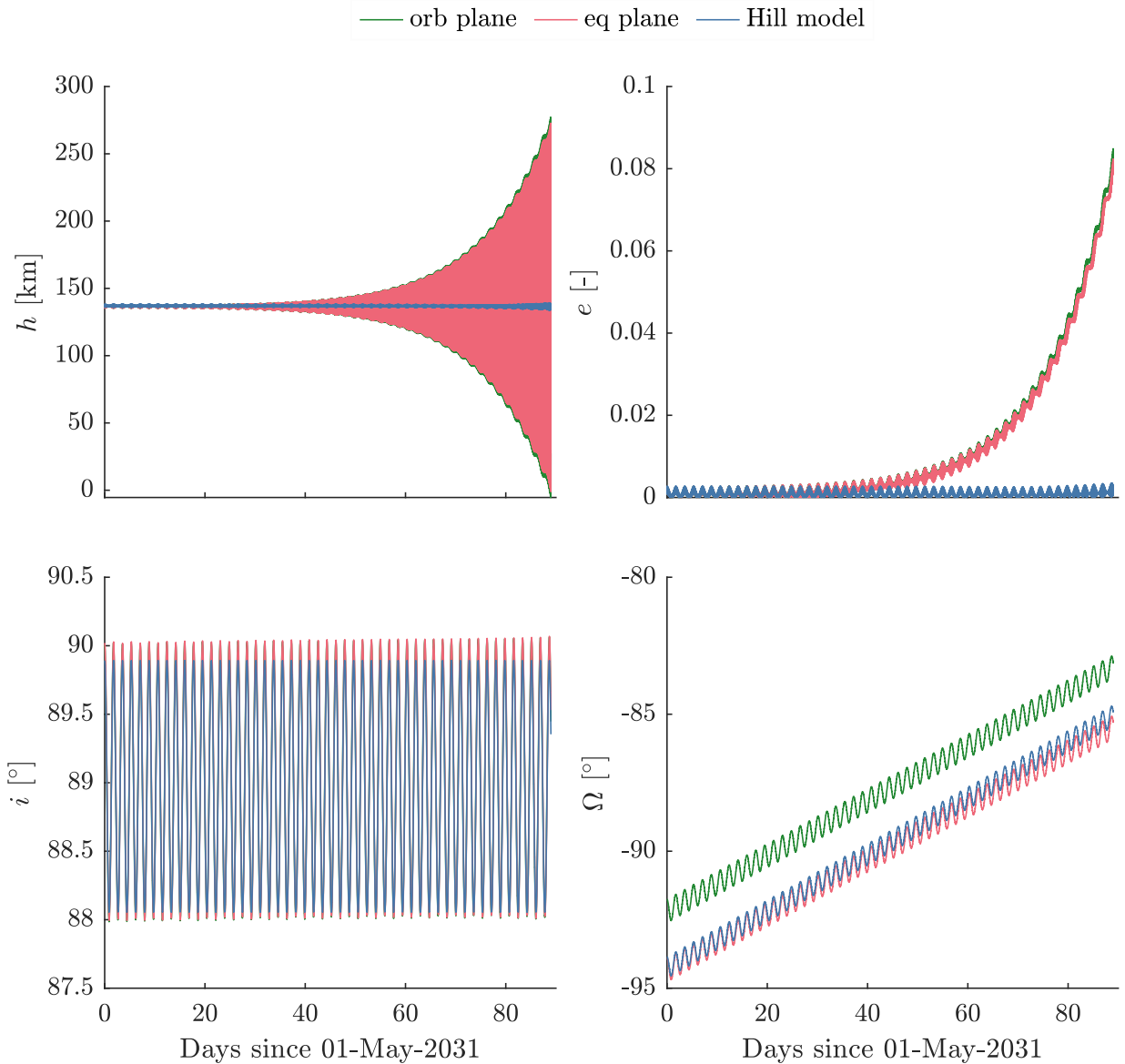


Figure 3.4: Comparison between the altitude h , eccentricity e , inclination i and longitude of the ascending node Ω of a 5:197 Europa RGTO propagated in the Hill model, against a full ephemeris force model starting on the equatorial plane or the orbital plane, but considering only the gravity field of Europa up to d/o 2 ($i = 89^\circ$, $t_0 = 2031 - 05 - 01$).

We investigated the evolution of the orbital elements of a given 5:197 RGTO around Europa, designed following the Hill model with $h = 134$ km and $i = 89^\circ$. We converted the initial state vector from the rotating frame to the inertial frame on 2031-05-01, assuming that the reference plane is either the equatorial plane or the osculating orbital plane. We then propagated the orbit in the BSW using the complete set of forces described in Sect. 2.2 for 90 days, until the spacecraft would crash on the surface of Europa (see Fig. 3.4). We only included the degree-2 gravity field of Europa for this test, since higher degree and order gravity field coefficients play a more decisive role, which we discuss in Sect. 3.4.3. In both cases, the eccentricity of the orbit starts to rapidly increase after a bit less than one month. The differences between the two approaches are quite small, but we can see that the eccentricity increases slightly faster when starting from the orbital plane than when starting from the equatorial plane, resulting in a crash on the surface after 89 days and after 90 days, respectively. We thus decided to assume in the rest of the study that the reference plane in the Hill model is the equatorial plane of the secondary body.

In Sect. 2.4.2, we decided to not enforce the zero-obliquity in our rotation models for our study. We analysed the impact of this decision on the stability of the orbit designed assuming zero-obliquity. In order to do this, we created an updated rotation model similarly to the work of Steinbrügge et al. [2019] by enforcing zero-obliquity. However, the differences with respect to the previously assumed rotation model are negligible.

It is important to note that propagation in a full ephemeris force model results in an orbit degradation after a while (see Fig. 3.4), even without considering higher degree and order gravity field coefficients neither in the force model nor in model used for the orbit design. The orbit at the start of the mission can be very different than the orbit at the end of the mission, thus not fulfilling the mission requirements anymore. Moreover, the orbit will inevitably crash on the surface of the moon at some point, unless regular corrections are applied. In this sense we developed a scheme to use these designed orbits taking into account regular manoeuvres.

3.4.2 Definition of an orbit scenario

A reference orbit designed in this section is characterized by its initial state vector at an arbitrary reference starting epoch. As previously described in Sect. 3.4.1, this initial state vector can be converted from the rotating frame to the inertial frame at the reference epoch, assuming that the orbit starts on the equatorial plane of Callisto or Europa. But in principle, any state vector from the reference orbit propagated in the Hill model can be used, at the chosen reference epoch.

For practical reasons, we restrict the possible initial locations to the equatorial plane of the moon (see Fig. 3.2). Since an $m:R$ RGTO completes R orbit revolutions before overlapping, there are R distinct ascending crossing points on the equatorial plane, as depicted in Fig. 3.5. Therefore, we get a list of state vectors $\mathbf{X}(t_k) = (x_k, y_k, 0, \dot{x}_k, \dot{y}_k, \dot{z}_k)$ from the reference orbit propagated in the rotating frame following the Hill model, with $k = 0, \dots, R-1$.

We define an “orbit scenario” by selecting one of these state vectors with $c_0 = k$ and

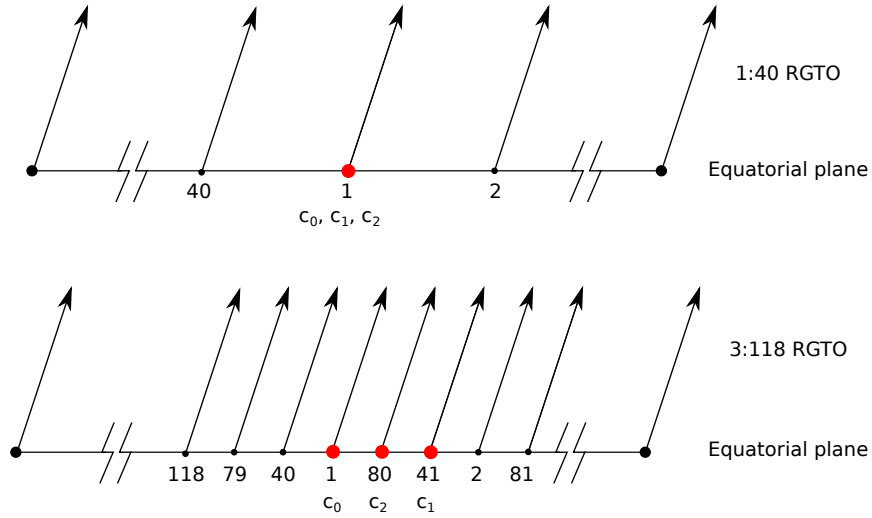


Figure 3.5: Distribution of the ascending orbit crossing points with respect to the equatorial plane for a 1:40 RGTO (top) and a 3:118 RGTO (bottom). The larger red dots denote the locations c_l of the probe ($l = 0, 1, 2$) at the start of the first three propagation arcs in the case of $c_0 = 1$.

assigning a reference epoch to t_{c_0} , which fixes the initial longitude of the ascending node Ω , as well as β_{Earth} (see Eq. 3.22). We thus have a direct relation between c_0 and β_{Earth} , meaning we can choose c_0 to get a given β_{Earth} , as shown in Fig. 3.6.

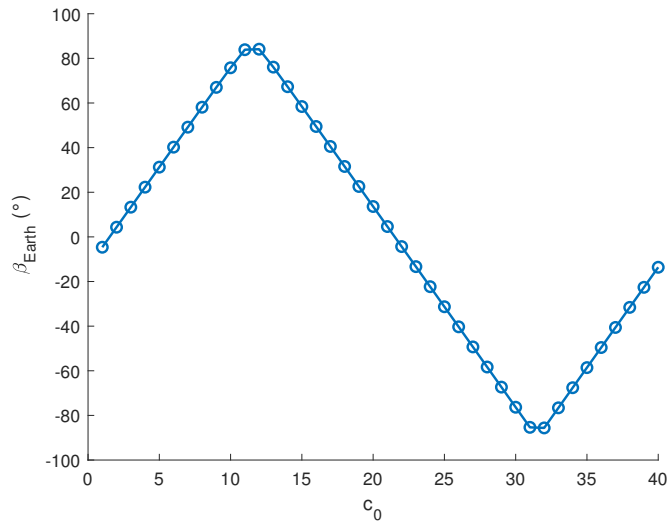


Figure 3.6: β_{Earth} as a function of the initial location number c_0 on the equatorial plane for a 1:40 RGTO around Europa starting on 2031-05-01.

Once the scenario is defined, the state vector $\mathbf{X}(t_{c_0})$ is converted from the rotating frame to the inertial frame, and the orbit can be propagated in a full ephemeris force model in the BSW (see Sect. 2.2). As shown in Sect. 3.4.1, the orbit perturbations shorten the lifetime of the mission. Thus, we can address this by applying periodic orbit corrections, which we

generate by, after a defined duration, resuming the orbit propagation from the reference orbit at another crossing point with the equatorial plane.

More precisely, if the orbit starts at crossing point c_0 , and it is propagated in arcs with a length of approximately one nodal day D_n (≈ 3.55 Earth days for Europa, ≈ 16.67 Earth days for Callisto), then for an $m:R$ RGTO the probe orbits R/m times during D_n .

This number is an integer only for $m = 1$, i.e., after one nodal day and R revolutions the probe will be at the same position on the equatorial plane again, see Fig. 3.5 (top). For $m \neq 1$ the length of the propagated arc is either shortened or increased with respect to one nodal day, implying that the probe ends up on the equatorial plane at a (different) crossing point c_1 . In Fig. 3.5 (bottom), the example of a 3:118 RGTO is shown, where the first arc is propagated for 41 revolutions. Then, for the second arc, the initial conditions at c_1 from the reference orbit are used for further propagating the orbit for an integer number of times close to R/m . In the example of the 3:118 RGTO the second arc was chosen to have 39 revolutions to end up at the equatorial plane at the crossing point c_2 (Fig. 3.5, bottom). In general, we choose a new arc l to end at the crossing point

$$c_l = c_0 + [l \cdot R/m], \quad (3.34)$$

where $[\cdot]$ is the ceiling function.

This is repeated in total m times until the probe has performed a total of R revolutions and ends at the same crossing point c_0 again. This in turn is repeated to cover the entire assumed mission duration of 3 months. Using new initial conditions from the reference orbit for each arc guarantees that the orbit remains stable and an approximate RGTO for the entire mission duration and this procedure thus mimics an orbit maintenance manoeuvre approximately every nodal day.

On the other hand, our approach introduces orbit discontinuities between the different arcs. These discontinuities are small enough to not be considered critical for geodetic parameters estimation at our target resolution. We discuss them in detail, and how they can be reduced in the following section.

3.4.3 Reducing the orbit discontinuities

In this work, we considered mission durations of several months. Propagating our designed orbits (issued from a simple model, see Sect. 3.2.1) within the BSW (with a full model, see Sect. 2.2) thus requires regular orbit corrections, as shown in Sect. 3.4.2. The velocity difference between two arcs can be seen as an orbit maintenance manoeuvre characterized by its Δv . We computed the total Δv for a 3-months mission, and verified whether it is compatible with a realistic Δv budget. Discontinuities in position are clearly not physical, but they are a direct consequence of our approach to maintain the ground track repetitivity of an RGTO. Even though we consider that orbit discontinuities are not critical for the scope of our investigations, they can be reduced if we use a force model in the orbit design with higher fidelity and closer to the model used in the BSW, at the expense of simplicity and short computation time. We decided to extend the Hill model (Sect. 3.2.1), by taking

into account the largest orbit perturbations, i.e., the influence of the higher degree and order gravity field coefficients of the central body [see Russell and Lara, 2006]. The potential U_p in Eq. (3.8) is then replaced by its extended form V (see Eq. 2.11).

The differential correction (Sect. 3.2.2) is then adapted according to the new force model, which is no longer axi-symmetric around the x -axis. We still look for orbits starting on the x -axis, but without enforcing that the velocity is perpendicular to the x -axis. The initial conditions are thus

$$\mathbf{r}(t_0) = (x_0, 0, 0) \quad \text{and} \quad \dot{\mathbf{r}}(t_0) = (\dot{x}_0, \dot{y}_0, \dot{z}_0). \quad (3.35)$$

Additionally, the periodicity of an $m:R$ RGTO is constrained in a more general way than Eq. (3.11), so that the orbit closes after the complete cycle duration T , i.e., after R orbit revolutions, by enforcing

$$\mathbf{r}(t_0 + T) = \mathbf{r}(t_0) \quad \text{and} \quad \dot{\mathbf{r}}(t_0 + T) = \dot{\mathbf{r}}(t_0). \quad (3.36)$$

The differential correction from Sect. 3.2.2 is then rewritten with the free variable \mathbf{Y} as

$$\mathbf{Y} = \begin{pmatrix} x_0 \\ \dot{x}_0 \\ \dot{y}_0 \\ \dot{z}_0 \\ T \end{pmatrix}, \quad \text{and the function } \mathbf{F}(\mathbf{Y}) = \begin{pmatrix} x_T - x_0 \\ y_T - y_0 \\ z_T - z_0 \\ \dot{x}_T - \dot{x}_0 \\ \dot{y}_T - \dot{y}_0 \\ \dot{z}_T - \dot{z}_0 \end{pmatrix} = \begin{pmatrix} x_T - x_0 \\ y_T \\ z_T \\ \dot{x}_T - \dot{x}_0 \\ \dot{y}_T - \dot{y}_0 \\ \dot{z}_T - \dot{z}_0 \end{pmatrix}, \quad (3.37)$$

where $\mathbf{r}(t_0 + T) = (x_T, y_T, z_T)$ and $\dot{\mathbf{r}}(t_0 + T) = (\dot{x}_T, \dot{y}_T, \dot{z}_T)$ are obtained by propagating (3.35) to $t = t_0 + T$. The constraint (3.36) can then be enforced by $\mathbf{F}(\mathbf{Y}) = 0$, which can be solved iteratively, identically to Eq. (3.13), but with the more general form

$$\delta\mathbf{Y} = \begin{pmatrix} \delta x_0 \\ \delta \dot{x}_0 \\ \delta \dot{y}_0 \\ \delta \dot{z}_0 \\ \delta T \end{pmatrix} \quad (3.38)$$

and

$$D\mathbf{F}(\mathbf{Y}) = \frac{\partial \mathbf{F}}{\partial \mathbf{Y}} = \begin{pmatrix} \Phi_{11} - 1 & \Phi_{14} & \Phi_{15} & \Phi_{16} & \dot{x}_T \\ \Phi_{21} & \Phi_{24} & \Phi_{25} & \Phi_{26} & \dot{y}_T \\ \Phi_{31} & \Phi_{34} & \Phi_{35} & \Phi_{36} & \dot{z}_T \\ \Phi_{41} & \Phi_{44} - 1 & \Phi_{45} & \Phi_{46} & \ddot{x}_T \\ \Phi_{51} & \Phi_{54} & \Phi_{55} - 1 & \Phi_{56} & \ddot{y}_T \\ \Phi_{61} & \Phi_{64} & \Phi_{65} & \Phi_{66} - 1 & \ddot{z}_T \end{pmatrix}, \quad (3.39)$$

with Φ_{ij} the elements of the STM defined in Eq. (3.16). Unlike in Sect. 3.2.2, we did not constrain the inclination, but similarly to Eq. (3.18), we reduced the problem by numerically enforcing the constraint $z_T = 0$ after the numerically integrated trajectory crosses $2R$ times the equatorial plane at $t = t_0 + T$. Introducing $z_T = 0$ into Eq. (3.13) and considering Eqs. (3.38) and (3.39) then yields

$$z_T = \Phi_{31}\delta x_0 + \Phi_{34}\delta \dot{x}_0 + \Phi_{35}\delta \dot{y}_0 + \Phi_{36}\delta \dot{z}_0 + \dot{z}_T \delta T \stackrel{!}{=} 0,$$

so that

$$\delta T = -\frac{1}{\dot{z}_T} (\Phi_{31}\delta x_0 + \Phi_{34}\delta \dot{x}_0 + \Phi_{35}\delta \dot{y}_0 + \Phi_{36}\delta \dot{z}_0).$$

We can rewrite Eq. (3.13), again by omitting the k indices, with a reduced function

$$\tilde{\mathbf{F}}(\mathbf{Y}) = -\mathbf{A} \cdot \delta \mathbf{Y}, \quad (3.40)$$

where

$$\mathbf{A} = \begin{pmatrix} \Phi_{11} - 1 & \Phi_{14} & \Phi_{15} & \Phi_{16} \\ \Phi_{21} & \Phi_{24} & \Phi_{25} & \Phi_{26} \\ \Phi_{41} & \Phi_{44} - 1 & \Phi_{45} & \Phi_{46} \\ \Phi_{51} & \Phi_{54} & \Phi_{55} - 1 & \Phi_{56} \\ \Phi_{61} & \Phi_{64} & \Phi_{65} & \Phi_{66} - 1 \end{pmatrix} - \frac{1}{\dot{z}_T} \begin{pmatrix} \dot{x}_T \\ \dot{y}_T \\ \ddot{x}_T \\ \ddot{y}_T \\ \ddot{z}_T \end{pmatrix} (\Phi_{31} \quad \Phi_{34} \quad \Phi_{35} \quad \Phi_{36}). \quad (3.41)$$

In the following, we analyse a 5:197 RGTO around Europa and a 1:146 RGTO around Callisto. We first compute the two RGTOs in the original Hill model following Sect. 3.2, i.e., with a degree and order (d/o) 2 gravity field. Then, we consecutively update these orbits in force models with increasing maximum degree of the gravity field ($n_{max} = 5, 10, 20, 30, 40$). Each designed orbit is then propagated in the BSW over 26 Europa days and 6 Callisto days, respectively, to assess orbit discontinuities. The orbital characteristics of the resulting updated RGTOs slightly differ in the case of Europa (Tab. 3.2). The inclination is reduced by 2° , and the eccentricity increases to from 0.0009 to 0.0024. Such a difference is expected, because of the different force models and because we did not constrain any orbital elements to a reference value (in contrast to Sect. 3.2.2). With increasing maximum degree n_{max} of the gravity field of Europa, the distance between the orbits of two different arcs is reduced. A d/o 10 gravity field is enough to reduce the distance by a factor 2.4. A gravity field with a higher maximum degree is needed to visibly reduce the total Δv (Fig. 3.7 left).

Table 3.2: Mean orbital elements and maximum orbit discontinuities for a 5:197 RGTO around Europa designed with higher fidelity force model.

| Gravity field max. degree | 2 | 10 | 20 | 30 |
|-----------------------------|------------------------|------------------------|------------------------|-----------------------|
| Semi-major axis altitude | 134 km | 133 km | 133 km | 133 km |
| Eccentricity | 0.0009 | 0.0014 | 0.0020 | 0.0024 |
| Inclination | 89.1° | 87.3° | 87.2° | 87.3° |
| Maximum position gap | 4.4 km | 1.8 km | 1.4 km | 1.2 km |
| Accumulated velocity change | 38.7 m s ⁻¹ | 34.6 m s ⁻¹ | 13.1 m s ⁻¹ | 7.9 m s ⁻¹ |

In the case of Callisto, the inclination also changes by a few degrees. However, the eccentricity is more severely affected (Tab. 3.3). The eccentricity of a 200 km altitude RGTO around Callisto can increase to more than 0.06 when considering a gravity field with coefficients of degree higher than 2. This behaviour is expected for very low altitude satellites (see Russell and Lara [2006]), depending on the gravity field considered. For instance, by deriving the degree 3 and 4 coefficients of our synthetic gravity field from a smoother

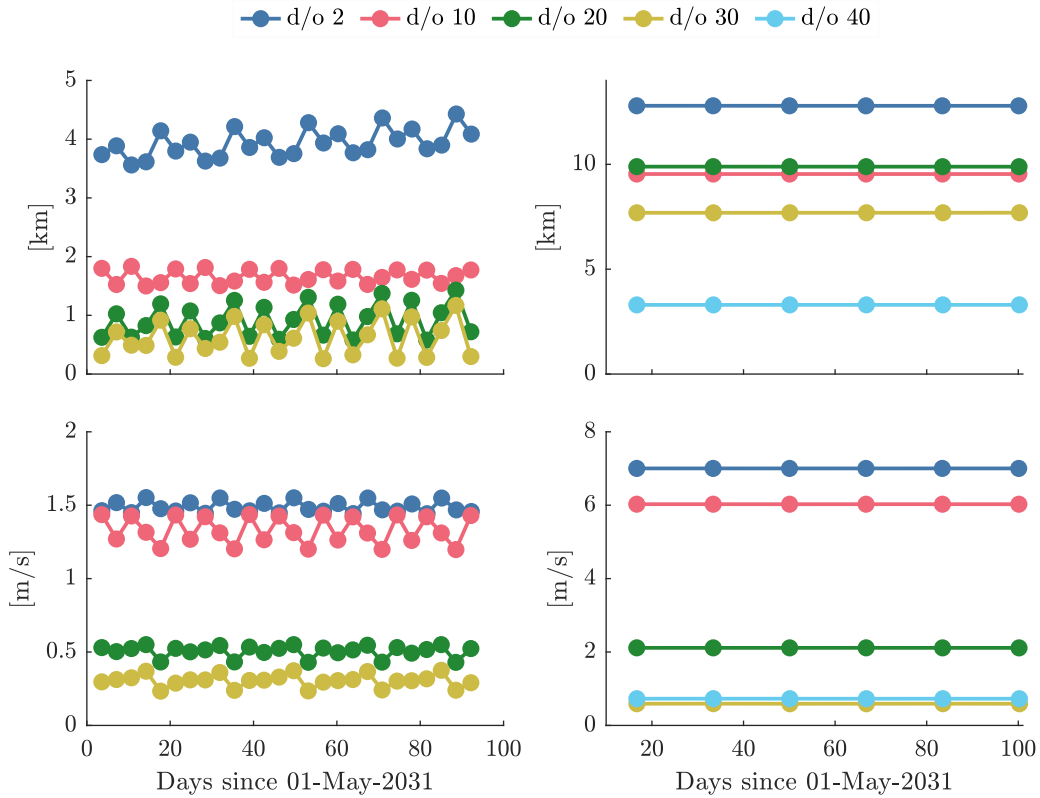


Figure 3.7: Amplitude of the orbit discontinuities for improved force-models for a 5:197 RGTO around Europa (left) and for a 1:146 RGTO around Callisto (right) when considering increasing degree gravity fields in the force model of the orbit design.

field such as Titan’s [Iess et al., 2010] instead of from the Moon’s (Sect. 2.2.1), we obtain lower values for these coefficients, similarly to Mazarico et al. [2015], which results in orbits designed with lower eccentricities for similar altitudes. Because Europa has a lower mass and a smaller radius, this effect is less pronounced for low altitude RGTO around Europa, despite the fact that we derived $d/o \geq 3$ of the synthetic gravity field of the two moons by rescaling the same gravity field model (see Sect. 2.2.1). The fact that using a higher d/o for the gravity field increases the eccentricities to a larger extend for Callisto can also be seen as an explanation for the larger orbit discontinuities (Fig. 3.7 right). In addition, less frequent manoeuvres (every 16.67 days instead of 3.55 days) also cause larger orbit corrections, i.e., larger manoeuvres and larger gaps between the consecutive arcs. We had to consider a gravity field up to degree and order 40 to reduce the distance between the ground tracks below 4 km. Because we are considering a 1:146 RGTO for Callisto, each manoeuvre occurs at the same location on the orbit cycle, similarly to Fig. 3.5 (top), leading to comparable orbit corrections, as opposed to the 5:197 RGTO around Europa, leading to a larger variability of the corrections magnitudes.

Using a higher degree gravity field for the design of the orbit increases the computational time required by the differential correction. In the rest of the study, we decided to consider only reference orbits designed in the original Hill model, i.e., with a degree-2 gravity field, despite the larger orbit discontinuities, as they remain small enough for the level of

Table 3.3: Mean orbital elements and maximum orbit discontinuities for a 1:146 RGTO around Callisto designed with higher fidelity force model.

| Gravity field max. degree | 2 | 10 | 20 | 30 | 40 |
|-----------------------------|------------------------|------------------------|------------------------|-----------------------|-----------------------|
| Semi-major axis altitude | 197 km | 198 km | 198 km | 200 km | 200 km |
| Eccentricity | 0.00007 | 0.01676 | 0.06500 | 0.06169 | 0.06183 |
| Inclination | 88.8° | 89.0° | 87.4° | 86.8° | 86.8° |
| Maximum position gap | 12.8 km | 9.5 km | 9.9 km | 7.7 km | 3.3 km |
| Accumulated velocity change | 42.0 m s ⁻¹ | 36.2 m s ⁻¹ | 12.7 m s ⁻¹ | 3.5 m s ⁻¹ | 4.4 m s ⁻¹ |

precision we expect to recover the geodetic parameters. However, the extended approach can be used for final selected orbits. Additionally, this allows us to focus on near circular orbits only.

Chapter 4

Orbit determination and geodetic parameter recovery using Doppler observations only

In this chapter, we focus on the determination of a probe's orbit around Europa or Callisto and the estimation of the body's global geodetic parameters exclusively from Doppler observations. The first analyses of this work were dedicated to the study of a probe in orbit around Europa, and we later included the study of a probe around Callisto. For this reason, there are a few differences between the simulation set-ups considered for Europa and Callisto, the latter being more comprehensive. The probe in orbit around Europa is assumed to be continuously tracked by the NASA DSN at X-band, with a fixed Doppler noise (0.1 mm s^{-1} 1-way at 60 s integration time). In the case of Europa, we focused on the gravity field estimation, leaving aside rotation parameters estimation. We considered X and/or Ka-band at 60 s integration time from the Chinese DSN for Callisto's orbiter, and analysed different tracking strategies, making use of the observation noise model described in Sect. 2.6.3. Non-gravitational accelerations were taken into account for orbits around Callisto, and we analysed different strategies on how to mitigate them in Sect. 4.5.

Irrespective of whether the probe is in orbit around Callisto or Europa, the simulation starts with the choice of an orbit scenario as detailed in chapter 3. The orbit is then propagated in the planetary extension of the Bernese GNSS Software [BSW; Dach et al., 2015, Arnold et al., 2015, Bertone et al., 2021a, Desprats et al., 2023], usually for 3 months starting from 1-May-2031, based on a reference force model (see Sect. 2.2). Both propagated orbits and reference force model will constitute our ground truth for later comparisons. Then, realistic two-way Doppler tracking measurements are generated along the orbit (see Sect. 2.6).

These measurements are used to reconstruct the orbit and to estimate geodetic parameters in a standard multi-arc least-squares process following the Celestial Mechanics Approach [CMA; Beutler et al., 2010], as described in Sect. 2.3. We add uncertainties with a standard deviation of $\sigma_{pos} = 50 \text{ m}$, $\sigma_{vel} = 1 \text{ mm s}^{-1}$ to the initial position and velocity of the a priori orbits for each estimation arc of length between 25 h and 400 h.

The recovered orbit and geodetic parameters are finally compared to the true orbit, and the reference force and rotation models, to assess the quality of our solution. The gravity field solution is compared to the reference gravity field (EURGLMo or CALGLMo) in terms of difference degree amplitudes Δ_n ,

$$\Delta_n = \sqrt{\frac{1}{2n+1} \sum_{m=0}^n (\Delta \bar{C}_{nm}^2 + \Delta \bar{S}_{nm}^2)}, \quad (4.1)$$

and difference order amplitudes Δ_m ,

$$\Delta_m = \sqrt{\frac{1}{m+1} \sum_{n=0}^{n_{max}} \Delta \bar{C}_{nm}^2}, \quad \Delta_{-m} = \sqrt{\frac{1}{m} \sum_{n=0}^{n_{max}} \Delta \bar{S}_{nm}^2}, \quad (4.2)$$

where $\Delta \bar{C}_{nm}$ and $\Delta \bar{S}_{nm}$ are the differences of the respective spherical harmonic coefficients of degree n and order m . Furthermore, we evaluate the error degree amplitudes, which are obtained from Eq. (4.1) by replacing the coefficient differences with the formal errors of the estimated coefficients. We also use the weighted RMS of the geoid height differences with respect to the reference gravity field as a global quality assessment. It is defined as

$$(\Delta g)_{\text{WRMS}} = \sqrt{\frac{\sum_{\phi, \lambda} \cos(\phi) \Delta g_{\phi, \lambda}^2}{\sum_{\phi, \lambda} \cos(\phi)}}, \quad (4.3)$$

where $\Delta g_{\phi, \lambda}$ is the difference of the geoid height at latitude ϕ and longitude λ between a given gravity field solution and the reference gravity field (see Eq. 2.14). When comparing high-degree gravity field models, a filter is usually applied to the geoid height differences $\Delta g_{\phi, \lambda}$, to reduce the noise in the high-degree gravity field coefficients. However, in this work, we only compute the geoid height differences considering the gravity field up to a given degree and order (d/o) n , usually the maximum degree for which the difference degree amplitude Δ_n is lower than the degree amplitude of the reference gravity field.

In a first section, we analyse the quality of the orbit solution and its weakness, which is a central prerequisite to consider the estimation of global parameters. The non-linear least-squares adjustment of orbit and geodetic parameters requires a priori values for the parameters. In case of the gravity field parameters, we then demonstrate that high-degree models can be estimated irrespective of whether the currently very limited knowledge of gravity fields of the Galilean moons or the true gravity field is introduced as a priori information. The latter strategy allows for more efficient subsequent analyses since iterations can be avoided. In Sect. 4.3, we focus on the quality of the recovered gravity field based on the considered orbit, taking Europa as an example, and highlight the importance of certain parameters. We then look at how the estimation of rotation parameters fits in our global estimation in the case of Callisto. Finally, we investigate non-gravitational accelerations mitigation strategies for a probe in orbit around Callisto.

4.1 Orbit determination quality

The first step of the CMA is to fit an orbit using only arc-specific parameters (see Tab. 2.1). Once the orbit is converged, we use this orbit as a priori information to estimate the complete set of parameters. In principle, arc-wise and global parameters can be estimated in a

common fit, at the expense of more computational resources.

In this section, the arc-specific parameters are estimated from a perturbed a priori orbit using a perfect a priori force model, i.e., the complete gravity field model which was used for the simulation. This first orbit recovery is repeated for at least 4 iterations until convergence is achieved, i.e., until the relative RMS of the residuals is below 0.5%, and for a maximum of 8 iterations. The simulation environment allows us to compare the reconstructed orbits with the true (simulated) orbits and to obtain a direct quality measure of our achievable orbit recovery. We furthermore estimate gravity field parameters in Sects. 4.1.3 and 4.1.4, once the arc-specific parameters are estimated, still using a perfect a priori force model. The corrections on these parameters are thus expected to be minimal, and this will be discussed in more depth in Sect. 4.2.

In the case of Europa, considering a fixed level of Doppler noise, the observations are weighted equally. For Callisto, since the Doppler observations were generated using the noise model described in Sect. 2.6.3, we applied a fixed ground station-based weight, corresponding to the expected level of noise. For a station in the northern hemisphere operating at Ka-band, we considered 3.5 mHz (corresponding to an Allan deviation of $\sigma_y(60\text{ s}) = 1.02 \times 10^{-13}$), for a station operating at X-band in the northern hemisphere, we instead considered a level of noise of 3.6 mHz ($\sigma_y(60\text{ s}) = 1.04 \times 10^{-13}$). Finally, for a southern station at Ka-band, we considered 1.35 mHz ($\sigma_y(60\text{ s}) = 4 \times 10^{-14}$), as the tropospheric noise is expected to be less important for a mission mid-2031 (see Sect. 2.6.3).

4.1.1 Orbit deficiencies

The determination of a probe's orbit around a celestial body using radio tracking from Earth is known to have degeneracies [Wood, 1986, Russell and Thurman, 1989], which can be explained by geometrical symmetries in the system. Bonanno and Milani [2002] pointed out that in the ideal case where the central body is spherically symmetric, and where the central body does not move with respect to the Earth, there is a symmetry around the line of sight from Earth to the central body. A rotation of the orbit of the probe around \mathbf{e}_1 , the unit vector from the central body to the Earth, would yield the same range-rate and range observations, resulting in indeterminate orbit components. In reality, the central body slightly moves with respect to the Earth during the estimation arc. This means that the rotation of the system around the line-of-sight is no longer a strict symmetry, but still leads to a poorly conditioned orbit.

The weakly determined components of the position \mathbf{r} and velocity $\dot{\mathbf{r}}$, with respect to the central body, are contained in a plane orthogonal to the line of sight from Earth to the central body. More precisely, the orbit is weakly determined in the directions \mathbf{e}_2 and \mathbf{e}'_2 , respectively, given by

$$\mathbf{e}_2 = \frac{\mathbf{r}_E \times \mathbf{r}}{\|\mathbf{r}_E \times \mathbf{r}\|}, \quad \text{and} \quad \mathbf{e}'_2 = \frac{\mathbf{r}_E \times \dot{\mathbf{r}}}{\|\mathbf{r}_E \times \dot{\mathbf{r}}\|}, \quad (4.4)$$

where \mathbf{r}_E is the position vector of the Earth with respect to the central body [Cicalò et al., 2016]. We thus consider the two following plane-of-sky frames $(\mathbf{e}_1, \mathbf{e}_2, \mathbf{e}_3)$ and $(\mathbf{e}_1, \mathbf{e}'_2, \mathbf{e}'_3)$ to

analyse the orbit differences, with

$$\mathbf{e}_1 = \frac{\mathbf{r}_E}{\|\mathbf{r}_E\|}, \quad \mathbf{e}_3 = \mathbf{e}_1 \times \mathbf{e}_2, \quad \text{and} \quad \mathbf{e}'_3 = \mathbf{e}_1 \times \mathbf{e}'_2. \quad (4.5)$$

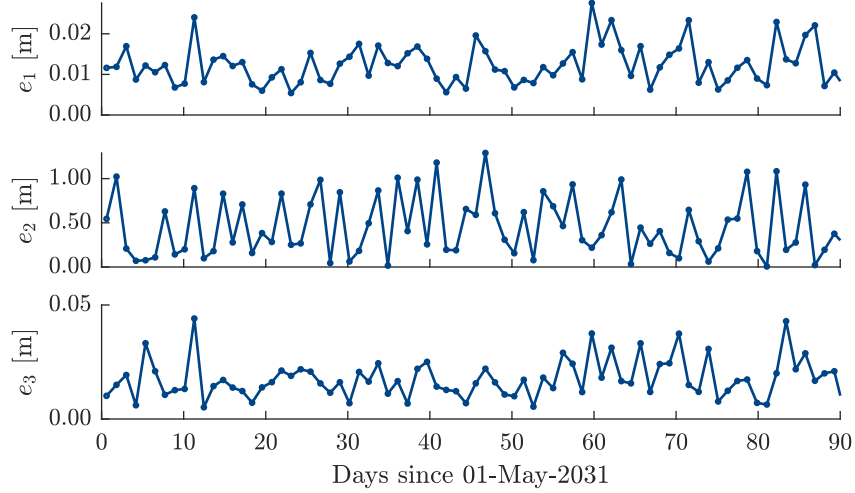


Figure 4.1: RMS of orbit differences for each arc in the $(\mathbf{e}_1, \mathbf{e}_2, \mathbf{e}_3)$ frame for a 5:197 ($i = 89^\circ$, $h = 134$ km, $\beta_{Earth} = -6^\circ$), using EURGLMo as gravity field model.

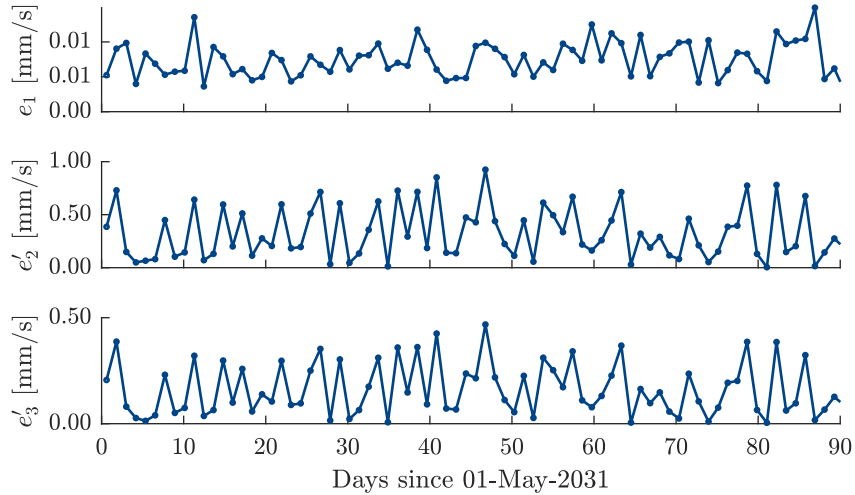


Figure 4.2: RMS of velocity differences for each arc in the $(\mathbf{e}_1, \mathbf{e}'_2, \mathbf{e}'_3)$ frame for a 5:197 RGTO ($i = 89^\circ$, $h = 134$ km, $\beta_{Earth} = -6^\circ$), using EURGLMo as gravity field model.

As an example, we fit six osculating orbital elements of 78 arcs of ~ 28 h to Doppler data which have been simulated from a 5:197 RGTO around Europa ($i = 89^\circ$, $h = 134$ km, $\beta_{Earth} = -6^\circ$), using EURGLMo up to degree and order (d/o) 90 as a priori gravity field model, resulting in a best case orbit in the absence of any mismodelling. We freely estimate one set of orbital elements per arc and we show in Fig. 4.1 and Fig. 4.2 the differences between the true orbit and the fitted orbit in the plane-of-sky frames, in terms of RMS of the differences between the position and velocity vectors. In the $(\mathbf{e}_1, \mathbf{e}_2, \mathbf{e}_3)$ frame, the

e_2 direction, perpendicular to the line of sight and to the position vector, ends up being the worst determined direction (up to 100 times worse than along e_1 and e_3 , see Fig. 4.1). The same goes for the velocity differences in the (e_1, e_2', e_3') frame, the differences in the e_2' direction are several orders of magnitude worse than in the other directions. However, the quality of the recovery (< 1.3 m in position and < 1 mm s $^{-1}$ in velocity) is still at a level acceptable for most mission goals.

Indeterminate components of the orbit increase the correlation between the estimated initial orbital elements. By describing the orbit using orbital elements with respect to the plane-of-sky, Wood [1986] showed that some orbital elements are indeterminate. Some configurations proved to be worse than others, in particular when the velocity of the celestial body is along the line-of-sight, or when the angle of the orbital plane with respect to the plane-of-sky is 0° or 180° (corresponding to $\beta_{Earth} = \pm 90^\circ$). Russell and Thurman [1989] quantified the influence of β_{Earth} and showed that orbit errors increase with the inclination, i.e., with decreasing β_{Earth} . Since we use a different parametrisation related to an inertial frame, the poor determination of the orbital elements discussed in Wood [1986] and Russell and Thurman [1989] is reflected in all the orbital elements we estimate, leading to significant correlations.

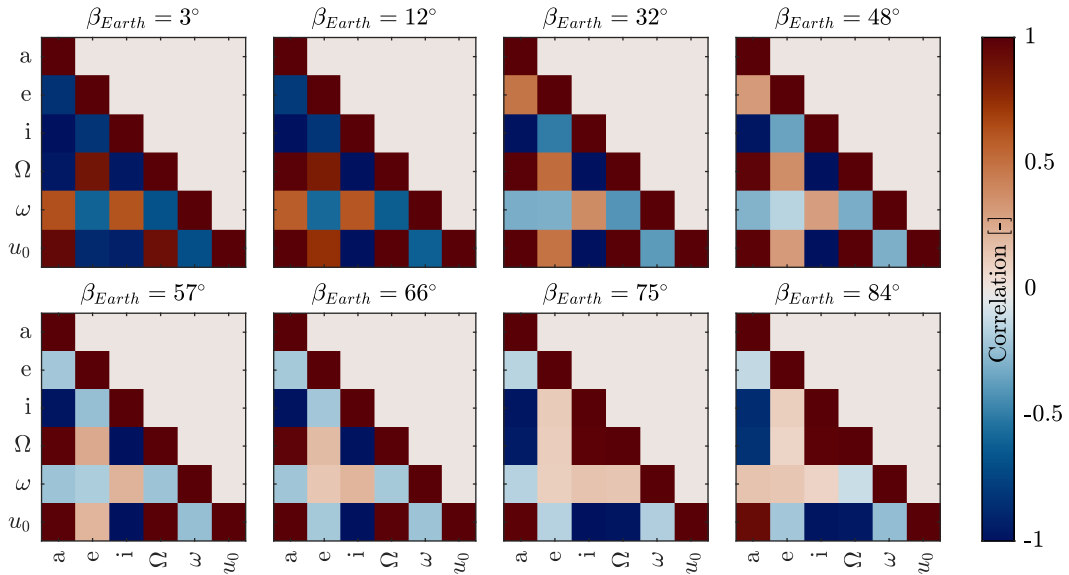


Figure 4.3: Correlations between orbital elements for different values of β_{Earth} . Each value corresponds to the maximum correlation over all ~ 28 h arcs for a 5:197 RGTO around Europa with $i = 89^\circ$, $h = 134$ km.

In Fig. 4.3, we plot the maximum correlation existing between the orbital parameters estimated in all the 78 estimation arcs, and for several values of β_{Earth} . This synthetic representation corresponds thus to a hypothetical worst case, and not to the most correlated arc. We can clearly see that the overall correlations increase with a smaller β_{Earth} , as suggested by Russell and Thurman [1989], especially visible in case of the correlations including the eccentricity e and the argument of periapsis ω . However, the correlation between orbit accuracy and β_{Earth} is less conspicuous, as shown in Fig. 4.5a.

There are several approaches to reduce the error of the indeterminate component of the orbit. This usually amounts to introducing external information, such as constraining poorly determined orbital elements to some a priori values, or constraining the rotation around the \mathbf{e}_1 axis to zero [Bonanno and Milani, 2002]. Another possibility is to consider longer estimation arcs, so that the amplitude of the relative motion of the probe with respect to the Earth is more important, thus reducing the symmetries.

4.1.2 Length of the estimation arc

In order to decrease the correlations between the different orbit parameters of one arc, we increased the length of the estimation arc. In practice, the duration of an arc is often limited by manoeuvres of the satellite. These can be desaturation manoeuvres, e.g., every 12 h for BepiColombo [Iafolla et al., 2011], or orbit corrections, whose frequency can be quite variable. In our simulation setup, we are limited by our manoeuvre handling (see Sect. 3.4.2), preventing us to consider estimation arcs longer than one Europa day or one Callisto day.

In the case of Europa, extending the arc length by a factor of 3 from ~ 28 h to ~ 86 h, allows for a significant reduction of the correlation, compare Fig. 4.3 and Fig. 4.4. The correlations including e are still decreasing with increasing β_{Earth} , but the ω correlations are less dependent on β_{Earth} . The orbit parameters are the least correlated with each other for $\beta_{Earth} = 48^\circ$, especially the semi-major axis a . However, the inclination i and the longitude of the ascending node Ω are still highly correlated with each other, with a and with the argument of latitude u_0 in case of a near face-on orbit.

The impact is also significant regarding the orbit differences. As shown in Fig. 4.1, the different RMS values of orbit differences can vary significantly from one arc to another. We thus considered the 0.95-quantile q_{95} of the arc-wise 3D RMS of orbit differences as a conservative measure of the orbit quality, which is less optimistic as the mean of the RMS values, but not as pessimistic as the maximum of the RMS values. Using this metric, one can see that 3 times longer estimation arcs can reduce the RMS of the orbit differences by a factor of at least 2 (Fig. 4.5a).

In case of Callisto, we increased the length of the estimation arc from ~ 25 h to ~ 400 h, corresponding approximately to 1 Callisto day. Figure 4.5b shows increasing accuracies with increasing duration of the estimation arc, for several values of β_{Earth} . The determination of near face-on orbits ($\beta_{Earth} = 83.6 \pm 3.2^\circ$) is visibly worse than near edge-on orbits ($\beta_{Earth} = 1.0 \pm 4.2^\circ$) regardless of the length of the estimation arcs (Fig. 4.5b), whereas in the case of Europa, the difference between this two extreme cases, $\beta_{Earth} = 84.6 \pm 1.1^\circ$ and $\beta_{Earth} = 3.1 \pm 0.5^\circ$, is less significant (Fig. 4.5a). In case of Callisto, the near edge-on orbits are even more accurate than the intermediate orbit configuration $\beta_{Earth} = -40.6 \pm 4.3^\circ$, and we notice that for the near edge-on case, the correlations between the inclination i and both the longitude of the ascending node Ω and the argument of latitude u_0 are significantly lower, below 0.5, compared to values higher than 0.9 in the other two cases. Such low correlations are not visible in the case of Europa (Fig. 4.4), but may explain why the orbit accuracy is better for $\beta_{Earth} \approx 1.0^\circ$ in case of Callisto. In the best and very ideal

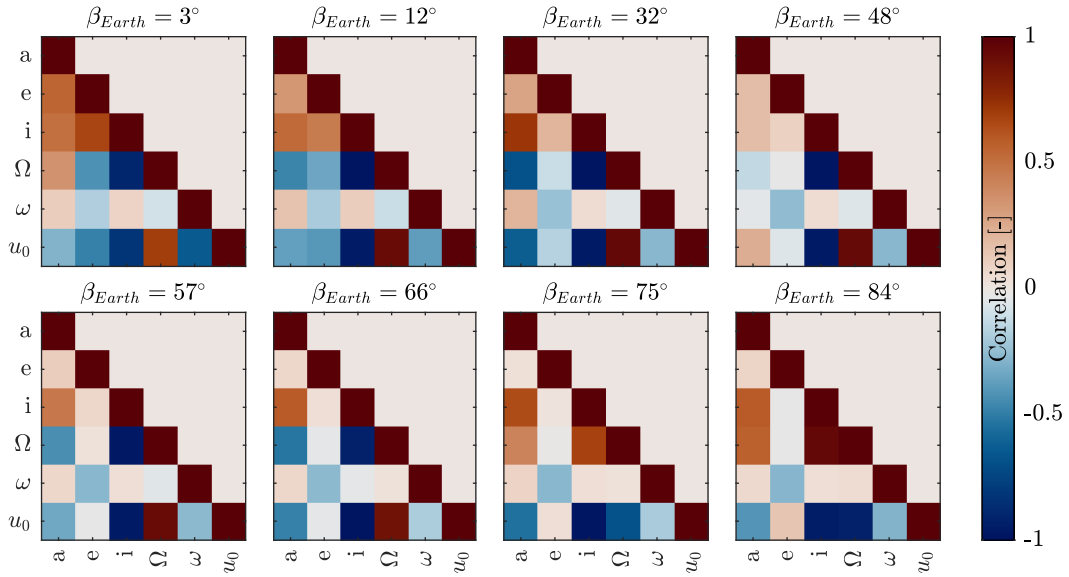


Figure 4.4: Correlations between orbital elements for different values of β_{Earth} . Each value correspond to the maximum correlation for all ~ 86 h arcs for a 5:197 RGTO around Europa with $i = 89^\circ$, $h = 134$ km.

case, the orbit can reach centimetre-level accuracy for a near edge-on orbit, considering ~ 400 h estimation arcs (see blue curve in Fig. 4.5b).

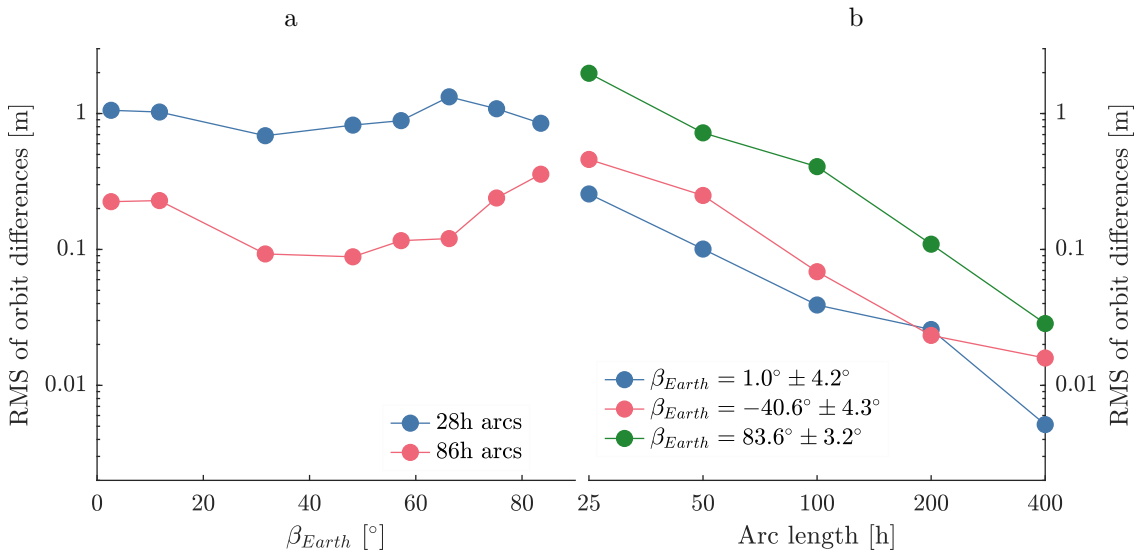


Figure 4.5: 0.95-quantile for the 3D RMS of orbit differences for different β_{Earth} and arc lengths in the case of a 5:197 RGTO around Europa (a) and a 5:731 RGTO around Callisto (b).

However, estimating very long arcs is not necessarily possible. The impact of any mismodelling would increase with longer arcs, and even if mismodellings could be absorbed by other parameters, their impact on the orbit would need to be carefully assessed (see e.g., Sect. 4.5). Additionally, as mentioned above, any unmodelled orbit manoeuvres would also

prevent the estimation of long arcs. It is a common orbit determination practice to split the arc around the manoeuvres epochs. However, some other approaches allow to decorrelate orbit parameters, such as the one briefly discussed in Sect. 4.1.1.

4.1.3 Importance of the ground station tracking

The Chinese and NASA Deep Space Networks are distributed on the surface of the Earth in a way that if a deep space probe is visible from Earth, then it can be tracked at nearly any time. However, not all DSN ground stations contribute equally to the observation of deep space probes, because of their location, and because of their capabilities or schedule. For instance, due to Earth's inclination with respect to the ecliptic, a probe in the Jovian system might be observed less by a station in the northern hemisphere compared to one in the southern hemisphere or vice versa. In case of a mission in mid-2031, such a probe would be visible for a longer part of the day in the southern hemisphere than in the northern hemisphere. Figure 4.6a shows the coverage of the three stations of the Chinese DSN (with a 10° -elevation threshold), and the ground track of a probe in the Jovian system for 90 days starting on 2031-05-01. A station in the southern hemisphere, e.g., Neuquén, will have the possibility to observe the probe longer than a station in the northern hemisphere (e.g., Jiamusi).

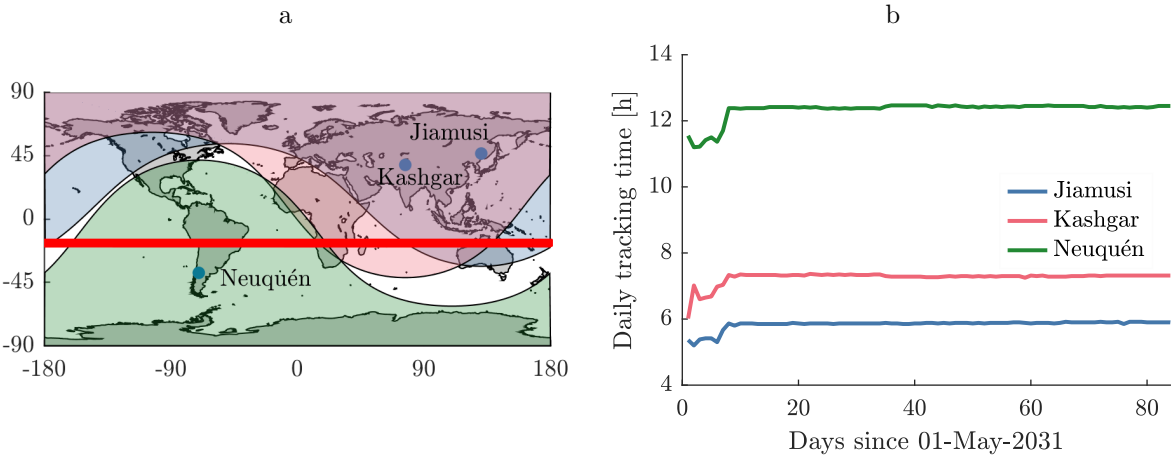


Figure 4.6: Coverage (a) and daily tracking time (b) for the 3 stations of the Chinese DSN. The red band correspond to the trajectory of the probe as seen from Earth.

The location of the station plays a role not only in the quantity of observables generated, but also in their quality. One of the most important contributions to our Doppler noise model is constituted by the wet troposphere, which is larger during summer (see Sect. 2.6.3). This means that for a mission in mid-2031, the tropospheric noise is more important for a station in the northern hemisphere than in the southern hemisphere. Moreover, Jiamusi ground station does not operate at Ka-band, but only at X-band, for which the plasma noise contribution is more important (see Sect. 2.6.3).

In this section, we investigate the influence of the ground station tracking on the quality of orbit determination, and on the subsequent gravity field solution. We limit our

investigation to the choice of the set of tracking stations for the whole mission, and we assume that when the probe is visible by the chosen set of stations, one (and only one) of them is tracking the probe. We consider a 5:731 RGTO around Callisto, with $h = 197$ km and $i = 89^\circ$. We set $\beta_{Earth} \in [67^\circ, 76^\circ]$ so that the probe is not occulted by Callisto for most of the mission duration. Figure 4.6b, shows the maximum tracking time per day and per station. The shorter tracking passes at the beginning of the mission are due to partial occultation of the probe’s orbit by Callisto.

We tested different combinations of observing stations from the Chinese DSN resulting in average daily tracking time between 5h50 and 22h25 (Tab. 4.1). We estimated one set of orbital elements for each arc, using a perfect a priori force model, but a perturbed a priori orbit, and computed the 3D RMS of the orbit differences for each arc. In order to focus on the general quality of the orbit, we computed the 0.95-quantile q_{95} to discard outliers. We afterwards estimated the gravity field up to d/o 100, and show in Tab. 4.2 the maximum degree of the gravity field which can be resolved, i.e., the maximum degree n for which the difference degree amplitude with respect to CALGLMo Δ_n (Eq. 4.1) is smaller than the CALGLMo degree-amplitude. We additionally computed the weighted RMS of the geoid height differences $(\Delta g)_{WRMS}$ of the gravity field solution up to d/o 90 with respect to CALGLMo (Tab. 4.2).

Table 4.1: Average daily tracking time and q_{95} RMS of orbit differences after fitting only orbit parameters, for different station schedules.

| Ground stations | Freq. band | Average daily tracking time | q_{95} RMS orbit differences |
|-------------------|------------|-----------------------------|--------------------------------|
| Jiamusi | X | 5h50 | 11.4 m |
| Kashgar | Ka | 7h14 | 7.78 m |
| Neuquén | Ka | 12h18 | 1.51 m |
| Jiamusi & Kashgar | X/Ka | 10h06 | 6.09 m |
| Jiamusi & Neuquén | X/Ka | 18h23 | 1.66 m |
| Kashgar & Neuquén | Ka | 19h34 | 1.46 m |
| All CDSN stations | X/Ka | 22h25 | 1.30 m |

The orbit fitted considering only observations from Jiamusi station is about ten times worse than an orbit fitted using the complete set of ground stations from the Chinese DSN, because Jiamusi ground station provides the least amount of observations, because these observations are limited to X-band, i.e. more sensitive to plasma noise, and because we considered a mission span during summer in the northern hemisphere. This is also visible in terms of gravity field solution, with the resulting $(\Delta g)_{WRMS}$ being about 5 times larger than in case of Neuquén. The orbit and gravity field solutions are slightly better in case of tracking from Kashgar only, thanks to the Ka-band capability, and due to $\sim 25\%$ more observations. However, the noise due to the wet summer troposphere is still dominant.

The inclusion of Neuquén in our selection of tracking ground stations significantly improves the solutions. A tracking from Neuquén provides more than twice as many observations

Table 4.2: Number of observations, geoid height weighted RMS and maximum degree recovered, after solving for all parameters, for different station schedules.

| Ground stations | Freq. band | Number of observations | $(\Delta g)_{\text{WRMS}}$ | Max degree |
|-------------------|------------|------------------------|----------------------------|------------|
| Jiamusi | X | 29 236 | 22.0 m | 78 |
| Kashgar | Ka | 36 313 | 16.6 m | 81 |
| Neuquén | Ka | 62 181 | 4.7 m | 92 |
| Jiamusi & Kashgar | X/Ka | 50 649 | 15.0 m | 81 |
| Jiamusi & Neuquén | X/Ka | 92 622 | 4.6 m | 90 |
| Kashgar & Neuquén | Ka | 98 548 | 4.5 m | 92 |
| All CDSN stations | X/Ka | 112 884 | 4.5 m | 92 |

than a tracking from Jiamusi alone. Because Neuquén operates during winter times in the considered scenario, the noise on each observation is in average 2.3 times smaller than the noise on observations from ground stations in the northern hemisphere, for the same frequency band. For all these reasons, considering tracking from Neuquén is necessary to achieve the level of accuracy of a “best case scenario” orbit and gravity field solution obtained by tracking the probe from all the ground stations of the Chinese DSN.

It is important to note that these results depend heavily on the mission’s time span, and on the observation noise we assumed in Sect. 2.6.3. Indeed, if the residual noise due to the wet troposphere delay can be calibrated, and if multi-link is possible to cancel the dispersive noise sources, then the contribution of each ground station is expected to change.

4.1.4 Orbit and global parameters

Once the orbit is fitted for every arc, the second step of the CMA is to set up the NEQs for all parameters to estimate, i.e., the arc-wise and the global parameters, and to solve for them (see Sect. 2.3). In this section, we address the quality of the orbit after global parameters are co-estimated, as opposed to a solution including only arc-wise parameters. We consider a 26:1023 RGTO around Europa, with $i = 89^\circ$, $h = 134$ km, and $\beta_{\text{Earth}} = 69^\circ$. We fit the orbit in 78 arcs covering 3 months, using a perfect a priori force model. In this ideal case, we reduce the Doppler residuals below 5 mHz (blue dots in Fig. 4.7a), when freely estimating only osculating elements for each of the ~ 28 h-long arcs, which corresponds to the applied Doppler white noise (0.1 mm s^{-1} 1-way). The orbit, estimated using only arc-wise parameters, can be recovered with a precision better than 2 m, similarly to the 5:197 RGTO discussed in Sect. 4.1.1.

However, when co-estimating gravity field parameters up to d/o 90, the quality of the orbit is degraded (see magenta dots in Fig. 4.7b). The main orbit differences are still in the \mathbf{e}_2 direction, but the RMS differences increase to a maximum of 5.3 m. On the other hand, the Doppler residuals are reduced, which is a consequence of enlarging the parameter space by estimating gravity field parameters (see Fig. 4.7a). Insight can be gained by inspecting the correlations between gravity field parameters and orbit parameters of

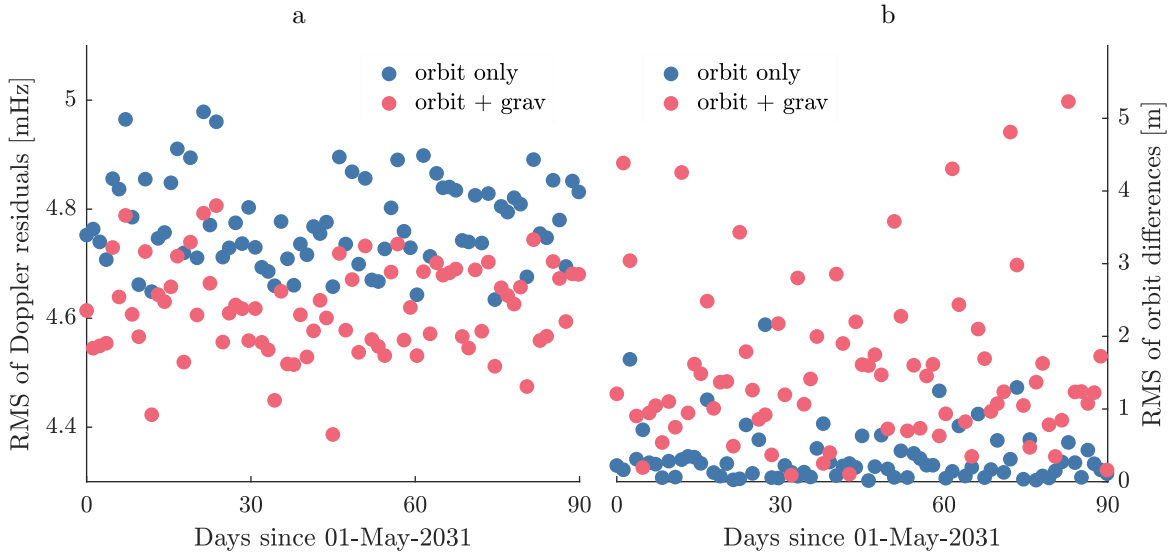


Figure 4.7: RMS of Doppler residuals (a) and orbit differences (b) for a 26:1023 RGTO around Europa ($i = 89^\circ$, $h = 134$ km, $\beta_{Earth} = 69^\circ$) for all 78 arcs, estimating only orbital parameters (blue) and estimating also gravity field parameters up to d/o 90 (magenta).

previously independent arcs. Figure 4.8 shows high correlations between orbit parameters of every 3^{rd} arc, which corresponds to every 1 Europa day. The ground tracks of these arcs on Europa’s surface are close to each other. This likely explains correlations when estimating the gravity field coefficients, as the tracks are then affected by the same components of the gravity field. In general, stronger correlations are visible every m Europa days for an $m:R$ RGTO. These new correlations between the orbit parameters explain why the orbit quality is degraded. Appropriate constraints on the orbit parameters can help to reduce these correlations, improving the overall orbit quality, and consequently the global solution.

4.2 Gravity field recovery strategies

In our two-step procedure, the arc-wise parameters are first iteratively estimated for every arc, while fixing the global parameters (e.g., gravity field coefficients) to their a priori value (see Fig. 2.6). However, the current knowledge of Europa and Callisto’s gravity field is limited to the degree-2 coefficients only [Anderson, 1998, 2001, Casajus et al., 2021]. If such a low-degree a priori gravity field is introduced, in order for the orbit fit to converge, additional parameters are needed on top of the initial conditions to compensate for the significant lack of information on the a priori force model. For the example of Europa, two solutions are considered in this section: using pseudo-stochastic pulses (Sect. 2.2.5) in our estimation or co-estimating in a first iteration the low-degree coefficients of the gravity field together with the orbital parameters. These solutions are compared to the true gravity field model EURGLMo, and we verify how well this comparison matches to the comparison of a reference solution with respect to EURGLMo, computed using a perfect a priori force model (up to d/o 90) and labelled EURSOL01 (Fig. 4.9).

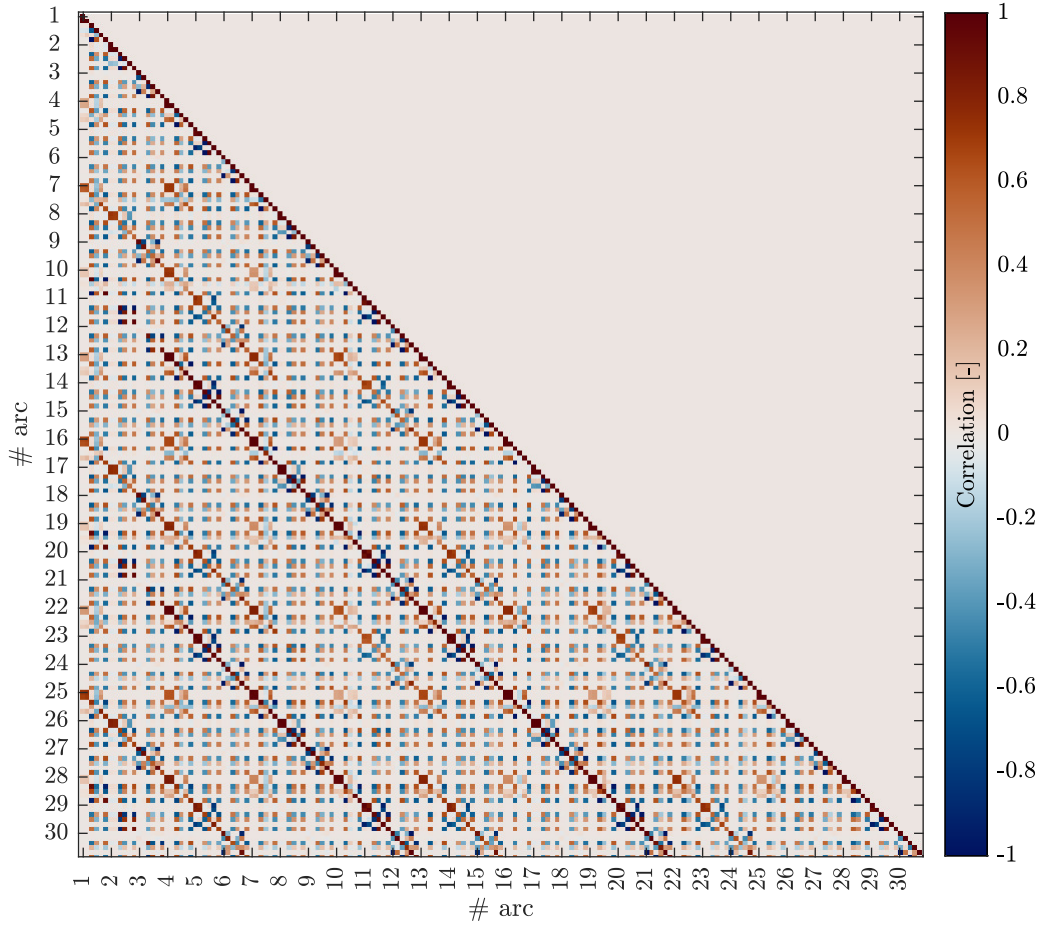


Figure 4.8: Correlations between initial osculating orbital elements of the first 30 arcs among the total 78 arcs for a 26:1023 RGTO around Europa.

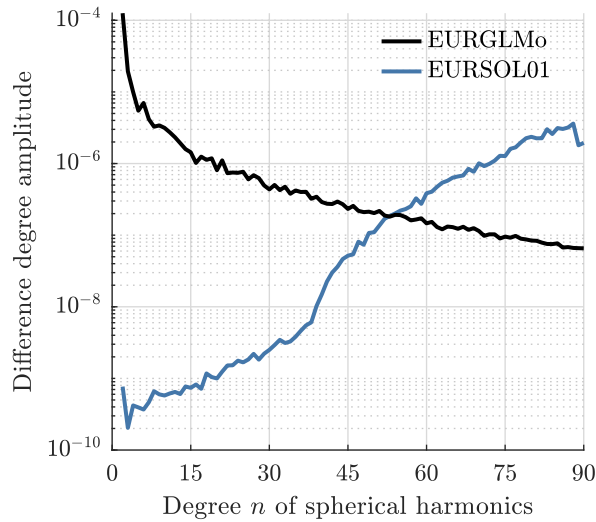


Figure 4.9: Difference degree amplitudes of the unconstrained reference solution EURSOL01, obtained from a 5:197 RGTO, $i = 89^\circ$, $\beta_{Earth} \approx -6^\circ$.

4.2.1 Using pseudo-stochastic pulses

Pseudo-stochastic pulses are instantaneous velocity changes (see Sect. 2.2.5). They are very useful additional parameters, e.g., to absorb modelling errors. We estimate a set of pulses every 60 min, corresponding to roughly twice per revolution, in all 3 directions (radial, along-track and cross-track) while constraining their amplitude to $\sigma_p = 1 \text{ mm s}^{-1}$.

With the help of such pulses, the data fit for all the arcs converged within 8 iterations when starting with a degree-2 a priori gravity field. The level of convergence in terms of Doppler residuals is still very far from the precision one could expect with a better a priori force model (Sect. 4.1), but this is to be expected from the limited knowledge of the gravity field. The orbits are also quite far (tens of kilometers) away from the true orbit. However, after this first step the nominal procedure can be pursued. The global parameters are successfully estimated after stacking the 3 months arc-wise NEQs, pre-eliminating all the arc-wise parameters (orbital elements and pseudo-stochastic pulses) and finally solving for the gravity field coefficients up to d/o 90.

The complete procedure is then iterated using the new gravity field as a priori information. The arc-wise parameters (initial osculating elements and pseudo-stochastic pulses) are not updated from one global solution to the other. They are instead re-estimated for each arc from their initial a priori value. Within a few iterations of the full process, the gravity field can be estimated to the same level of precision as when starting from the reference gravity field EURGLMo. In the first iteration, the RMS values of the pulses in radial, along-track and cross track direction are (35, 46, 1) mm/s. The magnitude of the pulses decreases at each iteration. They reach the level of (1, 2, 0.1) mm/s after a few iterations. At this point, pulses are not needed anymore to help the first orbit fit to converge, and we either apply tight constraints to 0 or fully omit them in order to preserve the low-degrees of our gravity field solution.

Considering a near edge-on orbit impacts the visible ground coverage as the probe vanishes behind the central body as seen from Earth (see Sect. 4.3.2 for more details). When considering an orbit for which no observations are lost because of occultations by Europa, only 3 to 4 iterations are needed to achieve the level of precision of EURSOL1 solution (Fig. 4.9) computed by starting from a perfect a priori gravity field.

However, when considering a near edge-on orbit, more iterations are needed to converge. This is due to the reduced visible ground coverage. As an example, 5 more iterations are needed for a nearly edge-on orbit (see Fig. 4.10 a) than for an orbit with $\beta_{Earth} = 67^\circ$. The effect of the reduced observed ground coverage can already be seen in the first iteration. The coefficients with a degree larger than 40 are not well estimated, which is in agreement with the results shown in Sect. 4.3.2.

An increase in convergence speed can be obtained by estimating gravity field coefficients up to d/o 90 but re-introducing the estimated gravity field solutions only up to d/o 40 as a priori information for the following iteration (see Fig. 4.10 b). Doing this for the first 2 iterations, within a total of 5 iterations, the gravity field parameters converge to the same

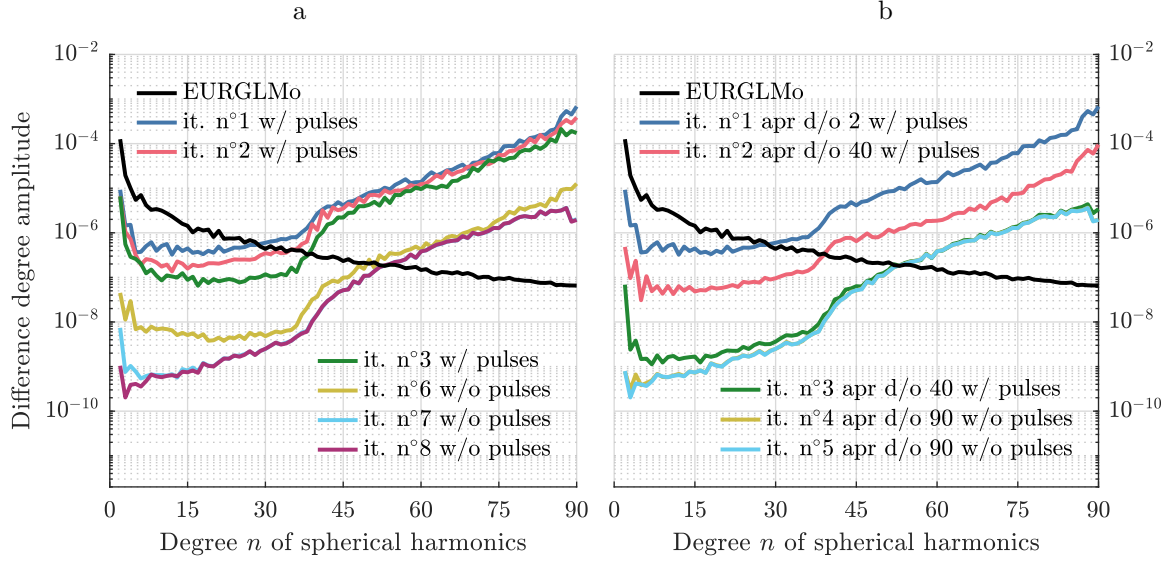


Figure 4.10: Difference degree amplitude of gravity field solutions estimated up to d/o 90 using pulses in the first iterations, and either reintroducing all gravity field parameters at every iteration (a) or reintroducing the gravity field parameters only up to d/o 40 for the first two iterations (b). 5:197 RGTO, $i = 89^\circ$, $\beta_{Earth} \approx -6^\circ$.

level of precision than when using a perfect a priori gravity field.

One drawback of this approach is that estimating pulses every 60 min during 3 months significantly increases the total number of parameters to be estimated to 15 131 (1.73 times more than with only orbit and gravity field parameters, see Tab. 2.1). Here, pulses are only considered as a useful tool to temporarily compensate for force model deficiencies.

4.2.2 Co-estimation of the low-degree gravity field coefficients

Another solution to cope with inaccurate a priori gravity information is to estimate low-degree gravity field coefficients along with the orbital elements in one common adjustment. Contrary to our nominal procedure, the orbital elements are thus never estimated alone. Normal equation systems (NEQs) including both orbit and gravity field parameters are set up for each arc but not solved, i.e., we do not compute an intermediate arc-wise orbit-only fit. The arc-wise NEQs are then stacked, the orbit parameters are again pre-eliminated, and the 3-months NEQ is inverted to compute the gravity field solution.

Co-estimating gravity field coefficients up to d/o 20 results in a total of 8746 parameters, which is approximately half the 15 131 parameters estimated when employing pseudo-stochastic pulses, as detailed in Sect. 4.2.1. With this method, one can estimate a reasonable medium-degree gravity field solution, in a single iteration, without using pulses (see Fig. 4.11). After this first iteration, the nominal procedure can be resumed until convergence: a first estimation of arc-wise parameters in an arc-wise fit, and then stacking all the NEQs to solve for a global orbit and gravity field solution.

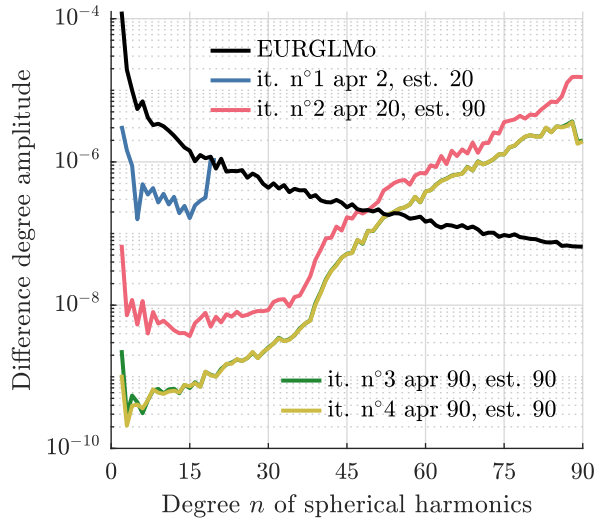


Figure 4.11: Difference degree amplitudes of gravity field solution recovered from a 5:197 RGTO with $i = 89^\circ$, $\beta_{Earth} \approx -6^\circ$, without pulses and estimating gravity field coefficients up to d/o 20 in the first iteration, and up to d/o 90 in the following iterations.

4.2.3 Comparison

The two methods presented in sections 4.2.1 and 4.2.2 converge to the same level towards the gravity field reference solution EURSOL01, which is computed using a perfect a priori force model, as shown in the previous sections. Because of the larger number of parameters, the use of pulses increases the total processing time. The differences in processing time using one CPU (core) per job (AMD EPYC microprocessor) on the current aiub-nodes at the UBELIX cluster are presented in Tab. 4.3.

Table 4.3: Number of iterations and computation time for all 3 methods for a 3-months d/o 90 gravity field recovery, starting with a d/o 2 a priori gravity field, considering that arc fits can be processed in parallel (par.) or not (seq.).

| Method | Number of iterations | Time | |
|------------------------------------|----------------------|-------|------|
| | | seq. | par. |
| Pulses (A) | 11 | 66h12 | 5h10 |
| Pulses (B) (remove d/o ≥ 40) | 8 | 44h50 | 3h33 |
| Low-degree co-estimation | 8 | 39h17 | 2h26 |

In the very first iteration, one can see that pulses are more efficient in reducing the RMS of Doppler residuals (Fig. 4.12a). This is to be expected due to the higher number of parameters to absorb model deficiencies. On the other hand, the differences with respect to the true orbits are larger when estimating pulses than when co-estimating gravity field coefficients (Fig. 4.12b). Re-injecting only the gravity field up to d/o 40 when using pulses markedly increases the convergence speed. Pulses (A) refers to the use of pulses (up to 5th iteration) and to consistently re-inject the 90-degree gravity field solution for each iteration. Pulses (B) refers to re-injecting only coefficients up to d/o 40 and using pulses until the 3rd itera-

tion. The dashed line represent the RMS reached when using a perfect a priori gravity field.

One can also note that when not estimating pulses anymore (6th iteration for (A) and 4th iteration for (B)) the Doppler residuals can temporarily increase, but then decrease even faster in the next iterations. This is not the case for the orbit differences: the RMS does not increase and the convergence is also faster after the pulses are not estimated anymore.

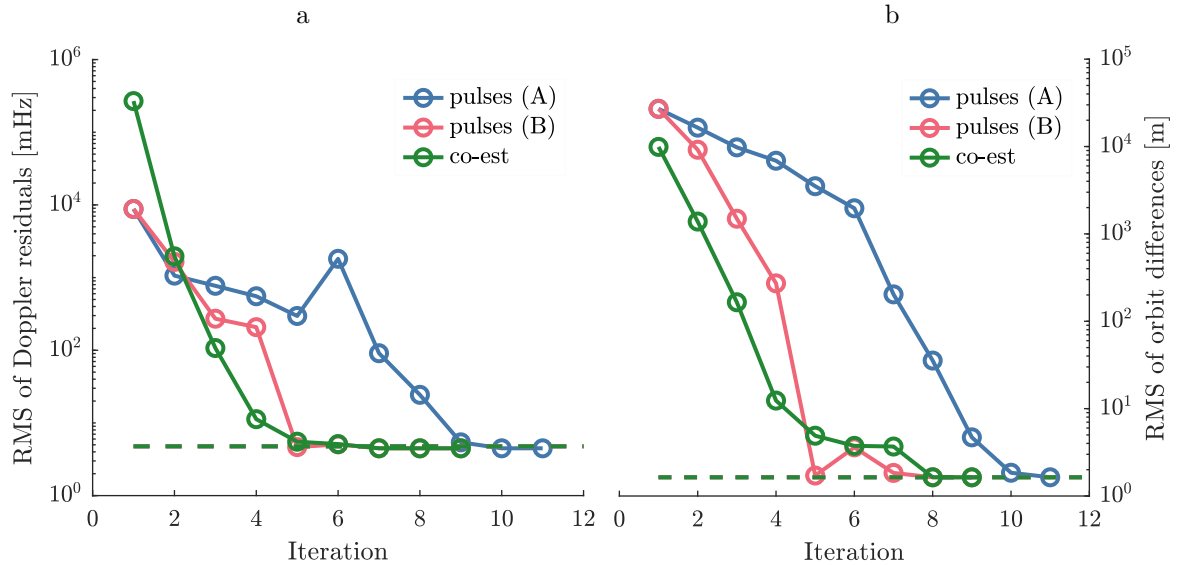


Figure 4.12: RMS of Doppler residuals (a) and orbit differences (b) with respect to iteration number for different methods.

It is important to emphasize that both methods converge to the same level of precision toward the reference solution EURSOL01. Convergence seems nevertheless faster when co-estimating the low-degree coefficients in the first iteration.

4.3 Low orbit design for gravity field recovery: case of Europa

In this section, we investigate the quality of gravity field recovery for multiple orbit scenarios defined in Sect. 3.4.2. We carefully analyse the influence of a set of parameters on the gravity field recovery, by isolating each of them as much as possible from the influence of the others. In particular, we treat the eclipses by Jupiter separately in Sect. 4.3.5, as their impact on the gravity field recovery can be critical. This also allows us to generalise our results to other celestial bodies which are not subject to such regular eclipses, e.g., Callisto.

We consider here the tracking of all three NASA DSN stations (Tab. 2.4) as baseline, and we confirmed that reducing the coverage to only one station does not significantly affect our results for the scope of this section. Non-gravitational forces were not considered in this section. We investigate their impact later in Sect. 4.5.

For computational time reasons, we use a perfect force model (i.e., the unperturbed simulated d/o 90 field) as a priori information for all our tests, to avoid iterating on the gravity field solution. As shown in Sect. 4.2, the gravity field can be recovered to a comparable level also when starting from a degree-2 a priori gravity field (corresponding to our current knowledge), albeit for the price of more iterations.

In all cases presented here, the Love number k_2 is co-estimated, resulting in uncertainties $< 1.3 \times 10^{-5}$ ($< 0.005\%$ relative to the expected signal), which would allow to distinguish between an ocean-bearing and ocean-free Europa [Wu et al., 2001, Wahr et al., 2006]. However, we found that the different scenarios investigated in this section only have a marginal impact on the recovery of k_2 , so that we will not further discuss this parameter.

4.3.1 Ground tracks repetition

The repetition cycle of an RGTO directly impacts the ground surface coverage, as mentioned in Sect. 3.1. The shorter the repetition cycle, the larger the cycle intertrack (see Tab. 3.1), resulting in a lower spatial resolution of the ground tracks, which limits the resolution of the estimated gravity field solution.

For a given gravity field degree n , the surface wavelength is given by the Jeans relation [see, e.g., Wieczorek, 2015]

$$\lambda_E = \frac{2\pi R_E}{\sqrt{n(n+1)}} \approx \frac{2\pi R_E}{n}. \quad (4.6)$$

According to the Nyquist criterion, a sampling of $\frac{\lambda_E}{2}$ allows to recover down to the shortest wavelength of $\frac{2\pi R_E}{n}$. In other words, to avoid aliasing [Sneeuw, 2000] when estimating a degree- n gravity field, the spatial resolution (or cycle intertrack δ_{eq}) of the ground tracks of an $m:R$ RGTO (see Eq. 3.3), must be smaller than this minimum sampling, i.e., $\delta_{eq} \leq \frac{\lambda_E}{2}$. Hence, from an $m:R$ RGTO we can expect the maximum resolvable degree n_{max} of a recovered gravity field to be given by

$$n_{max} = \frac{R}{2}. \quad (4.7)$$

It can be deduced from this equation that for $R \geq 180$, a degree-90 gravity field can be estimated without any aliasing. For an orbiter with an altitude between 100 km and 200 km, this corresponds to $m \geq 5$. There are other limiting factors on the quality of the recovered gravity field coefficients, e.g., the observation noise, and other parameters which we will discuss in the following sections. If we fix these parameters, and consider an orbit with an altitude $h \approx 134$ km and $\beta_{Earth} \approx 67^\circ$, the gravity field can be estimated unconstrained up to d/o 62 for every $m \geq 5$ (see when the curves for $m = 5$ and $m = 26$ cross the signal line in Fig. 4.13). Indeed, decreasing the repetition rate so that the ground tracks coverage becomes denser does not improve the quality of the gravity field solution.

On the other hand, when estimating the gravity field up to d/o 90 from an $m:R$ RGTO

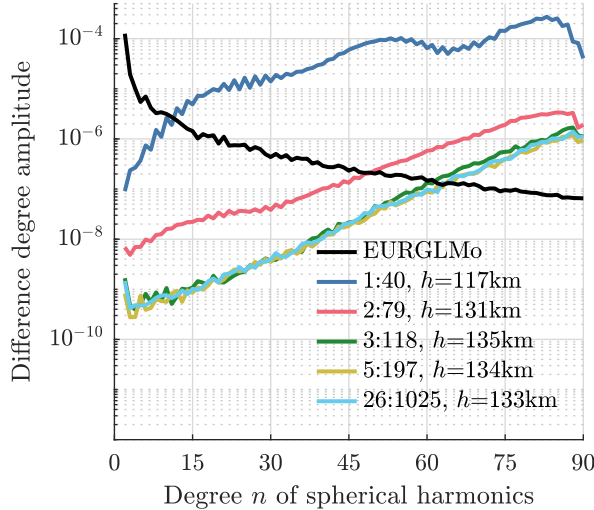


Figure 4.13: Difference degree amplitudes of Europa gravity fields recovered from different $m:R$ RGTO. $i = 89^\circ$, $\beta_{Earth} \approx 67^\circ$.

with $R < 180$, one expects an aliasing of the gravity field solution, increasing with decreasing values of R (see $m = 1, 2, 3$ in Fig. 4.13), meaning that some frequencies of the gravity field signal become indistinguishable. For the orbits considered in this study, aliasing is indeed visible as soon as one tries to estimate coefficients of degree larger than $20 \times m$. For $m=1,2$, a severe aliasing is visible over the entire spectrum.

A first approach to avoid aliasing would be to solve only for a gravity field solution up to d/o $20 \times m$. However, this necessarily induces an omission error, meaning that the signal from the higher degree coefficients (which are not estimated) leaks into the estimated gravity field coefficients (e.g., green curve in Fig.4.14, left, for $m = 3$). To prevent this, one can still estimate the gravity field up a higher degree (d/o 90 in our simulation scenario), while constraining all coefficients of the gravity field to zero using a Kaula law [Kaula, 1963] such that the constraint on each coefficient of degree n is

$$\sigma_K(n) = \frac{K}{n^2}, \quad (4.8)$$

with K being a positive constant. This results in tighter constraints on the high degree coefficients (which might diverge due to the limited data coverage) than on the low-degree coefficients. Here, K was empirically set to 0.5 to only prevent the high degree gravity field coefficients from diverging, and in principle depends on the celestial body. We were careful not to constrain the estimated parameters to their expected value.

In order to validate this approach, we also compute an “artificial” solution, for which the omission error is removed by estimating the gravity field up to d/o $20 \times m$, but assuming a perfect knowledge of the higher degree coefficients (magenta curve in Fig. 4.14, left). Fig. 4.14, left then confirms that the Kaula-constrained gravity field (yellow curve) solution tends towards the “artificial” solution (magenta curve).

When using a Kaula constraint, the gravity field can be estimated up to d/o 62 with $m = 3, 4$ with the same precision as with $m \geq 5$ (Fig. 4.14, right). A Kaula constraint

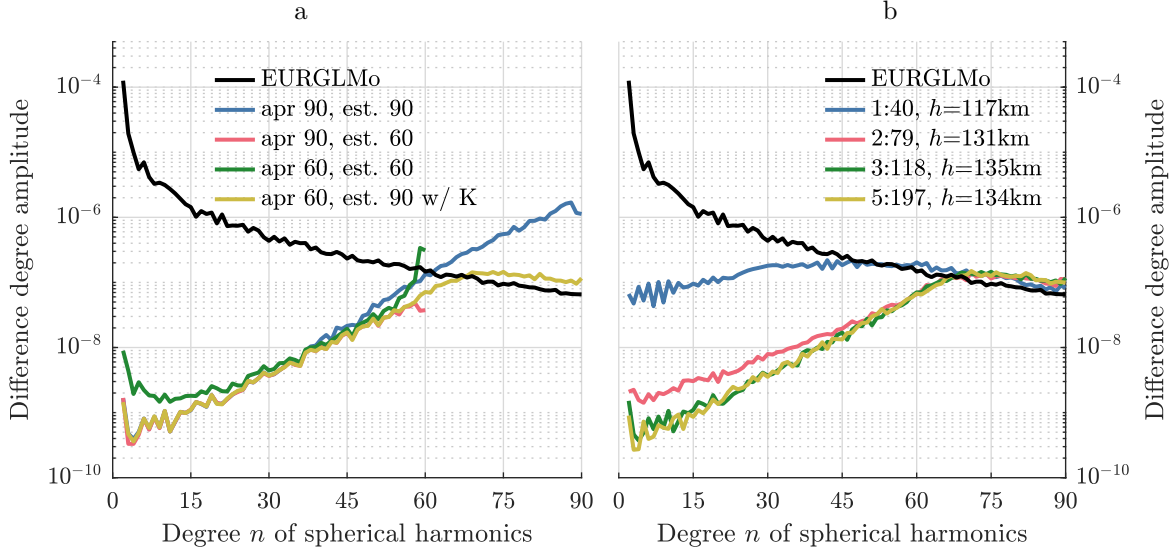


Figure 4.14: Difference degree amplitudes of several gravity field solutions from a 3:118 RGTO showing the benefit of a Kaula constraint (left) and from different $m:R$ RGTO with $m \leq 5$ using a Kaula constraint (right) with $i = 89^\circ$ and $\beta_{Earth} \approx 67^\circ$.

also improves the solution for $m \leq 2$, but the solution is still degraded in the low degrees. A tighter constraint could in principle further improve the results, but it would also risk biasing our solution.

4.3.2 Earth β -angle

The angle β_{Earth} between the orbital plane of the probe and the Earth direction plays a significant role in gravity field recovery. When this angle is below a certain threshold $\beta_{Earth,c}$, the probe vanishes behind Europa as seen from Earth for a portion of the orbit, which is thus not covered by observations collected from stations on Earth. In Europa fixed frame, these missing observations correspond to a latitude band around the equator on the far side of Europa with respect to Earth (Fig. 4.15). We define the critical latitude $\phi_c \geq 0$ as the latitude of the first observation missed so that for a near-circular and quasi-polar orbit

$$\cos(\phi_c) \cos(\beta_{Earth}) \approx \sqrt{1 - \left(\frac{R_E}{R_E + h}\right)^2}. \quad (4.9)$$

The line of sight from Earth is then blocked if the probe is on the far side of Europa, and if its latitude is between $+\phi_c$ and $-\phi_c$. As shown in Fig. 4.15, there are still observations between $+\phi_c$ and $-\phi_c$ when the probe is on the front side of Europa, as Europa rotates with respect to Earth. Larger β_{Earth} limit this effect to a narrower set of latitudes around the equator. The threshold $\beta_{Earth,c}$, below which the line of sight can be occulted, is deduced from Eq. (4.9) by setting $\phi_c = 0^\circ$, and is a function of the probe's altitude h , and the radius of Europa R_E (see Fig. 4.16).

At worst, the probe cannot be observed from Earth for $\sim 40\%$ of the orbit with a completely edge-on orbit ($\beta_{Earth} = 0^\circ$) with an altitude between 100 km and 200 km. This

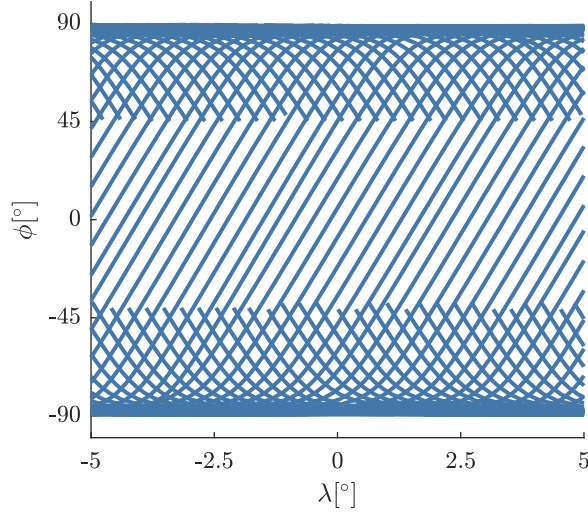


Figure 4.15: A 26:1023 RGTO with $\beta_{Earth} = 58^\circ$ will be only partially visible from Earth, as shown in this longitudinal zoom of its ground track ($\phi_c = 45^\circ$, $-5^\circ \leq \lambda \leq 5^\circ$).

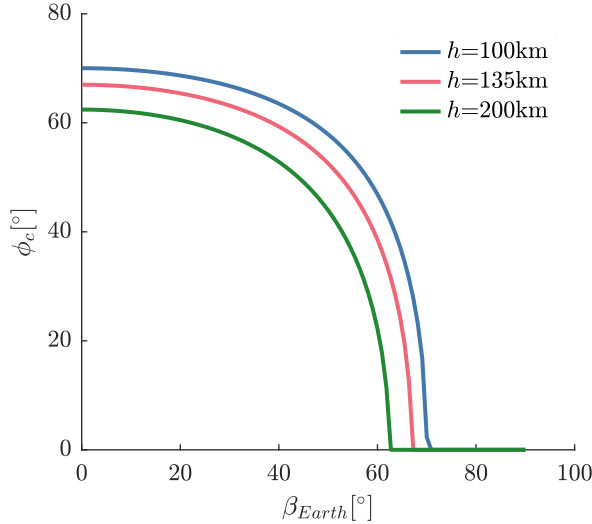


Figure 4.16: Critical latitude ϕ_c for which the line of sight is blocked on the far side of Europa with respect to Earth as a function of β_{Earth} . A near-circular and quasi-polar orbit is assumed.

highly affects the visible ground coverage. On the other hand, a completely face-on orbit ($\beta_{Earth} = 90^\circ$) will always be visible from Earth, but it is also much less suited to probe the gravity signal, as it will induce only relatively small velocity variations along the line of sight direction best sensed by Doppler measurements. To investigate the impact of different values of β_{Earth} on gravity field recovery, we focus in the following an 89° -inclined orbit, for which β_{Earth} is quasi constant during the 3 months mission period (see Sect. 3.3.2). We select a 26:1023 RGTO which does not repeat in 3 months and with an altitude of $h = 135$ km. According to Eq. (4.9), $\beta_{Earth,c} = 67.0^\circ$ for this orbit. We considered several initial positions of the orbital plane, i.e., several different β_{Earth} values, to investigate the influence of this parameter.

A high β_{Earth} degrades the estimation of the low-order gravity field coefficients (zonal and

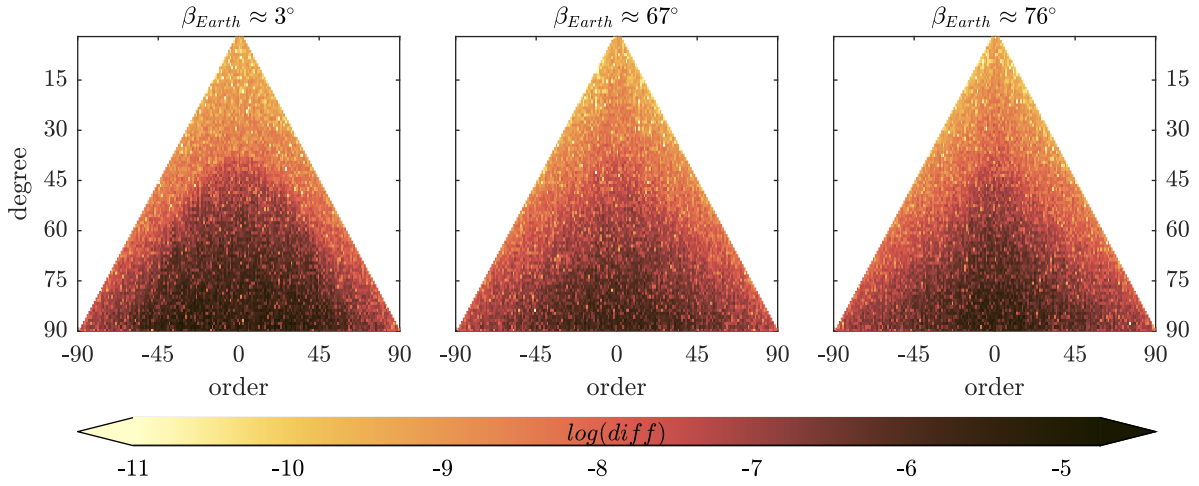


Figure 4.17: Difference with respect to EURGLMo of the freely estimated Europa gravity field coefficients recovered from a 26:1023 RGTO for several β_{Earth} values, with $h = 135$ km and $i = 89^\circ$.

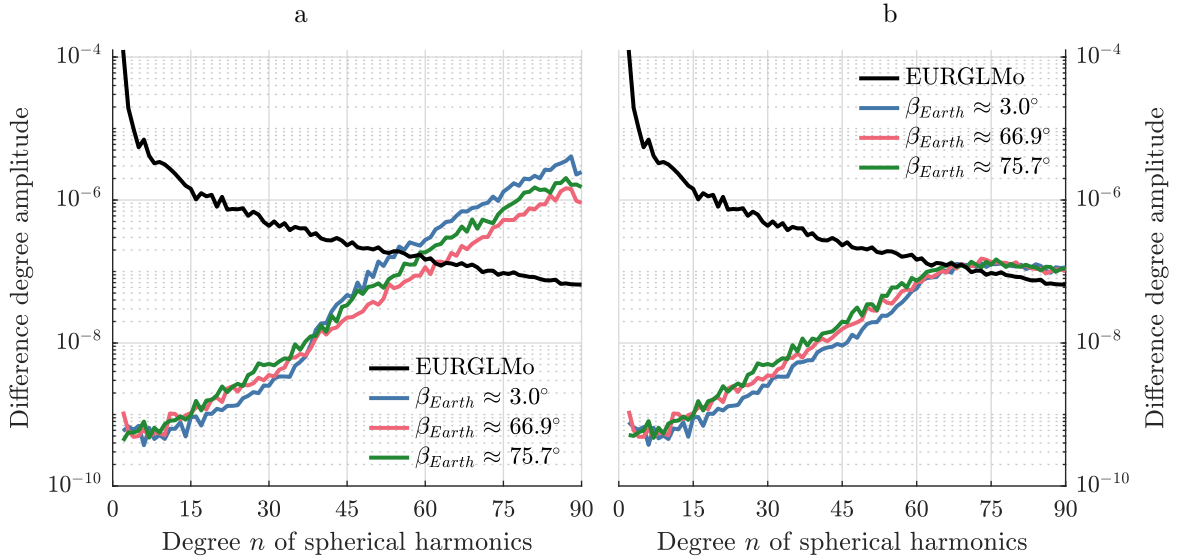


Figure 4.18: Difference degree amplitude of unconstrained recovered Europa gravity field solutions for different β_{Earth} angles (a) without and (b) with a Kaula constraint ($K = 0.5$), for a 26:1023 RGTO with $h = 135$ km and $i = 89^\circ$.

near zonal) as shown in Fig. 4.17. On the other hand, for very small β_{Earth} values the higher degree coefficients are not well determined (see Fig. 4.18a) because of the reduced ground surface coverage. Estimating the gravity field to a lower d/o would introduce an omission error, as shown in Sect. 4.3.1. A relatively loose Kaula constraint (Eq. 4.8) can be considered instead, to avoid a large omission error, affecting the lower-degree coefficients. Fig. 4.18b shows that the d/o > 35 are visibly improved in case of a near edge-on orbit ($\beta_{Earth} \approx 0^\circ$), and that for all degrees, the gravity field coefficients are better recovered from a near edge-on orbit than from a more face-on orbit ($\beta_{Earth} \approx 90^\circ$).

In conclusion, despite the reduced number of observations, a lower β_{Earth} improves the

quality of the estimated gravity field when using an appropriate Kaula constraint, as shown in Fig. 4.19. The shown geoid height differences are computed from gravity field solutions up to d/o 60, estimated using a Kaula constraint. One can note a small improvement of the overall quality of the recovered gravity field from an orbit with β_{Earth} slightly larger than $\beta_{Earth,c}$, with respect to β_{Earth} slightly smaller than $\beta_{Earth,c}$ (e.g., $\beta_{Earth} \in [66^\circ, 75^\circ]$ for $h = 135$ km), as soon as the line of sight with respect to Earth is not occulted. For $\beta_{Earth} \leq 75^\circ$, the weighted RMS of the geoid height differences $(\Delta g)_{WRMS}$ is at most 1.6 times larger in comparison to the case $\beta_{Earth} = 0^\circ$.

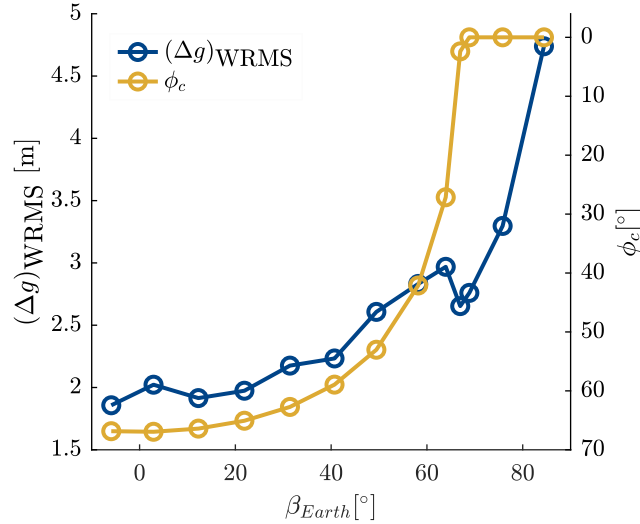


Figure 4.19: Weighted RMS of geoid height differences $(\Delta g)_{WRMS}$ of Kaula-constrained solutions (up to d/o 60) with respect to EURGLMo and half latitude band ϕ_c for which the probe is not observed on the far side of Europa as a function of β_{Earth} for 26:1023 RGTOs with $h = 135$ km and $i = 89^\circ$.

In a more general case, where β_{Earth} is not fixed, a combination of low β_{Earth} and β_{Earth} close to $\beta_{Earth,c}$ would be optimal to increase the precision of the recovered gravity field without relying on constraints to mitigate aliasing.

4.3.3 Altitude

We analyse the impact of the probe's altitude on gravity field recovery for 5: R RGTOs. For $m \geq 5$, the impact of ground track repetition on the studied m : R RGTO is negligible (see Sect. 4.3.1), i.e., these results are valid for any $m \geq 5$. We analyse orbit altitudes h between 100 km and 200 km. With an inclination $i = 89^\circ$ we fixed β_{Earth} to 69° , which is larger than $\beta_{Earth,c}$ for all considered altitudes (see Fig. 4.16), to avoid any aliasing due to ground coverage issues (see Sect. 4.3.2). We thus show only unconstrained solutions in this section.

Under these assumptions, the best gravity field solution can be obtained up to d/o 70 from a 5:202 RGTO, corresponding to an altitude of $h = 105$ km (Fig. 4.20a). For higher altitudes, i.e., lower values of R , high-degree gravity field coefficients cannot be properly estimated to the same extent. This behaviour is expected and a consequence of the spherical

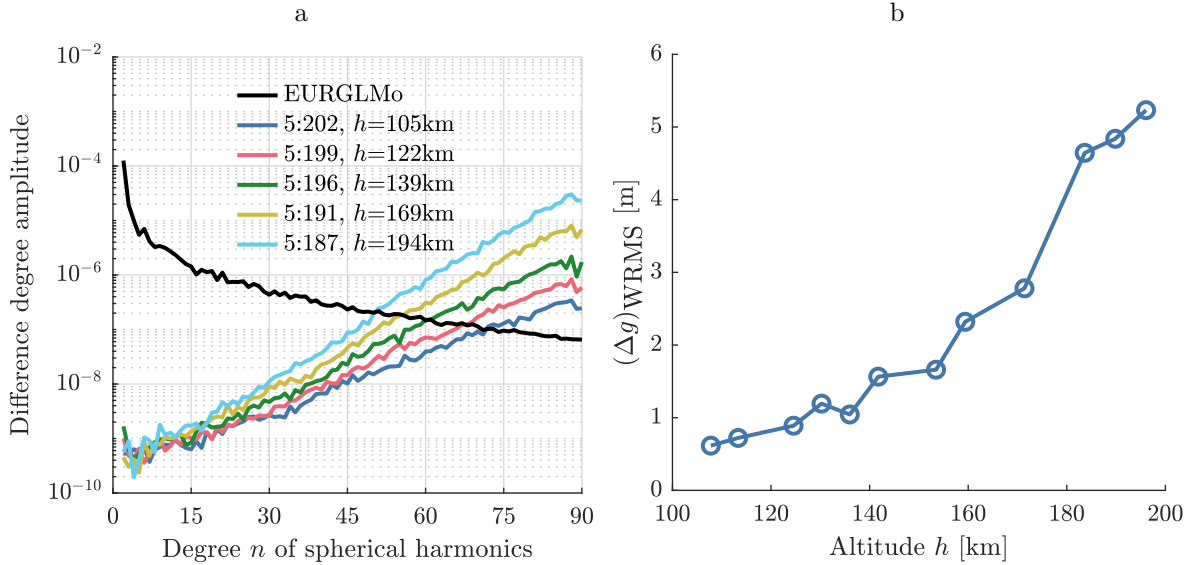


Figure 4.20: Europa gravity field solutions for orbits with different altitudes with $m=5$ and $\beta_{Earth} \approx 69^\circ$. Difference degree amplitudes (a) and weighted RMS of geoid height differences computed up to d/o 50 (b) with respect to the reference gravity field (EURGLMo).

harmonics decomposition given by Eq. (2.11): the coefficients of degree n are attenuated by a factor $\left(\frac{R_E}{r}\right)^n$. As a result, the higher the probe is, the less sensitive it is to the high degrees of the gravity field. For the same reason the impact of a higher altitude orbit is not the same for all degrees, e.g., for $R = 187$, at an altitude of $h = 194$ km, gravity field coefficients can only be estimated up to d/o 50.

Figure 4.20b illustrates the overall dependency of the gravity field quality with respect to the altitude of the orbit. Because β_{Earth} is not precisely 69° for all these tests, the weighted RMS is not rigorously monotonous. Indeed, as discussed in Sect. 4.3.2, the gravity field solution is very sensitive to β_{Earth} when the latter is close to $\beta_{Earth,c}$ (see Fig. 4.19). Nevertheless, the impact of β_{Earth} is minor at this scale, in comparison with the impact of altitude.

One should also note that stronger orbital perturbations from Europa's gravity field would be experienced from very low altitude orbits, e.g., 50 km altitude in case of the MAGIC mission proposal for Callisto (see Sect. 1.2.2). The number and magnitude of manoeuvres needed to maintain the orbit would instead be reduced with higher altitude orbits. As a consequence, from a mission point of view, a compromise has to be reached between the target resolution of the gravity field and what an acceptable number of manoeuvres is (which impacts the number of clean observations, and the total fuel consumption) to ensure a sufficient lifetime of the mission.

4.3.4 Inclination

As mentioned in Sect. 3.4.2, the choice of inclination impacts the variation of the β_{Earth} angle. For a mission mid-2031, a 89° -inclined orbit would enable a low variation of β_{Earth} .

This is very convenient in the frame of this study (as it allows to separate the impact of β_{Earth} from the impact of other parameters), but it is not imperative from a mission point of view. On the other hand, the variation of β_{Earth} of a probe on a 80° -inclined orbit would reach up to 60° in 3 months. A combination of several orbital plane configurations with respect to Earth would actually be beneficial to take advantage of both high and low values of β_{Earth} . As mentioned in Sect. 4.3.2, high values of β_{Earth} enable a denser coverage of Europa, while lower values of β_{Earth} would improve the estimation of the lower degrees of the gravity field.

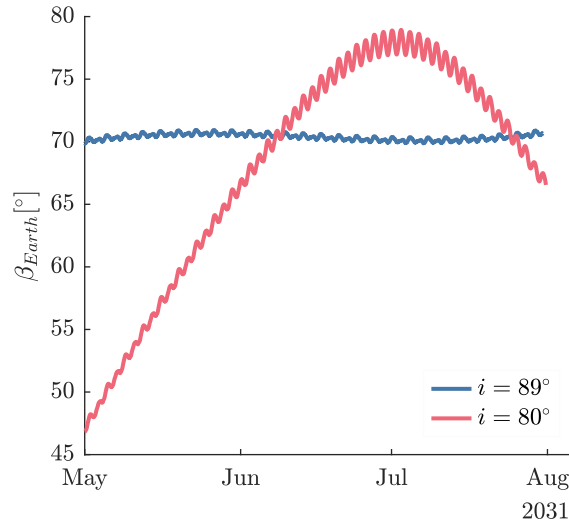


Figure 4.21: β_{Earth} angle variation over 3 months for a polar orbit around Europa, starting at $\beta_{Earth,0} = 70^\circ$, and for an 80° -inclined orbit, starting at $\beta_{Earth,0} = 47^\circ$.

We analyse two orbits, a polar orbit ($i = 89^\circ$), and an orbit with a 10° polar gap ($i = 80^\circ$). Variations of the β_{Earth} angle make a proper comparison of gravity field solutions recovered from the two differently inclined orbits a delicate matter. We decided to fix the mean value of β_{Earth} to 70° for these two orbits. In case of the polar orbit, we start with a β_{Earth} value of 70° and only have a small variation. In case of the 80° -inclined orbit, we start with $\beta_{Earth} = 47^\circ$ and observe a large variation (Fig. 4.21).

The consequence of a non-polar orbit is an unobserved set of latitudes, a “gap”, in the polar regions of the celestial body. The probe will then be less sensitive to the zonal and near-zonal gravity field coefficients [van Gelderen and Koop, 1997]. In terms of gravity field recovery, this means that the estimates of these coefficients will be degraded in comparison with the use of a polar orbit (Fig. 4.22). The impact on higher order gravity field coefficients is negligible. Some differences can also be seen in the near sectorials of high degrees, but this is a marginal effect due to the slightly lower altitude of the 5:196 non-polar RGTO with respect to the polar 5:197 RGTO.

4.3.5 Eclipses by Jupiter

The investigations in Sect. 4.3 have been so far performed without taking into account the eclipses of Jupiter, in order to assess the influence of each parameter as separately as

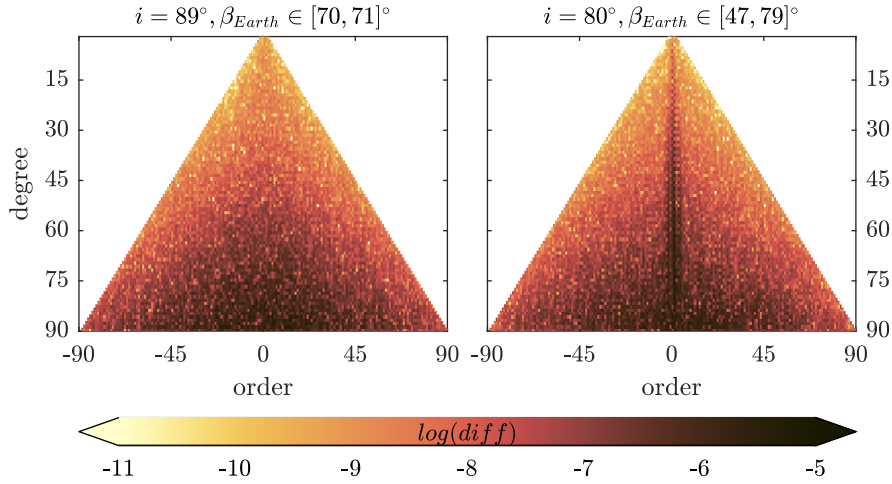


Figure 4.22: Differences with respect to EURGLMo of the Europa gravity field coefficients recovered from an 5:197 polar RGTO with $h = 134$ km (left) and from an 5:196 RGTO with a 10° polar gap and $h = 132$ km (right).

possible. However, as seen from Earth, Europa passes generally once per revolution behind Jupiter. As a result, a probe in a low altitude orbit around Europa cannot transmit to Earth for a short time, resulting in regular Doppler data gaps.

Moreover, because Europa is synchronously rotating, the missing data of consecutive orbits correspond to two unobserved small longitude bands on the surface, corresponding to the ascending and descending part of the orbit of the probe, i.e., approximately separated by 180° (see Fig. 4.23). If the orbit is near face-on, e.g., $\beta_{Earth} = 87^\circ$ in Fig. 4.23, the unobserved longitude band corresponding to the ascending part of the probe's orbit is covered by the descending part of the orbit half a Europa revolution later, when Europa is in front of Jupiter as seen from Earth, and vice-versa for the unobserved longitude band corresponding to the descending orbit. In the end, the two longitude bands corresponding to Jupiter's eclipses only have fewer associated Doppler observations.

However, for $\beta_{Earth} < \beta_{Earth,c}$, the probe is additionally passing behind Europa with respect to the Earth, as discussed in Sect. 4.3.2, resulting in an unobserved latitude band on either the ascending or descending part of the probe's orbit. As a result, some surface regions are not covered at all by Doppler data (see $\beta_{Earth} = 3^\circ$ and $\beta_{Earth} = 59^\circ$ in Fig. 4.23). This is of critical importance for a relatively short mission, for which the Earth-Jupiter-Europa configuration has not enough time to naturally evolve, and for low altitude probes.

Indeed, the gravity field recovered from orbits with $\beta_{Earth} = 3^\circ$ and $\beta_{Earth} = 59^\circ$ suffers from a significant aliasing (see Fig. 4.24a) due to the data gaps, similarly to RGTOs with high repetition (see Sect. 4.3.1), as soon as we try to recover a gravity field whose resolution is smaller than the coverage gap. However, unlike high repetition RGTOs, the gap is not evenly distributed along the equator, but very confined in a longitude range. This means that there is overall more information to exploit from this ground coverage,

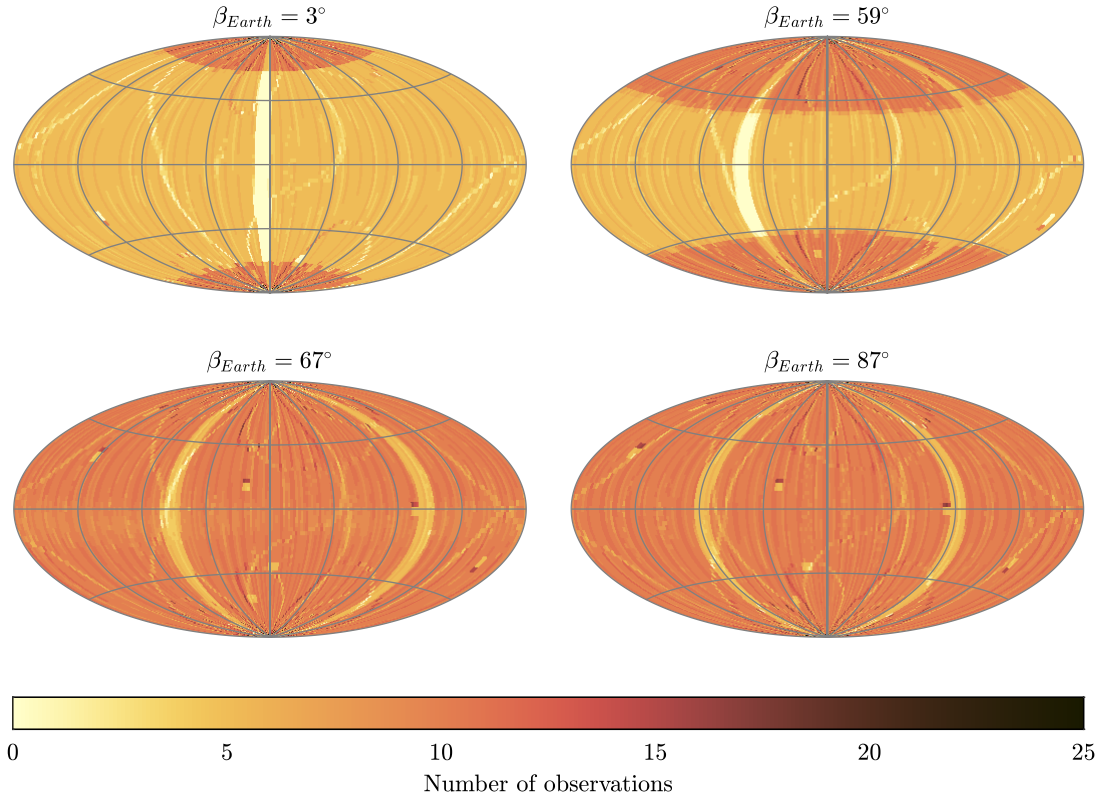


Figure 4.23: Ground coverage of Europa from a polar 5:197 RGTO with $h = 134$ km occulted by Europa and by Jupiter for 90 days, for different constant β_{Earth} . The 60 s-sampled Doppler observations are grouped in bins of 1.8° in longitude and 2.8° in latitude.

than from evenly distributed coverage gaps of same cumulative width.

One way to mitigate the effect of this coverage gap is to constrain the gravity field coefficients, e.g., considering a Kaula law (Eq. 4.8) to constrain each coefficient to zero based on its degree, similarly to Sect. 4.3.2. We also investigate constraining the coefficients order-wise, using

$$\sigma_K(m) = \frac{K}{m^\alpha}, \quad (4.10)$$

where m is the order of the associated gravity field coefficient. We found that for $\alpha = 1$, this law fitted well the order amplitude Δ_m of our reference gravity field.

In both cases, the scaling factor of the Kaula constraint is determined using Variance Component Estimation (see Sect. 2.3.3), leading to $K \approx 2.5$ for degree-wise Kaula constraint and $K \approx 0.002$ for order-wise Kaula constraint. Both approaches significantly reduce the aliasing for $\beta_{Earth} \leq \beta_{Earth,c} = 67^\circ$ with an order wise constraining allowing for the best solution (see Fig. 4.25). As in Sect. 4.3.2, we can say that β_{Earth} close to $\beta_{Earth,c}$ is optimal to obtain an unconstrained gravity field solution. However, contrary to Sect. 4.3.2, an excessively small β_{Earth} is not beneficial for the low degree gravity field coefficients, even when constrained by a Kaula law, as they are highly affected by an equatorial gap in the coverage.

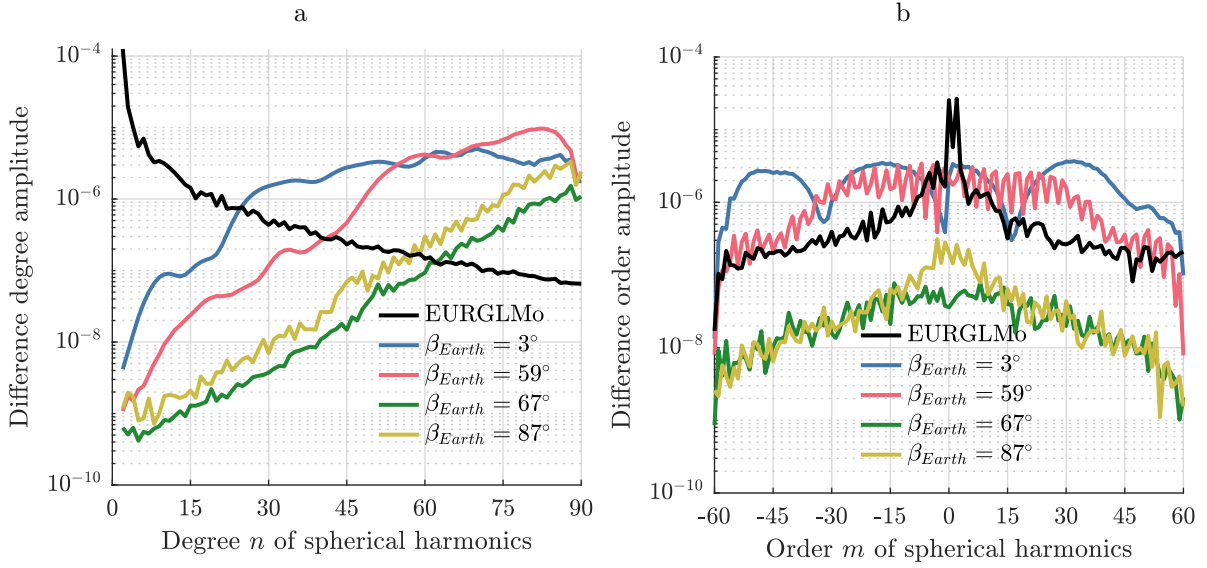


Figure 4.24: Difference degree amplitudes (a) and difference order amplitudes (degree ≤ 60) of unconstrained recovered gravity field solutions for 5:197 RGTO with different β_{Earth} angles, $h = 135$ km and $i = 89^\circ$.

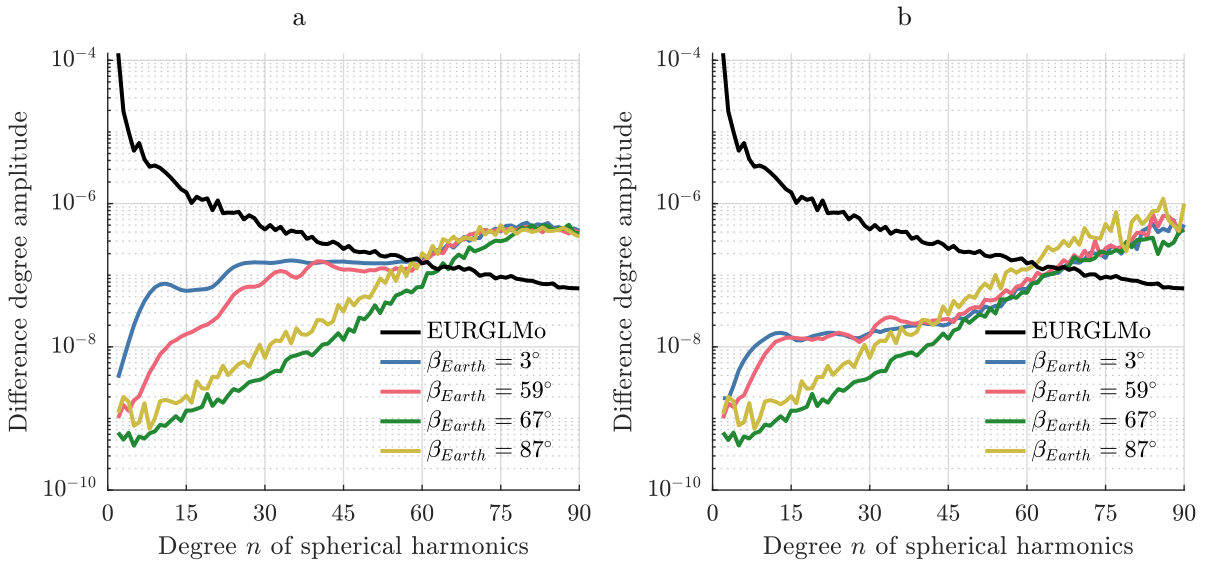


Figure 4.25: Difference degree amplitude of gravity field solutions for 5:197 RGTOs with $h = 135$ km, $i = 89^\circ$ and different β_{Earth} angles with (a) a degree-wise Kaula constraint ($K \approx 2.5$) and (b) an order-wise Kaula constraint ($K \approx 0.002$).

The eclipses of Callisto by Jupiter are rather rare compared to Europa, because of the non-zero inclination of Callisto's orbital plane with respect to the ecliptic, and especially because of the larger distance of Callisto with respect to Jupiter. For instance, we do not observe any eclipse in the three months considered in this work starting in 2031-05-01.

4.4 Estimation of rotation parameters

In the case of Callisto, we investigated the estimation of orientation and rotation parameters, as described in Sect. 2.4. We estimate a constant correction to the right ascension and declination of the north pole, parametrised by the coefficients α_0 and δ_0 . In addition, the rotation of Callisto is characterized by the location of the prime meridian and by its rate of change. The initial location at J2000 (2000-01-01, 12:00 TT) is fixed by the IAU working group [Archinal et al., 2018] and changing its value would translate in a rotation of our gravity field model. We thus estimated only time variable components, i.e., the rotation rate w_1 and the main longitudinal libration W_l . Since we only consider a 3 month mission, longer period variations of the orientation and rotation parameters are expected to be more challenging to estimate.

Table 4.4: Constraints σ , true errors Δ and formal errors f_{err} of rotation parameters estimated freely or using constraints determined empirically or via VCE.

| Constraining method | | $\alpha_0[^\circ]$ | $\delta_0[^\circ]$ | $w_1[^\circ/\text{day}]$ | $W_l[^\circ]$ |
|--|-----------------------------|--------------------|--------------------|--------------------------|---------------|
| No constraints | Δ ($\times 10^6$) | 68.5 | 1.09 | 0.028 | 0.696 |
| | f_{err} ($\times 10^6$) | 40.5 | 3.67 | 0.021 | 2.49 |
| Constraints of rotation parameters estimated using VCE | σ ($\times 10^6$) | 73.0 | 0.38 | 0.021 | 0.080 |
| | Δ ($\times 10^6$) | 57.9 | 0.026 | 0.012 | 0.001 |
| | f_{err} ($\times 10^6$) | 31.0 | 0.344 | 0.014 | 0.072 |
| VCE-derived constraints while not estimating w_1 | σ ($\times 10^6$) | 70.0 | 0.62 | - | 0.060 |
| | Δ ($\times 10^6$) | 55.2 | 0.071 | - | 0.001 |
| | f_{err} ($\times 10^6$) | 30.7 | 0.552 | - | 0.054 |
| VCE-derived constraints while fixing σ_{w_1} | σ ($\times 10^6$) | 70.0 | 0.60 | 0.005 | 0.061 |
| | Δ ($\times 10^6$) | 55.5 | 0.066 | 0.001 | 0.001 |
| | f_{err} ($\times 10^6$) | 30.7 | 0.537 | 0.005 | 0.055 |

We consider in this section a 5:731 RGTO around Callisto, with $i = 89^\circ$, $h = 200$ km, and $\beta_{Earth} = 72^\circ$, and we first freely estimate α_0 , δ_0 , w_1 , and W_l as global parameters together with the gravity field coefficients up to d/o 100, resulting in the true and formal errors presented in Tab. 4.4. We observe a high correlation of the rotation rate w_1 with non-zonal gravity field coefficients, especially for degrees larger than 3 (see Fig. 4.27 right). This results in a degradation of the low-degree gravity field coefficients in comparison to a solution for which the true rotation parameters were considered but not estimated (Fig. 4.26). The rotation rate w_1 is the most problematic parameter to estimate here. Indeed, when estimating only α_0 , δ_0 and W_l , the correlations between the gravity field coefficients are significantly reduced, although they are still moderately correlated with the orientation parameters (Fig. 4.27 left). Moreover, one can still see a high correlation between α_0 and δ_0 .

In order to reduce the correlations between the orientation and rotation parameters, we constrained them to their (true) a priori values. We used Variance Component Estimation to estimate constraints on all rotation and orientation parameters, which are given in

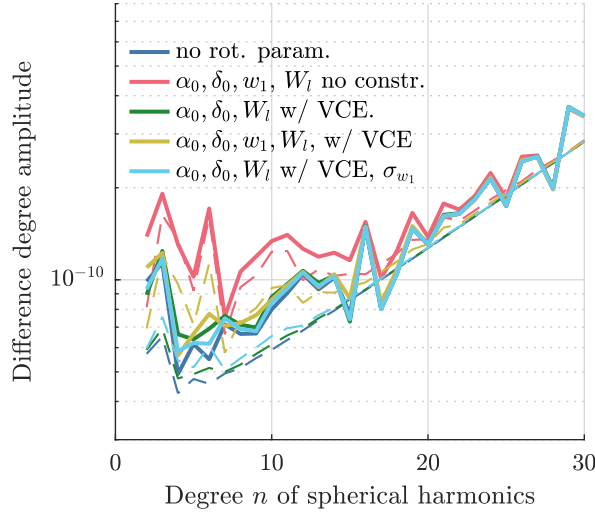


Figure 4.26: Difference (solid) and error (dashed) degree amplitude of Callisto gravity field solutions with respect to CALGMO, considering different constraints on rotation parameters.

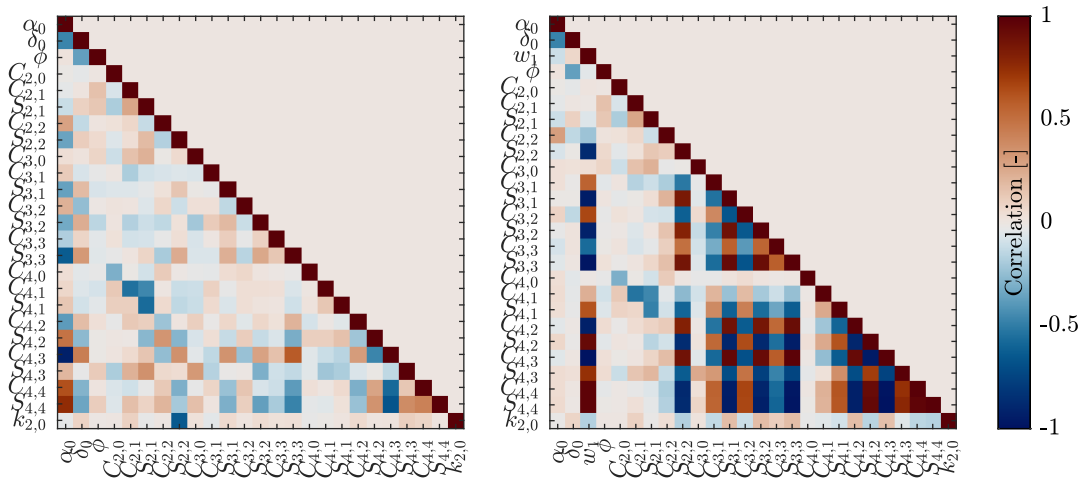


Figure 4.27: Correlations between the rotation parameters and the-low degree gravity field coefficients estimating all considered rotation parameters (right) and estimating all parameters but the rotation rate w_1 (left) in case of Callisto. All parameters are freely estimated.

Tab. 4.4. The formal errors of the estimated rotation parameters are significantly reduced, together with their true error. The formal errors are a bit larger than the true errors, except for α_0 . However, it is difficult to draw definitive conclusion from the true errors of a limited set of tests. The gravity field solution also improves with such constraints, as seen in Fig. 4.26. However, w_1 is still highly correlated with the gravity field coefficients (Fig. 4.28, left), because of the short mission duration. A VCE-derived constraint of $2.1 \times 10^{-8} \text{ }^\circ/\text{day}$ reduced the correlations in comparison to an unconstrained solution, but they are still large.

In absence of other types of measurement or a longer mission duration to improve the sensitivity to w_1 , we increase the constraint on w_1 to $5 \times 10^{-9} \text{ }^\circ/\text{day}$ and applied VCE to

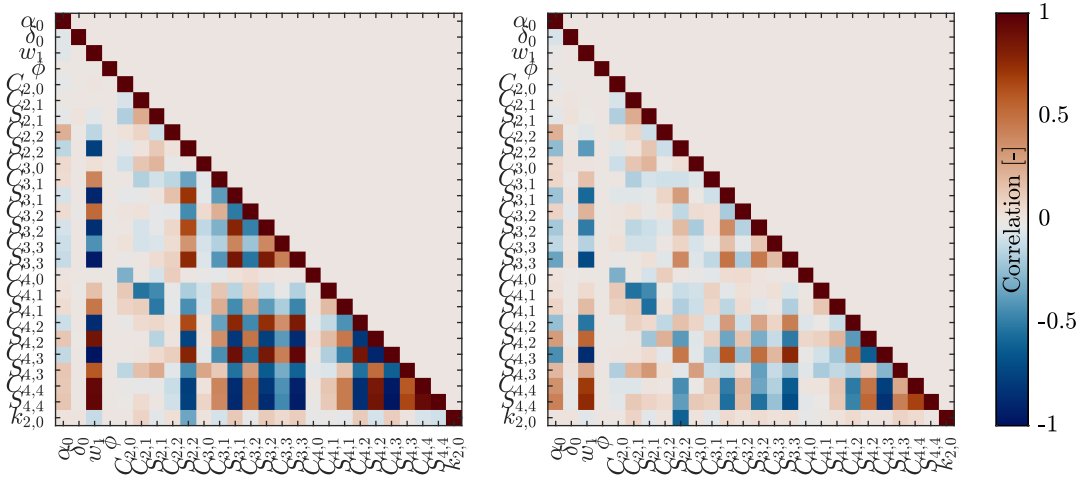


Figure 4.28: Correlations between the low-degree gravity field coefficients and the rotation parameters constrained using VCE for the constraints of all rotation parameters (left) or of all but the rotation rate w_1 (right) in case of Callisto.

determine the constraints on the other orientation and rotation parameters. The overall correlations are visibly reduced (Fig. 4.28, right), and the very low degrees of the gravity field are slightly improved (Fig. 4.26, light blue curve). With the exception of the declination of the north pole δ_0 , the formal errors of the rotation parameters are smaller when empirically constraining the rotation rate w_1 . The formal error of δ_0 is instead further reduced when using VCE to estimate all the constraints.

As discussed in Sect. 2.8.1, the MoI can be computed from degree-2 gravity field coefficients (Eq. 2.76), if we assume that Callisto is in hydrostatic equilibrium, or from the pole obliquity ϵ if we assume that Callisto is in a Cassini state (Eq. 2.83). We compute the uncertainty on ϵ from the uncertainties on the orientation of the north pole, i.e., on α_0 and δ_0 , assuming the orientation of the orbit pole is perfectly known. We compare in Tab. 4.5 the formal errors of the degree-2 gravity field coefficients and the rotation parameters we estimate with the formal uncertainties expected from JUICE with its 21 Callisto flybys, and foreseen by the MAGIC proposal with a 50 km orbiter extracted from covariance analyses in Genova et al. [2022]. First of all, we do not estimate the same set of parameters as in Genova et al. [2022]. We include in this work the estimation of the rotation rate w_1 and the main longitudinal libration W_1 . However, we have not considered the estimation of the tidal phase lag ϕ_{k_2} for the moment.

As expected, the benefit of a low altitude orbiter rather than a limited number of flybys is clear. In general, we observe comparable results to MAGIC [Genova et al., 2022] for the estimations presented in Tab. 4.5, if not better, despite the shorter mission (3 months compared to 1 year), and higher altitude orbiter (200 km compared to 50 km). These differences can be explained by our very conservative tracking schedule. Indeed, we consider Ka-band tracking from the 3 Chinese DSN ground stations, contrary to X-band tracking from only one DSN station. In addition, the estimation of the Love number k_2 yields formal uncertainties comparable to MAGIC.

Table 4.5: Formal uncertainties of the geophysical parameters of Callisto from JUICE and MAGIC simulations extracted from Genova et al. [2022] and completed with our results. J_2 and C_{22} refer to the unnormalised degree-2 gravity field coefficients.

| Geophysical parameter | Current knowledge | | JUICE | MAGIC | This work |
|------------------------------------|-------------------|-------------|--------------------|--------------------|--------------------|
| | Value | Uncertainty | | | |
| J_2 ($\times 10^{-7}$) | 327 | 8.0 | 1.5 | 0.002 | 0.002 |
| C_{22} ($\times 10^{-7}$) | 102 | 3.0 | 0.6 | 0.005 | 0.0003 |
| Mol determined with RDA | 0.3549 | - | 8×10^{-4} | 7×10^{-6} | 5×10^{-7} |
| α_0 [$^\circ$] | 268.72 | | 0.26 | 6×10^{-5} | 3×10^{-5} |
| δ_0 [$^\circ$] | 64.83 | | 0.08 | 7×10^{-5} | 5×10^{-7} |
| ϵ [$^\circ$] | -0.3 | | 0.1 | 6×10^{-5} | 7×10^{-4} |
| w_1 [$^\circ$ /day] | 21.57 | | - | - | 5×10^{-9} |
| W_l [$^\circ$] | 0 | | - | - | 6×10^{-8} |
| Mol determined with pole obliquity | - | | 0.07 | 4×10^{-5} | 2×10^{-3} |
| k_2 | | | 0.08 | 1×10^{-4} | 1×10^{-4} |
| ϕ_{k_2} [$^\circ$] | | | - | < 0.05 | - |

4.5 Mitigation strategies for non-gravitational accelerations: case of Callisto

The modelling of non-gravitational accelerations (NGA) is a critical and challenging component of orbit determination. In this work, we have not included them in our Europa analyses (Sects. 4.1, 4.2 and 4.3). For Callisto, considering solar and planetary radiation pressure as described in Sect. 2.2.4, the accelerations reach up to 10 nm/s^2 (see Fig. 4.29). However we assumed that these accelerations were perfectly modelled so far. In this section, we evaluate several ways to handle these non-gravitational accelerations over a 3 months mission with pseudo-stochastic pulses, realistic accelerometer data, or empirical accelerations.

For this, we consider a 5:731 RGTO with $h = 200 \text{ km}$ and $i = 89^\circ$ with different β_{Earth} and β_{Sun} angles, i.e., angles between the orbital plane and the Earth and the Sun directions, respectively. We investigated two scenarios: a near edge-on orbit with $\beta_{Earth} = 1.0^\circ \pm 4.2^\circ$ (and $\beta_{Sun} = -1.2^\circ \pm 4.2^\circ$), and a more face-on orbit, with no occultation by Callisto as seen from Earth ($\beta_{Earth} = 71.8^\circ \pm 4.7^\circ$) and no eclipses from the Sun ($\beta_{Sun} = -71.6^\circ \pm 3.6^\circ$). These two configurations yield different non-gravitational acceleration profiles, as the probe happens to be regularly in shadow in case of $\beta_{Sun} \approx -1^\circ$. Moreover, as discussed in Sect. 4.1.1, β_{Earth} also plays a significant role in the quality of the orbit recovered. For the Doppler data simulation we assumed continuous tracking of all three stations of the Chinese DSN.

As we will see in the following, the mitigation strategies that we consider here may require careful parameter constraining. Moreover, we studied how dependent some parameters are

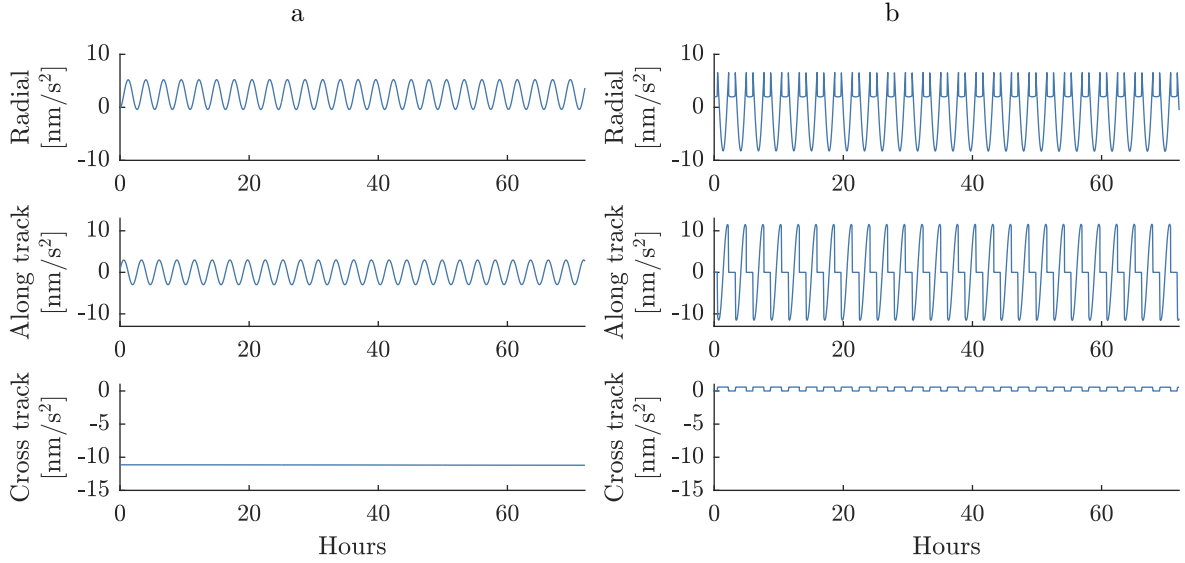


Figure 4.29: Non-gravitational accelerations in radial, along-track and cross-track direction for a 5:731 RGTO around Callisto with $h = 200$ km, $i = 89^\circ$ and with $\beta_{Sun} \approx -72^\circ$ (a) and $\beta_{Sun} \approx -1^\circ$ (b).

with respect to how long we consider them constant. For these reasons, we revised our processing scheme from Fig. 2.6 to Fig. 4.30. In particular, we restrict GRAVD2 to the orbit propagation and NEQ-setup, while we extensively use ADDNEQ2 to manipulate NEQs, apply VCE to estimate constraints on sets of parameters, and to compute solutions.

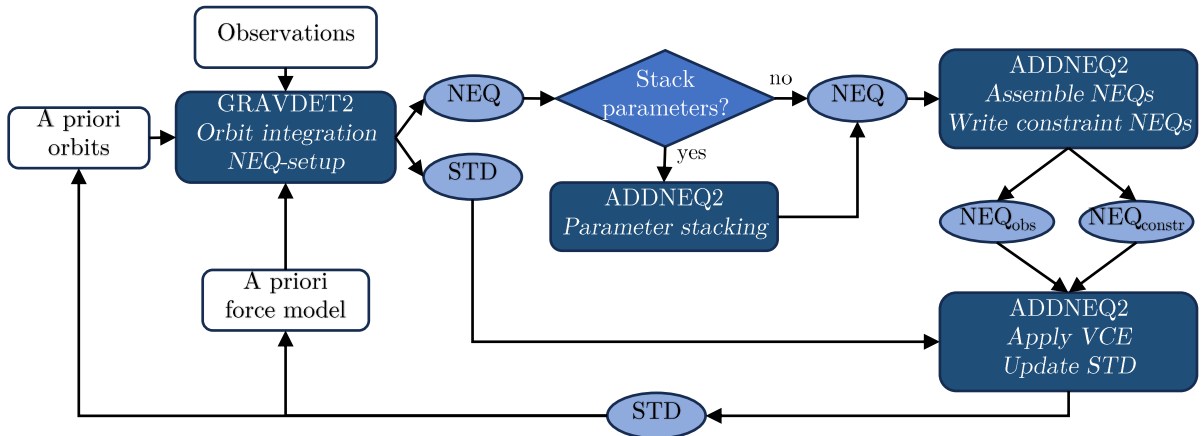


Figure 4.30: Orbit determination flowchart for non-gravitational acceleration handling.

4.5.1 Pseudo-stochastic pulses

As discussed in Sect. 2.2.5, pseudo-stochastic pulses (instantaneous velocity changes) can be used to absorb any mismodelling. In particular, we used them to empirically model non-gravitational accelerations, without any other means to model them. We set one pulse in

each direction (radial, along-track and cross-track) every 80 min, i.e., twice per orbit. However, pseudo-stochastic pulses have to be properly constrained. Indeed, if the constraints are too loose, the pulses may absorb more than the expected signal, leading for instance to a degradation of the orbit or gravity field solution. On the other hand, if the constraints are too tight, residual modelling errors might remain.

VCE allows to estimate constraints on collections of pulses, e.g., pulses contained within a given time interval. Constraints in different directions are estimated separately, and we vary the time span t_{const} on which we estimate these constraints, while continuing to estimate a set of orbital elements every $t_{arc} \approx 25$ h arcs. We evaluate the VCE-derived constraints on 25 h to 400 h intervals corresponding to 18 and 301 pulses in each direction, respectively (see Fig. 4.31). In average, for a 5:731 RGTO with $h = 200$ km, $i = 89^\circ$ and $\beta_{Earth} \approx 72^\circ$, the VCE-determined constraints are $20 \mu\text{m s}^{-1}$ in radial, $11 \mu\text{m s}^{-1}$ in along-track, and $5 \mu\text{m s}^{-1}$ in cross-track direction. However, the constraints vary significantly from one arc to the other, when they are estimated in ~ 25 h arcs and in ~ 50 h arcs. Constraints estimated on arcs longer than 100 h are more stable, as expected from the larger number of parameter per VCE-derived constraint. For $\beta_{Earth} \approx 1^\circ$, constraints are also more stable when applying VCE on longer time spans, with average constraints of $34 \mu\text{m s}^{-1}$ in radial, $25 \mu\text{m s}^{-1}$ in along-track, and 3mm s^{-1} in cross-track direction.

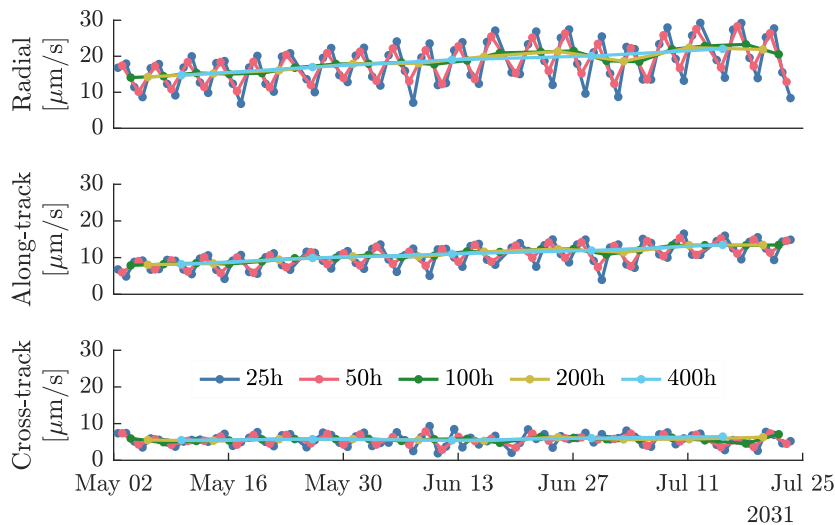


Figure 4.31: Pulses constraints estimated on different time spans t_{const} using VCE for $\beta_{Earth} \approx 72^\circ$.

As shown in Fig. 4.32, the orbit accuracy slightly improves when considering longer time spans to estimate constraints on the pulses (see blue and green curves for $t_{arc} = 25$ h), suggesting that VCE-derived constraints are more beneficial when estimated on long enough time spans. However, this improvement is less significant than the improvement related to considering longer arcs to estimate orbital elements (see magenta and yellow curves for $t_{arc} = t_{const}$), similarly to what was discussed in Sect. 4.1.2. Contrary to Fig. 4.5b, the orbit accuracy of a near edge-on orbit is significantly worse than for $\beta_{Earth} \approx 72^\circ$. This may be due the different non-gravitational accelerations profiles (Fig. 4.29). A shorter spacing

of the pulses might be able to account for higher frequency changes in these acceleration, at the expense of a larger number of parameters and a higher computational load and higher correlations with low gravity field coefficients (see Sect. 4.5.4). On the other hand, we also saw in Sect. 4.1.1 that a larger β_{Earth} decreases correlations between the orbital elements (see also Fig. 4.4). In case of unaccounted force model mismodelling, this might be more critical than in Sect. 4.1, where non-gravitational accelerations were considered.

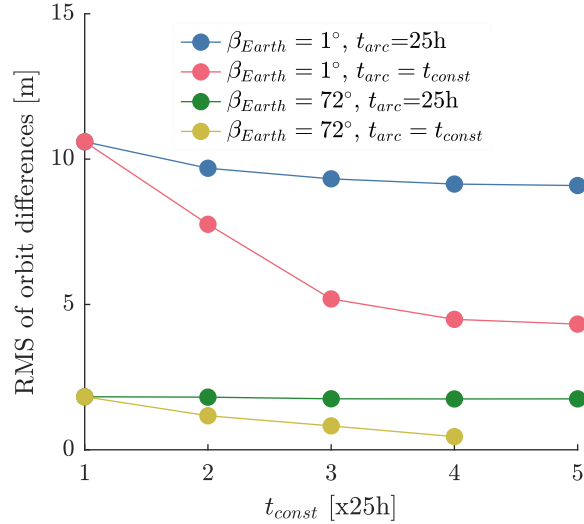


Figure 4.32: RMS of orbit differences for $\beta_{Earth} \approx 72^\circ$ and $\beta_{Earth} \approx 1^\circ$, estimating constraints using VCE on several time spans t_{const} , and several arc lengths t_{arc} .

In practice, one could still use an approximate model for non-gravitational accelerations (Sect. 2.2.4), and pseudo-stochastic pulses would rather be used to absorb residual mismodellings. Additionally, pulses are often complemented by more “physical” empirical accelerations, such as the ones discussed in Sect. 4.5.3.

4.5.2 On-board accelerometer

An accelerometer on board of the probe measures the non-gravitational accelerations acting on the probe and would in principle solve most issues from Sect. 4.5.1. However, errors on these measurements (Eq 2.53) also need to be accounted for. As discussed in Sect. 2.5, we simulated realistic accelerometer measurements with a scale factor $\lambda = 1$, a Gaussian white noise ε of standard deviation $\sigma = 10 \text{ nm/s}^2$ in all three directions, and constant biases over the entire mission. We considered equal biases in radial, along-track and cross-track direction, with a magnitude of 42 nm/s^2 .

In this work, we only addressed the estimation of accelerometer biases, and discarded the study of the accelerometer scale factor. In the reconstruction, we did not assume any a priori knowledge on the biases, and considered a zero a priori value. The estimation of biases proved to be very sensitive to the duration on which we consider them constant, but also to the constraint applied on these parameters. We thus investigated the stability of our solution depending on the bias validity time span, and estimated variance components

of global constraints in radial, along-track and cross-track directions. We considered here again two cases, a 5:731 RGTO with $h = 200$ km, $i = 89^\circ$ and either $\beta_{Earth} = 72^\circ$ or $\beta_{Earth} = 1^\circ$. For different arc lengths t_{arc} , we stacked the biases on 1 to 5 arcs, resulting in biases estimated on arcs lasting from 25 h to 400 h. For each case, we compute the RMS of the estimation errors for the entire mission duration, separately in each direction (Fig. 4.33).

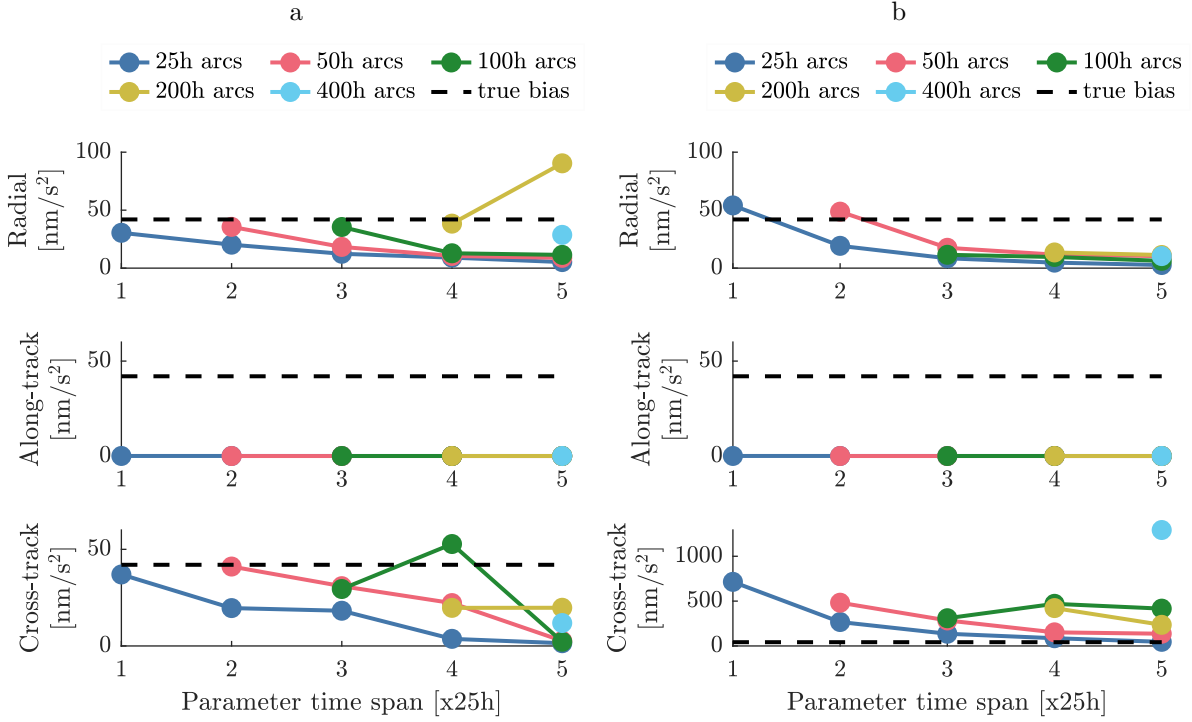


Figure 4.33: RMS error of estimated accelerometer biases and true biases (dashed line) for $\beta_{Earth} = 72^\circ$ (a) and $\beta_{Earth} = 1^\circ$ (b) for a 5:731 RGTO with $h = 200$ km and $i = 89^\circ$.

Biases in along-track direction are in all cases well estimated with errors below 1 nm/s^2 and constraining is in principle not necessary. We also get that, in general, stacking biases on several arcs with a fixed arc length, improves their estimation. This may be less visible in case of arcs longer than ~ 100 h, but this is likely because of the error representation in Fig. 4.33. Indeed, we estimate only 5 biases per direction when estimating them every ~ 400 h, as opposed to 80 biases per direction when estimating them every ~ 25 h. Computing the RMS error of the estimated biases is then less representative in terms of statistics for long arcs (see, e.g., radial biases in Fig. 4.33a).

However, in the case of $\beta_{Earth} = 72^\circ$, increasing the arc length does not improve the radial bias, when estimating one set of orbital elements and one different set of biases for each arc. Indeed, radial biases are highly correlated to the semi-major axis, and stacking biases on longer time spans than the estimation arc helps reducing correlations. This correlation can be also reduced by a tighter constraint on the radial bias. Estimates based on shorter arcs are also beneficial for the cross-track biases (see Fig. 4.33), leading to a more accurate orbit (see Fig. 4.34). Nevertheless, stacking biases does not significantly improve the orbits.

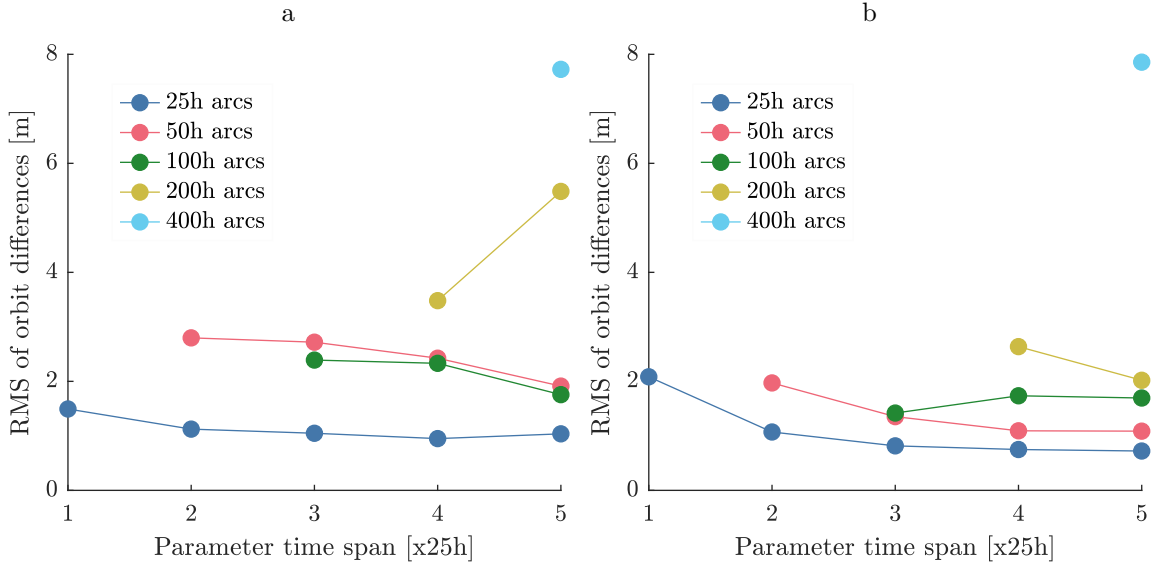


Figure 4.34: RMS error of orbit differences for $\beta_{Earth} = 72^\circ$ (a) and $\beta_{Earth} = 1^\circ$ (b) for a 5:731 RGTO with $h = 200$ km and $i = 89^\circ$, when estimating accelerometer biases.

In case of a near edge-on orbit ($\beta_{Earth} = 1^\circ$), the estimation of cross-track biases (Fig. 4.33b) is more challenging. Indeed, in this configuration the cross-track component of the orbit is weakly determined (see Sect. 4.1.1). As a result, the estimated bias errors can be several orders of magnitude larger than the true bias. However, these errors do not lead to significantly larger orbit errors (see Fig. 4.34b).

4.5.3 Empirical accelerations

In our study, we considered a cannonball for the spacecraft model, and a uniform albedo for Callisto (see Sect. 2.2.4), therefore Planetary Radiation Pressure (PRP) is a sinusoidal function with an offset (see, e.g., the radial and along-track components in Fig. 4.29a). Similarly, Solar Radiation Pressure (SRP) can be approximated by a piecewise constant function, equal to zero when the spacecraft is in the shadow of Callisto (see, e.g., Fig. 4.29b in cross-track direction).

Empirical parameters such as constant and once-per-revolution accelerations are particularly appropriate to model non-gravitational accelerations considered in this study. We thus considered once-per-revolution accelerations (cosines \mathbf{c}_1 and sines \mathbf{s}_1) and biases \mathbf{b}_0 in radial, along-track and cross-track direction to absorb the non-gravitational accelerations, leading to 3 empirical parameters per axis (see Sect. 2.2.5). In order to assess the estimated values of these parameters, we fitted directly the true acceleration signal with the same parameters (see Eq 2.25), and summarized the values of the bias magnitudes \mathbf{b}_0 and the amplitudes of the once-per-revolution accelerations ($\sqrt{\mathbf{c}_1^2 + \mathbf{s}_1^2}$) in Tab. 4.6 for $\beta_{Earth} = 72^\circ$ and $\beta_{Earth} = 1^\circ$.

Then, similarly to Sect. 4.5.2, we estimated the empirical accelerations for each estimation

Table 4.6: Empirical parameters fitting the true non-gravitational accelerations.

| | | Radial [nm/s ²] | Along-track [nm/s ²] | Cross-track [nm/s ²] |
|----------------------------|---------------|--------------------------------|-------------------------------------|-------------------------------------|
| $\beta_{Earth} = 72^\circ$ | Bias acc. | 2.4 | 0.0 | -11.2 |
| | Once-Per-Rev. | 2.7 | 2.9 | 0.0 |
| $\beta_{Earth} = 1^\circ$ | Bias acc. | -0.9 | 0.0 | 0.4 |
| | Once-Per-Rev. | 5.1 | 8.3 | 0.3 |

arc (from ~ 25 h to ~ 400 h) or stacking them for several arcs, while estimating six global constraints using VCE (one per direction and per parameter type). The RMS of the estimated parameters deviations with respect to the values from Tab. 4.6 are given in Fig. 4.35 for $\beta_{Earth} = 72^\circ$ and in Fig. 4.36 for $\beta_{Earth} = 1^\circ$. Here again, the biases in the along-track direction are very well estimated. However, the estimation of the radial biases is more challenging, whatever the arc length, because of the high correlation with the semi-major axis. The expected magnitude of the radial biases is at least 20 times smaller than the biases considered for the accelerometer in Sect. 4.5.2, which we were able to estimate, e.g., by stacking them on several estimation arcs. In conclusion, it seems that using only Doppler observations, in the analysed cases we cannot resolve biases lower than a few nm/s² in radial direction.

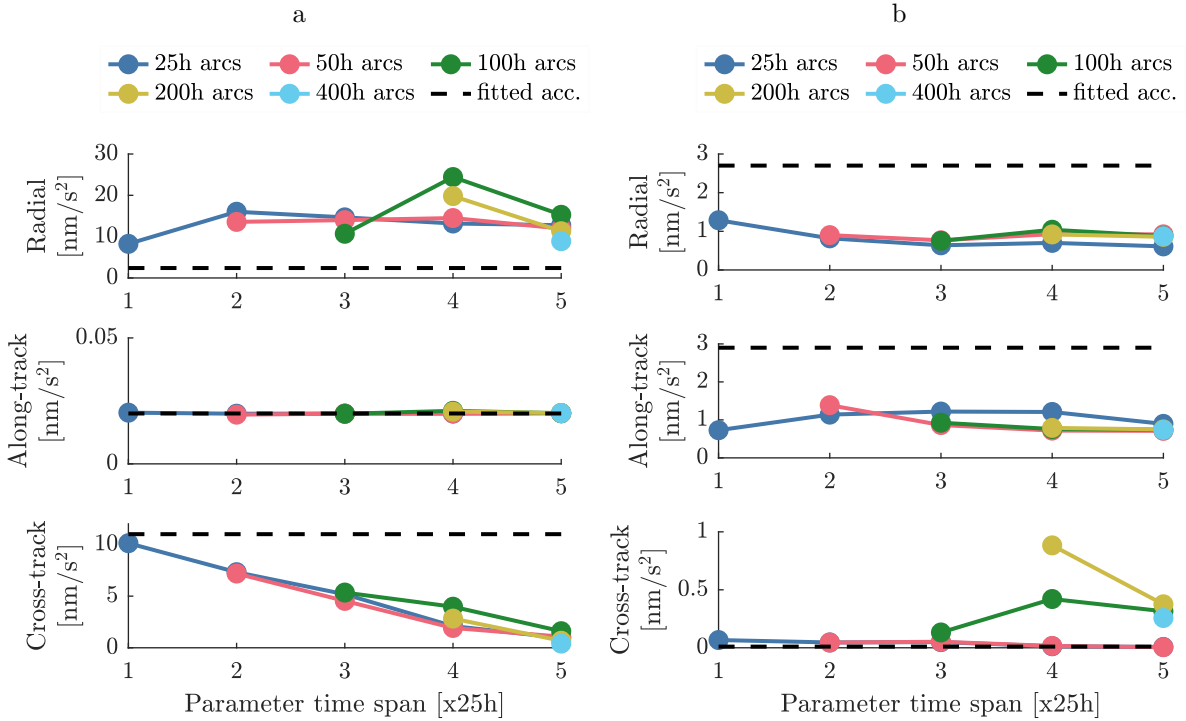


Figure 4.35: RMS error of estimated biases (a) and once-per-revolution amplitude (b) for $\beta_{Earth} = 72^\circ$ for a 5:731 RGTO with $h = 200$ km and $i = 89^\circ$.

Although the amplitude of the radial and along-track once-per-revolution accelerations are

also a few nm/s^2 , they can be reliably estimated since they do not correlate significantly with other orbital elements. The arc length and the number of stacked arcs do not seem to significantly influence their estimation error.

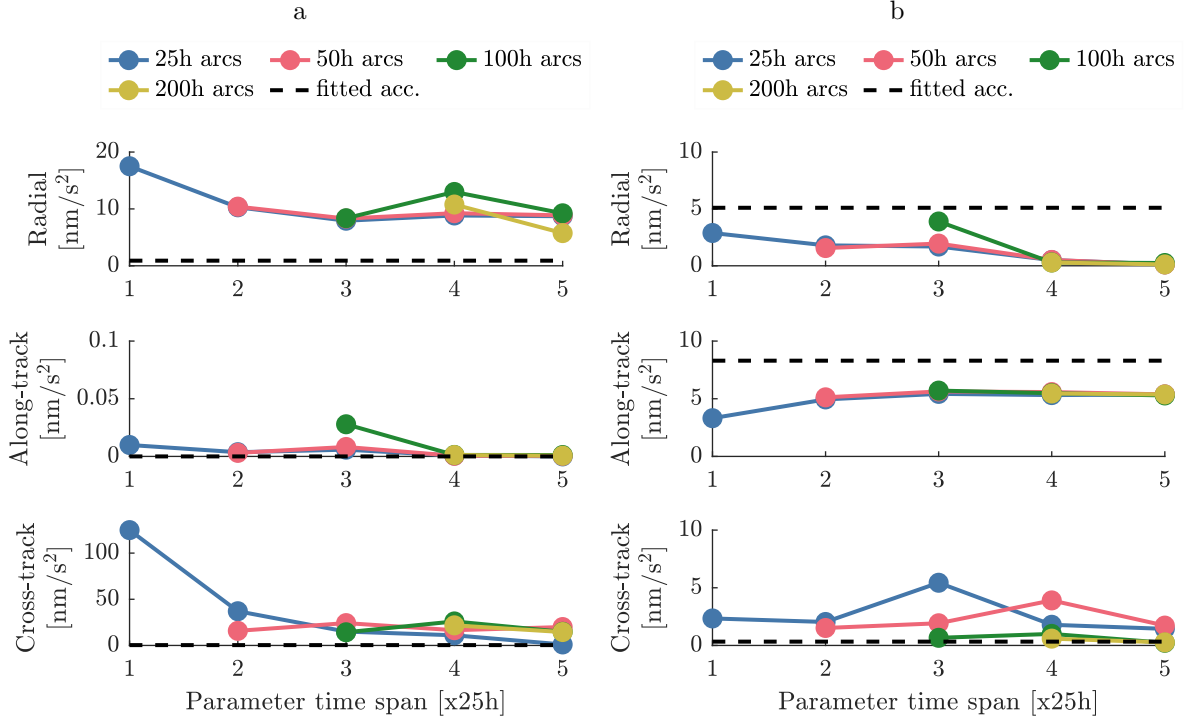


Figure 4.36: RMS error of estimated biases (a) and once-per-revolution amplitude (b) $\beta_{Earth} = 1^\circ$ for a 5:731 RGTO with $h = 200 \text{ km}$ and $i = 89^\circ$.

As discussed in Sect. 4.5.2, the cross-track components of the empirical acceleration are not well estimated for $\beta_{Earth} = 1^\circ$. However, since the magnitudes of these accelerations are relatively small in this configuration ($\beta_{Sun} \approx -1^\circ$), the impact on the orbit quality is not significant (see Fig. 4.37b), which might not be the case for larger non-gravitational acceleration in cross-track direction (e.g., for larger β_{Sun} , but still with an edge-on orbit). In the case of $\beta_{Earth} = 72^\circ$, the estimation of the cross-track biases is less problematic, and the estimation error is unambiguously reduced when increasing the arc length, or when stacking the biases over several arcs (see Fig. 4.35a). Although the estimation of the amplitude of the cross-track once-per-revolution accelerations appears to have larger errors for estimation arcs longer than 100 h, the expected value is below $1 \text{ nm}/\text{s}^2$, about the same level of error as in the other directions (Fig. 4.35b).

The general orbit accuracy is better than when using pseudo-stochastic pulses (Sect. 4.5.1) which is expected, as pulses do not physically represent the signal to be absorbed. Here again, the orbit differences generally get smaller when considering longer estimation arcs, as already discussed in Sect. 4.1.2. There is a significant improvement when stacking 2 arcs of 25 h with respect to estimating only one set of empirical parameters per arc. Other than that, there is no significant improvement when only stacking empirical parameters for several arcs without increasing the length of the estimation arc.

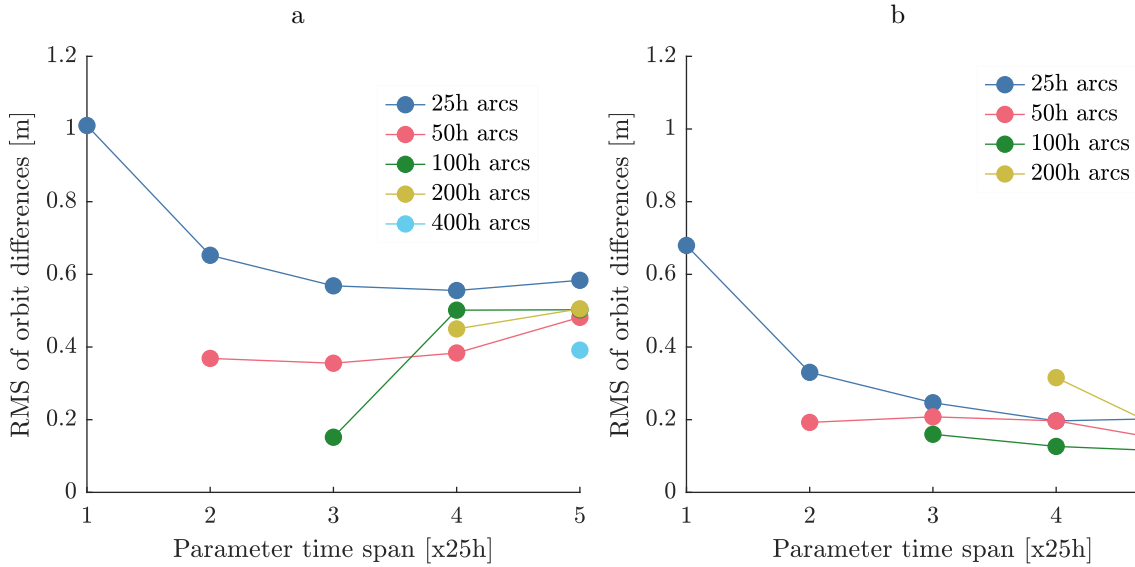


Figure 4.37: RMS error of orbit differences for $\beta_{Earth} = 72^\circ$ (a) and $\beta_{Earth} = 1^\circ$ (b) for a 5:731 RGTO with $h = 200$ km and $i = 89^\circ$, when estimating empirical accelerations.

The orbit differences are also smaller with respect to our investigation when considering an on-board accelerometer (Sect. 4.5.2). However, it is necessary to put in perspective this conclusion. The non-gravitational accelerations we considered are relatively small, of the same order of magnitude as the considered accelerometer white noise. Additionally, our simulated non-gravitational accelerations are relatively simple, which is why they can be efficiently absorbed by a few empirical parameters. In case of larger accelerations, e.g., fuel sloshing, an accelerometer would be more relevant [see *e.g.*, Cappuccio and Cascioli, 2018]. Additionally, an actual spacecraft would likely be very different from a simple cannonball model. The difficulty to model such a satellite, e.g., using an appropriate macro-model and attitude law, would result in non-gravitational accelerations more challenging to model by simple empirical parameters.

4.5.4 Comparison and impact on gravity field recovery

In this section, we compare the three different approaches we considered in this work to mitigate the impact of mismodelled non-gravitational accelerations. We estimate one set of orbital elements every ~ 25 h arcs for ~ 83 days. As discussed in the previous sections, stacking constant accelerations (accelerometer biases in Sect. 4.5.2 and empirical bias accelerations in Sect. 4.5.3) significantly improved their estimation, which results in improved orbits. However, stacking these parameters on long time spans may not be possible in practice because of manoeuvres, as already mentioned in Sect. 4.1.2. We thus stack accelerometer biases and empirical parameters on two arcs, so that we estimate them every ~ 50 h, already visibly improving the orbit (see Figs. 4.34 and 4.37). Additionally, we estimate one global constraint on each parameter type, in RSW using VCE, and after 7 iterations, we plot the orbit differences in Fig. 4.38.

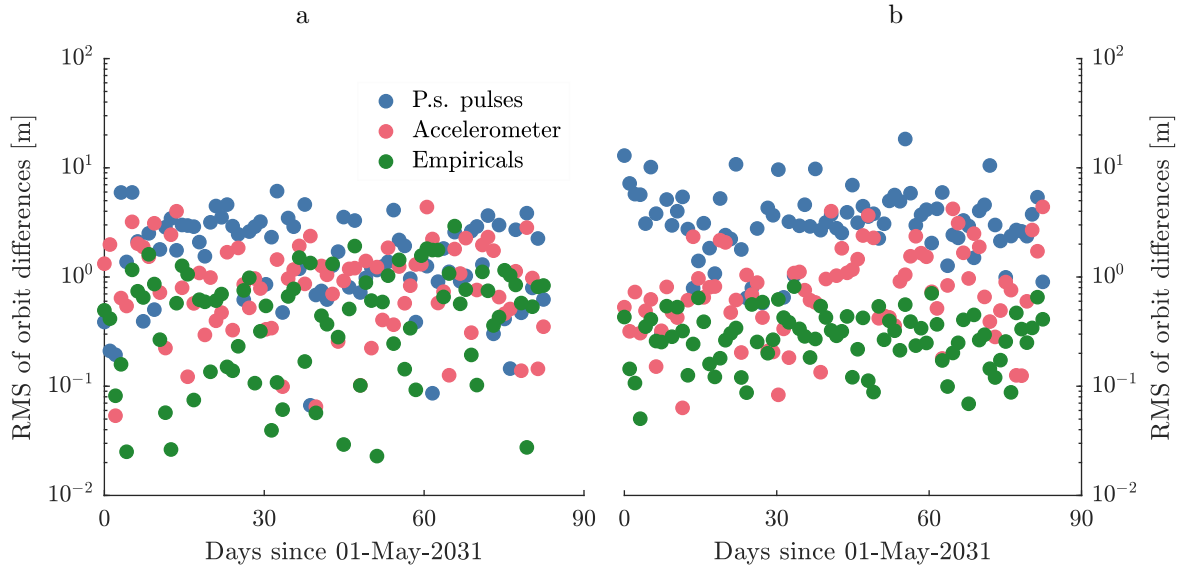


Figure 4.38: RMS of orbit differences of each arc with $t_{arc} = 25$ h for $\beta_{Earth} = 1^\circ$ and $\beta_{Sun} \approx -1^\circ$ (a) and for $\beta_{Earth} = 72^\circ$ and $\beta_{Sun} \approx -72^\circ$ (b) considering pseudo-stochastic pulses every 80 min, accelerometer measurements with 50 h biases or empirical parameters with 50 h biases and once-per-revolution accelerations.

The orbits fitted using pseudo-stochastic pulses are generally worse irrespective of whether $\beta_{Earth} = 1^\circ$ or $\beta_{Earth} = 72^\circ$. Indeed, pulses are less representative of the physical signal to absorb, in comparison to accelerometer biases for realistic accelerometer measurements, and to empirical parameters for simple non-gravitational accelerations. The difference is more pronounced in case of $\beta_{Earth} = 72^\circ$. First, the orbits fitted with pulses are slightly worse for a larger β_{Earth} , but the the orbits fitted following the two other strategies are visibly better. Indeed, the empirical parameters chosen to model the non-gravitational parameters are more adequate when the probe remains illuminated by the Sun and is never in the shadow of Callisto. The non-gravitational accelerations then result in a constant acceleration and a sinusoid (see Fig. 4.29), leading to reduced orbit differences in average. However, a higher sampling of the pulses may further improve the orbit, and also help to absorb other model deficiencies. This would come at the price of more parameters, and it is an interesting topic for future investigations.

Each strategy discussed in this section was found to efficiently improve the orbit in case of mismodelled non-gravitational accelerations. We now investigate how each of them affects the estimation of a full d/o 100 gravity field in a subsequent iteration in addition to the previously discussed parameters, for which we continue to estimate constraints using VCE. The strategies differ from each other mainly in the low degrees of the unconstrained gravity field parameters (see Fig. 4.39). The accelerometer performs similarly to the empirical modelling, and even slightly better in case of $\beta_{Earth} = 72^\circ$, for which the pseudo-stochastic pulses give only a slightly worse solution.

However, in the near edge-on case ($\beta_{Earth} = 1^\circ$), the pseudo-stochastic pulses significantly

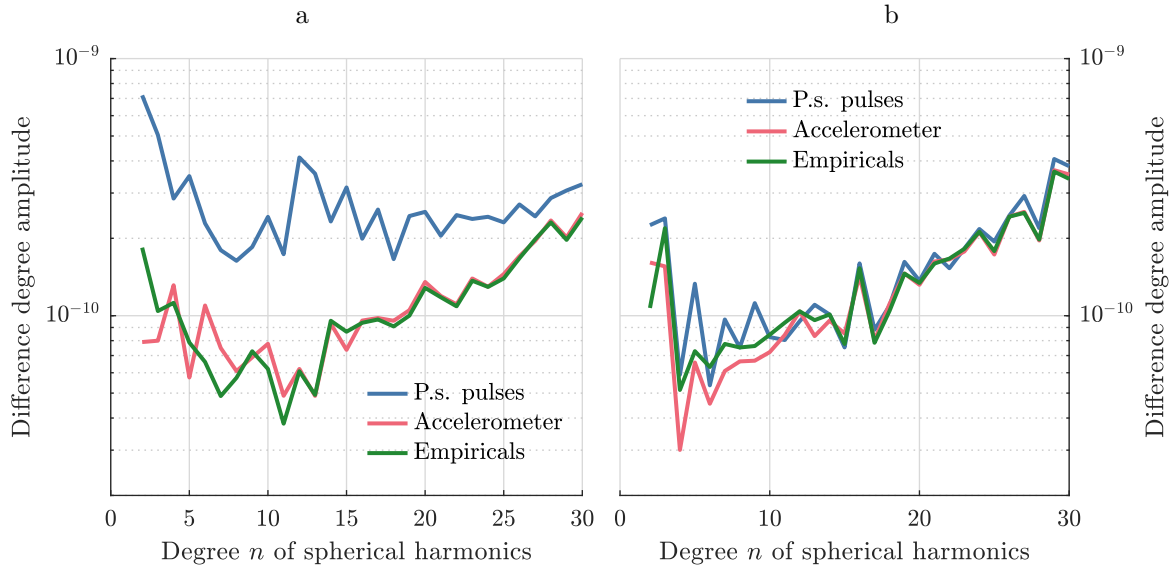


Figure 4.39: Difference degree amplitude of Callisto gravity field solutions with respect to CALGMO with $t_{arc} = 25$ h for $\beta_{Earth} = 1^\circ$ (a) and $\beta_{Earth} = 72^\circ$ (b) considering pseudo stochastic pulses every 80 min, accelerometer measurements with 50 h biases or empirical parameters with 50 h biases and once-per-revolution accelerations.

deteriorate the gravity field solution as they seem to absorb the gravity field signal. This can be due to unobserved pulses when the probe is located behind Callisto with respect to Earth. One solution would be to remove these pulses, or to apply a tight constraint to them. However, the non-gravitational acceleration would not be properly mitigated without a higher sampling of the pulses. Another solution may be to consider a uneven distribution of pulses, making sure that all pulses are observed.

Chapter 5

Combination of altimetry crossover and Doppler observables

In Chapter 4, we studied the orbit determination of a probe around a celestial body, Callisto or Europa, using Doppler observables only. We highlighted several challenges inherent to this type of observations, such as in the orbit deficiencies and the necessity to establish a link between the spacecraft’s antenna and a ground station on Earth to collect observations. This link is indeed subject to the availability of the station and to the absence of line-of-sight occultations. In this chapter, we discuss the advantages of an on-board laser altimeter which would have the benefit of providing observations regardless of these conditions. Its observations are still subject to other limitations such as pointing accuracy and power budget. In particular, we focus on the use of altimeter ranges in the form of crossovers (see Sect. 2.7.2), which may be seen in simplified terms as an observation of the spacecraft’s radial position in the generalised orbit determination process [Shum et al., 1990].

Altimetry crossovers have already been used in the framework of planetary orbiters such as Mars Global Surveyor [MGS; Rowlands et al., 1999, Neumann et al., 2001], Lunar Reconnaissance Orbiter [LRO; Rowlands et al., 2009, Mazarico et al., 2012, 2018], and Kaguya [Goossens et al., 2011], for which the crossover formulation is described in Rowlands et al. [1999]. Each track is projected on a sloped terrain and fitted using three-dimensional polynomials. The computed distance between the polynomials corresponding to two intersecting ground tracks is thus the quantity to minimise, providing sensitivity to directions other than the radial one [Goossens et al., 2011].

The inclusion of altimetry crossovers in the orbit determination of MGS allowed to improve the spacecraft trajectory and attitude [Rowlands et al., 1999, Neumann et al., 2001], but also the low-degree gravity field coefficients of Mars [Lemoine et al., 2001]. For LRO, the five distinct altimetry tracks from the multibeam altimeter allowed to significantly increase the number of crossovers [Rowlands et al., 2009], which resulted in an improved orbit during the first mission phases [Mazarico et al., 2012], and improved solutions for the lunar tides and gravity field [Mazarico et al., 2014]. However, Mazarico et al. [2018] did not include the crossovers for the orbit determination of LRO, as the improved gravity field model from GRAIL and the better-than-expected accuracy of the radio tracking lowered

the presumed benefit of crossovers with respect to the high computational effort needed to include them. Finally, the higher-altitude Kaguya orbiter benefited from the inclusion of crossover in the orbit determination procedure [Goossens et al., 2011].

Previous simulation studies combining altimetry crossovers and Doppler observations combination for planetary orbiters have been carried out by, e.g., Marabucci [2013], HosseiniArani [2020] for BepiColombo around Mercury, and by Villamil et al. [2021] for JUICE around Ganymede. Marabucci [2013] concluded that because of the high accuracy of the radio tracking of BepiColombo, the inclusion of altimetry crossover does not improve the orbit enough to justify the increase of computational complexity inherent to this observation type. On the other hand, Villamil et al. [2021] showed significant orbit improvements thanks to the inclusion of altimetry crossovers, especially when the probe’s line-of-sight is occulted from Earth (by Jupiter or by the Sun), or when the orbital plane is close to perpendicular to the Earth direction ($\beta_{Earth} = 90^\circ$). Moreover, they found that tidal Love number k_2 and the low degrees of Ganymede’s gravity field benefit from the inclusion of crossovers, and so does the estimation of accelerometer biases.

In this chapter, we investigate the benefits of a combination of altimetry crossovers and Doppler observables in terms of orbit determination and of geodetic parameters recovery, considering a 5:731 RGTO around Callisto, with an altitude $h = 200$ km, an orbital period of 2h45min, and an inclination $i = 89^\circ$, for 5 Callisto days (i.e., 83 days). We assume that the probe is tracked only by the Jiamusi ground station of the Chinese DSN, in X-band. As discussed in Sect. 4.1.3, this station tracking schedule is not very favourable, with at maximum 6 h/day availability. We analyse three different orbit configurations. The first orbit is nearly edge-on with $\beta_{Earth} = 1.0^\circ \pm 4.2^\circ$. In such a configuration, the probe is passing regularly behind Callisto with respect to Earth, which prevents the probe to be directly tracked by ground stations on Earth (see Sect. 4.3.2). In the two other scenarios the probe is never occulted by Callisto as seen from Earth with $\beta_{Earth} \gtrsim 67^\circ$. The second scenario’s orbit is at the limit, with $\beta_{Earth} = 71.8^\circ \pm 4.7^\circ$, while in the last scenario we have $\beta_{Earth} = 84.0^\circ \pm 2.6^\circ$, corresponding to a near face-on configuration.

After a description of the search for altimetry crossovers and of their combination with the Doppler-only procedure in Sect. 5.1, we investigate the added value of altimetry in terms of orbit quality (Sect. 5.2), estimation of accelerometer biases (Sect. 5.3), and the recovery of geodetic parameters such as rotation, orientation and gravity field coefficients, and also the estimation of k_2 and h_2 Love numbers (Sect. 5.4).

5.1 Combination procedure and search for crossover discrepancies

5.1.1 Description of the combination

Our combination of altimetry crossovers and Doppler observables relies on two software packages: the planetary extension of the Bernese GNSS Software [BSW; Dach et al., 2015], written in Fortran, and pyXover, a Python suite of altimetry analysis tools for planetary

geodesy [Bertone et al., 2020]. We established two interface points between these two software packages, as depicted in Fig. 5.1. First, the orbits generated in the BSW are stored in STD format. They are converted to SPK format using a new program STD2SPK developed for this project, and written following Sect. 2.1. This program provides orbit files which can be read by pyXover, using the SpiceyPy Python library [Annex et al., 2020], to simulate altimetry data in the pyAltsim program (see Sect. 2.7), and to geolocate the altimetry bouncing point in the pyGeoloc program. Second, all the relevant information concerning the crossovers computed in the pyXover program (location, discrepancies, partial derivatives ...) is exported to an ASCII file which is then read by XOVNEQ, another addition of this project to the BSW.

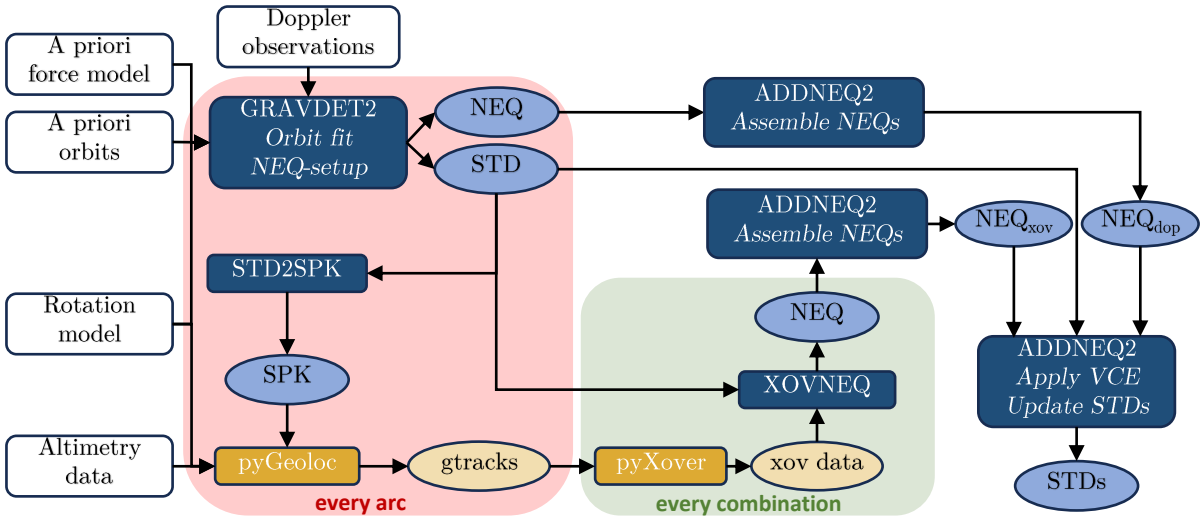


Figure 5.1: Flowchart for Doppler and altimetry crossovers combination.

The generalised orbit determination, based on a non-linear least-squares adjustment, is an iterative process (see Sect. 2.3.1). At every iteration, the probe’s orbit is integrated once more. Unlike Doppler observations, the crossover discrepancies and their locations change with respect to the orbit and the rotation model. Additionally, ground tracks may no longer intersect from one iteration to the other, or vice-versa, new intersections might be found. In every iteration, a computationally heavy search for crossovers is thus in principle required, which can be eased by leveraging crossover locations from the previous iteration. For these reasons, we first fit orbits using 83 days (80 arcs of ~ 25 h) of Doppler observables within the GRAVDET2 program (see detailed flowchart in Fig. 2.5), which constitute our baseline for the results presented in this chapter. We thereby reduce the number of iterations which require the computation of crossovers, as suggested, e.g., in Villamil et al. [2021].

Considering only a maximum tracking time of 6 h/day from Jiamusi ground station, we acquire 18 413, 29 305 and 29 429 two-way Doppler X-band observations, for $\beta_{Earth} = 1^\circ$, for $\beta_{Earth} = 72^\circ$ and for $\beta_{Earth} = 84^\circ$, respectively. In the final iteration of GRAVDET2, a NEQ is generated for each arc, containing all the parameters to be estimated (local and global). At the same time, the fitted orbit is exported to SPK format using the STD2SPK

program in order to be read by the pyGeoloc program of the pyXover package, using SPICE routines.

In pyGeoloc, the orbit is divided into several segments, called *gtracks*. Each gtrack corresponds to one revolution of the probe around Callisto. The gtracks are separated into two hemispheres, so that pyXover can later search for crossovers between each gtrack separately in the northern hemisphere and in the southern hemisphere. In the end, each gtrack is the projection of a part of the orbit, up to half a period long, onto the Callisto reference ellipsoid. One of the advantages offered by this splitting is the possibility to perform this geolocation step for each gtrack in parallel. In our work, we grouped the altimetry data in batches of 7 days, therefore our 83 days of data are splitted in 12 weeks, resulting in 760 gtracks in each hemisphere (because of the weekly division, one orbit revolution corresponds to up to 2 gtracks per hemisphere). For each altimetry observation in the gtrack object, pyGeoloc computes the latitude ϕ , longitude λ and elevation η of the laser spot bouncing point on the surface, based on the input SPK orbit and on light-time modelling. Additionally, the partial derivatives of ϕ , λ and η with respect to the estimated parameters are computed by finite differencing (except for h_2 , see Sect. 2.7.2).

Once the gtracks are processed, *combinations* between the week batches are formed. In our case, the 12 weeks of data result in a total of 78 combinations. pyXover therefore searches for crossovers within each of these combinations, and for each hemisphere. The search for crossovers is divided into two steps. A first rough search employs sub-sampled altimetry data points to limit the computational load. In case of a 10 Hz altimeter sampling rate operating at 200 km altitude above Callisto, we consider 1 observation for every 20. The distance between two sub-sampled points is then 0.076° , which corresponds to 3.2 km on the surface of Callisto. For the crossover search, the altimetry bouncing points are projected onto the surface, using a polar stereographic projection adapted for each hemisphere.

The second step is a fine search based on the results of the rough search. The neighbouring fully sampled data points are projected around each “roughly guessed” crossover to more precisely locate the crossover by interpolating between these points using a cubic spline. The crossover’s ϕ and λ result from the interpolation, while the crossover discrepancy ν is computed from the difference between the interpolated surface elevation η along each of the two tracks. The partial derivatives of ν with respect to all the estimated parameters are computed in a similar manner by finite differences. More details on the entire process can be found in Bertone et al. [2021b]. The search for crossovers results in $\sim 522\,000$ crossovers for $\beta_{Earth} = 1^\circ$, $\sim 520\,500$ crossovers for $\beta_{Earth} = 72^\circ$ and $\sim 521\,000$ crossovers for $\beta_{Earth} = 84^\circ$. As the orbit is quasi-polar, most of the crossovers are located at latitudes $> 70^\circ$ (see Fig. 5.2).

5.1.2 Distribution of the crossover discrepancies

Crossover discrepancies can be due to several factors: orbit modelling errors, a geophysical signal (e.g., tidal deformation), but also, as discussed in Sect. 2.7, intrinsic errors in the instruments and pointing errors. Moreover, a potentially significant error is introduced when

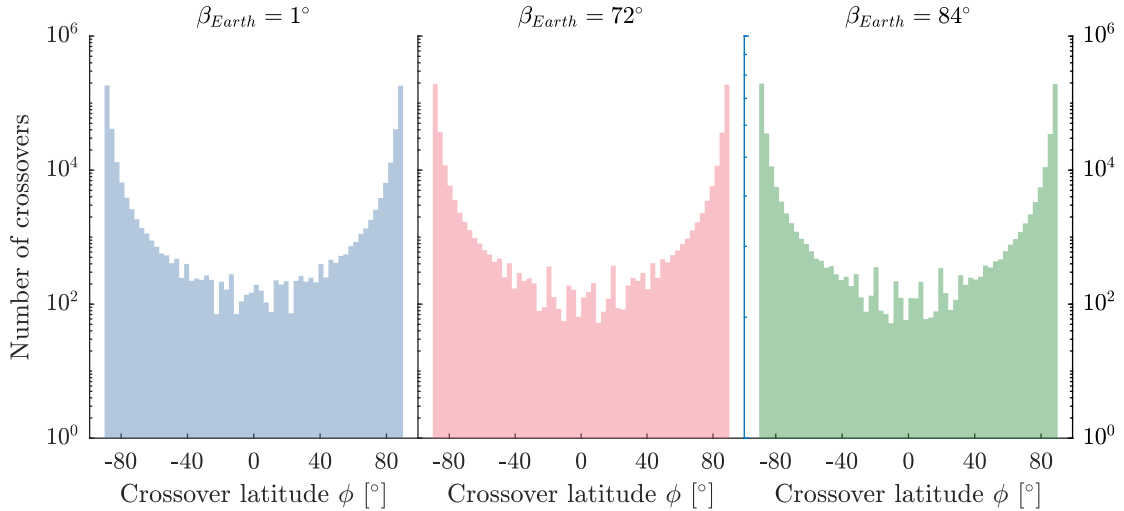


Figure 5.2: Distribution of the crossovers along latitudes ϕ for $\beta_{Earth} = 1^\circ$, $\beta_{Earth} = 72^\circ$, and $\beta_{Earth} = 84^\circ$. 95% of the crossovers are located at latitudes $> 70^\circ$.

interpolating the ground tracks between the altimetry bouncing points and the crossover coordinates. This interpolation error is strongly dependent on topography. In case of a 10 Hz sampling rate, the inter-spot distance, i.e., the distance between the bouncing points, is 160 m for the orbits considered in this chapter. The distance between the closest bouncing point and the crossover is then at maximum 80 m (half the inter-spot distance). However, we found that this distance is on average 26 m. We present in this section the distribution of the pre-fit crossover discrepancies for different topography models, different altimeter frequencies and when considering additive white noise or not. The standard deviations of the crossover discrepancies are summarized in Tab. 5.1.

We first consider a case without any topography at all, i.e., an ellipsoid, and without other sources of noise to validate our combination procedure. We found as expected that the crossover discrepancies are very low in this ideal case, with a standard deviation of 1 cm (see Fig. 5.3a). As soon as we introduce a DEM, with maximum effective resolution of several hundred meters to a few km, the discrepancies increase by an order of magnitude. This difference is due to the variation of altitude between two bouncing points (i.e., the slope). For more realistic cases, we additionally consider a simulated small-scale topography on top of large scale features modelled by our DEM. The elevation of a given point on the surface of Callisto is then the sum of both elevations. As a result, because of the increased surface roughness surface [Steinbrügge et al., 2018a, Bertone et al., 2021b], the interpolation errors become larger, up to 20 m (Fig. 5.3b). It is important to note that we assume some parameters for this texture based on past analyses at Mercury, which might not represent the actual unknown small-scale topography of Callisto. For instance, a smoother small-scale topography would yield a lower interpolation error. We additionally consider a “control case” where we replace all topography by a simple 12 m-white noise added to altimetry ranges, to evaluate the impact of a structured topography on the recovery of orbit and geodetic parameters. As shown in Fig. 5.3b, the two distributions of

pre-fit crossover discrepancies are similar but not identical, and the standard deviation of the white noise case is slightly lower.

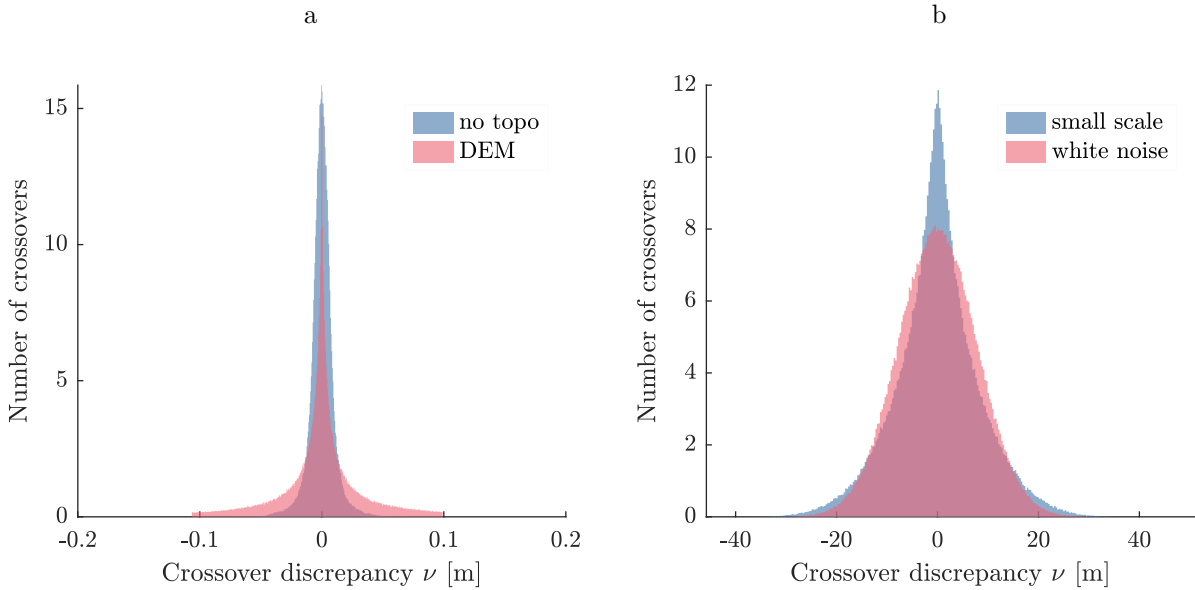


Figure 5.3: Distribution of the crossover discrepancies ν without topography or with a DEM (a), and with small-scale topography or with 12 m white noise on the DEM (b) at 10 Hz for $\beta_{Earth} = 1^\circ$.

The interpolation error depends on the topography, on the velocity of the probe with respect to the surface of Callisto, and on the sampling rate of the altimeter. The higher the probe, or the smoother the topography, the smaller the interpolation error. However, to test the impact of interpolation error on our solution, we fix the orbit of the probe and the topography, and increase the sampling rate of the altimeter. Increasing the sampling rate of the altimeter from 10 Hz [BepiColombo Laser Altimeter (BELA); Thomas et al., 2021] to 30 Hz [GAnymede Laser Altimeter (GALA); Hussmann et al., 2019] reduces the distance between the bouncing points, and thus reduces the a priori crossover discrepancies, as expected (see Fig. 5.4). The standard deviation of the discrepancies was reduced from 8.3 m to 6.4 m. However, because of the larger amount of data and computational burden, we only performed one test at 30 Hz with small-scale topography, and kept a 10 Hz sampling for our tests with different topography models.

Once the crossovers have been located, and once their discrepancies and partial derivatives are computed, these data are exported to XOVNEQ, a new BSW program developed for this study which uses the STD orbits previously generated by GRAVDET2 to compute crossover NEQs for each of the 78 week-combinations. In particular, XOVNEQ computes the partial derivatives according to the parametrization used by the BSW, based on the orbit correction parametrization used in pyXover (see Sect. 2.7.2). As of now, each crossover observation is assigned a unit weight. However, in the future, a more advanced weighting scheme may be considered, such as assessing the interpolation error based on the distance of a given crossover with respect to the surrounding altimetry bouncing points as in Bertone et al. [2021b].

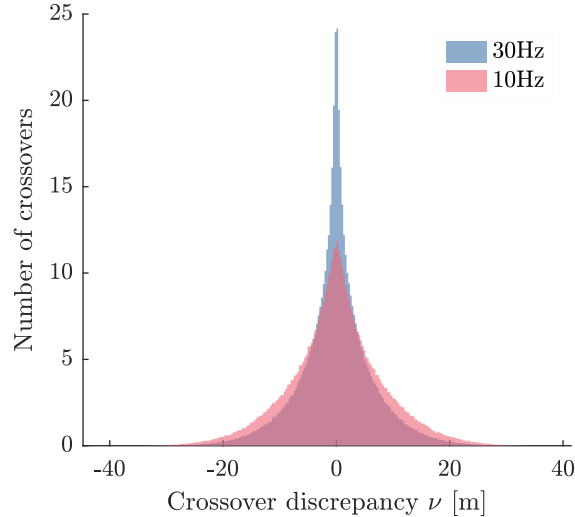


Figure 5.4: Distribution of the crossover discrepancies ν with small-scale topography at 10 Hz and 30 Hz for $\beta_{Earth} = 1^\circ$.

The Doppler NEQ and the crossovers NEQ are then stacked within the ADDNEQ2 program to form a global NEQ to be solved, as for the Doppler-only case (see Sect. 2.3.3). There are several ways to stack these multiple NEQs. For the time being, we first stack NEQs over time for each observation type separately, thus retrieving one “global” Doppler NEQ and one “global” crossover NEQ, which we then stack together with a given weight. Variance Component Estimation (VCE) is particularly useful to determine “optimal” weights, but we also experiment using empirically determined weights, which we discuss in the following section. We thus get orbit and geodetic solutions that we compare among several configurations.

5.2 Improvement of the estimated orbital elements

In Sect. 4.1, we illustrated the orbit deficiencies inherent to the orbit determination using Doppler observations. In this section, we investigate how much the orbit parameters can be improved by the addition of altimetry data on three Doppler-only fitted orbits with different geometries and different topography models, considering a perfect force modelling. We first focus on the near edge-on orbit ($\beta_{Earth} = 1.0^\circ \pm 4.2^\circ$), and consider different topography models (no topography at all, only a DEM, and synthetic small-scale topography on top of a DEM), two different altimeter sampling rates (10 Hz or 30 Hz), or simply 12 m-white noise added to altimeter ranges. We then fix the topography model to a small-scale topography on top of a DEM with a 10 Hz sampling rate, and add to the studied scenarios the two more face-on orbits ($\beta_{Earth} = 71.8^\circ \pm 4.7^\circ$ and $\beta_{Earth} = 84.0^\circ \pm 2.6^\circ$).

5.2.1 Impact of topography roughness on orbit parameters

As described in Sect. 5.1.1, the Doppler-only fitted orbits are used to search for crossovers as well as to compute the associated NEQs for each combination of weekly batches, which are

then assembled to form a global NEQ for all crossover observations. The global Doppler NEQ and the global crossover NEQ are subsequently combined, mainly following VCE-provided relative weights. However, in the less realistic cases for which we considered no noise on the altimetry data and we applied no topography or only a DEM, we find that increasing the weight given by VCE to favour the crossover dataset observations reduces the post-fit orbit differences. We show in Tab. 5.1 the ratio of the weight given to altimetry crossover discrepancies with respect to the weight given to the Doppler observations, empirically chosen in the three cases either without topography or with only a DEM, and derived following VCE in the other cases.

Table 5.1: Observation residuals and orbit differences for $\beta_{Earth} = 1^\circ$ and for topography models. The RMS of Doppler residuals is 0.78 mHz with Doppler only, while the RMS of the differences are 1.9 m.

| Topography | Weight ratio | Stdev ν [m] | | Dop. [mHz] | Orb. [m] |
|-------------------|----------------------|-----------------|----------|--------------|----------|
| | | pre-fit | post-fit | RMS post-fit | |
| No topography | 1×10^3 | 0.0098 | 0.00026 | 0.79 | 0.35 |
| DEM | 1 | 0.12 | 0.089 | 0.78 | 0.85 |
| Small-scale 30 Hz | 1.2×10^{-3} | 6.4 | 6.4 | 0.78 | 0.93 |
| Small-scale 10 Hz | 6.9×10^{-4} | 8.3 | 8.3 | 0.78 | 1.4 |
| White noise | 7.7×10^{-4} | 7.8 | 7.8 | 0.78 | 1.9 |

Considering a large scale DEM already limits the orbit improvement given by crossovers with respect to a Doppler-only fit, from $\sim 80\%$ when not considering topography to $\sim 50\%$. It is important to note that these tests are not realistic, since we do not consider any source of noise, which would further reduce the benefit of altimetry crossovers with respect to more realistic Doppler observations. However, our results constitute a first necessary validation of our simulation set-up. Only in the case of no topography or when using only a DEM, the crossover discrepancies are visibly reduced after the combination, at the price of a slight increase of the Doppler post-fit residuals.

In the more realistic cases, i.e., with small-scale topography or with additive white noise, the post-fit Doppler residuals and crossover discrepancies are overall very close to the values after the Doppler-only fit. However, the orbits are visibly improved (see Fig. 5.5) with respect to the Doppler-only solution when using a simulated small-scale topography, with the RMS of post-fit differences being reduced by $\sim 26\%$ (see Tab. 5.1). Increasing the sampling rate by a factor of 3, visibly improves the orbit by 33% with respect to the 10 Hz case. We note that there is no visible orbit improvement in the near edge-on case when using white noise instead of a fixed small-scale topography, as expected. Indeed, the discrepancy of a perfectly modelled crossover located precisely at the bouncing points of two perfect ground tracks would be affected only by the range noise, as the topography would cancel (see Eq. 2.65), and there would be no interpolation error. Thus, if the interpolation error is part of the range noise budget, and not a consequence of the considered small-scale topography, it would affect the error on the parameters we estimate by minimising the crossover discrepancies.

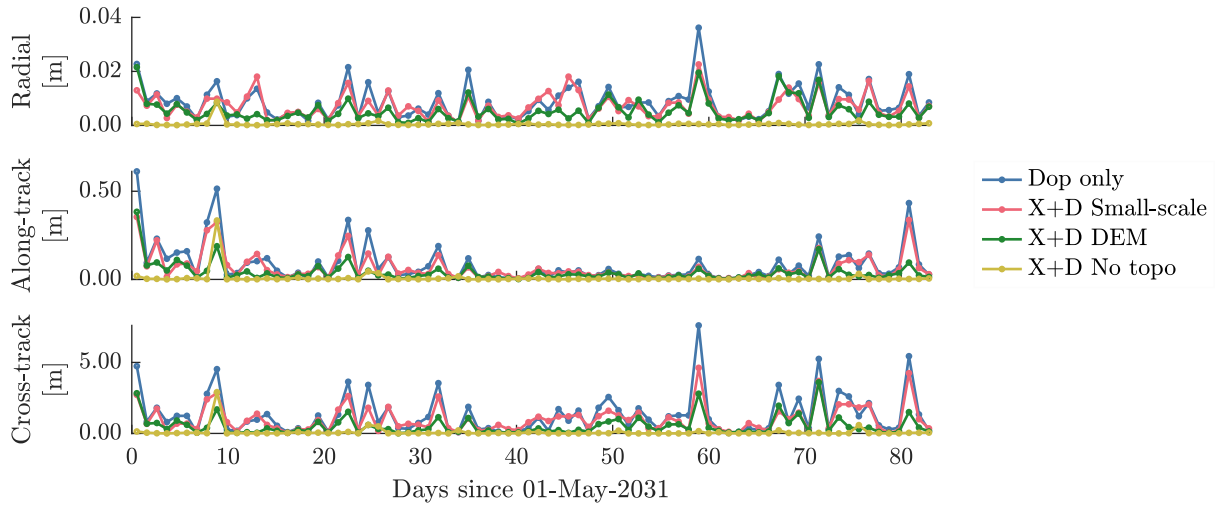


Figure 5.5: Daily RMS of the orbit differences for $\beta_{Earth} = 1^\circ$ considering only Doppler observations (D) and combining with crossovers (X) for different topography models.

Because of the nature of the altimetry crossover observables, one could expect the main improvement to happen in the radial direction. However, because a Doppler-fitted orbit is most weakly determined in the direction perpendicular to the radial direction (see Sect. 4.1.1), our orbit differences in the radial direction are already smaller, below 5 cm, than in the along-track and cross-track directions. Moreover, even small improvements in the radial direction induce improvements in the other directions. In particular, when the orbit is close to an edge-on configuration in these experiments, the direction weakly determined by Doppler observations is the cross-track direction, with some orbit differences larger than 5 m in case of a Doppler-only solution (see Fig. 5.5).

As discussed in Sect. 4.1.1, and as shown in Fig. 5.6 for a Doppler-only solution, the osculating orbital elements are highly correlated with each other for low β_{Earth} . Correlations are notably reduced when the altimetry crossovers are combined with Doppler observations. This is already quite visible even in the case small-scale topography is applied. There is a general decrease of correlations between every osculating orbital element of all 80 arcs for the near edge-on orbit as shown in Fig. 5.7.

5.2.2 Orbit improvement and orbit geometries

We discussed in Sect. 4.1 the influence of β_{Earth} on the orbit accuracy in case of only Doppler observations, and showed that the orbit errors are larger for more face-on orbits. Indeed, the global 3D RMS of the orbit differences is 1.9 m, 4.6 m and 7.0 m for $\beta_{Earth} = 1^\circ$, 72° and 84° , respectively. Contrary to an edge-on orbit, the error is shared between the along-track and cross-track directions, as can be seen in Fig. 5.8.

As discussed in Sect. 4.1, there are also large differences between the three orbit configurations in terms of correlations between the estimated initial orbital elements. We already

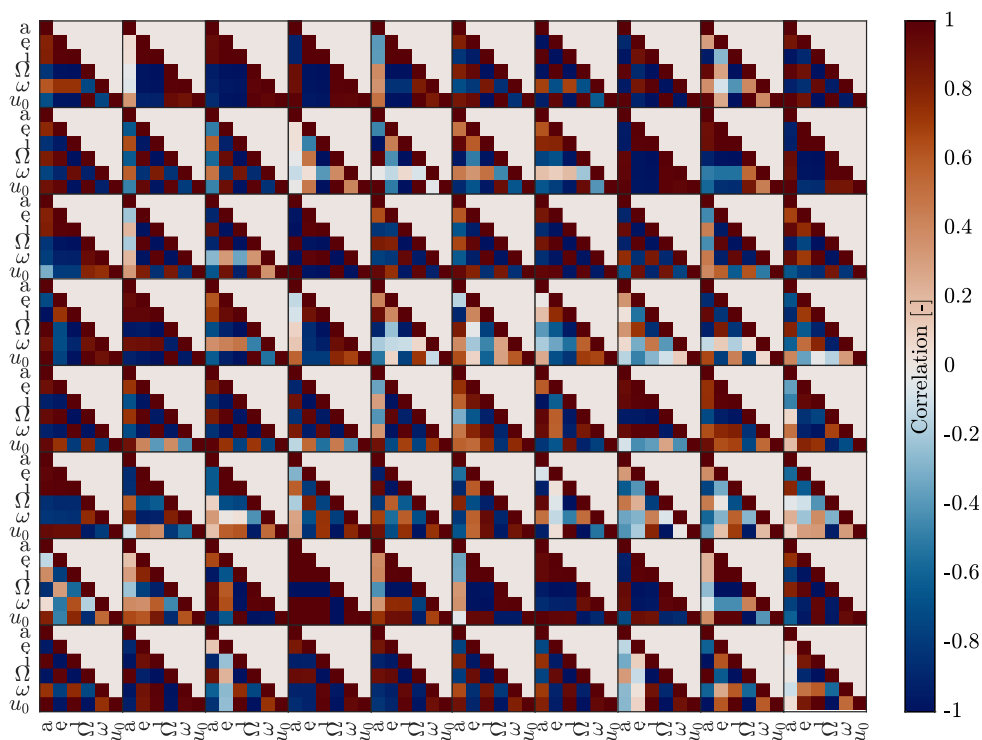


Figure 5.6: Correlation map between initial osculating orbital elements of 80 arcs for the near edge-on orbit fitted using only Doppler observations.

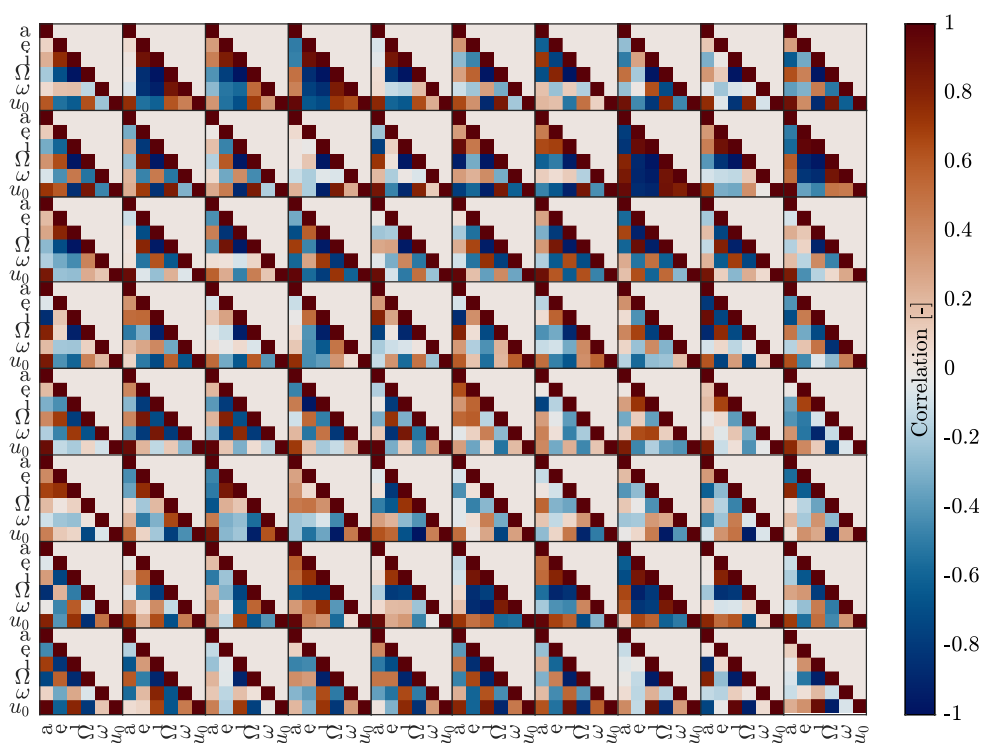


Figure 5.7: Correlation map between initial osculating orbital elements of 80 arcs for the near edge-on orbit fitted using Doppler and altimetry crossover observations with small-scale topography.

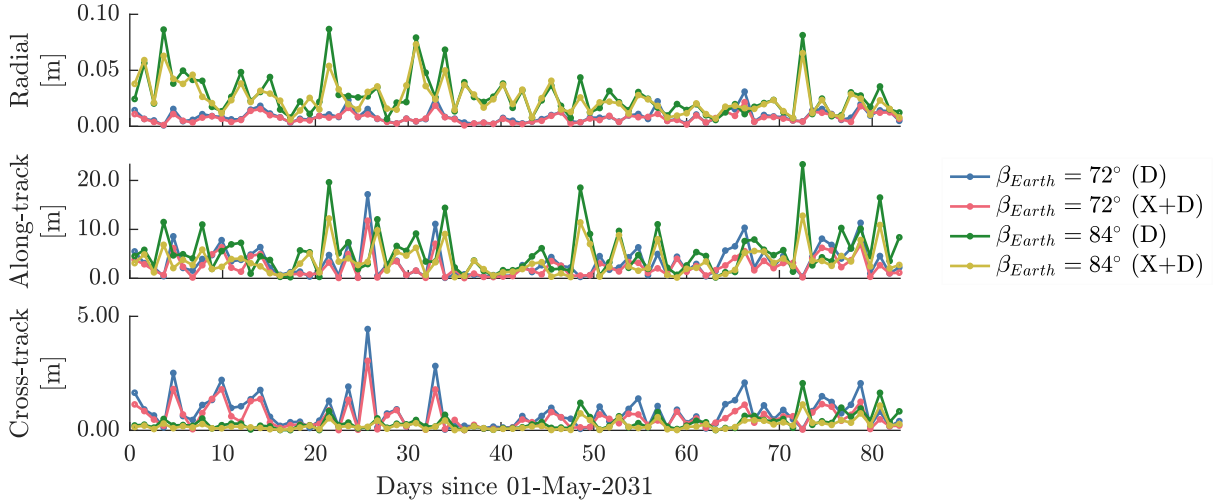


Figure 5.8: Daily RMS of the orbit differences for $\beta_{Earth} = 72^\circ$ and $\beta_{Earth} = 84^\circ$ considering only Doppler observations (D) and combining with crossovers (X) considering small scale topography.

showed in Fig. 5.6 that correlations are distributed over all orbital elements for low β_{Earth} . We alternatively plot these correlations for the three orbit configurations by representing the absolute correlations between each orbit parameter within each arc averaged over the 80 arcs (see Fig. 5.9 for Doppler only solutions). We get overall lowest correlations for the case $\beta_{Earth} = 72^\circ$, except for the correlations between inclination i and the argument of latitude u_0 . The near face-on orbit suffers from very high correlations between i , u_0 and the longitude of the ascending node Ω , as already mentioned in Sect. 4.1.2. We notice that for $\beta_{Earth} = 1^\circ$ the correlations between the inclination i and both the longitude of the ascending node Ω and the argument of latitude u_0 are significantly lower, below 0.5, compared to values higher than 0.9 in the other two cases. Such low correlations may explain why the orbit accuracy is better in this case.

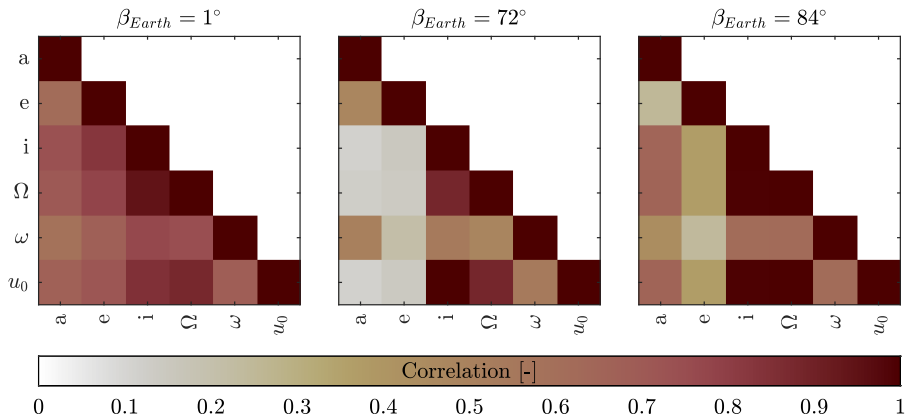


Figure 5.9: Absolute correlations between initial osculating orbital elements averaged over 80 arcs for different β_{Earth} using only Doppler observables.

We show in Tab. 5.2 the relative weights between altimetry crossover discrepancies and

Doppler observations derived following VCE as described in Sect. 5.1.1, along with the post-fit standard deviation of the crossover discrepancies, and the RMS of the orbit differences. The post-fit Doppler residuals and crossover discrepancies are overall very close to the values after the Doppler-only fit. However the orbits are visibly improved with respect to the Doppler only solution, with the RMS being reduced by $\sim 26\%$ and up to 36% in the near face-on case (see Tab. 5.2). The higher contribution of altimetry crossovers for β_{Earth} close to 90° agrees with the findings of Villamil et al. [2021].

Table 5.2: Crossover discrepancy residuals and orbit differences for different orbits. The RMS of Doppler residuals is 0.78 mHz in the three orbit cases with Doppler only and with or without adding altimetry crossovers.

| β_{Earth} avg. [$^\circ$] | Weight ratio | Stdev ν [m] post-fit | RMS orb. diff. [m] | |
|--------------------------------------|----------------------|-----------------------------|--------------------|----------|
| | | | pre-fit | post-fit |
| 1 | 6.9×10^{-4} | 8.3 | 1.9 | 1.4 |
| 72 | 6.5×10^{-4} | 8.5 | 4.6 | 3.3 |
| 84 | 6.5×10^{-4} | 8.6 | 7.0 | 4.5 |

Correlations are notably reduced when the altimetry crossovers are combined with Doppler observations (see Fig. 5.10). For the near face-on orbit ($\beta_{Earth} = 84^\circ$ in Fig. 5.10), the correlations between the osculating orbital elements are visibly reduced, but the correlations between i , Ω and u_0 remain large. In case $\beta_{Earth} = 72^\circ$, the improvement in correlations between orbital parameters is more moderate. However, the correlations between the semi-major axis a and i , Ω and u_0 slightly increase.

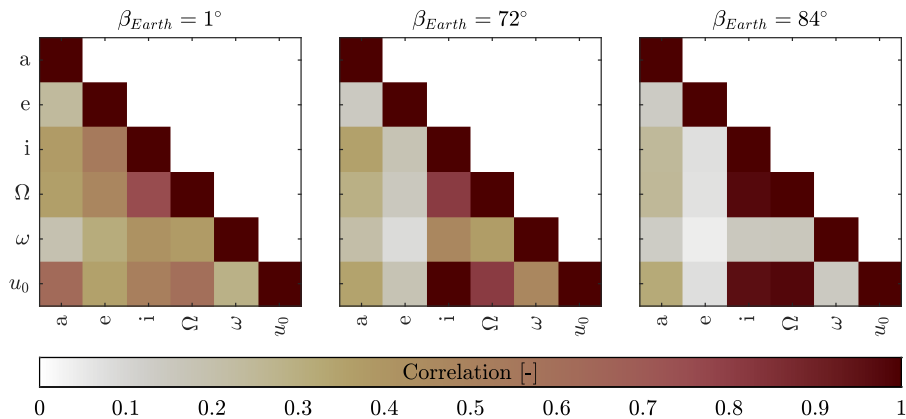


Figure 5.10: Absolute correlations between initial osculating orbital elements averaged over 80 arcs for different β_{Earth} fitted using Doppler observables and altimetry crossover observations with small-scale topography.

These results show how well the orbit solution can be improved with altimetry crossovers. However, we want to emphasize that more advanced weighting schemes among the crossover observations might provide even larger improvements, e.g., a latitude-dependent weight or a

higher weight when a crossover corresponds to a part of the orbit not observed by Doppler. This would be an interesting investigation for future work.

5.3 Impact on the estimation of accelerometer biases

We have seen in Sect. 4.5 that non-gravitational accelerations have to be carefully accounted for, or else they may harm the orbit solutions. More specifically, in case of an on-board accelerometer, the estimation of accelerometer biases can be very challenging (see Sect. 4.5.2). In this section, we evaluate how the combination of altimetry crossovers with Doppler observations can improve the estimation of the biases, and thus the overall orbit quality.

We assume a near edge-on orbit with $\beta_{Earth} = 1.0^\circ \pm 4.2^\circ$, tracked only by Jiamusi ground station, and we estimate biases in radial, along-track and cross-track directions every 25 h. As discussed in Sect. 4.5, the biases have to be carefully constrained. We follow the same procedure described in Fig. 4.30 to determine a first Doppler-only orbit solution and to estimate a first set of biases with their global constraints (using VCE). One can see in Fig. 5.11 that, apart from the along-track direction, the bias estimation error is rather large, especially in the cross-track direction. We saw in Sect. 4.5.2, that increasing the length of the estimation arc to more than 25 h helps reducing the estimation error, as well as considering biases constant on larger time spans (see Fig. 4.33b).

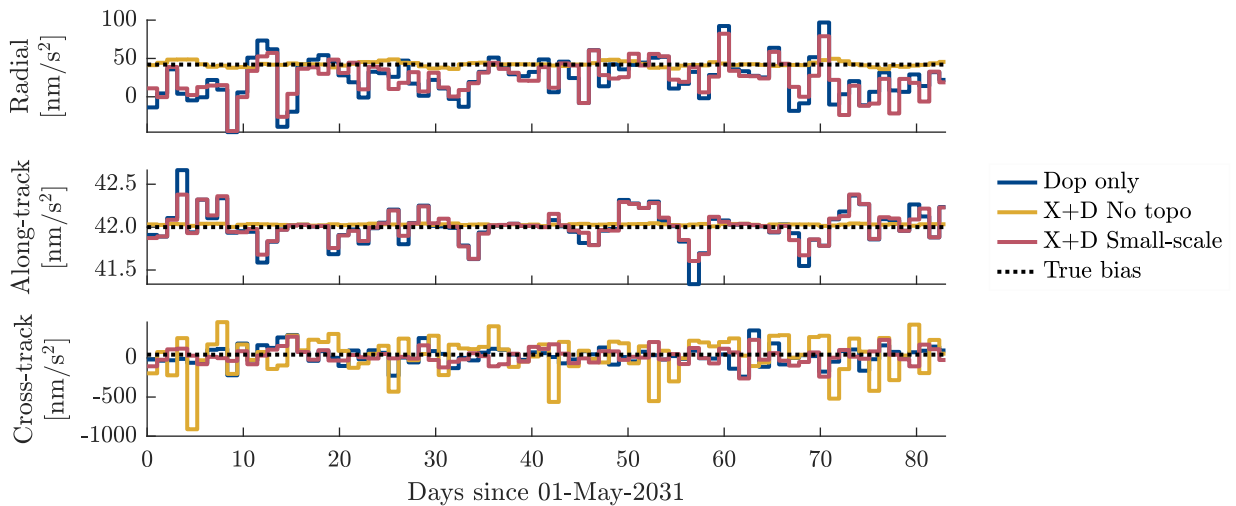


Figure 5.11: True and estimated accelerometer biases using Doppler only, Doppler and crossovers considering no topography and with small-scale topography, for $\beta_{Earth} = 1.0^\circ$.

Nevertheless, we postpone the study of different time spans to future work and thus focus for the moment only on the added value of crossovers in the case of 25 h arcs, and for one set of 3 biases per arc. We first combine the Doppler NEQ and the crossover NEQ. We use VCE in case of small-scale topography, while freely estimating all parameters, resulting in a weight close to the one given in Tab. 5.1. Similarly to Sect. 5.2.1, we tried different weight between observation types when not considering topography. We then estimate one

global bias constraint per direction using VCE on the combined VCE, as performed for the Doppler-only solution. We found that in case no topography is considered, weighting the crossover observations 10 times more than the Doppler observations resulted in minimal orbit differences, once VCE-derived constraints are applied to the accelerometer biases.

When not considering any topography, and any noise on the altimetry ranges, we can see a significant improvement on the estimation of the biases in radial direction, as can be expected from the geometry of the crossover discrepancy observable, but also in along-track direction (Fig. 5.12). On the other hand, the cross-track biases are visibly degraded. This behaviour may be explained by the large weight on the altimetry-derived observations, as they perform poorly in cross-track direction. Nevertheless, the cross-track bias errors are smaller when considering more realistic crossover observations, i.e., considering small-scale topography. We also notice improvements in radial and along-track biases estimation with respect to the Doppler-only solution, albeit less significant than in the no topography case. The orbit is visibly improved (Fig. 5.12) as the RMS of the differences between the estimated and the true orbit decreases, from 3.16 m in the Doppler-only case to 0.99 m when not considering topography. Because the improvement on the radial biases estimation is dampened when a small-scale topography is assumed, the orbit improvement is more moderate, as shown in Fig. 5.12, with the RMS of orbit differences is reduced to 2.25 m RMS of orbit differences.

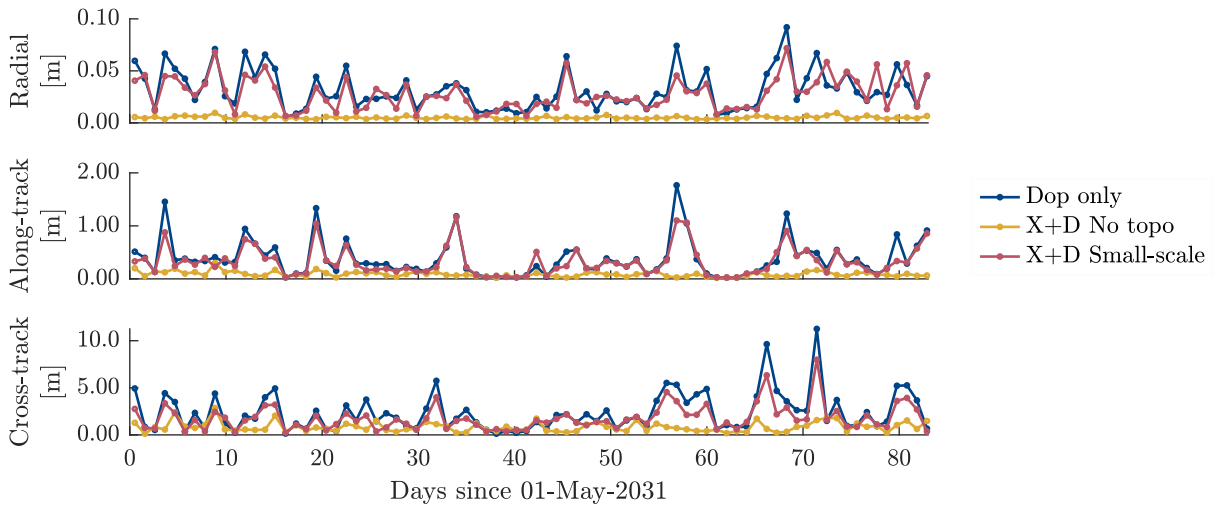


Figure 5.12: RMS of orbit differences for each arc using Doppler only, Doppler and crossovers considering no topography and with small-scale topography, for $\beta_{Earth} = 1.0^\circ$.

These preliminary results show the potential benefit of altimetry crossovers to mitigate the challenge posed by non-gravitational accelerations. In future work, a more thorough analysis, similarly to Sect. 4.5, would be required to more precisely assess the benefit of Doppler and altimetry crossover combination with, e.g., a more face-on orbit. For instance, investigating the impact on longer estimation arcs, by stacking biases similarly to Sect. 4.5.2, or by iterating on the whole combination.

5.4 Estimation of the complete set of geodetic parameters

After looking at the benefit of a combination between altimetry crossovers and Doppler observables in terms of orbit parameters, we study in this section its impact on the estimation of rotation and orientation parameters, and on the estimation of gravity field parameters and tidal Love numbers. We first focus on the near edge-on case ($\beta_{Earth} = 1.0^\circ \pm 4.2^\circ$), for which the depleted ground coverage may harm a freely estimated gravity field Doppler-only solution, as discussed in Sect. 4.3.2, and for which the coverage is even more depleted when considering Doppler observations from only one tracking station (see Fig. 5.13). We then extend the range of studied orbits with the two more face-on orbits, considering only small-scale topography. We estimate gravity field parameters up to d/o 100 and consider a perfect force modelling.

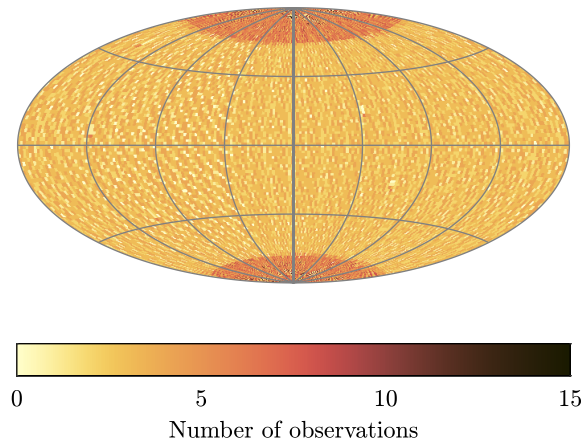


Figure 5.13: Ground coverage of Callisto from a polar orbiter with $h = 200$ km occulted by Callisto for 83 days, for $\beta_{Earth} = 1.0^\circ \pm 4.2^\circ$. The 60 s-sampled Doppler observations are grouped in bins of 1.8° in longitude and 2.8° in latitude.

5.4.1 Impact of topography roughness on rotation parameters only

We first evaluate the free estimation of the global parameters as performed in pyXover with altimetry data only, namely the constant terms of the north pole right ascension α_0 and declination δ_0 , the rotation rate of Callisto w_1 , the main longitudinal libration W_l , and the tidal Love number h_2 . Similarly to Sect. 5.2, we use VCE to determine an optimal weight between Doppler observations and altimetry crossovers, except for the ideal cases without small-scale topography and where no additional noise is considered, for which we fixed the weight to the values given in Tab. 5.1.

For each of the cases described in Sect. 5.2, we compare the formal errors (Tab. 5.3) and the true error (Tab. 5.4) of the previously mentioned parameters when using only Doppler observations (except for the Love number h_2), when using altimetry crossovers only, and when combining both types of observations (X+D). We additionally represented the formal

and true errors in Fig. 5.14, using Doppler only or combining them with crossovers observations. The combination of altimetry crossover discrepancies and Doppler observables results in a general improvement of the formal errors with respect to each observation type taken separately, except for h_2 in the ideal case of no topography.

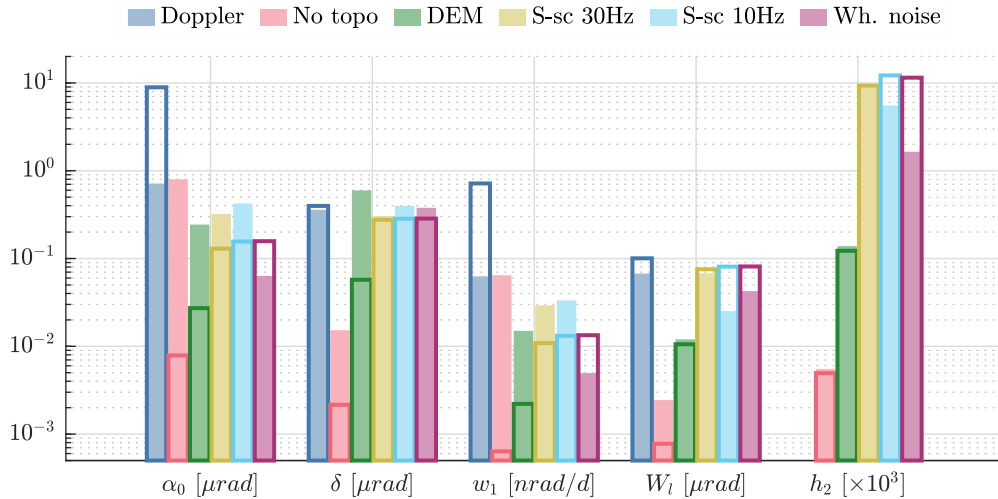
Table 5.3: Formal errors of the estimated rotation and orientation parameters and h_2 Love number, considering different observation types and different topography models for $\beta_{Earth} = 1^\circ$.

| Topography | Obs. type | $\alpha_0[^\circ]$ $\times 10^4$ | $\delta_0[^\circ]$ $\times 10^4$ | $w_1[^\circ/\text{day}]$ $\times 10^9$ | $W_l[^\circ]$ $\times 10^5$ | $h_2 [-]$ $\times 10^3$ |
|------------------------------------|-----------|-------------------------------------|-------------------------------------|---|--------------------------------|----------------------------|
| | Doppler | 5.1 | 0.23 | 41 | 0.58 | - |
| No topography | Crossover | 0.0017 | 0.0012 | 0.046 | 0.011 | 0.0018 |
| | X+D | 0.0045 | 0.0012 | 0.036 | 0.0044 | 0.0049 |
| DEM | Crossover | 0.024 | 0.041 | 0.55 | 0.075 | 0.17 |
| | X+D | 0.016 | 0.033 | 0.13 | 0.060 | 0.12 |
| Small-scale (30 Hz) | Crossover | 1.4 | 3.0 | 14 | 5.4 | 9.5 |
| | X+D | 0.074 | 0.16 | 0.62 | 0.43 | 9.3 |
| Small-scale (10 Hz) | Crossover | 2.2 | 4.4 | 27 | 7.4 | 14 |
| | X+D | 0.089 | 0.16 | 0.76 | 0.46 | 12 |
| White noise $\sigma=12\text{m}$ | Crossover | 2.1 | 4.1 | 18 | 6.9 | 14 |
| | X+D | 0.090 | 0.16 | 0.77 | 0.47 | 11 |

Regarding the true errors in Tab. 5.4, the benefit of a combined solution is also generally visible. In case no topography is considered, the true errors in the estimated parameters do not necessarily improve, but this may be due to the weight ratio between observation types, which we derived empirically in Sect. 5.2, without estimating rotation parameters. We notice that the true error of δ_0 increases for a few topography cases when including crossovers to Doppler observations. Moreover, when considering small-scale topography at 10 Hz, the true error on h_2 is larger when combining observations than when considering crossovers only. However, in order to unambiguously analyse the true errors of this small set of parameters, one would need to repeat the experiment with different initial conditions, for instance by performing a Markov Chain Monte-Carlo experiment. Considering a 30 Hz altimeter sampling rate improves the formal errors by $\sim 30\%$ and up to 50% for w_1 with respect to a 10 Hz altimeter in case of a crossover only solution, and between 0% and 30% in case of Doppler and crossover combination. Differences between small-scale topography and pure white noise in the case of 10 Hz are more subtle. Indeed, as seen in Fig. 5.3b, the distribution of the crossovers is comparable but not identical. The altimetry-only solution is worse in the case of small-scale topography, while differences are close when combining altimetry crossovers with Doppler observations.

Table 5.4: True errors of the estimated rotation and orientation parameters and Love number h_2 , considering different observation types and different topography models for $\beta_{Earth} = 1^\circ$.

| Topography | Obs. type | $\alpha_0 [^\circ]$ $\times 10^4$ | $\delta_0 [^\circ]$ $\times 10^4$ | $w_1 [^\circ/\text{day}]$ $\times 10^9$ | $W_l [^\circ]$ $\times 10^5$ | $h_2 [-]$ $\times 10^3$ |
|------------------------------------|-----------|--------------------------------------|--------------------------------------|--|---------------------------------|----------------------------|
| | Doppler | 0.41 | 0.21 | 3.6 | 0.39 | - |
| No topography | Crossover | 0.15 | 0.08 | 0.014 | 0.17 | 0.0067 |
| | X+D | 0.46 | 0.0087 | 3.7 | 0.014 | 0.0055 |
| DEM | Crossover | 0.41 | 0.59 | 2.3 | 0.37 | 0.7 |
| | X+D | 0.14 | 0.34 | 0.86 | 0.069 | 0.14 |
| Small-scale (30 Hz) | Crossover | 1.4 | 1.2 | 17 | 0.023 | 9.3 |
| | X+D | 0.18 | 0.17 | 1.7 | 0.39 | 8.9 |
| Small-scale (10 Hz) | Crossover | 2.5 | 7.7 | 8.1 | 0.4 | 0.5 |
| | X+D | 0.24 | 0.23 | 1.9 | 0.14 | 5.6 |
| White noise $\sigma=12\text{m}$ | Crossover | 2.5 | 1.9 | 13 | 6.8 | 1.8 |
| | X+D | 0.036 | 0.22 | 0.28 | 0.24 | 1.6 |


 Figure 5.14: True (filled bars) and formal (empty bars and solid line) errors of the estimation of rotation, and orientation parameters and the Love number h_2 , considering either only Doppler observations, or combining Doppler and crossover observations with different topography models, for $\beta_{Earth} = 1.0^\circ$.

5.4.2 Inclusion of the gravity field coefficients with different topographies

We then repeat the same experiment, but we also freely estimate the gravity field parameters and k_2 Love number. Altimetry crossover discrepancies alone did not allow for an estimation of the gravity field up to d/o 100. We thus compare the case of Doppler only (except for h_2 Love number) and the different cases of combination between altimetry crossovers and Doppler observations, in terms of formal errors in Tab. 5.5 and true errors in Tab. 5.6, which we represented in Fig. 5.15.

Table 5.5: Formal errors of the estimated rotation, and orientation parameters and of the h_2 and k_2 Love numbers, estimated with gravity field parameters when considering different observation types and different topography models, for $\beta_{Earth} = 1.0^\circ$.

| Topography Obs. type | $\alpha_0 [^\circ]$ $\times 10^4$ | $\delta_0 [^\circ]$ $\times 10^4$ | $w_1 [^\circ/\text{day}]$ $\times 10^6$ | $W_l [^\circ]$ $\times 10^5$ | $h_2 [-]$ $\times 10^3$ | $k_2 [-]$ $\times 10^3$ |
|-------------------------|--------------------------------------|--------------------------------------|--|---------------------------------|----------------------------|----------------------------|
| Doppler only | 14 | 0.81 | 24 | 21 | - | 4.2 |
| No topography | 0.015 | 0.01 | 0.0013 | 0.043 | 0.015 | 0.0046 |
| DEM | 0.16 | 0.12 | 0.017 | 0.88 | 0.37 | 0.012 |
| Small-scale (30 Hz) | 1.2 | 0.53 | 0.77 | 7.5 | 9.8 | 0.19 |
| Small-scale (10 Hz) | 1.3 | 0.54 | 1 | 8.6 | 13 | 0.52 |
| White noise | 1.3 | 0.54 | 0.98 | 8.4 | 12 | 0.64 |

Table 5.6: True errors of the estimated rotation, and orientation parameters and h_2 and k_2 Love numbers, considering different observation types and different topography models, estimated with gravity field parameters, for $\beta_{Earth} = 1.0^\circ$.

| Topography Obs. type | $\alpha_0 [^\circ]$ $\times 10^4$ | $\delta_0 [^\circ]$ $\times 10^4$ | $w_1 [^\circ/\text{day}]$ $\times 10^6$ | $W_l [^\circ]$ $\times 10^5$ | $h_2 [-]$ $\times 10^3$ | $k_2 [-]$ $\times 10^3$ |
|-------------------------|--------------------------------------|--------------------------------------|--|---------------------------------|----------------------------|----------------------------|
| Doppler only | 22 | 1.7 | 23 | 11 | - | 6.5 |
| No topography | 0.12 | 0.083 | 0.0027 | 0.22 | 0.057 | 0.053 |
| DEM | 0.90 | 0.19 | 0.038 | 3.7 | 0.6 | 0.22 |
| Small-scale 30 Hz | 1.1 | 0.81 | 0.68 | 5.3 | 6.7 | 0.20 |
| Small-scale 10 Hz | 1.4 | 0.91 | 0.69 | 5.6 | 10 | 0.13 |
| White noise | 1.1 | 0.94 | 1.6 | 16 | 6.2 | 1.5 |

As already mentioned, the ground coverage available from Doppler observations is limited in the case of a near edge-on orbit, which can lead to an aliasing of the gravity field solution, unless properly constrained. Additionally, the rotation rate is highly correlated with the non-zonal coefficients of the gravity field and its unconstrained estimation proved to be challenging (see Sect. 4.4). Nevertheless, we chose to analyse only unconstrained solutions in this section, to highlight the contribution of altimetry crossovers to make up for the depleted ground coverage and to reduce correlations between parameters in this challenging scenario.

The estimation of all the rotation and orientation parameters is improved in all the considered combinations with respect to a Doppler-only estimation, whether we look at the formal errors or the true errors. The only exception is the true error of the main longitudinal libration amplitude W_l when considering white noise only. However, as previously discussed, the true errors of a limited set of parameters of one test are indicative but not conclusive. The formal errors of the constant term of the right ascension of the north pole α_0 are reduced by at least one order of magnitude, thanks to the correlation between α_0

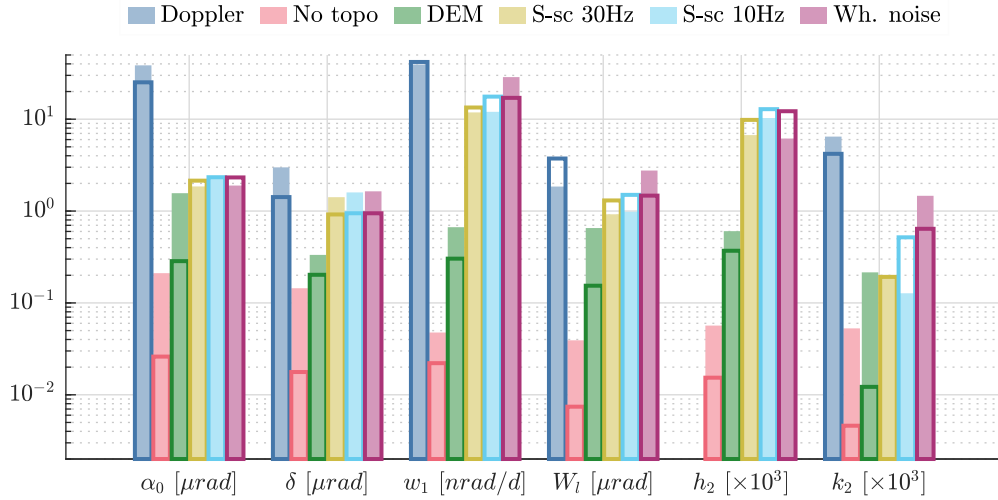


Figure 5.15: True (filled bars) and formal (empty bars and solid line) errors of the estimation of rotation, and orientation parameters and h_2 and k_2 Love numbers, considering different observation types and different topography models, estimated with gravity field parameters, for $\beta_{Earth} = 1.0^\circ$.

and δ_0 being reduced by a factor of minimum 4.8 (Figs. 5.16 and 5.17). δ_0 is more moderately improved as the formal errors are reduced only by 30% in the small-scale topography case, and white noise case alike.

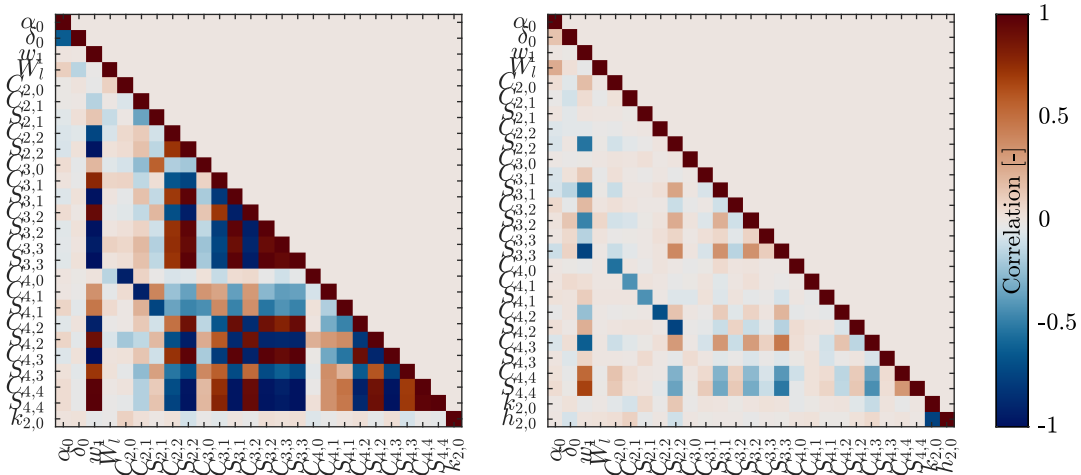


Figure 5.16: Correlations between the low-degree gravity field coefficients and rotation parameters using only Doppler observations (left) and combining with crossovers (right) without considering any topography, for $\beta_{Earth} = 1.0^\circ$.

Overall, the ideal cases without topography or with only the DEM drastically reduced the errors in all the considered parameters, but also the correlations between the rotation rate w_1 and the gravity field coefficients (Fig. 5.16). The correlation between α_0 and δ_0 is still largely reduced when considering small-scale topography, from -0.63 to -0.08 (Figs. 5.16 and 5.17). w_1 remains highly correlated with the gravity field coefficients, pointing that

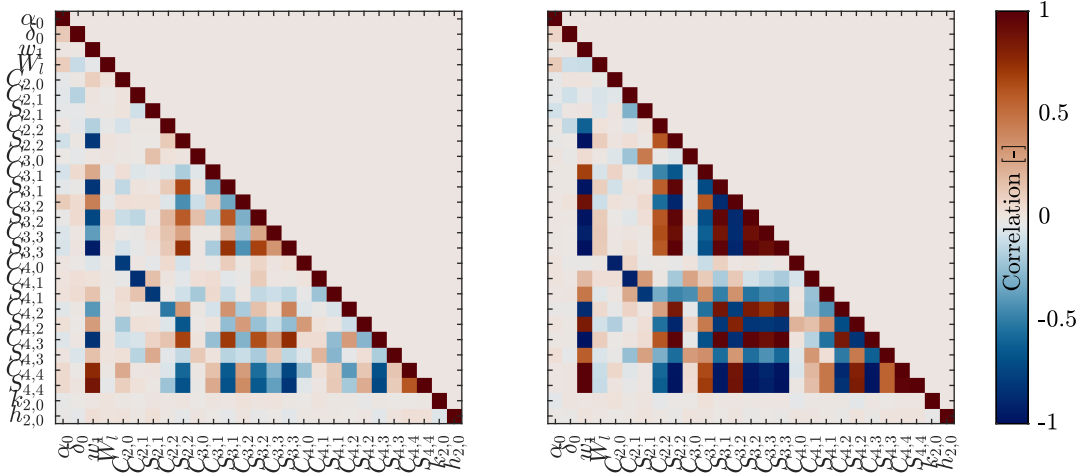


Figure 5.17: Correlations between the low-degree gravity field coefficients and rotation parameters estimated considering Doppler and crossovers observables with a DEM and without (left) or with (right) small-scale topography, for $\beta_{Earth} = 1.0^\circ$.

the benefits of altimetry are weakened when considered small-scale topography. However, we still note lower correlations with respect to a Doppler-only solution. For instance the correlations between w_1 and C_{21} , S_{21} , or C_{30} are reduced by a factor of at least 4, leading to lower correlations between these coefficients and the other gravity field coefficients (Fig. 5.17).

Formal errors on estimates of the Love number k_2 are also reduced, e.g., by a factor of 8 in case of small-scale topography at 10 Hz. The gravity field solution is significantly improved in the ideal cases (Fig. 5.18). In the case of small-scale topography with a 10 Hz sampling rate, the gravity field solution is still improved with respect to a Doppler-only solution. Unlike the orbit differences discussed in Sect. 5.2.1, we do not see a large difference on the estimates of the geodetic parameters when considering small-scale topography or an equivalent white noise.

We find that the gravity field and the rotation parameters, in particular, benefit from a combination of altimetry crossovers and Doppler observations in these cases. The depleted ground coverage is at least partially mitigated, and the correlations arising from the estimation of rotation and orientation parameters are reduced. Orbit improvements discussed in Sect. 5.2 clearly contribute to the improved estimates of these parameters. In this chapter, we estimated all the rotation parameters freely. However, constraining the rotation parameters as discussed in Sect. 4.4 may further reduce the correlations between the rotation rate w_1 and the gravity field parameters.

5.4.3 Contribution of altimetry for different orbit configurations

We present in this section the results for a Doppler only solution and a combination with altimetry crossovers, for the three different orbit geometries considered in this chapter, only considering small-scale topography on top of a DEM, with a 10 Hz altimeter sampling rate. We estimate gravity field parameters up to d/o 100, in addition to the Love number k_2 ,

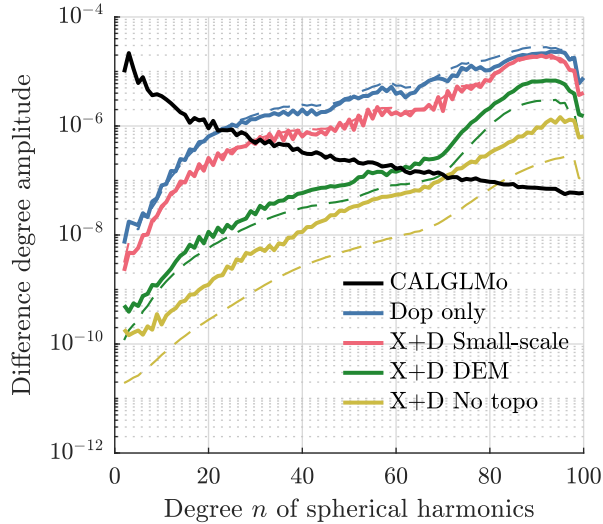


Figure 5.18: Difference degree amplitude of gravity field solutions considering different topography models, using only Doppler observations (Dop) or a combination of crossovers and Doppler (X+D) observations, for $\beta_{Earth} = 1.0^\circ$.

the right ascension α_0 and declination δ_0 of the north pole and the amplitude of the main longitudinal libration W_l . We decided to not estimate the rotation rate w_1 in this section, because of the high correlations with the gravity field parameters, as discussed in Sect. 5.4.2.

As discussed in Sect. 4.3.2, the observation geometry from Earth is critical for gravity field recovery using radio tracking observations. A near edge-on orbit ($\beta_{Earth} = 1^\circ$) provides a better gravity field sensitivity, as most of the gravity signal is along the line-of-sight from Earth. However, this benefit needs to be balanced with occultations of the line-of-sight by the Callisto for a part of the orbit as seen in Fig. 5.13. This effect, combined with the limited number of Doppler observations (only one tracking station) results in a gravity field solution suffering from aliasing. When estimating gravity field coefficients up to d/o 100, the signal from the high degree coefficients leaks into the lower degree coefficients (see Fig. 5.19a).

Constraining the coefficients to zero using, e.g., a Kaula law, limits aliasing due to the ground coverage as shown in Sect. 4.3.2. We thus apply a Kaula constraint as in Sect. 4.3.5, using VCE to derive the constant $K = 0.018$ for the Doppler-only solution. We note that the other parameters benefit from the suppressed aliasing due to the Kaula constraint (see Tab. 5.7). On the other hand, a near face-on orbit ($\beta_{Earth} = 84^\circ$) is detrimental in terms of gravity field recovery, as the gravity signal acting on the probe is mostly perpendicular to the line-of-sight, resulting in a lower Doppler sensitivity. However, despite using a Kaula-constraint in the case $\beta_{Earth} = 1^\circ$, the gravity field solution for the near face-on case performs better in the low degrees than in the near edge-on case. This may be explained by the relatively low number of observations for $\beta_{Earth} = 1^\circ$, and may change, e.g., in case of the probe would be tracked by more than one tracking station. The intermediate case $\beta_{Earth} = 72^\circ$ benefits from the absence of occultations of the line-of-sight from Callisto, and of better sensitivity to the gravity signal than a face-on orbit, resulting in a better

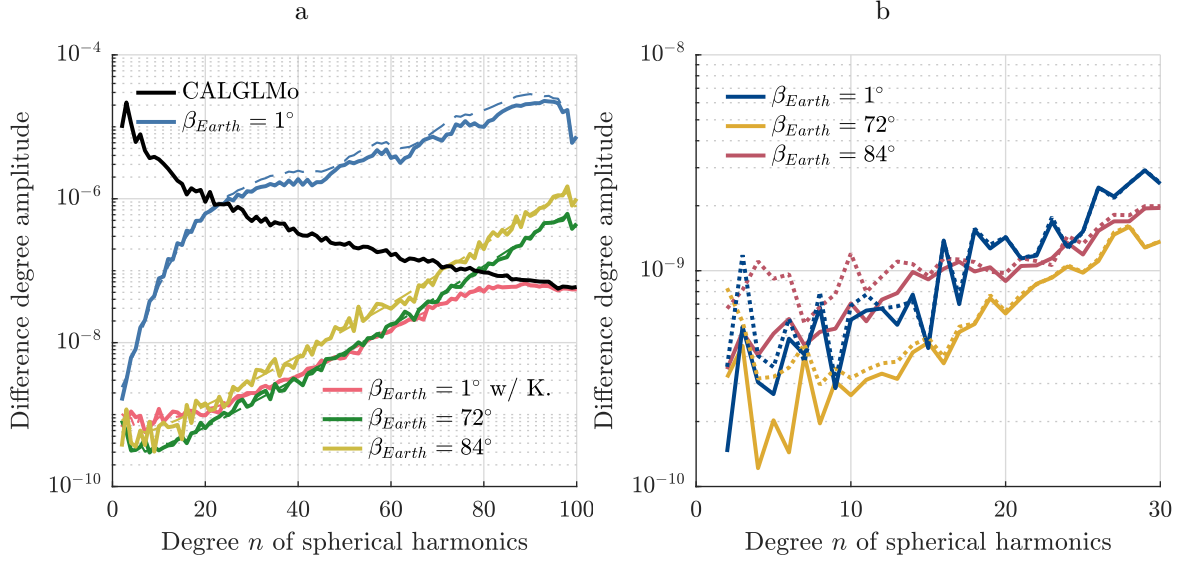


Figure 5.19: Difference degree amplitudes of gravity field solutions for different β_{Earth} , using only Doppler observations (solid line in (a), dotted line in (b)) and formal errors (dashed line in (a)) or combining with altimetry crossovers (solid line in (b)). A Kaula constraint was considered in case of a near edge-on orbit (magenta in (a), dark blue in (b)).

unconstrained gravity field solution.

Using VCE, we combine Doppler and altimetry crossovers observations to estimate the gravity field coefficients together with the rotation parameters. Because the gravity field solution still suffers from aliasing in case $\beta_{Earth} = 1^\circ$, we derived a Kaula-constraint using VCE, to bring the gravity field solution to a level comparable with the more face-on orbit configurations, similarly to the Doppler-only solution. The Kaula-constant K was estimated after the observations NEQs have been combined, resulting in $K = 0.00057$.

The freely estimated rotation parameters improve in all cases with respect to a Doppler-only solution (Tab. 5.7). The right ascension of the north pole α_0 significantly improves when adding crossover to Doppler observations as the formal errors are reduced by one order of magnitude in case $\beta_{Earth} = 1^\circ$, and divided by at least 7 in case of more face-on configurations. The improvement of the declination δ_0 is more moderate, but still appreciable, around 30%. We note more significant improvements in the main libration amplitude W_l and Love number k_2 in the near edge-on case, with an improvement of $\sim 50\%$ and $\sim 85\%$, respectively, in comparison with $\sim 30\%$ and $\sim 40\%$ in case $\beta_{Earth} = 72^\circ$ and $\beta_{Earth} = 84^\circ$. The formal errors on h_2 are overall 0.013, regardless of the β_{Earth} angle.

Moreover, the correlations between the rotation and the gravity field parameters decrease with the addition of altimetry data (Fig. 5.21). In the case of $\beta_{Earth} = 1^\circ$, we can still see correlations between the gravity field parameters only (Fig. 5.20), but this is due to the poor coverage previously discussed. The Kaula constraint helps to reduce these residual correlations, bringing the formal errors of the low degree gravity field coefficients in the

Table 5.7: True (Δ) and formal (f_{err}) errors of rotation, and orientation parameters and Love numbers h_2 and k_2 , estimated together with gravity field parameters.

| β_{Earth} | Obs | | $\alpha_0[^\circ]$ $\times 10^5$ | $\delta_0[^\circ]$ $\times 10^5$ | $W_l[^\circ]$ $\times 10^5$ | $h_2 [-]$ $\times 10^3$ | $k_2 [-]$ $\times 10^3$ |
|--------------------|-------|-----------|-------------------------------------|-------------------------------------|--------------------------------|----------------------------|----------------------------|
| 1° | D | Δ | 220 | 17.2 | 11 | - | 6.34 |
| | | f_{err} | 144 | 8.13 | 21.4 | - | 4.2 |
| | D + X | Δ | 13.8 | 9.17 | 6.31 | 10.1 | 0.127 |
| | | f_{err} | 13.4 | 5.42 | 8.54 | 12.9 | 0.518 |
| 1° Kaula | D | Δ | 151 | 14.2 | 2.12 | - | 0.436 |
| | | f_{err} | 122 | 7.29 | 12.6 | - | 3.42 |
| | D + X | Δ | 11.2 | 8.13 | 9.5 | 4.33 | 0.176 |
| | | f_{err} | 12 | 5.25 | 6.91 | 12.6 | 0.48 |
| 72° | D | Δ | 38.8 | 0.32 | 0.864 | - | 2.56 |
| | | f_{err} | 46.4 | 2.92 | 2.32 | - | 1.45 |
| | D + X | Δ | 2.78 | 0.67 | 0.0366 | 8.14 | 0.272 |
| | | f_{err} | 5.89 | 2.22 | 1.91 | 12.7 | 0.568 |
| 84° | D | Δ | 3.48 | 0.738 | 4.04 | - | 0.564 |
| | | f_{err} | 39.7 | 2.54 | 1.82 | - | 0.333 |
| | D + X | Δ | 1.13 | 1.5 | 3.03 | 29.6 | 0.473 |
| | | f_{err} | 5.7 | 1.77 | 1.38 | 13 | 0.189 |

range of the combined solution for a more face-on orbit.

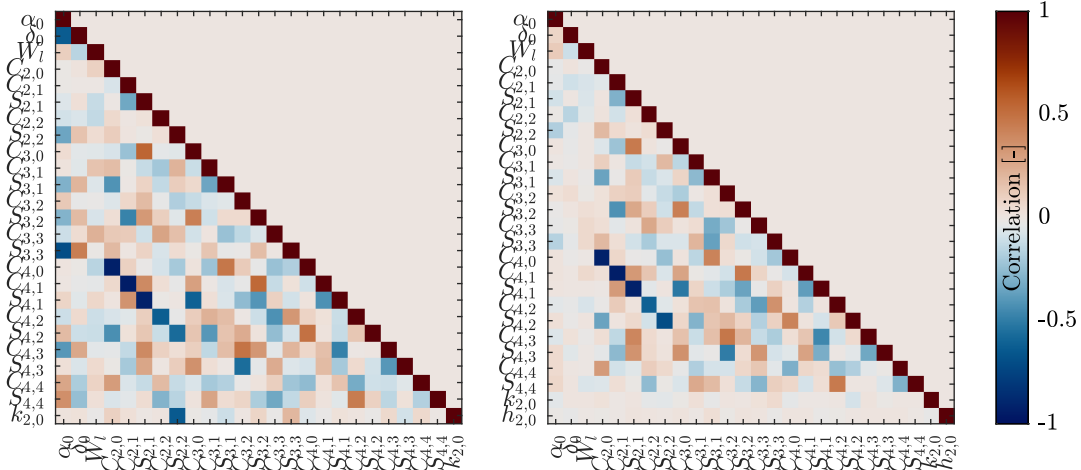


Figure 5.20: Correlations between the freely estimated low-degree gravity field coefficients and rotation parameters using only Doppler observations (left) and combining with crossovers (right) for $\beta_{Earth} = 1^\circ$.

The results presented in this chapter indicate a general improvement of orbit, rotation and gravity field parameters, thanks to the addition of altimetry crossovers in case the probe is poorly tracked. All orbit geometries benefit from the presence of an on-board altimeter,

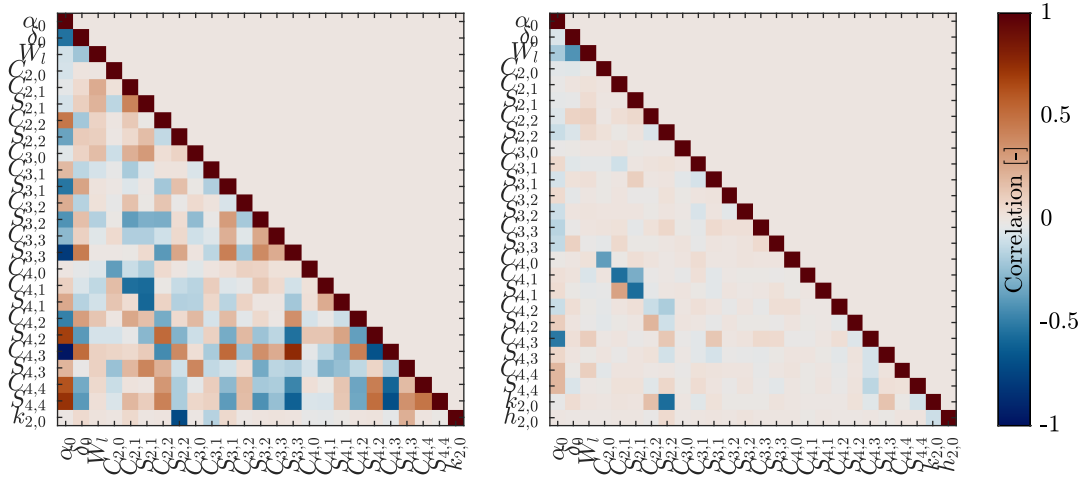


Figure 5.21: Correlations between the freely estimated low-degree gravity field coefficients and rotation parameters using only Doppler observations (left) and combining with crossovers (right) for $\beta_{Earth} = 72^\circ$.

even though the benefit is higher for more face-on orbits in terms of orbit accuracy or for more edge-on orbits in terms of rotation parameters. Additional analyses will be needed in order to conclude on the improvement of the gravity field solution even in the case of more favourable station schedule.

Chapter 6

Summary and conclusions

The Jupiter system is one of the highest priority targets for current and future space explorations, as many questions in a multitude of domains are still to be answered. The four Galilean moons, each interesting and unique worlds embedded in the complex Jovian environment, are going to be explored in detail by the JUICE and Europa Clipper missions. Like all other past missions to Jupiter, these missions are going to explore and investigate on the Galilean moons by means of multiple fly-bys, and JUICE will, for the first time ever, even enter into an orbit around Ganymede. Undoubtedly, a mission including a probe that enters a low orbit around a Galilean moon has the potential to explore and characterize the moon to a significantly higher degree, be it in terms of surface characterizations or the measurement of global geodetic parameters characterizing the interior of the moons or its tidal interaction with the Jupiter system.

The planned Chinese mission Tianwen-4 to the Jovian system aims to send an orbiter around Callisto, the outermost and most preserved of the four Galilean moons. This is a very exciting opportunity to have a detailed look at this moon that best reflects the origin of the Jovian and Solar Systems and which, like in case of Europa and Ganymede, potentially harbours a global ocean of liquid water below an ice crust. Data gathered by a probe that orbits Callisto for an extended time span will offer a much better characterization of the celestial body compared to data of a limited number of fly-bys.

In view of future missions including orbiters around Galilean moons it is then of vital importance to address questions related to sensitivity of different kind of data with respect to parameters of interest. This is the framework and context of the present PhD thesis. The main goal was to perform realistic closed-loop simulations for probes around Europa and Callisto to investigate the impact of a multitude of orbit and mission scenarios, observation types and processing strategies on the determination of orbit and geodetic parameters.

In a first stage, we developed an orbit design package to generate Repetitive Ground Track Orbits in the frame of the three-body problem extended with low degrees of the central body gravity field, allowing to set a large variety of orbit characteristics (altitude, inclination, ground surface coverage, orientation with respect to Earth direction). Based on designed orbits, realistic Doppler observables (from NASA's DSN and the Chinese DSN), accelerometer measurements and laser altimeter ranges were simulated by means of the high-fidelity ephemeris and force models in the planetary branch of the Bernese GNSS

Software (BSW) and pyXover. These data were used to reconstruct orbit and geodetic parameters in global least-squares adjustments, using different orbit parametrization and processing strategies. Comparison to the simulation truth then allowed to assess the impact of numerous details on the sensitivity with respect to parameters of interest.

The current knowledge of gravity field for Europa and Callisto is restricted to degree 2 in spherical harmonics expansion. We demonstrated that we can start our procedures with a degree-2 gravity field as a priori information and are able to estimate a full degree-90 gravity field model within a few iterations from Doppler measurements, either co-estimating the low degrees gravity coefficients in the first iterations, or making use of pseudo-stochastic pulses. The so-derived gravity field solution has the same accuracy as a solution obtained using the true gravity field model as a priori information within only one iteration. This validates the latter, more efficient strategy for all remaining tests.

In the case of Europa, we showed how critical the choice of an orbit is with respect to the quality of gravity field recovery. It is no surprise that the sensitivity of the probe with respect to the gravity field is reduced as the altitude increases, and that the polar gap widens as the orbit is less inclined, resulting in a reduced ground coverage. The ground coverage density, which we characterise by the ground track repetitions, is of natural importance as the short wavelengths of the gravity field cannot be resolved if the ground coverage is too sparse. However, depending on the expected resolution of the gravity field, it is not necessary to avoid ground track repetitions, which can be beneficial for other components of the mission, as they allow for repeated observations of the same point on the surface.

Observation geometry from Earth is also critical. In particular, the angle between the orbital plane and the Earth direction, β_{Earth} , is paramount to consider. Indeed, an edge-on orbit ($\beta_{Earth} = 0^\circ$) provides a better gravity field sensitivity, as most of the gravity signal is along the the line-of-sight from Earth. However, this benefit needs to be balanced with a few drawbacks: higher correlations between the estimated orbital elements within one arc, occultations of the line-of sight by the central body for a part of the orbit (which is larger the lower the altitude of the probe is), and the combination of the occultations by the central body and by Jupiter. The latter are more crucial in the case of Europa than for Callisto, and may result in large gaps in the ground coverage. On the other hand, a face-on orbit ($\beta_{Earth} = 90^\circ$) is detrimental in terms of orbit recovery because of increasing orbit deficiencies, and in terms of gravity field recovery, as the gravity signal acting on the probe is mostly perpendicular to the line-of-sight, resulting in a lower Doppler sensitivity. We also analysed the benefit of Kaula-constrained gravity field solutions to mitigate ground coverage related problems.

We introduced in the BSW the estimation of planetary orientation parameters and Love numbers, which can provide additional constrains on the internal structure of the celestial body. However, because we only considered a 3 months mission, we observed large correlations between the rotation rate of Callisto, and the gravity field parameters estimated using Doppler observations only. The Variance Component Estimation of rotation parameter constraints allowed for a small reduction of such correlations.

Because an accurate modelling of non-gravitational accelerations is a challenging component of orbit determination, we investigated several approaches to model them, using either pseudo-stochastic pulses, realistic accelerometer measurements, or empirical parameters. We found that a precise estimation of accelerometer biases is in general difficult to achieve on a daily basis, and requires proper constraining which we performed using VCE. Empirical parameters and pseudo-stochastic pulses can efficiently absorb such model deficiencies, but we found pulses to have a more negative impact on the orbit and on the gravity field estimation. However, this highly depends on the nature of the mismodelled signal.

Finally, we studied the benefits of extending Doppler-only solutions with altimetry crossovers using the pyXover software library. We focused on a scenario for which the probe is poorly tracked by Doppler measurements, and found that the estimation of orbit and geodetic parameters improved with the addition of crossovers. However, the improvement is highly dependent on the characteristics of our simulation, e.g., the underlying topography roughness. Moreover, the addition of altimetry data allowed for the consistent estimation of the Love number h_2 in a global solution, but also for a visible reduction of correlations among estimated parameters. We also expect the benefit on altimetry crossovers to increase for longer mission, as the number of crossovers would drastically increase.

In conclusion, during this work we developed an extensive simulation environment for orbiters visiting the complex environment of satellite systems in the outer Solar System, which allows for a proper evaluation of mission scenario performances in terms of orbit determination and estimation of geodetic and geophysical parameters. Our work allows the BSW to be applied to the analysis of future missions towards the Jovian moons, as well as other celestial bodies. For instance, the methodology and tools developed in this work could be applied to the analysis of real data from forthcoming planetary orbiter such as BepiColombo and JUICE, which carry an accelerometer and a laser altimeter on board, or even to Uranus exploration, a priority of the latest Decadal Strategy.

Bibliography

- C. H. Acton Jr. Ancillary data services of NASA's navigation and ancillary information facility. *Planetary and Space Science*, 44(1):65–70, 1996. 11, 37
- J. Anderson. Shape, Mean Radius, Gravity Field, and Interior Structure of Callisto. *Icarus*, 153(1):157–161, sep 2001. ISSN 0019-1035. doi: 10.1006/icar.2001.6664. 3, 14, 42, 52, 79
- J. Anderson, G. Schubert, R. Jacobson, E. Lau, W. Moore, and W. Sjogren. Distribution of rock, metals, and ices in Callisto. *Science*, 280(5369):1573–1576, 1998. 3
- J. D. Anderson. Europa's Differentiated Internal Structure: Inferences from Four Galileo Encounters. *Science*, 281(5385):2019–2022, sep 1998. doi: 10.1126/science.281.5385.2019. 3, 14, 42, 52, 79
- A. M. Annex, B. Pearson, B. Seignovert, B. T. Carcich, H. Eichhorn, J. A. Mapel, J. L. F. von Forstner, J. McAuliffe, J. D. del Rio, K. L. Berry, K.-M. Aye, M. Stefko, M. de Val-Borro, S. Kulumani, and S. ya Murakami. SpiceyPy: a Pythonic Wrapper for the SPICE Toolkit. *Journal of Open Source Software*, 5(46):2050, 2020. doi: 10.21105/joss.02050. 113
- B. A. Archinal, C. H. Acton, M. F. A'Hearn, A. Conrad, G. J. Consolmagno, T. Duxbury, D. Hestroffer, J. L. Hilton, R. L. Kirk, S. A. Klioner, D. McCarthy, K. Meech, J. Oberst, J. Ping, P. K. Seidelmann, D. J. Tholen, P. C. Thomas, and I. P. Williams. Report of the IAU working group on cartographic coordinates and rotational elements: 2015. *Celestial Mechanics and Dynamical Astronomy*, 130(3), feb 2018. doi: 10.1007/s10569-017-9805-5. 13, 16, 24, 25, 51, 96
- D. Arnold, S. Bertone, A. Jäggi, G. Beutler, and L. Mervart. GRAIL gravity field determination using the Celestial Mechanics Approach. *Icarus*, 261:182–192, nov 2015. doi: 10.1016/j.icarus.2015.08.015. 7, 18, 69
- S. Asmar and N. Renzetti. The Deep Space Network as an Instrument for Radio Science Research. Technical report, 1993. 29
- S. W. Asmar, J. W. Armstrong, L. Iess, and P. Tortora. Spacecraft Doppler tracking: Noise budget and accuracy achievable in precision radio science observations. *Radio Science*, 40(2):n/a–n/a, mar 2005. ISSN 0048-6604. doi: 10.1029/2004rs003101. 34
- R.-M. Baland and T. Van Hoolst. Librations of the Galilean satellites: The influence of global internal liquid layers. *Icarus*, 209(2):651–664, oct 2010. doi: 10.1016/j.icarus.2010.04.004. 45

- R.-M. Baland, T. Van Hoolst, M. Yseboodt, and Ö. Karatekin. Titan's obliquity as evidence of a subsurface ocean? *Astronomy & Astrophysics*, 530:A141, 2011. 45
- R.-M. Baland, M. Yseboodt, and T. V. Hoolst. Obliquity of the Galilean satellites: The influence of a global internal liquid layer. *Icarus*, 220(2):435–448, aug 2012. doi: 10.1016/j.icarus.2012.05.020. 45
- S. Bame, D. McComas, B. Barraclough, J. Phillips, K. Sofaly, J. Chavez, B. Goldstein, and R. Sakurai. The Ulysses solar wind plasma experiment. *Astronomy and Astrophysics Supplement Series (ISSN 0365-0138)*, vol. 92, no. 2, Jan. 1992, p. 237-265. *Research supported by DOE.*, 92:237–265, 1992. 1
- J. A. Barnes, A. R. Chi, L. S. Cutler, D. J. Healey, D. B. Leeson, T. E. McGunigal, J. A. Mullen, W. L. Smith, R. L. Sydnor, R. F. C. Vessot, and G. M. R. Winkler. • Characterization of Frequency Stability. *IEEE transactions on instrumentation and measurement*, IM-20:105–120, 1971. ISSN 0018-9456. doi: 10.1109/tim.1971.5570702. 34
- K. J. Becker, M. S. Robinson, T. L. Becker, L. A. Weller, K. L. Edmundson, G. A. Neumann, M. E. Perry, and S. C. Solomon. First global digital elevation model of Mercury. In *47th Annual Lunar and Planetary Science Conference*, number 1903, page 2959, 2016. 37
- S. Bertone, M. K. Barker, and E. Mazarico. Pyxover - a python suite of altimetry analysis tools for planetary geodesy, 2020. 8, 35, 113
- S. Bertone, D. Arnold, V. Girardin, M. Lasser, U. Meyer, and A. Jäggi. Assessing reduced-dynamic parametrizations for GRAIL orbit determination and the recovery of independent lunar gravity field solutions. *Earth and Space Science*, 8(6), jun 2021a. doi: 10.1029/2020ea001454. 7, 18, 31, 69
- S. Bertone, E. Mazarico, M. K. Barker, S. Goossens, T. J. Sabaka, G. A. Neumann, and D. E. Smith. Deriving Mercury geodetic parameters with altimetric crossovers from the Mercury Laser Altimeter (MLA). *Journal of Geophysical Research: Planets*, 126(4), apr 2021b. doi: 10.1029/2020je006683. 36, 37, 38, 39, 114, 115, 116
- B. Bertotti, G. Comoretto, and L. Iess. Doppler tracking of spacecraft with multi-frequency links. *Astronomy and Astrophysics (ISSN 0004-6361)*, vol. 269, no. 1-2, p. 608-616., 269:608–616, 1993. 35
- G. Beutler. *Methods of celestial mechanics. Vol. I: Physical, Mathematical, and Numerical Principles*. Springer Berlin, Heidelberg, 2005. ISBN 978-3-540-26870-3. doi: 10.1007/b138225. 9, 10, 18, 20, 56
- G. Beutler, A. Jäggi, L. Mervart, and U. Meyer. The celestial mechanics approach: theoretical foundations. *Journal of Geodesy*, 84(10):605–624, aug 2010. doi: 10.1007/s00190-010-0401-7. 18, 69
- G. Bignami, P. Cargill, B. Schutz, and C. Turon. *Cosmic vision: Space science for Europe 2015-2025*. ESA Publ. Division, 2005. 4
- B. G. Bills and F. Nimmo. Forced obliquity and moments of inertia of Titan. *Icarus*, 196(1):293–297, jul 2008. doi: 10.1016/j.icarus.2008.03.002. 43

- B. G. Bills and F. Nimmo. Rotational dynamics and internal structure of Titan. *Icarus*, 214(1):351–355, jul 2011. doi: 10.1016/j.icarus.2011.04.028. 43, 45
- B. G. Bills and B. R. Scott. Rotation models for the galilean satellites. *Planetary and Space Science*, 219:105474, sep 2022. doi: 10.1016/j.pss.2022.105474. 26
- M. Blanc, O. Prieto-Ballesteros, N. André, J. Gomez-Elvira, G. Jones, V. Sterken, W. Desprats, L. I. Gurvits, K. Khurana, G. Balmino, A. Blöcker, R. Broquet, E. Bunce, C. Cavel, G. Choblet, G. Colins, M. Coradini, J. Cooper, D. Dirkx, D. Fontaine, P. Garnier, D. Gaudin, P. Hartogh, H. Hussmann, A. Genova, L. Iess, A. Jäggi, S. Kempf, N. Krupp, L. Lara, J. Lasue, V. Lainey, F. Leblanc, J.-P. Lebreton, A. Longobardo, R. Lorenz, P. Martins, Z. Martins, J.-C. Marty, A. Masters, D. Mimoun, E. Palumba, V. Parro, P. Regnier, J. Saur, A. Schutte, E. C. Sittler, T. Spohn, R. Srama, K. Stephan, K. Szegő, F. Tosi, S. Vance, R. Wagner, T. V. Hoolst, M. Volwerk, J.-E. Wahlund, F. Westall, and P. Wurz. Joint Europa Mission (JEM): a multi-scale study of Europa to characterize its habitability and search for extant life. *Planetary and Space Science*, 193:104960, nov 2020a. doi: 10.1016/j.pss.2020.104960. 6, 50
- M. Blanc, C. Wang, L. Li, M. Li, L. Wang, Y. Wang, Y. Wang, Q. Zong, N. Andre, O. Mousis, D. Hestroffer, and P. Vernazza. Gan De: Science Objectives and Mission Scenarios For China’s Mission to the Jupiter System. In *EGU General Assembly Conference Abstracts*, page 20179, mar 2020b. doi: 10.5194/egusphere-egu2020-20179. 6, 7
- D. D. Blankenship, D. A. Young, W. B. Moore, and J. C. Moore. Radar sounding of Europa’s subsurface properties and processes: The view from Earth. *Europa*, pages 631–654, 2009. 44
- S. Bolton, J. S. Team, et al. The Juno mission. *Proceedings of the International Astronomical Union*, 6(S269):92–100, 2010. 2
- C. Bonanno and A. Milani. Symmetries and Rank Deficiency in the Orbit Determination around Another Planet. *Celestial Mechanics and Dynamical Astronomy*, 83(1/4):17–33, 2002. doi: 10.1023/a:1020110226569. 71, 74
- T. Böttcher, L. Huber, L. L. Corre, J. Leitner, D. McCarthy, R. Nilsson, C. Teixeira, S. V. Araujo, R. C. Wilson, F. Adjali, M. Altenburg, G. Briani, P. Buchas, A. L. Postollec, and T. Meier. The HADES mission concept – astrobiological survey of Jupiter’s icy moon Europa. *International Journal of Astrobiology*, 8(4):321–329, aug 2009. doi: 10.1017/s147355040999022x. 6
- A. Boutonnet and G. Varga. JUICE: Definition of the GCO with Cycles. Technical report, ESA, 2020. URL ftp://spiftp.esac.esa.int/data/ANCDR/JUICE/man/JUICE_CReMA_Issue_4_Revision_2/Memo_20200429_JUICE_GCO_Cycles.pdf. 49
- P. Cappuccio and G. Cascioli. ESA’s JUICE End-to-End Orbit Determination Simulation to Calibrate On-Board Accelerometer. In *14th Pegasus Student Conference*, Apr. 2018. doi: 10.13016/M2RA3D-VLPM. 28, 107
- P. Cappuccio, A. Hickey, D. Durante, M. D. Benedetto, L. Iess, F. D. Marchi, C. Plainaki, A. Milillo, and A. Mura. Ganymede’s gravity, tides and rotational state from JUICE’s

- 3GM experiment simulation. *Planetary and Space Science*, 187:104902, aug 2020. doi: 10.1016/j.pss.2020.104902. 4, 28
- P. Cappuccio, M. D. Benedetto, D. Durante, and L. Iess. Callisto and Europa Gravity Measurements from JUICE 3GM Experiment Simulation. *The Planetary Science Journal*, 3(8):199, aug 2022. doi: 10.3847/psj/ac83c4. 5
- L. G. Casajus, M. Zannoni, D. Modenini, P. Tortora, F. Nimmo, T. V. Hoolst, D. Buccino, and K. Oudrhiri. Updated Europa gravity field and interior structure from a reanalysis of Galileo tracking data. *Icarus*, page 114187, oct 2021. doi: 10.1016/j.icarus.2020.114187. 14, 79
- L. G. Casajus, A. I. Ermakov, M. Zannoni, J. T. Keane, D. Stevenson, D. R. Buccino, D. Durante, M. Parisi, R. S. Park, P. Tortora, and S. J. Bolton. Gravity Field of Ganymede After the Juno Extended Mission. *Geophysical Research Letters*, 49(24), dec 2022. doi: 10.1029/2022gl099475. 3, 14, 30, 42
- E. Chen, F. Nimmo, and G. Glatzmaier. Tidal heating in icy satellite oceans. *Icarus*, 229: 11–30, 2014. ISSN 0019-1035. doi: 10.1016/j.icarus.2013.10.024. URL <https://www.sciencedirect.com/science/article/pii/S0019103513004533>. 43
- S. Cicalò, G. Schettino, S. D. Ruzza, E. M. Alessi, G. Tommei, and A. Milani. The BepiColombo MORE gravimetry and rotation experiments with the orbit14 software. *Monthly Notices of the Royal Astronomical Society*, 457(2):1507–1521, feb 2016. doi: 10.1093/mnras/stw052. 71
- M. Cinelli, C. Circi, and E. Ortore. Polynomial equations for science orbits around Europa. *Celestial Mechanics and Dynamical Astronomy*, 122(3):199–212, apr 2015. doi: 10.1007/s10569-015-9616-5. 51, 59
- K. Clark, G. Tan-Wang, J. Boldt, R. Greeley, I. Jun, R. Lock, J. Ludwinski, R. Pappalardo, T. V. Houten, and T. Yan. Return to Europa: Overview of the Jupiter Europa Orbiter mission. *Advances in Space Research*, 48(4):629–650, mar 2009. doi: 10.1109/aero.2009.4839315. 6
- O. L. Colombo. Altimetry, orbits and tides. Technical report, 1984. 49
- R. Dach, S. Lutz, P. Walser, and P. Fridez. *Bernese GNSS Software Version 5.2*. University of Bern, Bern Open Publishing, 2015. doi: 10.7892/boris.72297. 7, 10, 23, 49, 69, 112
- M. E. Davies, V. K. Abalakin, M. Bursa, J. H. Lieske, B. Morando, D. Morrison, P. K. Seidelmann, A. Sinclair, B. Yallop, and Y. Tjuflin. Report of the IAU/IAG/COSPAR working group on cartographic coordinates and rotational elements of the planets and satellites: 1994. *Celestial Mechanics and Dynamical Astronomy*, 63:127–148, 1995. 26
- W. Desprats, S. Bertone, D. Arnold, A. Jäggi, and M. Blanc. Influence of low orbit design and strategies for gravity field recovery of Europa. *Planetary and Space Science*, 226: 105631, feb 2023. doi: 10.1016/j.pss.2022.105631. 8, 18, 22, 69

- M. Di Benedetto, P. Cappuccio, S. Molli, L. Federici, and A. Zavoli. Analysis of 3GM Callisto Gravity Experiment of the JUICE Mission. *Planetary and Space Science*, 2021. doi: 10.48550/ARXIV.2101.03401. 5
- C. J. Donlon, R. Cullen, L. Giulicchi, P. Vuilleumier, C. R. Francis, M. Kuschnerus, W. Simpson, A. Bouridah, M. Caleno, R. Bertoni, et al. The Copernicus Sentinel-6 mission: Enhanced continuity of satellite sea level measurements from space. *Remote Sensing of Environment*, 258:112395, 2021. 49
- E. Doornbos. *Thermospheric density and wind determination from satellite dynamics*. Springer Science & Business Media, 2012. 17
- D. Durante, D. Hemingway, P. Racioppa, L. Iess, and D. Stevenson. Titan's gravity field and interior structure after cassini. *Icarus*, 326:123–132, jul 2019. doi: 10.1016/j.icarus.2019.03.003. 42
- D. Durante, T. Guillot, L. Iess, D. J. Stevenson, C. R. Mankovich, S. Markham, E. Galanti, Y. Kaspi, M. Zannoni, L. G. Casajus, G. Lari, M. Parisi, D. R. Buccino, R. S. Park, and S. J. Bolton. Juno spacecraft gravity measurements provide evidence for normal modes of jupiter. *Nature Communications*, 13(1), aug 2022. doi: 10.1038/s41467-022-32299-9. 16
- R. O. Fimmel, W. Swindell, and E. Burgess. Pioneer Odyssey. NASA SP-349. *NASA Special Publication*, 349, 1977. 1
- W. M. Folkner, J. G. Williams, D. H. Boggs, R. S. Park, and P. Kuchynka. The planetary and lunar ephemerides DE430 and DE431. *Interplanetary Network Progress Report*, 196(1):42–196, 2014. 12
- P. Gao and D. J. Stevenson. Nonhydrostatic effects and the determination of icy satellites' moment of inertia. *Icarus*, 226(2):1185–1191, nov 2013. doi: 10.1016/j.icarus.2013.07.034. 3, 41, 42
- A. Genova, D. E. Smith, R. Canup, T. Hurford, S. Goossens, E. Mazarico, G. A. Neumann, M. T. Zuber, F. Nimmo, M. Wieczorek, and E. Bierhaus. Geodetic investigations of the mission concept MAGIC to reveal Callisto's internal structure. *Acta Astronautica*, 195: 68–76, jun 2022. doi: 10.1016/j.actaastro.2022.02.013. 5, 6, 45, 46, 98, 99
- S. Goossens, K. Matsumoto, D. D. Rowlands, F. G. Lemoine, H. Noda, and H. Araki. Orbit determination of the SELENE satellites using multi-satellite data types and evaluation of SELENE gravity field models. *Journal of Geodesy*, 85(8):487–504, feb 2011. doi: 10.1007/s00190-011-0446-2. 111, 112
- S. Goossens, E. Mazarico, Y. Ishihara, B. Archinal, and L. Gaddis. Improving the geometry of Kaguya extended mission data through refined orbit determination using laser altimetry. *Icarus*, 336:113454, jan 2020. doi: 10.1016/j.icarus.2019.113454. 36
- O. Grasset, M. K. Dougherty, A. Coustenis, E. J. Bunce, C. Erd, D. Titov, M. Blanc, A. Coates, P. Drossart, L. N. Fletcher, H. Hussmann, R. Jaumann, N. Krupp, J.-P. Lebreton, O. Prieto-Ballesteros, P. Tortora, F. Tosi, and T. V. Hoolst. JUPITER ICy

- moons Explorer (JUICE): An ESA mission to orbit Ganymede and to characterise the Jupiter system. *Planetary and Space Science*, 78:1–21, apr 2013. ISSN 0032-0633. doi: 10.1016/j.pss.2012.12.002. 4, 50
- R. Greeley, J. Klemaszewski, R. Wagner, G. I. Team, et al. Galileo views of the geology of Callisto. *Planetary and Space Science*, 48(9):829–853, 2000. 2
- R. Greeley, C. F. Chyba, J. Head, T. B. McCord, W. B. McKinnon, R. T. Pappalardo, P. H. Figueredo, et al. Geology of Europa. *Jupiter: The planet, satellites and magnetosphere*, pages 329–362, 2004. 2
- C. Hansen, S. Bolton, A. Sulaiman, S. Duling, F. Bagenal, M. Brennan, J. Connerney, G. Clark, J. Lunine, S. Levin, et al. Juno’s close encounter with Ganymede—an overview. *Geophysical Research Letters*, 49(23):e2022GL099285, 2022. 2, 14
- O. Hartkorn and J. Saur. Induction signals from Callisto’s ionosphere and their implications on a possible subsurface ocean. *Journal of Geophysical Research: Space Physics*, 122(11): 11–677, 2017. 3
- G. He, M. Liu, X. Gao, X. Du, H. Zhou, and H. Zhu. Chinese deep space stations: a brief review [antenna applications corner]. *IEEE Antennas and Propagation Magazine*, 64(1): 102–111, 2022. 29
- D. Hemingway, L. Iess, R. Tajeddine, and G. Tobie. The interior of Enceladus. *Enceladus and the icy moons of Saturn*, pages 57–77, 2018. doi: 10.2458/azu_uapress_9780816537075-ch. 42
- A. HosseiniArani. *BepiColombo Laser Altimeter (BELA) performance evaluation: from laboratory tests to simulations of flight observations*. PhD thesis, Universität Bern, 2020. 36, 112
- S. M. Howell and R. T. Pappalardo. NASA’s Europa Clipper - a mission to a potentially habitable ocean world. *Nature Communications*, 11(1), Mar. 2020. ISSN 2041-1723. doi: 10.1038/s41467-020-15160-9. 2, 3, 5
- W. Hubbard and J. Anderson. Possible flyby measurements of galilean satellite interior structure. *Icarus*, 33(2):336–341, 1978. 41
- H. Hussmann, K. Lingenauber, R. Kallenbach, K. Enya, N. Thomas, L. M. Lara, C. Althaus, H. Araki, T. Behnke, J. M. Castro-Marin, H. Eisenmenger, T. Gerber, M. Herranz de la Revilla, C. Hüttig, K. Ishibashi, J. Jiménez-Ortega, J. Kimura, M. Kobayashi, H.-G. Lötze, A. Lichopoj, F. Lüdicke, I. Martínez-Navajas, H. Michaelis, N. Namiki, H. Noda, J. Oberst, S. Oshigami, J. P. Rodríguez García, J. Rodrigo, K. Rösner, A. Stark, G. Steinbrügge, P. Thabaut, S. del Togno, K. Touhara, S. Villamil, B. Wendler, K. Wickhusen, and K. Willner. The Ganymede laser altimeter (GALA): key objectives, instrument design, and performance. *CEAS Space Journal*, 11(4):381–390, Oct. 2019. ISSN 1868-2510. doi: 10.1007/s12567-019-00282-8. 4, 36, 38, 116
- V. Iafolla, D.-M. Lucchesi, S. Nozzoli, and F. Santoli. The BepiColombo mission to Mercury: Reaction wheels desaturation manoeuvres and the ISA accelerometer ΔV measurements. *Planetary and Space Science*, 59(1):51–62, 2011. 74

- L. Iess, N. J. Rappaport, R. A. Jacobson, P. Racioppa, D. J. Stevenson, P. Tortora, J. W. Armstrong, and S. W. Asmar. Gravity Field, Shape, and Moment of Inertia of Titan. *science*, 327:1367–1369, 2010. ISSN 0036-8075. doi: 10.1126/science.1182583. 42, 67
- L. Iess, M. Di Benedetto, M. Marabucci, P. Racioppa, et al. Improved Doppler tracking systems for deep space navigation. In *International Symposium on Space Flight Dynamics (ISSFD)*, 2012. 34
- L. Iess, M. D. Benedetto, N. James, M. Mercolino, L. Simone, and P. Tortora. Astra: Interdisciplinary study on enhancement of the end-to-end accuracy for spacecraft tracking techniques. *Acta Astronautica*, 94(2):699–707, feb 2014a. doi: 10.1016/j.actaastro.2013.06.011. 34, 35
- L. Iess, D. J. Stevenson, M. Parisi, D. Hemingway, R. A. Jacobson, J. I. Lunine, F. Nimmo, J. W. Armstrong, S. W. Asmar, M. Ducci, and P. Tortora. The Gravity Field and Interior Structure of Enceladus. *Science*, 344:78–80, 2014b. ISSN 0036-8075. doi: 10.1126/science.1250551. 42
- K. H. Ilk, J. Flury, R. Rummel, P. Schwintzer, W. Bosch, C. Haas, J. Schröter, D. Stammer, W. Zahel, H. Miller, et al. Mass transport and mass distribution in the Earth system. Technical report, Institut für Astronomische und Physikalische Geodäsie, 2005. 13
- R. A. Jacobson. JUP310, 2013. URL https://naif.jpl.nasa.gov/pub/naif/generic_kernels/spk/satellites/a_old_versions/jup310.bsp. 12, 15, 16, 26
- A. Jäggi. *Pseudo-stochastic Orbit Modeling of Low Earth Satellites using the Global Positioning System*. PhD thesis, Universität Bern, 2007. 18
- A. Jäggi, G. Beutler, U. Meyer, H. Bock, and L. Mervart. The Role of Position Information for the Analysis of K-Band Data: Experiences from GRACE and GOCE for GRAIL Gravity Field Recovery. In N. Sneeuw, P. Novák, M. Crespi, and F. Sansò, editors, *VIII Hotine-Marussi Symposium on Mathematical Geodesy*, pages 157–163, Cham, 2015. Springer International Publishing. ISBN 978-3-319-30530-1. 7
- H. M. Jara-Orué and B. L. Vermeersen. The forced libration of Europa’s deformable shell and its dependence on interior parameters. *Icarus*, 229:31–44, 2014. ISSN 0019-1035. doi: 10.1016/j.icarus.2013.10.027. URL <https://www.sciencedirect.com/science/article/pii/S0019103513004569>. 45
- X. Jia, M. G. Kivelson, K. K. Khurana, and W. S. Kurth. Evidence of a plume on Europa from Galileo magnetic and plasma wave signatures. *Nature Astronomy*, 2(6):459–464, 2018. 3
- Q. Jing and M. Li. Integrated trajectory optimization for Jupiter missions with single-satellite-aided capture. *Celestial Mechanics and Dynamical Astronomy*, 135(6):57, 2023. doi: .org/10.1007/s10569-023-10169-w. 7
- W. M. Kaula. Determination of the Earth’s gravitational field. *Reviews of Geophysics*, 1(4):507–551, 1963. doi: <https://doi.org/10.1029/RG001i004p00507>. URL <https://agupubs.onlinelibrary.wiley.com/doi/abs/10.1029/RG001i004p00507>. 86

- W. M. Kaula. *Theory of Satellite Geodesy, applications of satellites to Geodesy*. Blaisdell Publishing Company, Waltham, MA., USA, 1966. 13
- K. Khurana, M. Kivelson, C. Russell, R. Walker, and D. Southwood. Absence of an internal magnetic field at Callisto. *Nature*, 387(6630):262–264, 1997. 3
- K. Khurana, M. Kivelson, D. Stevenson, G. Schubert, C. Russell, R. Walker, and C. Polanskey. Induced magnetic fields as evidence for subsurface oceans in Europa and Callisto. *Nature*, 395(6704):777–780, 1998. 3
- K. K. Khurana, M. G. Kivelson, and C. T. Russell. Searching for Liquid Water in Europa by Using Surface Observatories. *Astrobiology*, 2(1):93–103, 2002. doi: 10.1089/153110702753621376. PMID: 12449858. 44
- M. G. Kivelson, K. K. Khurana, C. T. Russell, M. Volwerk, R. J. Walker, and C. Zimmer. Galileo Magnetometer Measurements: A Stronger Case for a Subsurface Ocean at Europa. *Science*, 289(5483):1340–1343, aug 2000. doi: 10.1126/science.289.5483.1340. 3
- A. J. Kliore, D. P. Hinson, F. M. Flasar, A. F. Nagy, and T. E. Cravens. The ionosphere of Europa from Galileo radio occultations. *Science*, 277(5324):355–358, 1997. 30
- J. Kusche. Noise variance estimation and optimal weight determination for GOCE gravity recovery. *Advances in Geosciences*, 1:81–85, 2003. doi: 10.5194/adgeo-1-81-2003. URL <https://adgeo.copernicus.org/articles/1/81/2003/>. 21
- V. Lainey, L. Duriez, and A. Vienne. Synthetic representation of the Galilean satellites' orbital motions from L1 ephemerides. *Astronomy & Astrophysics*, 456(2):783–788, aug 2006. doi: 10.1051/0004-6361:20064941. 15, 26
- M. Lara and R. Russell. Computation of a Science Orbit About Europa. *Journal of Guidance, Control, and Dynamics*, 30(1):259–263, jan 2007. doi: 10.2514/1.22493. 52
- M. Lasser. *Noise Modelling for GRACE Follow-On Observables in the Celestial Mechanics Approach*. PhD thesis, Universität Bern, 2023. 21
- F. G. Lemoine, D. E. Smith, D. D. Rowlands, M. Zuber, G. Neumann, D. Chinn, and D. Pavlis. An improved solution of the gravity field of Mars (GMM-2B) from Mars Global Surveyor. *Journal of Geophysical Research: Planets*, 106(E10):23359–23376, 2001. 111
- F. G. Lemoine, S. Goossens, T. J. Sabaka, J. B. Nicholas, E. Mazarico, D. D. Rowlands, B. D. Loomis, D. S. Chinn, G. A. Neumann, D. E. Smith, and M. T. Zuber. GRGM900c: A degree 900 lunar gravity model from GRAIL primary and extended mission data. *Geophysical Research Letters*, 41(10):3382–3389, may 2014. doi: 10.1002/2014GL060027. 14
- J. Lieske. Poles of the Galilean satellites. *Astronomy and Astrophysics*, 75:158–163, 1979. 24
- M. Marabucci. *The determination of the Hermean gravity and topography from radio science and laser altimeter data of the mission BepiColombo*. PhD thesis, Sapienza Università di Roma, Facoltà di Ingegneria, 2013. 112

- E. Mazarico, D. D. Rowlands, G. A. Neumann, D. E. Smith, M. H. Torrence, F. G. Lemoine, and M. T. Zuber. Orbit determination of the Lunar Reconnaissance Orbiter. *Journal of Geodesy*, 86(3):193–207, sep 2012. doi: 10.1007/s00190-011-0509-4. 111
- E. Mazarico, M. K. Barker, G. A. Neumann, M. T. Zuber, and D. E. Smith. Detection of the lunar body tide by the Lunar Orbiter Laser Altimeter. *Geophysical Research Letters*, 41(7):2282–2288, 2014. 111
- E. Mazarico, A. Genova, G. A. Neumann, D. E. Smith, and M. T. Zuber. Simulated recovery of Europa’s global shape and tidal Love numbers from altimetry and radio tracking during a dedicated flyby tour. *Geophysical Research Letters*, 42(9):3166–3173, may 2015. doi: 10.1002/2015gl063224. 15, 67
- E. Mazarico, G. A. Neumann, M. K. Barker, S. Goossens, D. E. Smith, and M. T. Zuber. Orbit determination of the Lunar Reconnaissance Orbiter: Status after seven years. *Planetary and Space Science*, 162:2–19, nov 2018. doi: 10.1016/j.pss.2017.10.004. 36, 111
- E. Mazarico, D. Buccino, J. Castillo-Rogez, A. J. Dombard, A. Genova, H. Hussmann, W. S. Kiefer, J. I. Lunine, W. B. McKinnon, F. Nimmo, et al. The Europa Clipper Gravity and Radio Science Investigation. *Space Science Reviews*, 219(4):30, 2023. doi: .org/10.1007/s11214-023-00972-0. 5, 30
- W. B. McKinnon. Mystery of Callisto: Is it undifferentiated? *Icarus*, 130(2):540–543, 1997. 3, 42
- A. Milani, A. M. Nobili, and P. Farinella. *Non-gravitational perturbations and satellite geodesy*. 1987. 17
- W. B. Moore and G. Schubert. The tidal response of Europa. *Icarus*, 147(1):317–319, 2000. doi: 10.1006/icar.2000.6460,. 44
- W. B. Moore and G. Schubert. The tidal response of Ganymede and Callisto with and without liquid water oceans. *Icarus*, 166(1):223–226, nov 2003. doi: 10.1016/j.icarus.2003.07.001. 44
- D. Morrison and N. D. Morrison. Photometry of the Galilean satellites. In *IAU Colloq. 28: Planetary Satellites*, page 363, 1977. 17
- D. Morrison and J. Samz. *Voyage to Jupiter:(NASA SP-439)*. *US Government Printing Office, Washington, DC*, 1980. 1
- T. D. Moyer. Formulation for Observed and Computed Values of Deep Space Network Data Types for Navigation, 2003. 29, 30, 31
- W. H. Munk, G. J. MacDonald, and D. L. Anderson. The rotation of the Earth: a geophysical discussion, 1977. 41
- G. A. Neumann, D. D. Rowlands, F. G. Lemoine, D. E. Smith, and M. T. Zuber. Crossover analysis of Mars Orbiter Laser Altimeter data. *Journal of Geophysical Research: Planets*, 106(E10):23753–23768, 2001. 38, 111

- F. Nimmo and R. Pappalardo. Ocean worlds in the outer solar system. *Journal of Geophysical Research: Planets*, 121(8):1378–1399, 2016. doi: 10.1002/2016JE005081. 43, 44
- E. Ortore, C. Circi, and M. Cinelli. Optimal orbits around Ganymede for the JUICE mission. *Aerospace Science and Technology*, 46:282–286, oct 2015. ISSN 1270-9638. doi: 10.1016/j.ast.2015.07.021. 49
- R. S. Park, B. Bills, B. B. Buffington, W. M. Folkner, A. S. Konopliv, T. J. Martin-Mur, N. Mastrodemos, T. P. McElrath, J. E. Riedel, and M. M. Watkins. Improved detection of tides at Europa with radiometric and optical tracking during flybys. *Planetary and Space Science*, 112:10–14, jul 2015. doi: 10.1016/j.pss.2015.04.005. 5
- T. A. Pavlak. *Trajectory design and orbit maintenance strategies in multi-body dynamical regimes*. PhD thesis, Purdue University, 2013. 53
- S. Peale and M. H. Lee. A primordial origin of the Laplace relation among the Galilean satellites. *Science*, 298(5593):593–597, 2002. 3
- G. Petit and B. Luzum. IERS Conventions (2010). Technical report, International Earth Rotation and Reference Systems Service, 2010. 15
- C. B. Phillips and R. T. Pappalardo. Europa Clipper Mission Concept: Exploring Jupiter’s Ocean Moon. *Eos, Transactions American Geophysical Union*, 95(20):165–167, may 2014. doi: 10.1002/2014eo200002. 4, 5
- P. H. Phipps. *Distribution of plasma in the Io plasma torus from radio occultations during the Juno epoch*. PhD thesis, Boston University, 2019. 30
- R. Radau. Mémoires et observations. Remarques sur la théorie de la figure de la Terre. *Bulletin Astronomique, Serie I, vol. 2, pp. 157-161*, 2:157–161, 1885. 41
- N. Rambaux, T. V. Hoolst, and Ö. Karatekin. Librational response of Europa, Ganymede, and Callisto with an ocean for a non-Keplerian orbit. *Astronomy & Astrophysics*, 527:A118, feb 2011. doi: 10.1051/0004-6361/201015304. 27, 45
- N. Rappaport, B. Bertotti, G. Giampieri, and J. D. Anderson. Doppler measurements of the quadrupole moments of titan. *Icarus*, 126:313–323, 1997. ISSN 0019-1035. doi: 10.1006/icar.1996.5661. 41
- J. H. Roberts, W. B. McKinnon, C. M. Elder, G. Tobie, J. B. Biersteker, D. Young, R. S. Park, G. Steinbrügge, F. Nimmo, S. M. Howell, et al. Exploring the Interior of Europa with the Europa Clipper. *Space Science Reviews*, 219(6):46, 2023. doi: .org/10.1007/s11214-023-00990-y. 3, 44
- C. J. Rodriguez-Solano. Impact of albedo modelling on GPS orbits. Master’s thesis, 2009. 17
- L. Roth, J. Saur, K. D. Retherford, D. F. Strobel, P. D. Feldman, M. A. McGrath, and F. Nimmo. Transient Water Vapor at Europa’s South Pole. *Science*, 343(6167):171–174, jan 2014. ISSN 0036-8075. doi: 10.1126/science.1247051. 3

- D. D. Rowlands, D. E. Pavlis, F. G. Lemoine, G. A. Neumann, and S. B. Luthcke. The use of laser altimetry in the orbit and attitude determination of mars global surveyor. *Geophysical Research Letters*, 26(9):1191–1194, may 1999. doi: 10.1029/1999gl1900223. 38, 111
- D. D. Rowlands, F. G. Lemoine, D. S. Chinn, and S. B. Luthcke. A simulation study of multi-beam altimetry for lunar reconnaissance orbiter and other planetary missions. *Journal of Geodesy*, 83(8):709–721, nov 2009. doi: 10.1007/s00190-008-0285-y. 111
- C. T. Russell. *The Cassini-Huygens Mission*, volume 114. Springer, 2005. URL <https://ui.adsabs.harvard.edu/abs/2005chm..book.....R.2>
- C. T. Russell. *The Galileo Mission*. Springer Science & Business Media, 2012. 2
- R. Russell and M. Lara. Repeat Ground Track Lunar Orbits in the Full-Potential Plus Third-Body Problem. In *AIAA/AAS Astrodynamics Specialist Conference and Exhibit*. American Institute of Aeronautics and Astronautics, aug 2006. doi: 10.2514/6.2006-6750. 65, 66
- R. Russell and S. Thurman. An analytic development of orbit determination for a distant, planetary orbiter. *The Telecommunications and Data Acquisition Report*, 1989. 71, 73
- R. P. Russell. Global search for planar and three-dimensional periodic orbits near Europa. *The Journal of the Astronautical Sciences*, 54(2):199–226, jun 2006. ISSN 0021-9142. doi: 10.1007/bf03256483. 53
- T. Sasaki, G. R. Stewart, and S. Ida. Origin of the different architectures of the Jovian and Saturnian satellite systems. *The Astrophysical Journal*, 714(2):1052, 2010. 1
- B. V. Semenov. SPacecraft Kernel description. https://naif.jpl.nasa.gov/pub/naif/toolkit_docs/FORTRAN/req/spk.html, 2021. Last accessed on 2023-12-08. 11
- L. F. Shampine and M. W. Reichelt. The MATLAB ODE suite. *SIAM journal on scientific computing*, 18(1):1–22, 1997. 49
- A. Shapira, A. Stern, S. Prazot, R. Mann, Y. Barash, E. Detoma, and B. Levy. An Ultra Stable Oscillator for the 3GM experiment of the JUICE mission. In *2016 European Frequency and Time Forum (EFTF)*, pages 1–5. IEEE, 2016. 4
- I. I. Shapiro. Fourth test of general relativity. *Physical Review Letters*, 13(26):789, 1964. 30
- S. S. Sheppard, D. J. Tholen, M. Alexandersen, and C. A. Trujillo. New Jupiter and Saturn Satellites Reveal New Moon Dynamical Families. *Research Notes of the AAS*, 7(5):100, 2023. 1
- C. Shum, B. Schutz, B. Tapley, and B. Zhang. Altimeter crossover methods for precision orbit determination and the mapping of geophysical parameters. *Journal of the Astronautical Sciences*, 38:355–368, 1990. 38, 111

- B. A. Smith, L. A. Soderblom, T. V. Johnson, A. P. Ingersoll, S. A. Collins, E. M. Shoemaker, G. Hunt, H. Masursky, M. H. Carr, M. E. Davies, et al. The Jupiter system through the eyes of Voyager 1. *Science*, 204(4396):951–972, 1979. 1
- D. E. Smith, M. T. Zuber, R. M. Canup, T. Hurford Jr, B. Bierhaus, M. T. Bland, V. J. Bray, J. E. Connerney, A. Genova, C. Johnson, et al. MAGIC, A Discovery Proposal to the Icy Moon Callisto. In *AGU Fall Meeting Abstracts*, volume 2019, pages P34C–03, 2019. 6
- D. E. Smith, F. Nimmo, K. Khurana, C. L. Johnson, M. Wieczorek, M. T. Zuber, C. Paty, A. Genova, E. Mazarico, L. Prockter, G. A. Neumann, J. E. Connerney, E. B. Bierhaus, S. J. Goossens, M. K. Barker, P. B. James, J. Head, and Brown. Callisto: A Guide to the Origin of the Jupiter System [White paper]. 2020. 3, 6, 7
- N. Sneeuw. *A Semi-Analytical Approach to Gravity Field Analysis from Satellite Observations*. Dissertation, Technische Universität München, 2000. 85
- W. B. Sparks, B. E. Schmidt, M. A. McGrath, K. P. Hand, J. R. Spencer, M. Cracraft, and S. E. Deustua. Active cryovolcanism on Europa? *The Astrophysical Journal Letters*, 839(2):L18, 2017. 3
- G. Steinbrügge, A. Stark, H. Hussmann, F. Sohl, and J. Oberst. Measuring tidal deformations by laser altimetry. A performance model for the Ganymede Laser Altimeter. *Planetary and Space Science*, 117:184–191, Nov. 2015. ISSN 0032-0633. doi: 10.1016/j.pss.2015.06.013. 4, 36
- G. Steinbrügge, D. Schroeder, M. Haynes, H. Hussmann, C. Grima, and D. Blankenship. Assessing the potential for measuring Europa’s tidal Love number h₂ using radar sounder and topographic imager data. *Earth and Planetary Science Letters*, 482:334–341, Jan. 2018a. ISSN 0012-821X. doi: 10.1016/j.epsl.2017.11.028. 5, 115
- G. Steinbrügge, A. Stark, H. Hussmann, K. Wickhusen, and J. Oberst. The performance of the BepiColombo Laser Altimeter (BELA) prior launch and prospects for Mercury orbit operations. *Planetary and Space Science*, 159:84–92, Sept. 2018b. ISSN 0032-0633. doi: 10.1016/j.pss.2018.04.017. 36
- G. Steinbrügge, T. Steinke, R. Thor, A. Stark, and H. Hussmann. Measuring Ganymede’s Librations with Laser Altimetry. *Geosciences*, 9(7):320, jul 2019. doi: 10.3390/geosciences9070320. 4, 26, 62
- S. A. Stern. The New Horizons Pluto Kuiper belt mission: an overview with historical context. *New Horizons: Reconnaissance of the Pluto-Charon System and the Kuiper Belt*, pages 3–21, 2009. 2
- N. Thomas, H. Hussmann, T. Spohn, L. Lara, U. Christensen, M. Affolter, T. Bandy, T. Beck, S. Chakraborty, U. Geissbühler, et al. The BepiColombo laser altimeter. *Space science reviews*, 217:1–62, 2021. 37, 116
- P. Tricarico. Multi-layer hydrostatic equilibrium of planets and synchronous moons: theory and application to Ceres and to solar system moons. *The Astrophysical Journal*, 782(2): 99, feb 2014. doi: 10.1088/0004-637x/782/2/99. 41

- P. Truscott, D. Heynderickx, A. Sicard-Piet, and S. Bourdarie. Simulation of the radiation environment near Europa using the geant4-based PLANETOCOSMICS-J model. *IEEE Transactions on Nuclear Science*, 58(6):2776–2784, 2011. 6
- M. van Gelderen and R. Koop. The use of degree variances in satellite gradiometry. *Journal of Geodesy*, 71(6):337–343, may 1997. doi: 10.1007/s001900050101. 92
- T. Van Hoolst and V. Dehant. Influence of triaxiality and second-order terms in flattenings on the rotation of terrestrial planets I. Formalism and rotational normal modes. *Physics of the Earth and Planetary Interiors*, 134(1-2):17–33, 2002. 42
- T. Van Hoolst and C. Jacobs. Mercury’s tides and interior structure. *Journal of Geophysical Research: Planets*, 108(E11), 2003. 36
- T. Van Hoolst, N. Rambaux, Ö. Karatekin, V. Dehant, and A. Rivoldini. The librations, shape, and icy shell of Europa. *Icarus*, 195(1):386–399, may 2008. doi: 10.1016/j.icarus.2007.12.011. 13, 27, 42, 43
- T. Van Hoolst, R.-M. Baland, and A. Trinh. On the librations and tides of large icy satellites. *Icarus*, 226(1):299–315, sep 2013. doi: 10.1016/j.icarus.2013.05.036. 41, 45
- S. Villamil, D. Dirkx, A. Stark, and H. Hussmann. Improvement of orbit determination using laser altimeter crossovers: JUICE mission case study. *Acta Astronautica*, 182: 587–598, may 2021. doi: 10.1016/j.actaastro.2021.02.005. 36, 112, 113, 122
- J. M. Wahr, M. T. Zuber, D. E. Smith, and J. I. Lunine. Tides on Europa, and the thickness of Europa’s icy shell. *Journal of Geophysical Research: Planets*, 111(E12):n/a–n/a, dec 2006. ISSN 0148-0227. doi: 10.1029/2006je002729. 6, 15, 45, 85
- Q. Wang. Prospect of International Cooperation in China Lunar & Planetary Exploration Programs. In *73rd International Astronautical Congress (IAC 2022)*, 2022. 7
- Y. Wei, Z. Yao, and W. Wan. China’s roadmap for planetary exploration. *Nature Astronomy*, 2(5):346–348, 2018. 7
- M. A. Wieczorek. Gravity and topography of the terrestrial planets. *Treatise on geophysics*, 10:165–206, 2015. 45, 85
- L. J. Wood. Orbit determination singularities in the Doppler tracking of a planetary orbiter. *Journal of Guidance, Control, and Dynamics*, 9(4):485–494, jul 1986. doi: 10.2514/3.20136. 71, 73
- X. Wu, Y. E. Bar-Sever, W. M. Folkner, J. G. Williams, and J. F. Zumberge. Probing Europa’s hidden ocean from tidal effects on orbital dynamics. *Geophysical Research Letters*, 28(11):2245–2248, jun 2001. ISSN 0094-8276. doi: 10.1029/2000gl012814. 6, 44, 45, 85
- M. Zannoni and P. Tortora. Numerical Error in Interplanetary Orbit Determination Software. *Journal of Guidance, Control, and Dynamics*, 36(4):1008–1018, jul 2013. ISSN 0731-5090. doi: 10.2514/1.59294. 32, 34

Scientific environment and publications

The research conducted in scope of this thesis has been carried out at the Astronomical Institute of the University of Bern (AIUB). It has been supported by the Swiss National Science Foundation (SNSF, grant no. 200021_185056 “Callisto geodesy: A simulation study to support further space missions to the Jovian system”). Results were presented at the occasion of several international conferences. Calculations were performed on UBELIX (<https://www.id.unibe.ch/hpc>), the HPC cluster at the University of Bern. Moreover, the following scientific publications are related to it.

Influence of low orbit design and strategies for gravity field recovery of Europa. William Desprats, Stefano Bertone, Daniel Arnold, Adrian Jäggi, Michel Blanc. *Planetary and Space Science*, Volume 226, 2023. doi:10.1016/j.pss.2022.105631. <https://www.sciencedirect.com/science/article/pii/S0032063322002173>

Combination of altimetry crossover and Doppler observables for orbit determination and geodetic parameter recovery: application to Callisto. William Desprats, Stefano Bertone, Daniel Arnold, Martin Lasser, Adrian Jäggi, Michel Blanc. *Submitted to Acta Astronautica*.

Declaration

I declare herewith that this thesis is my own work and that I have not used any sources other than those stated. I have indicated the adoption of quotations as well as thoughts taken from other authors as such in the thesis. I am aware that the Senate pursuant to Article 36 paragraph 1 litera r of the University Act of September 5th, 1996 and Article 69 of the University Statute of June 7th, 2011 is authorized to revoke the doctoral degree awarded on the basis of this thesis. For the purposes of evaluation and verification of compliance with the declaration of originality and the regulations governing plagiarism, I hereby grant the University of Bern the right to process my personal data and to perform the acts of use this requires, in particular, to reproduce the written thesis and to store it permanently in a database, and to use said database, or to make said database available, to enable comparison with theses submitted by others.

Curriculum vitae

Name: William Desprats
Date of birth: 09 January 1993
Place of birth: Albi, France

Education

2007–2010 Baccalauréat in Maths, Physics, Engineering Sciences
Louis Rascol High School, Albi, France.

2010–2011 Advanced undergraduate program of Engineering School
INSA Strasbourg, France.

2011–2014 Advanced undergraduate program in Maths & Physics
Lapérouse High School, Albi, France.

2014–2018 Master of Science in Aerospace engineering
Specialisation in Conception and Operation of Space Systems and
in Earth Observation and Sciences of the Universe
ISAE-SUPAERO, Toulouse, France.

2020–2024 PhD Candidate in Physics with special qualification in Astronomy
Astronomical Institute, University of Bern.

Work Experience

2016–2017 Internship
IRAP, Toulouse, France.

2017 Internship
Astronomical Institute, University of Bern.

2018 Internship
CNES, Toulouse, France.

2018–2019 Space Flight Dynamic Engineer
CS Group, Toulouse, France.

2019–2020 Research Assistant
Astronomical Institute, University of Bern.

